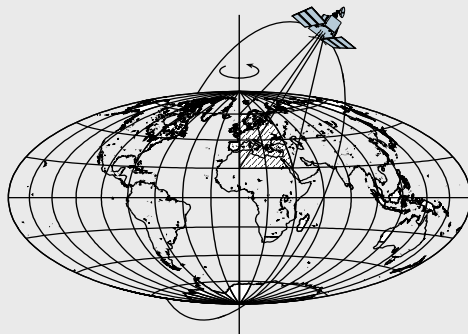


On Improving the Accuracy and Reliability of GPS/INS-Based Direct Sensor Georeferencing

by

Yudan Yi



Report No. 484

Geodetic Science and Surveying

The Ohio State University
Columbus, Ohio 43210

December 2007

ON IMPROVING THE ACCURACY AND RELIABILITY
OF GPS/INS-BASED DIRECT SENSOR GEOREFERENCING

by

Yudan Yi

Geodetic Science and Surveying Graduate Program

The Ohio State University

2007

ABSTRACT

Due to the complementary error characteristics of the Global Positioning System (GPS) and Inertial Navigation System (INS), their integration has become a core positioning component, providing high-accuracy direct sensor georeferencing for multi-sensor mobile mapping systems. Despite significant progress over the last decade, there is still a room for improvements of the georeferencing performance using specialized algorithmic approaches. The techniques considered in this dissertation include: (1) improved single-epoch GPS positioning method supporting network mode, as compared to the traditional real-time kinematic techniques using on-the-fly ambiguity resolution in a single-baseline mode; (2) customized random error modeling of inertial sensors; (3) wavelet-based signal denoising, specially for low-accuracy high-noise Micro-Electro-Mechanical Systems (MEMS) inertial sensors; (4) nonlinear filters, namely the Unscented Kalman Filter (UKF) and the Particle Filter (PF), proposed as alternatives to the commonly used traditional Extended Kalman Filter (EKF).

The network-based single-epoch positioning technique offers a better way to calibrate the inertial sensor, and then to achieve a fast, reliable and accurate navigation solution. Such an implementation provides a centimeter-level positioning accuracy independently on the baseline length. The advanced sensor error identification using the Allan Variance and Power Spectral Density (PSD) methods, combined with a wavelet-based signal de-noising technique, assures reliable and better description of the error characteristics, customized for each inertial sensor. These, in turn, lead to a more reliable and consistent position and orientation accuracy, even for the low-cost inertial sensors. With the aid of the wavelet de-noising technique and the customized error model, around 30 percent positioning accuracy improvement can be found, as compared to the solution using raw inertial measurements with the default manufacturer's error models. The alternative filters, UKF and PF, provide more advanced data fusion techniques and allow the tolerance of larger initial alignment errors. They handle the unknown nonlinear dynamics better, in comparison to EKF, resulting in a more reliable and accurate integrated system. For the high-end inertial sensors, they provide only a slightly better performance in terms of the tolerance to the losses of GPS lock and orientation convergence speed, whereas the performance improvements are more pronounced for the low-cost inertial sensors.

TABLE OF CONTENTS

		Pages
	Abstract.....	ii
Chapters:		
1	Introduction.....	1
	1.1 Background and motivation.....	1
	1.2 Structure of the dissertation.....	7
2	GPS/INS integration.....	8
	2.1 Introduction to the Global Positioning System.....	8
	2.1.1 One-way GPS measurement model.....	8
	2.1.2 Double-difference GPS measurement model.....	11
	2.1.3 GPS velocity and orientation determination.....	13
	2.2 Introduction to the Inertial Navigation System.....	13
	2.2.1 INS principle.....	13
	2.2.2 INS error characteristics.....	16
	2.2.3 INS initialization and initial alignment.....	19
	2.3 Introduction to GPS/INS integration.....	20
	2.3.1 GPS/INS integration mode.....	20
	2.3.2 Linear filtering – Kalman Filter.....	23
	2.3.3 Nonlinear filtering.....	25
	2.3.3.1 Extended Kalman Filter.....	25
	2.3.3.2 Other nonlinear filters.....	26
	2.4 OSU GPS/INS AIMS™ system.....	28
3	Instantaneous positioning technique support network mode.....	34
	3.1 Motivation.....	34
	3.2 Real-time kinematic instantaneous GPS positioning approach.....	37
	3.2.1 Double-difference GPS positioning model with ionospheric pseudo-observations.....	37
	3.2.2 Single-epoch GPS ambiguity resolution.....	40

3.2.3	Stochastic model based on variance component model.....	44
3.2.4	Partial integer ambiguity fixing strategy.....	46
3.2.5	Integer ambiguity bridging between consecutive epochs.....	46
3.3	Analysis of experimental static data.....	47
3.3.1	Baseline-by-baseline mode.....	47
3.3.2	Network mode.....	52
3.4	Analysis of experimental kinematic data.....	53
3.5	Summary and conclusions.....	58
4	Extended stochastic inertial-sensor error identification and modeling.....	60
4.1	Primary INS error sources.....	60
4.2	INS dynamic error modeling.....	64
4.3	INS stochastic error identification and modeling.....	65
4.3.1	INS random error identification.....	66
4.3.1.1	Allan variance analysis.....	66
4.3.1.2	Power spectral density (PSD) method	69
4.3.1.3	Numerical examples.....	71
4.3.1.4	Summary of the INS stochastic error identification using the Allan variance analysis and the PSD method.....	77
4.3.2	INS random error modeling.....	79
4.3.3	Performance comparisons of the customized error model as compared to the default error model from manufacturer's error specifications.....	81
5	Wavelet-based signal de-noising technique.....	83
5.1	Wavelet signal de-noising technique for a low cost MEMS IMU.....	83
5.2	The effects of the wavelet-based de-noising on the initial static coarse alignment.....	90
5.3	The effects of the wavelet-based de-noising on the kinematic navigation solutions.....	91
5.4	The effects of the wavelet de-noising, combined with the customized stochastic error model on kinematic navigation solutions.....	92
6	Alternatives to the Extended Kalman Filter.....	96
6.1	Nonlinear Bayesian filtering.....	97
6.1.1	Conceptual solution.....	97
6.1.2	Unscented Kalman Filter.....	100
6.1.2.1	The implementation using the UKF.....	101
6.1.3	Particle Filter.....	103
6.1.3.1	Monte Carlo approximation.....	103

6.1.3.2	Importance sampling.....	103
6.1.3.3	Sequential importance sampling.....	104
6.1.3.4	Sequential importance resampling.....	107
6.1.3.5	Choice of importance density.....	108
6.1.4	Computational aspects of the UKF, the PF and the EKF.....	109
6.1.5	Computational optimization for the UKF, the PF and the EKF.....	111
6.2	Navigation performance analysis.....	114
6.2.1	Previously reported performance analysis.....	114
6.2.2	Performance analysis for the low-cost MEMS IMU400CC.....	115
6.2.2.1	Orientation performance using the EKF, the UKF and the EPF.....	117
6.2.2.2	Position performance using the EKF, the UKF and the EPF..	127
6.3	Summaries of alternative nonlinear filters.....	131
7	Conclusions, contributions and recommendations.....	133
7.1	Conclusions.....	133
7.2	Contributions.....	134
7.3	Recommendations.....	135
A	Inertial data preprocessing.....	137
B	INS stochastic error identification and modeling.....	144
	Bibliography.....	194

CHAPTER 1

INTRODUCTION

1.1 Background and motivation

In the last two decades, research related to the integration of both the Global Positioning System (GPS) and the Inertial Navigation System (INS) has received a lot of interest in the mobile mapping community (see, for example, Bossler *et al.*, 1991; Bossler, 1992; Salychev & Schaffrin, 1992; Schwarz *et al.*, 1993; Wang *et al.*, 1995; El-Sheimy, 1996; Grejner-Brzezinska, 1997 & 1999; Applanix Corp., 2007). With a full GPS constellation, the GPS sensors can provide stable long-term high-accuracy position and orientation estimates for a moving platform, with the sampling rates of up to 20Hz. However, the system may easily experience short-term losses of signals due to the signal blockage, interference or jamming, especially in urban environments. The self-contained INS or Inertial Measurement Unit (IMU), is not subject to the geometric line-of-sight constraints that GPS suffers from, and can provide short-term high-accuracy position and orientation estimates with high sampling rates (>20Hz). The INS is a navigation system based on the IMU sensor assembly. Note that in this dissertation, the terms INS and IMU will be used as synonyms. The accuracy of the INS will degrade with time due to the uncompensated gyro and accelerometer errors. The resulting errors in the horizontal components (i.e. North and East of position; roll and pitch of orientation) are bounded by the Schuler period, whereas the errors in the height and heading are unbounded (see, for example, Grejner-Brzezinska *et al.*, 1998).

Due to the complementary error characteristics of GPS and INS, GPS/INS fusion has become a standard configuration and a core positioning component for geospatial data collection and mapping tasks. The GPS/INS fusion can continuously provide accurate position and orientation. The position and orientation determination by direct use of GPS/INS fusion is referred to as the direct sensor georeferencing or direct platform orientation (DPO), which is understood as direct measurement of the exterior orientation parameters (EOP, including the three position coordinates and three orientation angles) of the imaging sensors of a multi-sensor integrated system. GPS/INS-based direct sensor georeferencing supports airborne surveying, remote sensing, targeting, guidance and monitoring of moving vehicles, installed in airborne, marine and land-based platforms. In a modern multi-sensor integrated system customized for mapping tasks, land-based or

airborne, the GPS/INS fusion is mandatory as a core component supporting DPO of the image sensors, such as digital cameras, Light Detection And Ranging (LiDAR) devices, multi-spectral or hyper-spectral scanners, or Interferometric Synthetic Aperture Radar (InSAR) and Synthetic Aperture Radar (SAR) instruments. If high-end imaging sensors are used, the accuracy of the navigation performance of the GPS/INS component determines the ultimate accuracy of the mapping products (Grejner-Brzezinska *et al.*, 2005a & 2005b). In recent years, with the emergence of several university-developed prototypes of GPS/INS integrated systems, such as GPSVanTM (Bossler *et al.*, 1991; Bossler, 1992), VISATTM (El-Sheimy, 1996), AIMSTM (Grejner-Brzezinska, 1997), and commercial products, such as Applanix POS/AV (Scherzinger, 1997), GPS aided by INS has been successful in providing position and orientation for precise 3-D surveying and navigation (Grejner-Brzezinska, 1999).

An example application of a GPS/INS-based LiDAR terrain mapping system is illustrated in Figure 1.1. The fundamental georeferencing equation (1.1), shown below for a LiDAR sensor, is the primary tool for applying the directly determined EOP to transform the measured sensor coordinates to the ground coordinates of targets in the selected mapping frame (Grejner-Brzezinska *et al.*, 2005a & 2005b; Yi & Grejner-Brzezinska, 2006b). The accuracy of the resulting coordinates depends upon a number of factors, such as LiDAR error specifications (e.g. the range measurement accuracy, the scan angle range, scan angle errors and footprint size, etc.), the spatial locations of the sensor within the platform (i.e., translational and rotational misalignments), the navigation trajectory (mainly the vertical component) and orientation (mainly the horizontal components: roll and pitch) as well as their solution accuracy. The spatial location of the sensor within the platform can be accurately determined by the sensor calibration procedure. If a well-calibrated LiDAR sensor is used, the target accuracy of the derived surface terrain model is mainly dependent on the position and orientation accuracy provided by GPS/INS. In order to evaluate the sensitivity of the sensor position and orientation accuracy to the realized ground target accuracy, a Monte Carlo simulation with 200 particles was performed to demonstrate the horizontal and vertical accuracy of a ground point for a modern LiDAR sensor commonly used in airborne mapping applications (as shown in Table 1.1).

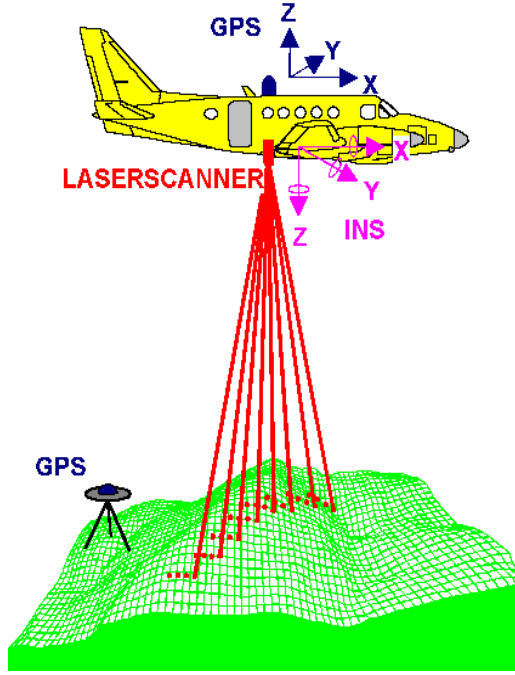


Figure 1.1. GPS/INS-based direct sensor orientation for LiDAR terrain mapping application.

$$r_{M,k} = r_{M,INS} + R_{INS}^M (R_L^{INS} \cdot r_L + b_{INS}) \quad (1.1)$$

where: $r_{M,k}$ is the vector of 3D coordinates of point k in the mapping frame; $r_{M,INS}$ is the vector of 3D coordinates for the INS in the mapping frame obtained by GPS/INS; R_{INS}^M is the rotation matrix between the INS body frame and the mapping frame, measured by the INS; R_L^{INS} is the boresight rotation matrix between the laser sensor frame and the INS body frame; r_L is the vector of 3D object coordinates in the laser frame; b_{INS} is the vector of three boresight offset biases between laser sensor frame and the INS body frame.

In Table 1.1, the following simulation parameters were used: The flight height is 1000 m above the ground; the translational and rotational sensor misalignment accuracies are ± 1 cm and ± 10 arcsec, respectively; the LiDAR range and scan angle measurement accuracies are ± 1 cm and ± 5 arcsec; the effects of the horizontal orientation components

(roll and pitch) and of the scan angle are not considered here (i.e., zero value for the roll, pitch and scan angle); the local navigation system (i.e., NEU) is selected as the target mapping coordinate system.

Navigation accuracy (1σ)		Target position accuracy (1σ)	
σ_{POS} [m] magnitude	σ_{ORI} [arcsec] magnitude	σ_{NE} [m] magnitude	σ_{U} [m] magnitude
0.01	10.0	0.12	0.02
0.01	30.0	0.26	0.02
0.01	90.0	0.75	0.02
0.01	180.0	1.48	0.02
0.01	720.0	5.92	0.04
0.05	10.0	0.14	0.05
0.05	30.0	0.27	0.05
0.05	90.0	0.75	0.05
0.05	180.0	1.48	0.05
0.05	720.0	5.92	0.07
0.10	10.0	0.19	0.10
0.10	30.0	0.30	0.10
0.10	90.0	0.76	0.10
0.10	180.0	1.49	0.10
0.10	720.0	5.92	0.11

Table 1.1. Simulated ground-target position accuracy for an airborne GPS/INS/LiDAR mapping system.

Clearly, high-accuracy position and orientation for the ground-target geo-registration require the best navigation performance of the GPS/INS systems. The centimeter- to decimeter-level positioning accuracy of the ground target point requires centimeter and around 0.0028° (10 arcsec) accuracy in sensor position and orientation. These accuracies are currently provided under favorable GPS geometry and continuity of the dual-frequency GPS signals, in conjunction with the navigation-grade IMUs. It should be emphasized that these systems, however, are very expensive.

Skaloud (2002) lists the achievable orientation accuracy for GPS/INS systems, as a function of the gyro grade, assuming GPS update rates anywhere between 1 and 15 seconds (Table 1.2). The attitude error characteristics can be decomposed into a time-dependent spectrum. Namely, a one-second interval primarily corresponds to the noise, while at 1-3 min the short-term drifts prevail, which may not be fully observable by GPS, even at a 1-second update rate. The absolute orientation error over longer periods of time (with GPS aiding) depends on the dynamics of the trajectory; this means

that performing maneuvers along the trajectory would improve the gyro bias estimation. The error includes the unmodelled part of the long-term gyro drift, not observable by GPS, the unmodelled short-term gyro drift, and the noise.

Time defining the orientation error characteristics	Navigation grade sensor (typically, RLG)		Tactical grade sensor (typically FOG, DTG)	
	pitch and roll [°] (arcsec)	heading [°] (arcsec)	pitch and roll [°] (arcsec)	heading [°] (arcsec)
1 s	0.0008–0.0014 (2.88–5.04)	0.0008–0.002 (2.88–7.2)	0.001–0.02 (3.6–72)	0.001–0.05 (3.6–180)
1-3 minutes	0.0014–0.003 (5.04–10.8)	0.004–0.005 (14.4–18)	0.005–0.04 (18–144)	0.008–0.1 (28.8–360)
Absolute-longer time	Same as for 1-3 minutes but maneuver-dependent			

Table 1.2. Orientation performance based on GPS/INS integration (Skaloud, 2002).

In order to improve the ultimate accuracy of the final mapping products without increasing the cost of the sensors, the navigation algorithms and data processing routines will have to be improved. Currently, a substantial research effort is directed towards further improvement in the navigation performance (for example, Nassar, 2003; Grejner-Brzezinska *et al.*, 2005a & 2005b; Yi *et al.*, 2005; Yi *et al.*, 2005; Yi & Grejner-Brzezinska, 2006a & 2006b). The majority of the existing GPS/INS implementations for DPO are based on the high-end navigation-grade inertial sensors, whose prices are still rather high, as already mentioned, while the performance of the consumer-grade inertial sensors still does not meet the high-accuracy requirements of the majority of the mapping projects. With the growing scope of applications of the scanning imaging systems and increasing need for automation of imaging processes, *the primary objective* of this dissertation is to further improve the accuracy and reliability of the GPS/INS integrated systems designed for mobile mapping applications, especially in confined environments causing frequent losses of GPS lock and lower positioning accuracy due to long GPS baselines. With the rapid emergence of the low-cost micro-electro-mechanical-sensor (MEMS) IMUs, *the second objective*, is to extend the applicability of the low-end MEMS IMU to DPO. The nonlinear Bayesian filters have been of interest to the navigation community in the last few years as an alternative approach to multi-sensor integration. Thus, *the third objective*, is to test several representative nonlinear filter designs, as alternatives to the Extended Kalman Filter (EKF) in GPS/INS integration.

In order to meet the objectives specified here, novel algorithms and data reduction procedures as well as state-of-the-art approaches to sensor error modeling are implemented in this dissertation to improve the performance of the existing high-end

sensors, and to support the use of low-end sensors in mapping applications. Four approaches to potential improvements in GPS/INS-based DPO performance in both land-based and airborne platforms are investigated in this dissertation, including (1) a single-epoch GPS positioning technique supporting the network mode as an alternative to the commonly used single-baseline solution, which dominates the position accuracy of GPS/INS integrated systems, and can provide better calibration to the inertial sensor errors; (2) extended stochastic error modeling of inertial sensors; (3) wavelet-based signal de-noising, which mainly applies to the low-end MEMS sensors; (4) nonlinear filters as alternatives to the Extended Kalman Filter. The example analysis for these approaches using experimental and simulated data indicates that 1) it is possible to further improve the navigation performance and ultimately the target accuracy using multi-sensor integrated systems, and 2) it is feasible to exploit the capability of the low-cost MEMS IMU integrated with GPS and other navigation/orientation sensors but only for low-accuracy mobile mapping applications.

Except for the aforementioned techniques investigated in this dissertation, other techniques might also be beneficial to the objectives described here. Figure 1.2 illustrates the possible approaches to achieve the research objectives for an example system based on the tightly-coupled integration. For example, the accurate gravity compensation using the Deflection of Verticals (DOVs) results in better navigation performance for the high-end inertial sensor (see, for example, Grejner-Brzezinska & Wang, 1998; Jekeli, 2001; Grejner-Brzezinska *et al.*, 2003; Grejner-Brzezinska *et al.*, 2005a & 2005b). The automatic trigger to request periodical stops of the vehicle can improve the performance of the land-base GPS/INS integrated system by performing the zero-velocity measurement update (ZUPT) (see, for example, Grejner-Brzezinska *et al.*, 2001a & 2001b). In the GPS/INS-based imaging systems, the image component feedback can also bound the INS error drifts when GPS is not available in the confined environments (see, for example, Hassan *et al.*, 2006; Moafipoor, 2006; Veth and Raquet, 2006). Other sensors, for example, the altimeter, the magnetic sensors, pseudolites, and multiple GPS antenna systems supporting attitude estimation, can form a more reliable GPS/INS-based multi-sensor integrated system (see, for example, Yi *et al.*, 2003; Grejner-Brzezinska & Yi, 2003; Grejner-Brzezinska *et al.*, 2006).

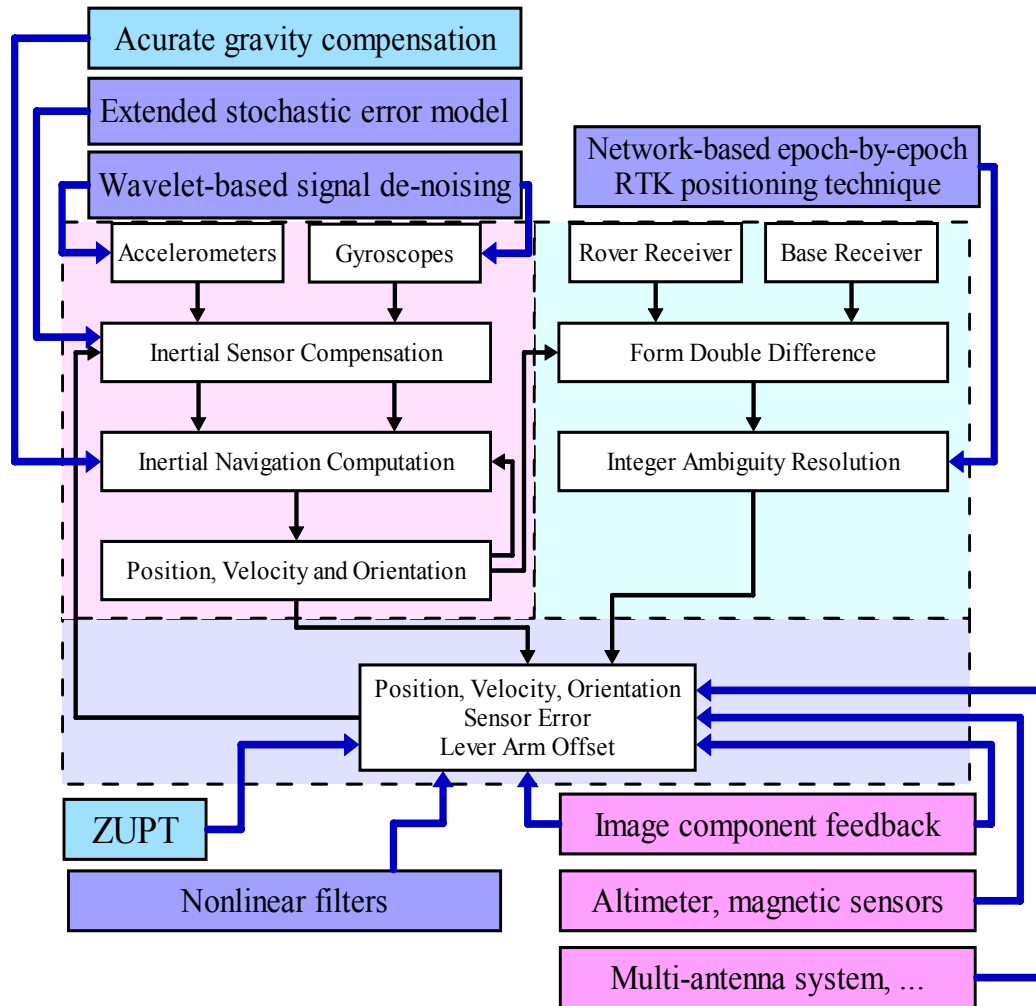


Figure 1.2. Possible approaches to achieve research objectives in this dissertation.

1.2 Structure of the dissertation

Chapter 1 is the introduction, which summarizes the background and motivation of this dissertation. Chapter 2 reviews the GPS, INS and their integration techniques, and describes the hardware, algorithms and software suites used in and developed for this dissertation. Chapter 3 reviews the conventional mathematical model for GPS, as used in GPS/INS integration, and introduces the single-epoch GPS positioning technique supporting network mode to provide distance-independent and epoch-independent kinematic solutions with the uniform and reliable accuracy. Chapter 4 investigates the extended stochastic error identification and modeling techniques for inertial sensors. Chapter 5 introduces the wavelet-based signal de-noising technique to improve the performance of inertial sensors, especially the low-cost MEMS IMUs. The nonlinear filters, as alternatives to EKF, are investigated in Chapter 6. The conclusions and recommendations are presented in Chapter 7.

CHAPTER 2

GPS/INS INTEGRATION

This chapter provides a brief introduction to the Global Positioning System, the Inertial Navigation System, and their integration principles. The mathematical models for the GPS-only and INS-only positioning algorithms, as well as the filtering technique for their integration, are summarized here. The software and hardware components designed for and analyzed in this dissertation are introduced and illustrated at the end of this chapter.

2.1 Introduction to the Global Positioning System (GPS)

Even though the Global Positioning System was originally designed by the U.S. Department of Defense (DoD) for military purposes, currently, civilian applications are expanding rapidly, thereby supporting a number of navigation and positioning services worldwide under all-weather, any-time conditions. GPS is a radio navigation system that allows the determination of the target position and velocity based on simultaneous range measurements to multiple known signal-transmitting stations, i.e., GPS satellites, by measuring the travel time of the radio-navigation signal (Hofmann-Wellenhof *et al.*, 1997; Leick, 1995). The satellite navigation system using GPS-like radio signals from the satellites to provide the navigation services to the users with global coverage are referred to as Global Navigation Satellite Systems (GNSS), which currently includes, the fully operational USA-based GPS, the Russian GLObal NAVigation Satellite System (GLONASS), the future European Galileo positioning system (Galileo), the Japan Quasi Zenith Satellite System (QZSS), and the Chinese Compass satellite system. Only the GPS is considered explicitly in this dissertation.

2.1.1 One-way GPS measurement model

With the full operational capability of the GPS constellation realized in 1995 and advanced GPS receiver tracking techniques, the dual frequency geodetic-grade GPS sensor has become the primary positioning device in multi-sensor integration for direct sensor georeferencing. The basic, one-way raw GPS observations for one receiver and one satellite of the dual frequency GPS sensors include the code pseudo-ranges (derived using C/A_1 , $P_1(Y_1)$, and $P_2(Y_2)$ codes) and the carrier-phase pseudo-ranges (Φ_1 and Φ_2)

measurements for position determination, and the Doppler measurements (D_1 and D_2) for velocity determination. Currently, three Block IIR-M GPS satellites also broadcast a second civilian code measurement C/A_2 on L_2 frequency (1227.60MHz) and a third civilian code measurement P_5 will be available on the new L_5 frequency (1176.45MHz) in the future. These GPS observations are biased by several error sources. The GPS observations come with a stochastic error model representing their noise characteristics, to be used in the least-squares adjustment process that determines the position and velocity. The major nuisance error sources, which affect the GPS observations, include satellite and receiver clock biases and drifts, satellite orbit errors, atmospheric (i.e., ionospheric and tropospheric) delays, environment-related multipath effects, hardware related inter-channel and inter-frequency biases, etc. Equations (2.1-2.6) show the mathematical models that relate these one-way GPS observations for receiver i and satellite k to the unknown parameters (position and velocity vectors) and other major nuisance terms. Various carrier-phase linear combinations are also widely used, together with the raw one-way GPS observations, and a general carrier-phase linear combination form is shown in equation (2.7).

$$P_{i,1}^k = \rho_i^k + c(dt_i - dT^k) + T_i^k + M_{i,1}^k + I_i^k + e_{i,1}^k \quad (2.1)$$

$$P_{i,2}^k = \rho_i^k + c(dt_i - dT^k) + T_i^k + M_{i,2}^k + \beta I_i^k + B_i - B^k + e_{i,2}^k \quad (2.2)$$

$$\Phi_{i,1}^k \equiv \lambda_1 \varphi_{i,1}^k = \rho_i^k + c(dt_i - dT^k) + T_i^k + \lambda_1 m_{i,1}^k - I_i^k + \lambda_1 (N_{i,1}^k + N_{i,1}^{k*}) + \lambda_1 \varepsilon_{i,1}^k \quad (2.3)$$

$$\Phi_{i,2}^k \equiv \lambda_2 \varphi_{i,2}^k = \rho_i^k + c(dt_i - dT^k) + T_i^k + \lambda_2 m_{i,2}^k - \beta I_i^k + \lambda_2 (N_{i,2}^k + N_{i,2}^{k*}) + \lambda_2 \varepsilon_{i,2}^k \quad (2.4)$$

$$D_{i,1}^k = \dot{\rho}_i^k + \dot{T}_i^k + \lambda_1 \dot{m}_{i,1}^k - \dot{I}_i^k + v_{i,1}^k \quad (2.5)$$

$$D_{i,2}^k = \dot{\rho}_i^k + \dot{T}_i^k + \lambda_2 \dot{m}_{i,2}^k - \beta \dot{I}_i^k + v_{i,2}^k \quad (2.6)$$

$$\begin{aligned} \varphi_{i,mn}^k &= \frac{\rho_i^k}{\lambda_{mn}} + \frac{c(dt_i - dT^k)}{\lambda_{mn}} + \frac{T_i^k}{\lambda_{mn}} + (m \cdot m_{i,1}^k + n \cdot m_{i,2}^k) - (m + n \frac{f_1}{f_2}) \frac{I_i^k}{\lambda_1} + \\ &[m(N_{i,1}^k + N_{i,1}^{k*}) + n(N_{ij,2}^{kl} + N_{i,2}^{k*})] + (m\varepsilon_{i,1}^k + n\varepsilon_{i,2}^k) \end{aligned} \quad (2.7)$$

where the subscript i stands for a GPS receiver; the superscript k stands for a GPS satellite; the subscripts 1 and 2 stand for the carrier frequencies on L_1 and L_2 ; m and n are integer coefficients for the carrier-phase linear combinations; dot above the variables stands for the time derivative; $()_i^k$ represents the one-way variables relating to receiver i and satellite k ; $()_i$ represents the variables relating to receiver i only; $()^k$ represent the variables relating to satellite k only; P_1 , P_2 and Φ_1 , Φ_2 represent the code and

carrier-phase pseudo-range measurements on L_1 and L_2 in meters; D_1 and D_2 represent the Doppler measurements on L_1 and L_2 in meters per second; φ_1 and φ_2 represent the carrier-phase pseudo-range measurements on L_1 and L_2 in cycles; $\rho_i^k = \|\mathbf{r}^k - \mathbf{r}_i\| = \sqrt{(X^k - X_i)^2 + (Y^k - Y_i)^2 + (Z^k - Z_i)^2}$ is the geometric range between the receiver i and satellite k ; \mathbf{r} is the position vector for the receiver or satellite in a selected coordinate system; $\dot{\rho}_i^k = \frac{(\mathbf{r}^k - \mathbf{r}_i)^T}{\|\mathbf{r}^k - \mathbf{r}_i\|} (\dot{\mathbf{r}}^k - \dot{\mathbf{r}}_i)$, and $\dot{\mathbf{r}}$ is the velocity vector for the receiver and satellite; c is the velocity of light; dt and dT are the receiver and satellite clock errors; M_1, M_2 and m_1, m_2 are the multipath errors for code and carrier-phase measurements on L_1 and L_2 , respectively; $I = \frac{40.3 \cdot \text{TEC}}{f_1^2}$ is the ionospheric delay on the L_1 code measurement; TEC is Total Electron Contents along the ray of the GPS signals; the $\beta = \frac{f_1^2}{f_f^2}$ is the coefficient for the ionospheric delay on L_2 with respect to the ionospheric delay on L_1 ; λ_1, λ_2 and f_1, f_2 are the wavelengths and frequencies on L_1 and L_2 , respectively; N_1, N_2 and N_1^*, N_2^* are the carrier-phase integer ambiguities and initial non-integer fractional parts on L_1 and L_2 , respectively; N_1^* and N_2^* also include the inter-frequency bias terms on L_1 and L_2 carrier-phase measurements (φ_1 and φ_2) with respect to L_1 code measurements (P_1), which are inseparable from the actual initial non-integer fractional phase on both frequencies; the e_1, e_2 and $\varepsilon_1, \varepsilon_2$ are the code and carrier-phase pseudo-range measurement noises on L_1 and L_2 , respectively; v_1 and v_2 are the code and Doppler measurement noises on L_1 and L_2 , respectively; B_i and B^k are the differential code biases (DCBs) for receiver i and satellite k .

These major error terms shown in equations (2.1-2.7) should be 1) compensated using appropriate a priori models, or 2) estimated together with the unknown parameters, or 3) eliminated using some specific methodologies, such as forming linear combinations, or 4) simply ignored (if applicable or feasible) according to the purposes of the required applications. For example, GPS satellite clock errors can be modeled as a second order polynomial function using the broadcast coefficients in the navigation message, or can be compensated using the ultra-rapid, rapid or final precise satellite clock products that are provided with various time latencies and various accuracies. The International GNSS Service (IGS) (<http://igsceb.jpl.nasa.gov/>) can provide the ultra-rapid, rapid or final precise satellite orbit products instead of the broadcast satellite orbit product in the navigation message to minimize the satellite orbit errors. Most of the tropospheric delay effects can

be eliminated using a priori tropospheric models, for example, the Hopfield model (Hopfield, 1969). The Klobuchar ionospheric model, using the broadcast ionospheric coefficients in the navigation message, can only compensate around 50 percent of the ionospheric delay effects (see, for example, ICD-GPS-200). The IGS CODE (Center for Orbit Determination in Europe) analysis center generates the daily Global Ionospheric Maps (GIMs), which are much better than the broadcast Klobuchar ionospheric model. GIMs are produced using the measurements from about 200 globally distributed GPS/GLONASS sites (<http://www.aiub.unibe.ch/ionosphere.html>). The GIMs are delivered in an IONospheric map EXchange (IONEX) data format, supporting the exchange of 2- and 3-dimensional Total Electron Content (TEC) in a geographic grid (Schaer & Gurtner, 1998). The GIM products are also delivered as a Klobuchar-style ionospheric coefficients derived from the global ionospheric model.

The dual-frequency GPS receivers will allow the cancellation of the first-order ionospheric delay using the ionospheric-free linear combinations between L_1 and L_2 frequencies. As a by-product of the GIMs, the satellite instrumental biases (i.e., satellite differential code biases, DCBs) for all the GPS/GLONASS satellites are also provided by IGS to compensate for the satellite instrumental bias (B^k) term in equation (2.2). Multipath effects are difficult to model and are normally decreased using advanced antenna hardware designs. The inter-channel biases between different satellite channels (not shown in equations (2.1-2.7)) are only considered for very high-accuracy (for example, millimeter level) applications. GPS carrier-phase integer ambiguities are very important when dealing with the carrier-phase positioning, and numerous techniques, often referred to as Ambiguity Resolution (AR), have been proposed to estimate or eliminate them (see, for example, Euler & Schaffrin, 1990; Teunissen, 1993 & 1994; Hatch 1990; Hatch & Euler, 1994).

2.1.2 Double-difference GPS measurement model

Normally, in order to provide the highest accuracy for real-time kinematic (RTK) applications, the differential GPS (DGPS) in a double-difference (DD) mode between two receivers and two satellites using high-accuracy carrier-phase measurements, though biased by the ambiguities, is commonly applied. In the double-difference mode, the observations between two receivers (base and rover) and two satellites are differenced, which allows for canceling (or a significant reduction) the majority of common error sources while leaving some differential distance-dependent errors (i.e., differential GPS orbit and clock errors as well as differential atmospheric delays that become significant for long baselines). The aforementioned data reduction and/or data compensation by the a priori error models and differential techniques simplify the mathematical models shown in equations (2.1-2.7), and equations (2.8-2.13) are normally implemented in the majority of GPS software packages used for position and velocity determination. Both the one-way and double-difference models are equivalent (i.e., lead to identical least-squares

adjustment results) under the conditions presented by Schaffrin & Grafarend (1986). Such GPS double-difference data processing model will be used in this dissertation discussed in Chapter 3.

$$\bar{P}_{ij,1}^{kl} = \rho_{ij}^{kl} + T_{ij}^{kl} + I_{ij}^{kl} + e_{ij,1}^{kl} \quad (2.8)$$

$$\bar{P}_{ij,2}^{kl} = \rho_{ij}^{kl} + T_{ij}^{kl} + \beta I_{ij}^{kl} + e_{ij,2}^{kl} \quad (2.9)$$

$$\bar{\Phi}_{ij,1}^{kl} \equiv \lambda_1 \bar{\varphi}_{ij,1}^{kl} = \rho_{ij}^{kl} + T_{ij}^{kl} - I_{ij}^{kl} + \lambda_1 N_{ij,1}^{kl} + \lambda_1 \varepsilon_{ij,1}^{kl} \quad (2.10)$$

$$\bar{\Phi}_{ij,2}^{kl} \equiv \lambda_2 \bar{\varphi}_{ij,2}^{kl} = \rho_{ij}^{kl} + T_{ij}^{kl} - \beta I_{ij}^{kl} + \lambda_2 N_{ij,2}^{kl} + \lambda_2 \varepsilon_{ij,2}^{kl} \quad (2.11)$$

$$\bar{D}_{ij,1}^{kl} = \dot{\rho}_{ij}^{kl} + v_{ij,1}^{kl} \quad (2.12)$$

$$\bar{D}_{ij,2}^{kl} = \dot{\rho}_{ij}^{kl} + v_{ij,2}^{kl} \quad (2.13)$$

$$\bar{\varphi}_{ij,mn}^{kl} = \frac{\rho_{ij}^{kl}}{\lambda_{mn}} - \left(m + n \frac{f_1}{f_2}\right) \frac{I_{ij}^{kl}}{\lambda_1} + (mN_{ij,1}^{kl} + nN_{ij,2}^{kl}) + (m\varepsilon_{ij,1}^{kl} + n\varepsilon_{ij,2}^{kl}) \quad (2.14)$$

Where the subscripts i and j stand for receivers; the superscripts k and l stand for satellites; $(\cdot)_{ij}^{kl} = [(O_j^l - O_i^l) - (O_j^k - O_i^k)]$ represents the double-difference variable relating to two receivers (i and j) and two satellites (k and l); the measurements (\bar{P}_1 , \bar{P}_2 , $\bar{\Phi}_1$, $\bar{\Phi}_2$, \bar{D}_1 , \bar{D}_2 , $\bar{\varphi}_1$ and $\bar{\varphi}_2$) represent the corresponding measurements after GPS error model reduction, mitigation, or simplification.

The position accuracy for a single baseline can attain a centimeter to a sub-meter accuracy, depending on the base-rover separation, after resolving the double-difference carrier-phase integer biases (i.e., the ambiguities) based on the GPS integer ambiguity resolution, referred to as On-The-Fly (OTF) (see, for example, Yang *et al.*, 1994) GPS technique for real-time kinematic applications. The basic principle of the OTF technique is as follows: firstly, the code pseudo-range measurements are incorporated with the carrier-phase pseudo-range measurements to estimate the double-difference float ambiguities using the least-squares adjustment; then, a search algorithm is applied to optimally determine the double-difference integer ambiguities from the float values and their corresponding variance-covariance matrix; the final estimates (i.e. the coordinates of the receiver position) are based on the high-accuracy double-difference carrier-phase measurements with the resolved double-difference integer ambiguity biases. The AR together with its validation procedure plays a key role in the high-accuracy

Real-Time-Kinematic (RTK) positioning. Several methods of AR and its validation exist; and a very comprehensive literature review for the ambiguity resolution and validation can be found in Kim & Langley (2000). Recent research on the subject of ambiguity resolution and validation can be found in, for example, Verhagen (2004 & 2005), Teunissen & Verhagen (2004 & 2007). Currently, OTF implemented over a single baseline (i.e., one reference receiver and one rover receiver) within a short distance (normally less than 20 kilometer (km)), using observations from multiple epochs is the most commonly used GPS technique; however, single-epoch methods and network-based kinematic positioning supporting longer baselines (normally, over 20 km) have become of interest recently, as will be explained in Chapter 3.

2.1.3 GPS velocity and orientation determination

The velocity determination using GPS is mainly based on Doppler (i.e., phase-rate) measurements, and its accuracy ranges from centimeter (cm) to millimeter (mm) per second depending on the satellite velocity accuracy, the level of receiver dynamics, atmospheric (tropospheric and ionospheric) higher-order effects, multipath effects and the measurement noise (see, for example, Ryan *et al.*, 1997; Serrano *et al.*, 2004). The basic principle of the GPS-based orientation determination takes the advantage of the mm-level positioning accuracy of the double-difference carrier-phase positioning technique, achievable for very short baselines (around 1-2 m); the orientation of the vehicle can be derived using multiple GPS antennas (at least 3 non-coplanar GPS antennas) installed in a vehicle. The accuracy of the orientation determination can be attained to a few arc-minutes in yaw (heading), pitch and roll, depending on the antenna separation, using carrier-phase measurements in double-difference mode (see, for example, Lu, 1994).

2.2 Introduction to the Inertial Navigation System (INS)

2.2.1 INS principle

Besides GPS, the self-contained Inertial Navigation System is the most commonly-used navigation system. The modern origin of inertial navigation dates back to the 1940s and early 1950s, where Inertial Measurement Units, including three orthogonal accelerometers and three orthogonal gyroscopes, were used to detect and measure translational and rotational motions (linear accelerations sensed by accelerometers and angular rates sensed by gyroscopes) based on the physical laws of nature (see, for example, Titterton & Weston, 1997; Farrell & Barth, 1999; Jekeli, 2001).

An example review of the recent inertial navigation history can be found in King (1998). Newton's second law of motion, instrumental for inertial navigation, as defined in the inertial (non-rotation) frame, is shown in equation (2.15) below. The 3-dimensional kinematic acceleration vector ($\ddot{\mathbf{r}}$) in the inertial frame (referred to as *i*-frame) can be computed from the sensed linear acceleration vector (\mathbf{f}) of the three orthogonal

accelerometers, combined with the gravity vector (\mathbf{g}) which is normally computed from a pre-defined gravity model, for example the normal ellipsoidal gravity model. Given the initial 3-dimensional position and velocity in the i -frame, the kinematic accelerations ($\ddot{\mathbf{r}}$) can be directly integrated to obtain the 3-dimensional position and velocity also in the i -frame. However, a navigation coordinate system (referred to as n -frame), different from the i -frame is often adopted for the inertial navigation system. A transformation matrix (\mathbf{C}_b^n), maintained by the orientation angles that are normally determined from the angular rates of the three orthogonal gyroscopes, is used to define the transformation from the IMU body frame (referred to as b -frame) to the n -frame. The determination of the initial position, velocity and orientation is referred to as the INS initialization and alignment procedure. The desired position and orientation are normally expressed through their geodetic coordinates (latitude, longitude and ellipsoidal height), and through three rotation angles (roll, pitch and yaw). The aforementioned procedure to determine the position, velocity and orientation, given their initial values, is referred to as the INS dynamic navigation equation, and can be expressed through nine nonlinear differential navigation equations (see, for example, Farrell & Barth, 1999; Jekeli, 2001). The three non-linear orientation (pitch, roll and yaw) parameter determination based on the sensed angular-rate measurements, will become ill-posed when the pitch angle θ approaches $\pm 90^\circ$. An alternative approach in terms of quaternions is widely implemented to avoid such a singularity in most of the inertial applications, and the transformation matrix can be constructed in either way using quaternions or three orientation angles (Farrell & Barth, 1999; Jekeli, 2001). The nonlinear differential navigation equations, using the quaternion algorithm, are shown in equations (2.16-2.18) and the Euler solutions of these nonlinear differential equations are shown in equations (2.19-2.21).

$$\ddot{\mathbf{r}}^b = \mathbf{f}^b + \mathbf{g}(\mathbf{r}^b) \quad (2.15)$$

$$\dot{\mathbf{r}}^n = \mathbf{v}^n - \boldsymbol{\omega}_{en}^n \times \mathbf{r}^n \quad (2.16)$$

$$\dot{\mathbf{v}}^n = \mathbf{C}_b^n \mathbf{f}_{ib}^b + \mathbf{g}^n - (\boldsymbol{\omega}_{in}^n + \boldsymbol{\omega}_{ie}^n) \times \mathbf{v}^n \quad (2.17)$$

$$\dot{\mathbf{q}} = \frac{1}{2} A \mathbf{q} = \frac{1}{2} B \boldsymbol{\omega} \quad (2.18)$$

$$\mathbf{r}_{k+1} = \mathbf{r}_k + (\mathbf{v}_k - \boldsymbol{\omega}_{en}^n \times \mathbf{r}_k) \Delta t \quad (2.19)$$

$$\mathbf{v}_{k+1} = \mathbf{v}_k + [\mathbf{C}_b^n \mathbf{f}_{ib}^b + \bar{\mathbf{g}} + (\boldsymbol{\omega}_{in}^n + \boldsymbol{\omega}_{ie}^n) \times \mathbf{v}_k] \Delta t \quad (2.20)$$

$$\mathbf{q}_{k+1} = \exp\left(\frac{1}{2} \int_{t_k}^{t_{k+1}} \mathbf{A} dt\right) \mathbf{q}_k = \exp\left(\frac{\Sigma}{2}\right) \mathbf{q}_k = \mathbf{q}_k \cdot \mathbf{q}_\Delta \quad (2.21)$$

$$\begin{cases} \boldsymbol{\omega}_{en}^n = [\dot{\lambda} \cos \phi & -\dot{\phi} & -\dot{\lambda} \sin \phi]^T \\ \boldsymbol{\omega}_{ie}^n = [\boldsymbol{\omega}_e \cos \phi & 0 & \boldsymbol{\omega}_e \sin \phi]^T \\ \boldsymbol{\omega}_{in}^n = \boldsymbol{\omega}_{ie}^n + \boldsymbol{\omega}_{en}^n \end{cases} \quad (2.22)$$

$$(\mathbf{a} \times) = \text{skew}_3(\mathbf{a}) = \begin{bmatrix} 0 & -\mathbf{a}_3 & \mathbf{a}_2 \\ \mathbf{a}_3 & 0 & -\mathbf{a}_1 \\ -\mathbf{a}_2 & \mathbf{a}_1 & 0 \end{bmatrix}. \quad (2.23)$$

$$\text{skew}_4(\mathbf{a}) = \begin{bmatrix} \mathbf{a}_0 & -\mathbf{a}_1 & -\mathbf{a}_2 & -\mathbf{a}_3 \\ \mathbf{a}_1 & \mathbf{a}_0 & -\mathbf{a}_3 & \mathbf{a}_2 \\ \mathbf{a}_2 & \mathbf{a}_3 & \mathbf{a}_0 & -\mathbf{a}_1 \\ \mathbf{a}_3 & -\mathbf{a}_2 & \mathbf{a}_1 & \mathbf{a}_0 \end{bmatrix} \quad (2.24)$$

Where the superscripts and subscripts (b , n , i and e) refer to the coordinate frames (b : body-frame, n : navigation frame, i : inertial frame, e : earth-centered-earth-fixed frame); \mathbf{r} , \mathbf{f} , \mathbf{v} and \mathbf{g} are the position, acceleration (i.e., force), velocity, and gravity vectors; the variables with one dot above represent their first-order time derivatives; the variables with two dots above represent their second-order time derivatives; $\boldsymbol{\omega}_{ib}^b = [\omega_1, \omega_2, \omega_3]^T$ is the vector of angular rates, sensed by the three gyroscopes in the b -frame and coordinated in the b -frame; $\boldsymbol{\omega} = [\omega_0, \omega_1, \omega_2, \omega_3]^T$ with $\omega_0=0$ is the 4-dimensional angular rate vector; $\mathbf{q} = [q_0, q_1, q_2, q_3]^T$ is the 4-dimensional quaternion vector; $A = \text{skew}_4^T(\boldsymbol{\omega})$ and $B = \text{skew}_4(\mathbf{q})$ where the definition of $\text{skew}_4()$ for a 4-dimensional vector $\mathbf{a} = [a_0 \ a_1 \ a_2 \ a_3]^T$ is shown in (2.24); $\Sigma = A \cdot \Delta t$; (\times) denotes the 3-dimensional skew matrix operation defined as $\text{skew}_3()$ and shown in equation (2.23) on a 3-dimensional vector $\mathbf{a} = [a_1 \ a_2 \ a_3]^T$; $\Delta\boldsymbol{\theta} = [\Delta\theta_1, \Delta\theta_2, \Delta\theta_3]$ is a vector of incremental angles, sensed by the three gyroscopes in the body frame and coordinated in the body frame; \mathbf{q}_Δ is the 4×1 vector of angle quaternions for $\Delta\boldsymbol{\theta}$; $\mathbf{f}_{ib}^b = [f_1, f_2, f_3]^T$ is the vector of accelerations, sensed by the three accelerometers in the body frame and coordinated in the body frame; ω_e is the earth rotation rate; λ and ϕ are the geodetic longitude and the geodetic latitude.

The INS principles require an accurate gravity model to compensate the local gravity vector \mathbf{g} shown in equation (2.15) in order to produce an accurate kinematic acceleration; traditionally, a normal gravity model or a higher-order spherical-harmonics gravity model is used, while accurate Deflections Of the Vertical (DOVs) can also be included in the

navigation equations to improve the INS navigation performance (Grejner-Brzezinska & Wang, 1998; Jekeli, 2001).

Several INS mechanization methods exist. The most widely used INS mechanization today is the strapdown system where IMUs are physically and firmly mounted to the platform, and the inertial measurements are mathematically transformed to the navigation frame. Thus, the IMUs are subjected to the entire range of the platform dynamics. The advantage of the strapdown inertial navigation system (SINS), compared to other existing mechanizations (such as the gimballed inertial system), lies in the smaller size, less weight, less power consumption and lower costs. The majority of the currently implemented GPS/INS-integrated system for direct sensor georeferencing is based on the strapdown mechanization.

2.2.2 INS error characteristics

Even if the best initial conditions are provided, perfect position, velocity and orientation still cannot be achieved by the inertial navigation according to the non-linear nature of the differential dynamic navigation equations shown in equations (2.16-2.18), and due to the contamination of the inertial measurements by the systematic and random errors. The primary error sources for the INS include: 1) IMU (accelerometers and gyroscopes) instrumental errors, for example gyroscope and accelerometer misalignment errors, biases and drifts; 2) the gravity model errors, including gravity anomalies and Deflections of the Verticals; 3) numerical computation errors; 4) the selected inertial navigation model errors; for example, an EKF is widely used to obtain a sub-optimal solution to the non-linear differential navigation equations; 5) initial position, velocity and alignment errors; 6) other errors, such as analog-to-digital quantization errors, etc. As a result, these errors will accumulate and the final navigation errors will grow with time, due to the time integration involved in the solutions of the nonlinear differential dynamic navigation equations.

The most significant error sources for the inertial navigation are the sensor instrumental errors, which dominate the navigation performance. There are inertial sensors of different grade that utilize various technologies suitable for different applications. The principle of a gyroscope sensor can vary, and the currently available mechanizations include 1) mechanical gyros, measuring the reactions of a spinning proof mass; 2) optical gyros, including Ring Laser Gyros (RLG) and Fiber Optic Gyros (FOG), based on a particular property of light in a rotating frame known as *Sagnac* effect (Jekeli, 2001); and 3) MEMS gyros, using vibrating ceramic plates that utilize the Coriolis force to output angular rate independently of acceleration (Jekeli, 2001). Table 1.2 lists the orientation accuracy as a function of the gyroscopes. The accelerometers could be mechanized as 1) mechanical accelerometers using a proof mass, for example the force feedback pendulum; and 2) solid-state accelerometers, such as the MEMS accelerometer, using differential capacitance to sense the acceleration (Titterton & Weston, 1997).

According to the error propagation with time, an INS can be categorized as 1) low-accuracy, tactical grade system with an accuracy worse than $\pm 4\text{km/hr}$, 2) medium-accuracy, navigation-grade system with an accuracy of $\pm 1\text{-}4\text{km/hr}$, or 3) as high-accuracy system, typically rated at $\pm 0.2\text{-}1\text{km/hr}$ or better (Jekeli, 2001). In order to evaluate the errors driven by the initialization, computation, instrument, gravity model, and other errors, the dynamic error model can be derived using the nominal state vectors based on the first-order Taylor approximation for the non-linear dynamic navigation equations. The linearized error dynamic equation (including the system description noise) is expressed as a state-vector-based linear differential equation in (2.25) and can be easily implemented using a Kalman Filter (KF), including a 9-dimensional navigation error state sub-vector (3 for the position, 3 for the velocity and 3 for the orientation) $x_{\text{pv}\psi}$, an accelerometer error state sub-vector x_f , a gyroscope error state sub-vector x_ω , and a 3-dimensional gravity disturbance state sub-vector x_g (Siouris, 1993; Farrell & Barth, 1999; Jekeli, 2001). A detailed linear error model for the navigation state sub-vector, called psi-angle error model (Bar-Itzhack & Berman, 1988), is shown in equation (2.26). The psi-angle error model is widely implemented in GPS/INS-integrated systems for mobile mapping applications. The detailed forms of the \mathbf{F}_{11} matrix blocks of equation (2.25) when using the psi-angle error model, as shown in equation (2.26), are listed in equations (2.27-2.32).

$$\begin{bmatrix} \dot{x}_{\text{pv}\psi} \\ \dot{x}_f \\ \dot{x}_\omega \\ \dot{x}_g \end{bmatrix} = \begin{bmatrix} \mathbf{F}_{11} & \mathbf{F}_{12} & \mathbf{F}_{13} & \mathbf{F}_{14} \\ 0 & \mathbf{F}_{22} & 0 & 0 \\ 0 & 0 & \mathbf{F}_{33} & 0 \\ 0 & 0 & 0 & \mathbf{F}_{44} \end{bmatrix} \begin{bmatrix} x_{\text{pv}\psi} \\ x_f \\ x_\omega \\ x_g \end{bmatrix} + \begin{bmatrix} v_{\text{pv}\psi} \\ v_f \\ v_\omega \\ v_g \end{bmatrix} \quad (2.25)$$

$$\begin{cases} \delta \dot{\mathbf{r}} = \delta \mathbf{v} - \boldsymbol{\omega}_{en}^n \times \delta \mathbf{r} \\ \delta \dot{\mathbf{v}} = \mathbf{C}_b^n \delta \mathbf{f}_{ib}^b + \mathbf{f}^n \times \boldsymbol{\psi} + \delta \bar{\mathbf{g}} - (\boldsymbol{\omega}_{in}^n + \boldsymbol{\omega}_{ie}^n) \times \delta \mathbf{v} \\ \dot{\boldsymbol{\psi}} = \delta \boldsymbol{\omega}_{in}^n - \mathbf{C}_b^n \delta \boldsymbol{\omega}_{ib}^b - \boldsymbol{\omega}_{in}^n \times \boldsymbol{\psi} \end{cases} \quad (2.26)$$

$$\mathbf{F}_{11} = \begin{bmatrix} \mathbf{F}_{\text{pp}} & \mathbf{F}_{\text{pv}} & 0 \\ \mathbf{F}_{\text{vp}} & \mathbf{F}_{\text{vv}} & \mathbf{F}_{\text{v}\psi} \\ 0 & 0 & \mathbf{F}_{\psi\psi} \end{bmatrix} \quad (2.27)$$

$$\mathbf{F}_{\text{pp}} = \begin{bmatrix} 0 & (\boldsymbol{\omega}_{en}^n)_3 & -(\boldsymbol{\omega}_{en}^n)_2 \\ -(\boldsymbol{\omega}_{en}^n)_3 & 0 & (\boldsymbol{\omega}_{en}^n)_1 \\ (\boldsymbol{\omega}_{en}^n)_2 & -(\boldsymbol{\omega}_{en}^n)_1 & 0 \end{bmatrix}, \quad \mathbf{F}_{\text{pv}} = \begin{bmatrix} 1 & 0 & 0 \\ 0 & 1 & 0 \\ 0 & 0 & 1 \end{bmatrix} \quad (2.28)$$

$$\mathbf{F}_{\mathbf{v}\mathbf{p}} = \begin{bmatrix} -\frac{(\mathbf{g} + (\mathbf{f}^n)_3)}{R_N} & 0 & 0 \\ 0 & -\frac{(\mathbf{g} + (\mathbf{f}^n)_3)}{R_N} & 0 \\ 0 & 0 & \frac{2 \cdot (\mathbf{g} + (\mathbf{f}^n)_3)}{R_N} \end{bmatrix} \quad (2.29)$$

$$\mathbf{F}_{\mathbf{v}\mathbf{v}} = \begin{bmatrix} 0 & (\boldsymbol{\omega}_{ie}^n + \boldsymbol{\omega}_{in}^n)_3 & -(\boldsymbol{\omega}_{ie}^n + \boldsymbol{\omega}_{in}^n)_2 \\ -(\boldsymbol{\omega}_{ie}^n + \boldsymbol{\omega}_{in}^n)_3 & 0 & (\boldsymbol{\omega}_{ie}^n + \boldsymbol{\omega}_{in}^n)_1 \\ (\boldsymbol{\omega}_{ie}^n + \boldsymbol{\omega}_{in}^n)_2 & -(\boldsymbol{\omega}_{ie}^n + \boldsymbol{\omega}_{in}^n)_1 & 0 \end{bmatrix} \quad (2.30)$$

$$\mathbf{F}_{\mathbf{v}\boldsymbol{\psi}} = \begin{bmatrix} 0 & -(\mathbf{f}^n)_3 & (\mathbf{f}^n)_2 \\ (\mathbf{f}^n)_3 & 0 & -(\mathbf{f}^n)_1 \\ -(\mathbf{f}^n)_2 & (\mathbf{f}^n)_1 & 0 \end{bmatrix} \quad (2.31)$$

$$\mathbf{F}_{\boldsymbol{\psi}\boldsymbol{\psi}} = \begin{bmatrix} 0 & (\boldsymbol{\omega}_{in}^n)_3 & -(\boldsymbol{\omega}_{in}^n)_2 \\ -(\boldsymbol{\omega}_{in}^n)_3 & 0 & (\boldsymbol{\omega}_{in}^n)_1 \\ (\boldsymbol{\omega}_{in}^n)_2 & -(\boldsymbol{\omega}_{in}^n)_1 & 0 \end{bmatrix} \quad (2.32)$$

$$\mathbf{F}_{12} = \begin{bmatrix} 0 & 0 \\ \mathbf{F}_{\mathbf{v}\mathbf{f}_b} & \mathbf{F}_{\mathbf{v}\mathbf{f}_s} \\ 0 & 0 \end{bmatrix}, \quad \mathbf{F}_{\mathbf{v}\mathbf{f}_b} = \mathbf{C}_b^n, \quad \mathbf{F}_{\mathbf{v}\mathbf{f}_s} = \mathbf{C}_b^n \begin{bmatrix} (\mathbf{f}_{ib}^b)_1 & 0 & 0 \\ 0 & (\mathbf{f}_{ib}^b)_2 & 0 \\ 0 & 0 & (\mathbf{f}_{ib}^b)_3 \end{bmatrix} \quad (2.33)$$

$$\mathbf{F}_{13} = \begin{bmatrix} 0 & 0 \\ 0 & 0 \\ \mathbf{F}_{\boldsymbol{\psi}\boldsymbol{\omega}_b} & \mathbf{F}_{\boldsymbol{\psi}\boldsymbol{\omega}_{sf}} \end{bmatrix}, \quad \mathbf{F}_{\boldsymbol{\psi}\boldsymbol{\omega}_b} = -\mathbf{C}_b^n, \quad \mathbf{F}_{\boldsymbol{\psi}\boldsymbol{\omega}_{sf}} = -\mathbf{C}_b^n \begin{bmatrix} (\boldsymbol{\omega}_{ib}^b)_1 & 0 & 0 \\ 0 & (\boldsymbol{\omega}_{ib}^b)_2 & 0 \\ 0 & 0 & (\boldsymbol{\omega}_{ib}^b)_3 \end{bmatrix} \quad (2.34)$$

$$\mathbf{F}_{22} = 0, \quad \mathbf{F}_{33} = 0, \quad \mathbf{F}_{14} = 0, \quad \mathbf{F}_{44} = \beta \mathbf{I}_3 \quad (2.35)$$

where: the dot above the variables denotes the time derivative of the corresponding variables; $x_{\mathbf{p}\mathbf{v}\boldsymbol{\psi}}$, $x_{\mathbf{f}}$, $x_{\boldsymbol{\omega}}$, and $x_{\mathbf{g}}$ are the state sub-vectors for the navigation parameters (i.e., position, velocity, and orientation), accelerometer sensor errors, gyro sensor errors, and gravity disturbances, with \mathbf{F}_{11} , \mathbf{F}_{12} , \mathbf{F}_{13} , \mathbf{F}_{14} , \mathbf{F}_{22} , \mathbf{F}_{33} and \mathbf{F}_{44} as their corresponding dynamics matrices; $v_{\mathbf{p}\mathbf{v}\boldsymbol{\psi}}$, $v_{\mathbf{f}}$, $v_{\boldsymbol{\omega}}$, and $v_{\mathbf{g}}$ are the “*driven process*” noise vectors for these state sub-vectors, representing their stochastic error properties; $\delta \mathbf{r}$, $\delta \mathbf{v}$, $\boldsymbol{\psi}$, and $\delta \bar{\mathbf{g}}$ represent the disturbances from the normal values for the position, velocity, orientation, and gravity vectors; $\delta \boldsymbol{\omega}_{in}^n$ contains the higher-order effects of the position and velocity,

coupled with the orientation; \mathbf{F}_{pp} , \mathbf{F}_{pv} , \mathbf{F}_{vp} , \mathbf{F}_{vv} , $\mathbf{F}_{v\psi}$ and $\mathbf{F}_{\psi\psi}$ are the detailed sub-matrix components of \mathbf{F}_{11} , as expressed in the psi-angle error model; the detailed sub-matrices of the \mathbf{F}_{12} , \mathbf{F}_{13} , \mathbf{F}_{14} , \mathbf{F}_{22} , \mathbf{F}_{33} and \mathbf{F}_{44} blocks are dependent on the stochastic error characteristics of the inertial sensor error modeling and the gravity assumptions; if the sensor errors of an accelerometer (or a gyro) are assumed to contain a bias term modeled as a random walk process and a scale-factor term modeled as a random constant process, the corresponding detailed sub-matrices of \mathbf{F}_{12} and \mathbf{F}_{13} are \mathbf{F}_{vf_b} , $\mathbf{F}_{vf_{sf}}$, $\mathbf{F}_{\psi\omega_b}$ and $\mathbf{F}_{\psi\omega_{sf}}$, shown in equation (2.33, 2.34 and 2.35); \mathbf{I} is the identity matrix; if the gravity disturbance is assumed to be the 1st order Gaussian-Markov process with coefficient β , \mathbf{F}_{14} and \mathbf{F}_{44} are shown in equation (2.35).

2.2.3 INS initialization and initial alignment

As mentioned earlier, the initial position and velocity must be provided in order to compute the position and velocity along the trajectory based on the integration of the raw sensed accelerations; also the initial orientation must be known to maintain the direction-cosine matrix to transform the sensed accelerations from the body frame to the designed navigation frame. These two requirements are referred to as the INS initialization and initial alignment. Normally, the initial position is provided from the external sources, such as, for example, GPS and other radio navigation systems. While the initial velocity can be assumed zero with respect to the earth for a stationary INS, it may also be precisely determined using external sources, such as the GPS Doppler measurements. The initial orientation can be determined based on the known directions of acceleration and angular-rate vectors (gravity and earth's rotation) for a stationary INS, referred to as self-alignment, using the gyro-compassing technique (see, for example, Jekeli, 2001), and other external sources, such as, for example, GPS-based orientation determination using multiple antennas, etc. Besides the determination of the initial position, velocity, and orientation in the initialization and alignment procedure, some of the major INS systematic errors, including the accelerometer and gyroscope biases and bias drifts, must be determined. Normally, the coarse alignment is performed to determine the initial orientations, followed by the fine alignment. This way, the orientation and the INS systematic error sources are determined, based on the linear estimation techniques (normally a Kalman Filter) and using the zero-velocity measurements for the stationary INS (referred to as ZUPT); other aiding information from the external positioning and navigation sources can be used for the moving INS (also referred to as in-flight alignment) (Siouris, 1993; Titterton & Weston, 1997; Farrell & Barth, 1999; Jekeli, 2001).

2.3 Introduction to GPS/INS integration

2.3.1 GPS/INS integration mode

As stated in Chapter 1, the complementary error characteristics of GPS and INS result in the widespread implementation of GPS/INS integration for multi-sensor mobile mapping applications. Fusion of GPS and INS measurements can be accomplished by three approaches: 1) the loosely-coupled approach; 2) the tightly-coupled approach and 3) the ultra-tightly-coupled approach. In the loosely-coupled mode, the GPS and inertial sensors individually process their raw measurements (code and carrier-phase pseudo-ranges for the GPS sensors, sensed accelerations and angular-rates for the inertial sensors) to obtain the navigation solution (i.e., position, velocity, and orientation) for each system, respectively; the final navigation solution and the inertial sensor errors are determined by fusing the two individual navigation solutions together, for example with KF. In the tightly-coupled approach, the GPS and inertial sensors process their raw measurements simultaneously and optimally to estimate the position, velocity, and orientation of the platform together with the inertial sensor errors in a single filter. In the ultra-tightly-coupled mode, the integrated navigation solution is fed back to predict the code and carrier-phase pseudo-ranges of the GPS receiver to aid the carrier tracking loops in the high-dynamic or jamming environments. Since the ultra-tightly-coupled approach involves the access to the GPS hardware tracking loops, it is not available to the general user community. The loosely-coupled approach is commonly implemented in the GPS/INS integrated systems due to its simplicity, although it may experience difficulties, especially in urban environments, since it requires at least four available GPS satellites to compute the navigation solution directly from the GPS sensors. The tightly-coupled integrated system has already proven to be superior to the loosely-coupled system and allows for partial GPS information, although only few applications exist due to its complexity and difficulty to implement; see, for example, Gautier & Parkinson (2003).

Figures 2.1 and 2.2 illustrate the workflow for both the loosely-coupled and the tightly-coupled GPS/INS integrations implemented in this dissertation for a mobile mapping application. Both loosely-coupled and tightly-coupled integrations implemented here include 1) the INS data processing module; 2) the GPS data processing module and 3) the GPS/INS data fusion module. The INS data processing module is the same for both integration methods. It takes the outputs (i.e., accelerations (\mathbf{f}_{xyz}) and angular-rates (ω_{xyz}) or accelerometer-integrated-velocities ($\Delta\mathbf{V}_{xyz}$) and gyroscope-integrated-angles ($\Delta\theta_{xyz}$)) from the accelerometers and gyroscopes and compensates them using inertial sensor error models. A sub-module “*Inertial Navigation Computation*” in Figures 2.1 and 2.2 outputs the position, velocity, and orientation according to equations (2.19, 2.20 and 2.21) given the navigation solution (i.e., position, velocity, and orientation) from the previous epoch. In the GPS data processing module of the loosely-coupled integration, the double-difference measurements are firstly formed from the GPS observations ($P_1, P_2, L_1,$

L_2 , D_1 and D_2) of the rover and base receivers using the approximate rover coordinates and the fixed reference coordinates; then, an integer ambiguity resolution follows to fix the double-difference carrier-phase integers; the position vector of the rover receiver is directly solved from the double-difference carrier-phase measurements after the removal of the double-difference carrier-phase integer ambiguities; the velocity of the rover receiver is computed from the double-difference Doppler measurements. The GPS/INS data fusion module of the loosely-coupled integration combines the navigation solutions from both the GPS and INS data processing modules to optimally estimate a final version of position, velocity, orientation, acceleration and gyroscope sensor error models (biases, drifts, etc.) and the lever arm offset of the GPS measurement center (for example, antenna carrier-phase center or antenna reference point) with respect to the inertial sensor body center.

In the GPS data processing module of the tightly-coupled integration, the double-difference measurements are formed from the GPS observations of the rover and base receivers using the predicted coordinates from the INS data processing module (with the compensation of the lever arm offset) for the rover receivers and the fixed reference coordinates for the base receivers. The integer ambiguity resolution procedure follows. The GPS/INS data fusion module of the tightly-coupled integration directly fuses the double-difference carrier-phase measurements after the removal of the double-difference carrier-phase integer ambiguities, and the double-difference Doppler measurements, with the navigation solution of the INS data processing to form an integrated solution (i.e., the position, velocity, orientation, inertial sensor errors, lever arm offset, and etc.). As mentioned in Section 2.1.2, several integer ambiguity resolution used in the loosely-coupled system and the tightly-coupled system exist, the detailed implemented technique in this dissertation will be discussed in Chapter 3.

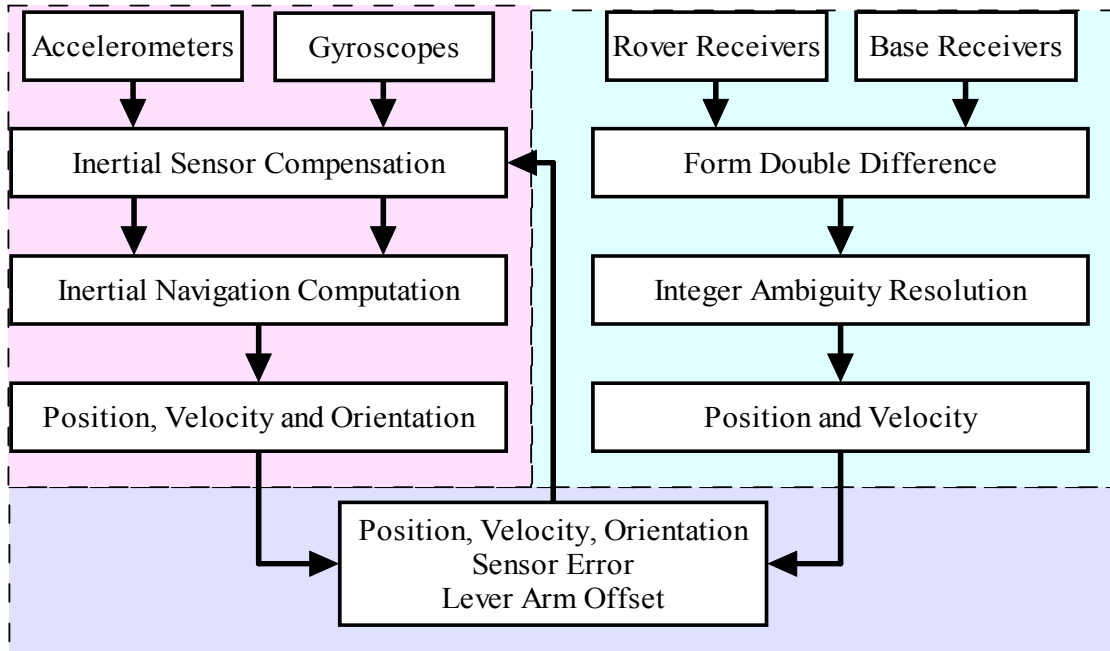


Figure 2.1. The workflow of a loosely-coupled GPS/INS integration implemented for a mobile mapping application.

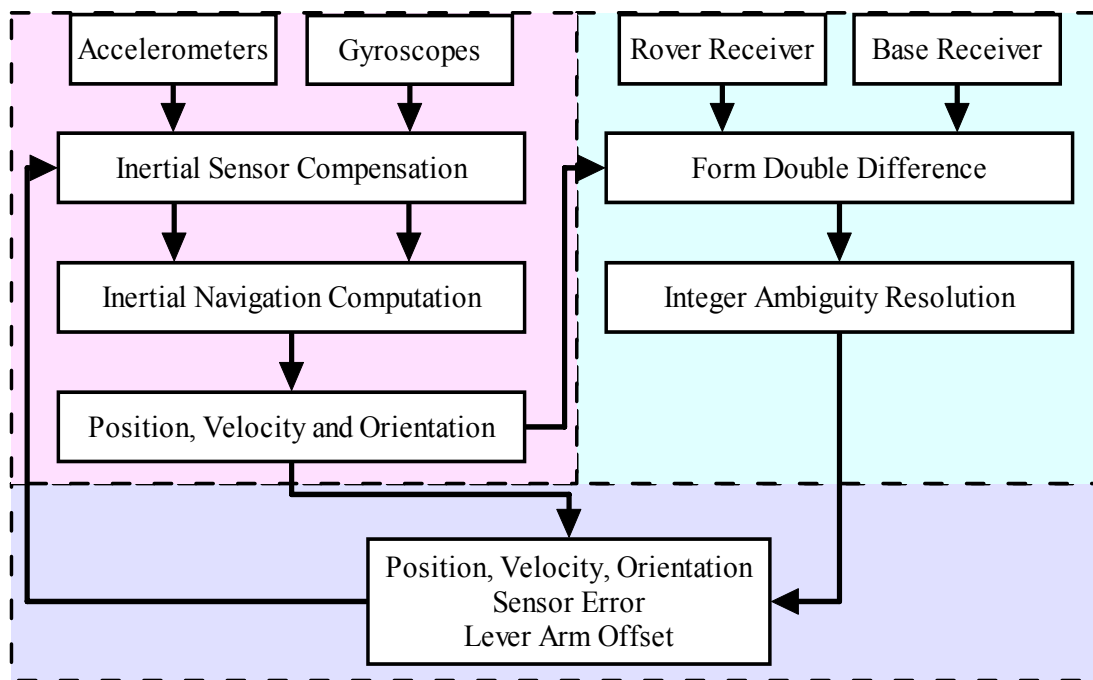


Figure 2.2. The workflow of a tightly-coupled GPS/INS integration implemented for a mobile mapping application.

2.3.2 Linear filtering – Kalman Filter

No matter which integration scheme is used, a filtering technique must be applied to optimally estimate the position, velocity, and orientation together with the sensor errors (and other parameters, such as lever arm offset) when fusing the GPS and IMU measurements. After Kalman (1960) had published his famous paper, Kalman filtering has become the industrial standard to recursively provide an online minimum mean squared error (MMSE) estimate of the signals (referred to as the state vector: the minimal set of data to sufficiently describe the system's dynamic behavior) from noisy observations for the linear dynamic system. The Kalman Filter (KF) can be derived from the statistical or probabilistic viewpoint; see Jazwinski (1970) for an early review of the Kalman Filter. The solution of the Kalman Filter is recursively based on the previous estimate and the input data to optimally achieve the current estimate. Due to storing only the previous estimate with its mean squared errors, it is computationally more efficient than computing the estimate directly from the entire set of past measurements at each filtering step. Considering a continuous linear dynamic system, expressed in a state vector form, it can be converted to a discrete linear dynamic system, referred to as *system* (also called: *process* or *dynamic*) model (or equation) by means of the discretization procedure. In order to estimate the state vector, a set of measurements, which relate the state vector based on the measurement model (or equation), must be observed. Equations (2.36 and 2.37) present the system model and the measurement model for the discrete linear dynamic system, which is only complete with the *initial condition* (2.38). Equations (2.39-2.45) show the optimal unbiased linear estimate of the unknown state vector, given the initial state vector, x_0 , and its mean squared error matrix, P_0 , (see, for example, Gelb, 1974 for more details on Kalman Filter).

$$\text{System model} \quad x_k = \Phi_{k-1,k} x_{k-1} + v_{k-1}, \quad E\{v_j v_k^T\} = \delta_{jk} Q_k, \quad (2.36)$$

$$\text{Measurement model} \quad z_k = H_k x_k + n_k, \quad E\{n_j n_k^T\} = \delta_{jk} R_k, \quad E\{v_j n_k^T\} = 0 \quad (2.37)$$

$$\text{Initial condition} \quad (\hat{x}_0 - x_0) \sim (0, P_0) \quad (2.38)$$

$$\text{Predicted state error covariance matrix} \quad P_k^- = \Phi_{k-1,k} P_{k-1} \Phi_{k-1,k}^T + Q_k \quad (2.39)$$

$$\text{Predicted state estimates} \quad \hat{x}_k^- = \Phi_{k-1,k} \hat{x}_{k-1} \quad (2.40)$$

$$\text{Predicted measurements} \quad \hat{z}_k^- = H_k \hat{x}_k^- \quad (2.41)$$

$$\text{Predicted measurement error covariance matrix} \quad P_z = H_k P_k^- H_k^T + R_k \quad (2.42)$$

$$\begin{array}{l} \text{Computed Kalman gain} \\ \text{matrix} \end{array} \quad K_k = P_k^- H_k^T P_z^{-1} \quad (2.43)$$

$$\begin{array}{l} \text{Updated mean squared error} \\ \text{covariance matrix} \end{array} \quad \begin{aligned} & P_k \\ &= (I - K_k H_k) P_k^- (I - K_k H_k)^T + K_k R_k K_k^T \\ &= P_k^- - K_k P_z K_k^T \\ &= P_k^- - P_k^- H_k^T K_k^T \\ &= P_k^- - (K_k H_k P_k^-) \end{aligned} \quad (2.44)$$

$$\text{Updated state vector} \quad \hat{x}_k = \hat{x}_k^- + K_k (z_k - \hat{z}_k^-) \quad (2.45)$$

Here, the subscripts j and k (and $k-1$) denote the epochs in the time domain; Φ is the transition matrix taking the state vector x from epoch $k-1$ to epoch k ; the process noise vector v is assumed to be additive white noise with zero mean and covariance matrix Q ; z is the observation vector, and H is the measurement matrix; the measurement noise vector n is also assumed to be additive white noise with zero mean and covariance matrix R ; δ_{jk} is the delta operator, $\delta_{jk}=1$ if $j=k$ and $\delta_{jk}=0$ if $j \neq k$; $E\{\}$ is the expectation operator; P is the mean squared error matrix of the estimated state vector; K is the Kalman gain matrix; \hat{x}_k^-

and P_k^- are the predicted state and its error covariance matrix; \hat{x}_k and P_k are the MMSE estimate of the state vector and its error covariance matrix.

Due to the divergence phenomenon of the state vector's error covariance matrix, P , caused by the numerical inaccuracies in Kalman filtering, the so-called square-root filter, where the matrix P is propagated in the square-root form by using the Cholesky factorization, is normally used to overcome the numerical instability; see, for example, Bierman (1977). In order to accommodate the uncertainties in the process description noise covariance matrix, Q , of the system model, and in the measurement noise covariance matrix R of the measurement model, normally an adaptive Kalman filter (AKF) can be applied to identify the process and measurement noises (Mohamed & Schwarz, 1999). Two commonly used adaptive approaches are: 1) the multiple-model-based adaptive estimation (MMAE), and 2) the innovation-based adaptive estimation (IAE). In the MMAE, several KFs run parallel with different models, using different statistical information on Q and R to obtain several optimal estimates, and a weighting scheme is applied to compute the final estimates. In contrast, in the IAE, the error covariance matrixes Q and R are identified using the so-called "innovation" (or "residual") sequences. The identification procedure for Q and R based on N continuous innovation sequences is shown in equations (2.46 and 2.47) in accordance with Mohamed & Schwarz (1999). The identified error covariance matrices are used in equations

(2.39-2.45) instead of the predefined error covariance matrices in the conventional Kalman filter.

$$\text{Innovation} \quad \tilde{e}_k = z_k - H_k \hat{x}_k^-, \quad \hat{C}_k = \frac{1}{N} \sum_{i=k-N+1}^k \tilde{e}_i \tilde{e}_i^T \quad (2.46)$$

$$\text{Identification} \quad \hat{R}_k = \hat{C}_k - H_k P_k^- H_k^T, \quad \hat{Q}_k \approx K_k \hat{C}_k K_k^T \quad (2.47)$$

Here, \tilde{e}_k is the “*innovation*” at epoch k ; \hat{C}_k is the “*innovation*” matrix obtained from N continuous “*innovation*” sequences.

A new unconventional filter, called “*wave filter*”, was proposed by Salychev & Schaffrin (1992) in order to compensate the system disturbances (i.e., any quasi-systematic uncertainties) in the system model (2.36) of the traditional Kalman Filter, using a wave process expressed by a combination of some known basis functions. More details about the “*wave filter*” can be found in Salychev (1995 & 1998).

2.3.3 Nonlinear filtering

The problem of the GPS/INS fusion system is traditionally represented in a nonlinear probabilistic state-space formulation, as shown in equations (2.48, 2.49 and 2.50). It includes: (1) a nonlinear system model to describe the evolution of the state vector in the time domain, and (2) a nonlinear (or linear) measurement model to relate the noisy measurements to the state vector, and update the state vector when new measurements are available, as well as (3) some initial conditions along with further assumptions. Here, the system model is based on the nonlinear differential navigation equations together with linear (or nonlinear) stochastic error models for the sensor errors, as well as the system and environment parameters under some stochastic assumptions. The measurement model can be nonlinear or linear, depending on the measurement type; for example, GPS code and carrier-phase pseudo-range (and/or range-rate) measurements, or the computed GPS navigation solution.

2.3.3.1 Extended Kalman Filter

Due to the nonlinearities of the system model (and/or the measurement model), the well-known Extended Kalman Filter (EKF) (Jazwinski, 1970) has been widely used to provide a sub-optimal (or approximate optimal) nonlinear estimation (state estimation of the nonlinear dynamic system) by means of a linearization procedure using a first-order Taylor approximation. The linearized system and measurement models are shown in equations (2.51 and 2.52). EKF is currently widely implemented in a number of GPS/INS-integrated systems (see, for example, Grejner-Brzezinska, 1997 & 1999; Jekeli,

2001). As mentioned earlier, a linear error model, called psi-angle error model, for the GPS/INS-integrated system is listed in equation (2.26).

$$\text{System model} \quad x_{k+1} = f(x_k, v_k), \quad v_k \sim (0, Q_k) \quad (2.48)$$

$$\text{Measurement model} \quad z_k = h(x_k, n_k), \quad n_k \sim (0, R_k) \quad (2.49)$$

$$\text{Initial conditions} \quad (\hat{x}_0 - x_0) \sim (0, P_0) \quad (2.50)$$

all random errors are uncorrelated

$$\begin{aligned} \text{System model} \\ \text{linearization} \end{aligned} \quad x_{k+1} \approx \Phi_{k+1,k} x_k + G_k v_k, \quad (2.51)$$

$$\Phi_{k+1,k} = \left. \frac{\partial f}{\partial x} \right|_{x=\hat{x}_k}, \quad G_k = \left. \frac{\partial f}{\partial v} \right|_{v=0}$$

$$\begin{aligned} \text{Measurement model} \\ \text{linearization} \end{aligned} \quad z_k \approx H_k x_k + F_k v_k, \quad (2.52)$$

$$H_k = \left. \frac{\partial h}{\partial x} \right|_{x=\hat{x}_k^-}, \quad F_k = \left. \frac{\partial h}{\partial n} \right|_{n=0}$$

where the subscripts denote the time epochs; x , v , z and n are the state vector, the process description noise vector, the measurement vector and the measurement noise vector, respectively; x_k indicates the state vector at epoch k ; $\hat{x} - x$, v and n are mutually independent; f and h denote the nonlinear system and measurement functions; process and measurement noises are assumed to have a zero-mean; \hat{x}_k is the optimal state estimate at epoch k and \hat{x}_k^- is the predicted state estimate at epoch k ; Φ and G are the matrices forming the linearized system model; F and H are the matrices forming the linearized measurement model.

2.3.3.2 Other nonlinear filters

Even though the EKF is widely used in various nonlinear applications, it may experience difficulties with heavily skewed nonlinear systems and it is only reliable for nonlinear systems, which are almost linear in the time scale of the update intervals, due to the first-order linearization of the EKF. Also the EKF requires deriving a corresponding linear model for nonlinear systems using a linearization procedure, which makes it difficult to be implemented in some complicated nonlinear applications. It is also

impossible to use the EKF for the nonlinear discontinuous systems, whose Jacobian matrices shown in equations (2.51) and (2.52) cannot be derived analytically. In reality, various prior constraints also introduce nonlinearities, which is difficult for the EKF to handle. Such example can be the constraints (in the form of state equality or state inequality equations) to the navigation trajectories or velocities, in case of target tracking applications. See more discussion about the drawbacks of the EKF in, for example (Julier *et al.*, 1995; Julier & Uhlmann, 1997; Wan & van der Merwe, 2001; Ristic *et al.*, 2004).

In the last few decades, several nonlinear filters, for example, the Sigma Point Kalman Filters (SPKF) (van der Merwe & Wan, 2003 & 2004) or Linear Regression Kalman Filters (LRKF) (Lefebvre *et al.*, 2002), the Particle Filters (PF) (Liu & Chen, 1998; Doucet *et al.*, 2001), the Ensemble Kalman Filter (EnKF) (Evensen 1994, 1997 & 2007), and etc., have been proposed as the alternatives to the EKF for the nonlinear applications.

The SPKFs are a family of nonlinear filters using a so-called derivativeless statistical linearization, as compared to the analytical linearization of the EKF (Gelb, 1974), which include the Unscented Kalman Filter (UKF) based on unscented transformation (UT) (Julier *et al.*, 1995; Julier & Uhlmann, 1997), the Central Difference Kalman Filter (CDKF) based on Sterling's interpolation formulas (Press *et al.*, 1992; Ito & Xiong, 2000). The PF and EnKF both are sample-based nonlinear filters based on the sequential Monte Carlo (SMC) methods to represent the probability density of the state vector using a set of random samples associated with the corresponding weights. The PF behaves differently from the EnKF with a procedure called the sequential importance sampling and re-sampling (more details in Chapter 6). Similar to the PF and EnKF, the SPKF is also a sample-based nonlinear filter and also utilizes a set of samples associated with the corresponding weights to represent the state estimates and state error covariance matrix. However, the samples used in the SPKF are *deterministically* selected, as compared to the *randomly* generated samples in the PF and the EnKF. Similarly to the EKF, the three nonlinear filters (i.e., the SPKF, the PF and the EnKF) include two stages: 1) the prediction of the state estimates and the state error covariance matrix in the time update stage; and 2) the update of the state estimates and the state error covariance matrix once new measurements are available. The predictions of the state estimates and the state error covariance matrix using the SPKF, the PF and the EnKF, are directly based on the nonlinear system model, using the samples associated with weights, thus the requirements deriving the linearized model for these filters are eliminated and they are referred to as derivative-free filters, as compared to the EKF. The predicted measurements and the predicted measurement error covariance matrix can also be based on the directly nonlinear measurement model using the samples associated with weights.

The SPKF and the PF have been proven superior to the EKF in some example nonlinear applications (see, for example, Julier *et al.*, 1995; Julier & Uhlmann, 1997; Doucet *et al.*, 2001; Wan & van der Merwe, 2001; Ristic *et al.*, 2004; van der Merwe &

Wan, 2003 & 2004). The UKF of the SPKF and the PF, summarized in the probability framework and referred to as nonlinear Bayesian filters, are implemented in this dissertation and discussed in Chapter 6, to investigate their navigation performance as compared to that of the EKF.

2.4 OSU GPS/INS AIMS™ system

The research conducted in this dissertation is related to the continuation of the implementation of the Airborne Integrated Mapping System (AIMS™) originally designed for the high-end navigation-grade inertial sensor, LN100, using the EKF and single-baseline differential GPS data processing technique, developed at the Center for Mapping (CFM), The Ohio State University (OSU), in 1997, see for example, (Grejner-Brzezinska, 1997). The current implementation of the OSU GPS/INS AIMS™ system includes:

- ✓ Extended hardware suite, including multiple inertial sensors supported by multiple GPS and precise time synchronization (as well as data acquisition software):
 - LN100, LN200 (Northrop Grumman)
 - Two H764G and two HG1700 (Honeywell)
 - MEMS IMU400CC-100 (Crossbow)
- ✓ Extended GPS/INS software suite developed by the author of this dissertation:
 - Extended IMU error modeling to cover different grades of the inertial sensors using
 - ◆ Allan-variance analysis in the time domain
 - ◆ PSD (Power Spectral Density) method in the frequency domain
 - IMU data preprocessing using wavelet-based signal de-noising
 - Initial alignment module
 - Loosely-coupled integrated module designed for
 - ◆ Low-end inertial sensor
 - ◆ Initial coarse parameter estimation (e.g., lever arm) for tightly-coupled original AIMSTM integration module
 - Network-based single-epoch kinematic GPS processor
 - Alternatives to EKF (i.e., nonlinear Bayesian Filters)
 - ◆ Unscented Kalman Filter
 - ◆ Particle Filter
 - Extended gravity compensation error model, suitable for rugged terrain (not discussed here); see, for example, Grejner-Brzezinska *et al.* (2005b).

Figures 2.3 and 2.4 below illustrate the current OSU GPS/INS AIMS™ system hardware implementation and configuration for a land-based installation. A total of six different inertial sensors, including two navigation-grade H764G sensors, one navigation-grade LN100, one tactical-grade HG1700, one tactical-grade LN200 and one consumer-grade IMU400CC, are mounted on the same rigid portable platform installed in

a GMC suburban vehicle. This hardware setup allows cross calibration and testing of various inertial sensors for navigation accuracy and suitability for a specific mapping tasks. Two geodetic-grade antennas are mounted on the roof in front and back of the vehicle. Table 2.1 presents the detailed sensor manufacturer specifications. Most of the datasets for the example analyses provided in this dissertation are collected by using the OSU AIMS™ GPS/INS hardware suite and processed by using the extended OSU AIMS™ GPS/INS software suite.

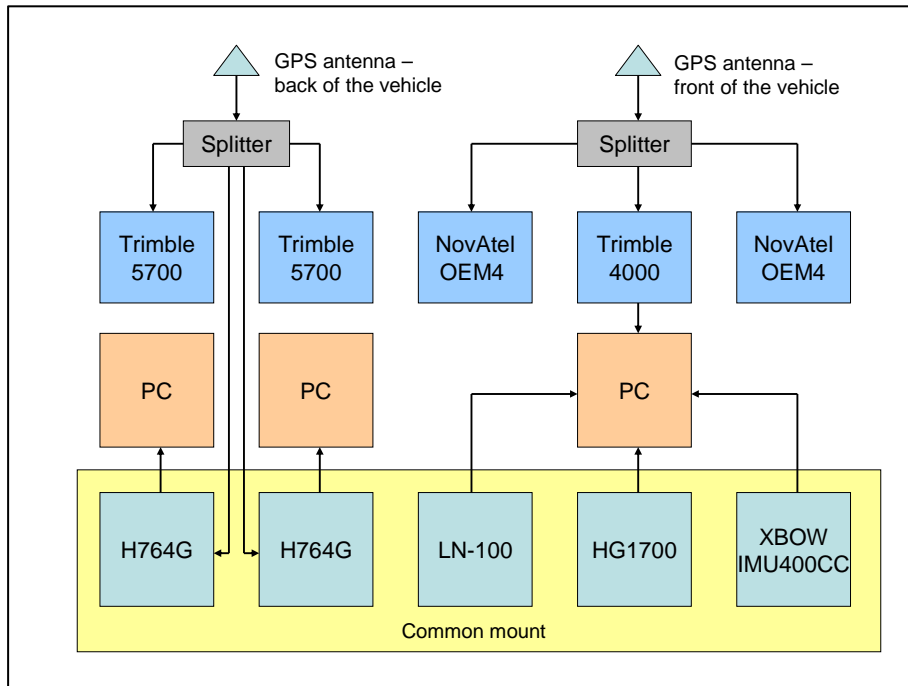


Figure 2.3. OSU GPS/INS AIMS™ hardware implementation.



Figure 2.4. OSU GPS/INS AIMS™ hardware configuration.

Sensor grade	Sensor name	Type	Characteristics
Navigation	LN100 Gyroscope	Non-dithered 18cm Zero Lock™ Laser Gyro	bias = 0.003°/h rw = 0.001°/h ^{1/2} sf < 1ppm
	LN100 Accelerometer	Miniature Accelerometer A4	bias = 25μg sf = 40ppm ma = 2arcsec wh = 5μg/Hz ^{1/2}
Navigation	H764G Gyroscope	Dithered GG1320AN RLG	bias = 0.0035°/h rw = 0.0035°/h ^{1/2} sf = 5ppm
	H764G Accelerometer	QA2000	bias = 25μg wh = 8.3μg (100Hz bw) sf = 100ppm
Tactical	HG1700 Gyroscope	Dithered GG1308 RLG	bias = 2.0°/h rw = 0.125~0.3°/h ^{1/2} sf = 150ppm
	HG1700 Accelerometer	RBA500	bias = 1.0mg wh = 0.2mg (100Hz bw) sf = 300ppm ma = 12m-rad
Consumer	IMU400CC Gyroscope	Non-dithered Silicon MEMS Gyro	bias = 1°/sec rw = 2.25°/h ^{1/2} sf = 1%
	IMU400CC Accelerometer	Silicon MEMS Accelerometer	bias = 8.5mg sf = 1% rw = 0.1m/s/h ^{1/2}

Table 2.1. Manufacturer's specifications for the inertial sensors (sf ≡ scale factor; ma ≡ misalignment; wh ≡ white noise; rw ≡ random walk; bw = bandwidth).

The post-processing of the GPS/INS data using the OSU AIMS™ GPS/INS software suite, can be separated into two steps: 1) The GPS and INS data pre-processing, and 2) the GPS/INS data fusion using the loosely-coupled integration or the tightly-coupled integration (the implementations in this dissertation are shown in Figures 2.1 and 2.2). The GPS data pre-processing includes: 1) GPS RINEX data conversion from the manufacturer proprietary data format using the manufacturer provided software or TEQC (<http://facility.unavco.org/software/teqc/teqc.html>) for each type of GPS receiver currently included in the hardware assembly; 2) the preparation of the related data and/or products, downloadable from either IGS (<http://igsb.jpl.nasa.gov>), NGS

(<http://www.ngs.noaa.gov/>), or CODE (<http://www.aiub.unibe.ch/ionosphere.html>), for example, the precise (ultra-rapid, rapid or final) GPS orbit products, global broadcast GPS navigation data, global ionospheric model, satellite differential code bias (can be used for network-based ionospheric error modeling), and CORS reference station data; 3) the determination of the station coordinates of the reference stations to be used; and 4) the determination of the kinematic rover position. Figures 2.5 and 2.6 illustrate the detailed procedures for the GPS and INS pre-processing and the GPS/INS integration, used in this dissertation.

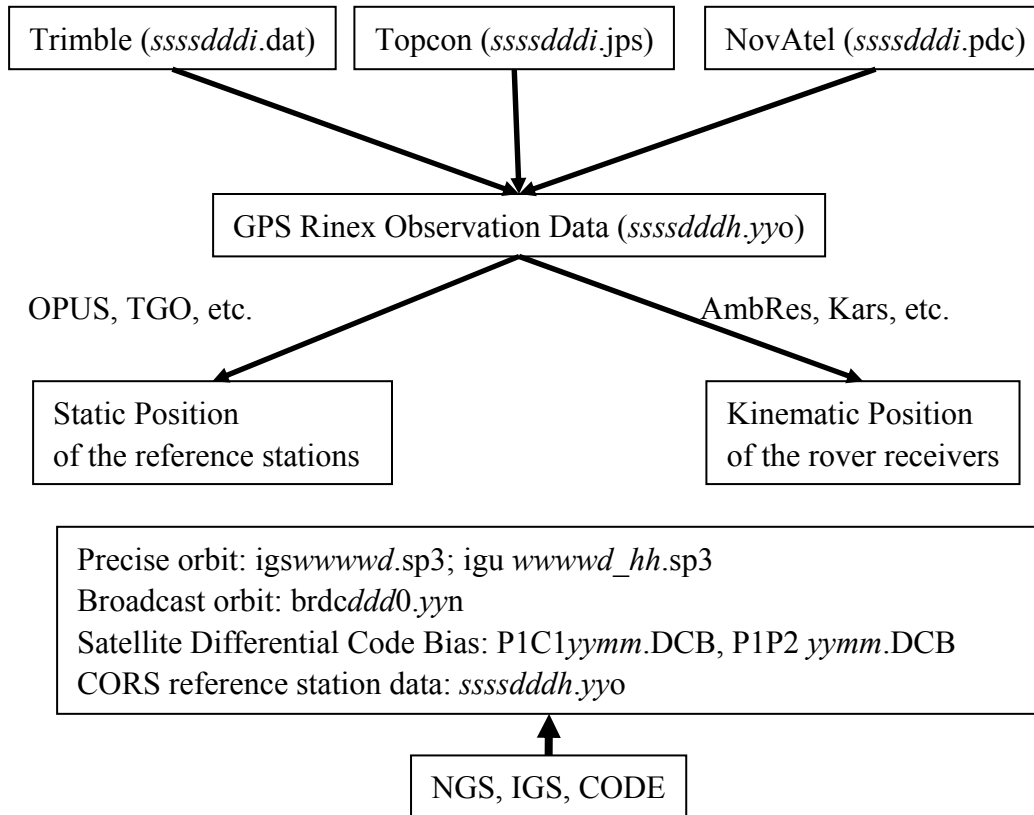


Figure 2.5. GPS data pre-processing (Note: *ssss*: 4-character site ID; *ddd*: day of year (1-366); *i*: session index number; *h*: single letter for hour of day (a-x = 0-23); *yy*: 2-digit year; *www*: 4-digit GPS week; *d*: day of week (0-6); *hh*: 2-digit hour of day (00-23); *mm*: 2-digit month of year (00-12); OPUS = Online Positioning User Service (<http://www.ngs.noaa.gov/OPUS/>); TGO = Trimble Geomatics Office; AmbRes is a kinematic GPS software developed at CFM, OSU; Kars is a kinematic GPS software developed by NGS).

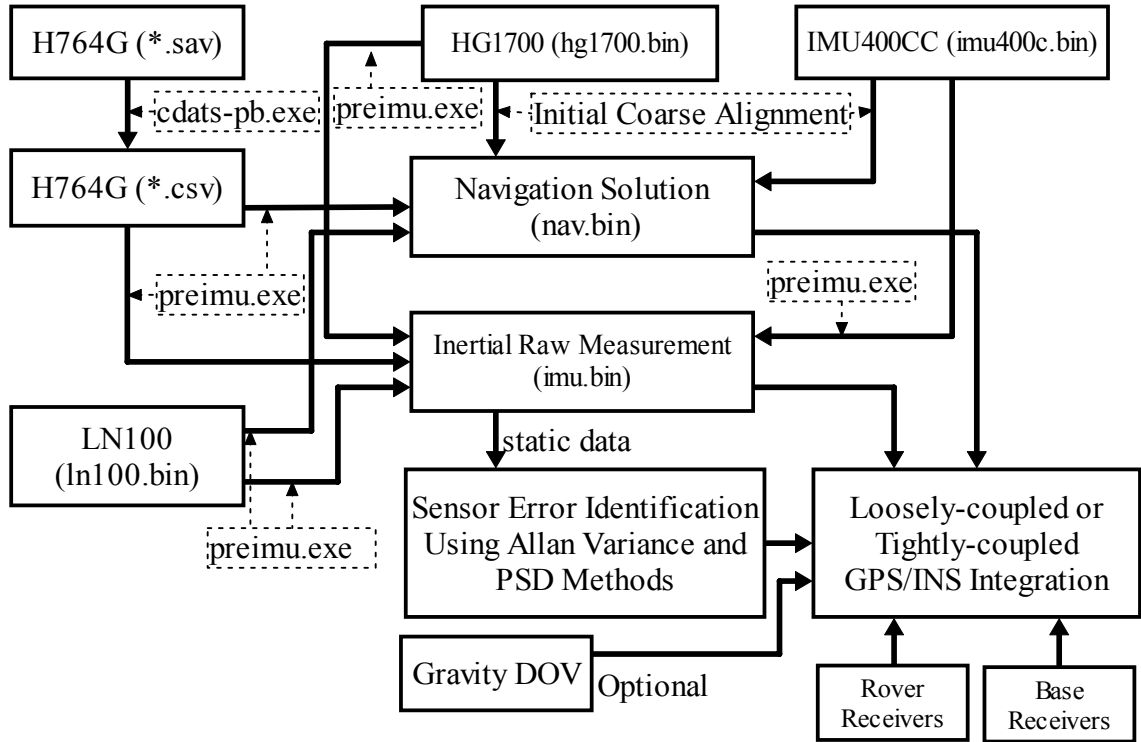


Figure 2.6. The workflow of the INS data pre-processing and GPS/INS integration (*cdats-pb.exe* is a program provided by Honeywell to convert the raw binary data of H764G to ASCII data format; *preimu.exe* is a program developed for this dissertation to convert different data format of different inertial sensor to standard data formats (*nav.bin* and *imu.bin*); *Initial Coarse Alignment* is a module to provide initial orientation for HG1700 and IMU400CC using the gyro-compassing technique; If the data in *imu.bin* is collected from a stationary experiment, the sensor error identification techniques using Allan variance and PSD methods can be applied to derive a *customized* sensor error model on a sensor-by-sensor basis; the gravity DOV information is an optional input to the GPS/INS integration module).

CHAPTER 3

INSTANTANEOUS POSITIONING TECHNIQUE SUPPORTING NETWORK MODE

This chapter starts with the motivation and a concept design of the implemented instantaneous (i.e., single-epoch) real-time kinematic (RTK) relative positioning technique supporting multiple reference and rover receivers with the capabilities to be operated in either network or baseline mode. Then the mathematical model of the single-epoch positioning technique is presented and its performance is analyzed using some example analyses.

3.1 Motivation

The GPS double-difference carrier-phase positioning technique is widely used to achieve the highest accuracy in real-time kinematic positioning applications, using the high-accuracy double-difference carrier-phase measurements after the removal of the double-difference integer ambiguity. Clearly, the double-difference integer ambiguity resolution plays an important role in the real-time kinematic positioning technique. The traditional RTK OTF double-difference integer ambiguity resolution requires a certain initialization time, normally ranging from several seconds to a few minutes, depending on the quality of the GPS data and the double-difference residual level. Also, it does experience difficulties in some critical situations where losses of GPS lock frequently occur, especially in the urban environment. The frequent re-initialization of the double-difference integer ambiguity resolution may result in a lower reliability and less consistent accuracy. In the last few years, the GPS carrier-phase instantaneous (i.e., epoch-by-epoch (EBE), or single-epoch) double-difference integer ambiguity resolution technique has attracted a lot of interest in the GPS community; see, for example, (Bock *et al.*, 2000; Han & Rizos, 1996; Han, 1997a & 1997c; Hatch, 1990; Kashani *et al.*, 2005; Pratt *et al.*, 1997; Yi & Grejner-Brzezinska, 2004). The single-epoch double-difference positioning technique can provide the instantaneous navigation solution, relying only on data from one epoch, using the single-epoch integer ambiguity resolution and, thus, eliminating the initialization and cycle-slip detection and repairing procedure of the traditional RTK OTF technique. Compared with the correlated RTK solution, it can also provide a faster, epoch-independent solution with fewer requirements and shorter computational time. However, due to the fact that it uses data from only one epoch, the

single-epoch position solution might be less reliable, as compared with the traditional RTK OTF, where the accumulated information from multiple epochs is used. Currently, the single-epoch positioning technique has been developed for static surveying or deformation monitoring as well as for RTK applications; for instance, a centimeter-level position accuracy and $\pm 0.01^\circ$ orientation accuracy from two antennas separated by 2.5 meters have been reported by Geodetics Inc. (2005). An independently developed implementation of the double-difference single-epoch RTK positioning with some special data processing strategies to improve the ambiguity fixing rate and the quality control is described in this dissertation, and its performance will be discussed in the following section.

In the double-difference data processing mode, the most common error sources between two receivers and two satellites are removed or largely reduced, leaving only some fractional parts of the distance-dependent error sources, as already mentioned in Chapter 2. The removal of the distance-dependent errors becomes less effective with the increasing length of the baselines. It results in poorer reliability of the double-difference integer ambiguity resolution and lower positioning accuracy, especially for kinematic medium (tens of kms) and longer (hundreds of kms) baselines. The traditional approaches to handle longer baselines mainly take the advantage of the carrier-phase wide-lane (L_w) or ionospheric-free (L_3) linear combinations to expand the effective wavelength in order to facilitate a more reliable outcome of the double-difference integer ambiguity resolution, or to remove the distance-dependent double-difference ionospheric delays. Compared with the high-accuracy carrier-phase L_1 measurements, the carrier-phase L_w or L_3 measurement will provide less positioning accuracy due to the increased measurement noise.

In order to improve the reliability of the long-range solutions, the network-based positioning approaches (Han, 1997b; Raquet, 1998; Schaffrin & Bock, 1988; Vollath *et al.*, 2000; Fotopoulos & Cannon, 2001; Yi & Grejner-Brzezinska, 2003; Wielgosz *et al.*, 2004; Kashani *et al.*, 2005) have been widely investigated in recent years as alternatives to the traditional single-baseline RTK positioning, especially for medium and longer baselines. Due to the growing availability of the local, regional and global permanently tracking GPS networks, methods based on multiple GPS reference stations are being implemented to achieve almost distance-independent kinematic solutions with uniform reliability and positioning accuracy. Example approaches include the linear combination of baselines (Han, 1997b), the network adjustment approach (Raquet, 1998), and the Virtual Reference Station (VRS) approach (Vollath *et al.*, 2000). Normally, the network approach will allow for a *weighted* solution with improved reliability and fault-tolerance level, as compared to the single-baseline solution, and will improve the double-difference integer ambiguity resolution by means of, for example, geometric constraints of the GPS integer ambiguity (Yi & Grejner-Brzezinska, 2004). The most significant improvement from the network approach, as compared to the single-baseline method, is that instead of

the traditional error reduction technique, such as the carrier-phase ionospheric-free linear combination, an advanced GPS bias reduction technique is developed to achieve the uniform high-accuracy distance-independent kinematic positioning quality by removing the spatially correlated GPS error sources. These spatially correlated GPS error sources for mobile rover receivers are predicted: 1) in the spatial domain using some spatial interpolation techniques, based on the GPS error models derived from multiple reference stations, and 2) in the time domain, to enable a fast double-difference integer ambiguity resolution and even support single-epoch kinematic positioning (for example, Bock *et al.*, 2000; Wielgosz *et al.*, 2004; Yi & Grejner-Brzezinska, 2004; Kashani *et al.*, 2005). Given the approximate coordinates of a rover receiver, its distance-dependent errors are predicted using a spatial interpolation method, for example, the Inverse-Distance Weighted Observations (IDWO), the MultiQuadric method (MQ), the Minimum Curvature Splines (MC), the GeoStatistics Predictor such as Kriging, etc. (Yi & Grejner-Brzezinska, 2004). The prediction in the temporal domain mainly uses a time series analysis technique; for example, the Auto-Regressive Integrated Moving Average (ARIMA) process, as developed by Box & Jenkins (1976), can be used according to Yi & Grejner-Brzezinska (2004). The combination of the kinematic single-epoch positioning approach and the network-based GPS error reduction technique results in a more robust kinematic instantaneous positioning method supporting multiple reference and rover receivers with the capability to provide RTK positioning using one reference receiver (baseline mode) or more than one reference receivers (network mode). Figure 3.1 illustrates such a concept, designed to support RTK positioning in both real-time and post-processing modes.

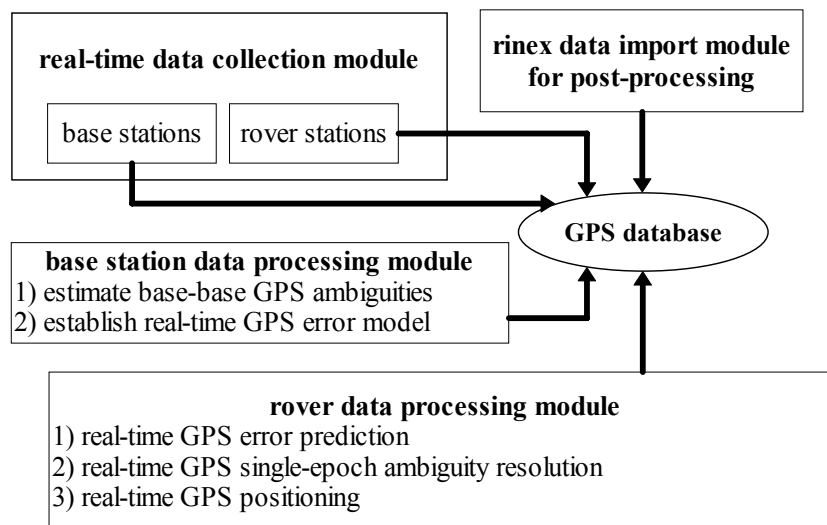


Figure 3.1. Concept of the network-based real-time kinematic instantaneous GPS positioning approach implemented in this dissertation.

3.2 Real-time kinematic instantaneous GPS positioning approach

3.2.1 Double-difference GPS positioning model with ionospheric pseudo-observations

Dual-frequency GPS receivers have become a part of the standard configuration in surveying and mapping, especially for the high-accuracy mobile mapping applications. Equations (2.8-2.14) in Chapter 2, list the double-difference measurement model for the GPS double-difference code and carrier-phase pseudo-ranges ($\bar{P}_{ij,1}^{kl}$, $\bar{P}_{ij,2}^{kl}$, $\bar{\Phi}_{ij,1}^{kl}$ and $\bar{\Phi}_{ij,2}^{kl}$) after the GPS error model reduction, between two satellites (k and l) and two receivers (reference receiver i and rover receiver j) as a function of the unknowns (i.e., double-difference geometric term (ρ_{ij}^{kl}), double-difference tropospheric delay residual (T_{ij}^{kl}), double-difference ionospheric delay residual (I_{ij}^{kl}) and double-difference ambiguities ($N_{ij,1}^{kl}$ and $N_{ij,2}^{kl}$). The double-difference tropospheric delay residual (T_{ij}^{kl}) is normally ignored for short baselines, while it may be significant for the long baseline, which can be compensated by estimating the differential zenith tropospheric delay residuals (ZTD) between two receivers. In the application discussed in this dissertation, the double-difference tropospheric delay residual is ignored. Following the symbols used in Chapter 2, equation (3.1) re-parameterizes the unknowns of the double-difference geometric terms (ρ_{ij}^{kl}) of a reference satellite k and n satellites (l_1, l_2, \dots, l_n), into three unknown coordinates of the rover receiver j . Actually, due to the nonlinearities shown in equations (2.8-2.14), the coordinate increments (δX_j , δY_j and δZ_j) of the rover receiver j are solved with respect to the approximate 3-dimensional coordinates (X_{j0} , Y_{j0} and Z_{j0}) using a linearization procedure, instead of directly solving for the rover coordinates (X , Y and Z). The double-difference carrier-phase wide-lane (L_w) measurement ($\bar{\Phi}_{ij,w}^{kl}$) of the carrier-phase L_1 and L_2 linear combination is used instead of the double-difference carrier-phase L_2 measurement ($\bar{\Phi}_{ij,2}^{kl}$), due to the easily resolved wide-lane integer ambiguity ($N_{ij,w}^{kl}$). Since the measurements on L_2 may not be available, for example, in the single-frequency receivers or in case of the losses of GPS on L_2 in the dual-frequency receivers, equation (3.1) can be easily modified to accommodate the missing L_2 measurements by removing the related terms (i.e., y_{P_2} and y_{Φ_w}).

The double-difference ionospheric delays are negligible for short baselines up to a

few tens of kilometers, whereas they may be significant for the longer baselines. Thus, following Schaffrin & Bock (1988), additional double-difference ionospheric pseudo-observations ($I_{ij,0}^{kl}$), based on a priori ionospheric model, are incorporated in equation (3.1) together with the code and carrier-phase measurements ($\bar{P}_{ij,1}^{kl}$, $\bar{P}_{ij,2}^{kl}$, $\bar{\Phi}_{ij,1}^{kl}$ and $\bar{\Phi}_{ij,w}^{kl}$) to facilitate the double-difference integer ambiguity resolution.

The value of the double-difference ionospheric delay (i.e., z_0 in equations 3.1 and 3.4) can be changed according to the adopted a priori ionospheric model, and its standard deviation (i.e., the square root of its variance) since it is a function of the accuracy of the a priori ionospheric model, which normally can be of the mm-level per one-kilometer baseline. The a priori ionospheric model can, for instance, be the broadcast Klobuchar ionospheric model or the GIM discussed in Chapter 2, or the spatially network-derived ionospheric model (see, for example, Yi & Grejner-Brzezinska, 2003 & 2004), or the temporally predicted ionospheric model (see, for example, Yi & Grejner-Brzezinska, 2003 & 2004). A detailed scheme using the L_1 and L_2 measurements with the weighted constraints on the residual ionospheric effects can be found in Schaffrin & Bock (1988). A more detailed a priori model for the double-difference ionospheric delays can be fitted from the observed double-difference ionospheric delays computed from the double-difference carrier-phase ionospheric-only (i.e., geometry-free) linear combinations after the removal of the double-difference integer ambiguities. Figure 3.2 illustrates the standard deviation of the observed vertical double-difference ionospheric delays as a function of the baseline length; here, the fitted linear model is $y=ax+b$ with $a=0.166$ [mm/km] and $b=8.242$ [mm]. The fitted double-difference ionospheric model will be different under various ionospheric conditions, which are functions of the solar and geomagnetic activities. An indicator of the level of the geomagnetic activity is, for example, the Kp index, which can be found at (http://www.gfz-potsdam.de/pb2/pb23/GeoMag/niemegk/kp_index/quicklook.html).

$$\begin{bmatrix} y_{P_1} \\ y_{P_2} \\ y_{\Phi_1} \\ y_{\Phi_w} \\ z_0 \end{bmatrix} = \begin{bmatrix} A_1 & I_n & 0 & 0 \\ A_1 & \beta I_n & 0 & 0 \\ A_1 & -I_n & \lambda_1 I_n & 0 \\ A_1 & -\beta_1 I_n & 0 & \lambda_w I_n \\ 0 & I_n & 0 & 0 \end{bmatrix} \begin{bmatrix} \xi_1 \\ \xi_2 \\ \xi_3 \\ \xi_4 \end{bmatrix} + \begin{bmatrix} e_{P_1} \\ e_{P_2} \\ e_{\Phi_1} \\ e_{\Phi_w} \\ e_0 \end{bmatrix} \sim \begin{bmatrix} \Sigma_{P_1} & & & & \\ & \Sigma_{P_2} & & & \\ & & \Sigma_{\Phi_1} & & \\ & & & \Sigma_{\Phi_w} & \\ & & & & \Sigma_0 \end{bmatrix} \quad (3.1)$$

$$y_{P_1} = \begin{bmatrix} \bar{P}_{ij,1}^{kl} - \rho_{ij,0}^{kl} \\ \bar{P}_{ij,1}^{kb} - \rho_{ij,0}^{kb} \\ \vdots \\ \bar{P}_{ij,1}^{kn} - \rho_{ij,0}^{kn} \end{bmatrix} \quad y_{P_2} = \begin{bmatrix} \bar{P}_{ij,2}^{kl} - \rho_{ij,0}^{kl} \\ \bar{P}_{ij,2}^{kb} - \rho_{ij,0}^{kb} \\ \vdots \\ \bar{P}_{ij,2}^{kn} - \rho_{ij,0}^{kn} \end{bmatrix} \quad y_{\Phi_1} = \begin{bmatrix} \bar{\Phi}_{ij,1}^{kl} - \rho_{ij,0}^{kl} \\ \bar{\Phi}_{ij,1}^{kb} - \rho_{ij,0}^{kb} \\ \vdots \\ \bar{\Phi}_{ij,1}^{kn} - \rho_{ij,0}^{kn} \end{bmatrix} \quad y_{\Phi_w} = \begin{bmatrix} \bar{\Phi}_{ij,w}^{kl} - \rho_{ij,0}^{kl} \\ \bar{\Phi}_{ij,w}^{kb} - \rho_{ij,0}^{kb} \\ \vdots \\ \bar{\Phi}_{ij,w}^{kn} - \rho_{ij,0}^{kn} \end{bmatrix} \quad (3.2)$$

$$z_0 = \begin{bmatrix} I_{ij,0}^{kl_1} \\ I_{ij,0}^{kl_2} \\ \vdots \\ I_{ij,0}^{kl_n} \end{bmatrix} \quad \xi_1 = \begin{bmatrix} \delta X_j \\ \delta Y_j \\ \delta Z_j \end{bmatrix} \quad \xi_2 = \begin{bmatrix} I_{ij}^{kl_1} \\ I_{ij}^{kl_2} \\ \vdots \\ I_{ij}^{kl_n} \end{bmatrix} \quad \xi_3 = \begin{bmatrix} N_{ij,1}^{kl_1} \\ N_{ij,1}^{kl_2} \\ \vdots \\ N_{ij,1}^{kl_n} \end{bmatrix} \quad \xi_4 = \begin{bmatrix} N_{ij,w}^{kl_1} \\ N_{ij,w}^{kl_2} \\ \vdots \\ N_{ij,w}^{kl_n} \end{bmatrix} \quad (3.3)$$

$$A_1 = \begin{bmatrix} \left(\mathbf{u}_{ij}^{kl_1} \right)_0 & \left(\mathbf{u}_{ij}^{kl_1} \right)_1 & \left(\mathbf{u}_{ij}^{kl_1} \right)_2 \\ \left(\mathbf{u}_{ij}^{kl_2} \right)_0 & \left(\mathbf{u}_{ij}^{kl_2} \right)_1 & \left(\mathbf{u}_{ij}^{kl_2} \right)_2 \\ \vdots & \vdots & \vdots \\ \left(\mathbf{u}_{ij}^{kl_n} \right)_0 & \left(\mathbf{u}_{ij}^{kl_n} \right)_1 & \left(\mathbf{u}_{ij}^{kl_n} \right)_2 \end{bmatrix} \quad (3.4)$$

Here, superscripts k and l (l_1, l_2, \dots, l_n) denote the satellites; subscripts i and j denote the receivers; the receiver i is the reference receiver with known fixed coordinates; the receiver j is the rover receiver, whose actual coordinates are to be solved and approximate coordinates (X_{j0} , Y_{j0} and Z_{j0}) are given; y_{P_1} , y_{P_2} , y_{Φ_1} and y_{Φ_w} are the vectors of the GPS double-difference observed-minus-calculated (OMC) code and carrier-phase observations; the calculated observations are based on the reference coordinates of receiver j , the approximate rover coordinates of receiver i and the known satellite coordinates of satellites k and l ; z_0 is the vector of pseudo-observations for the double-difference ionospheric delays; A_1 is a part of the design matrices; ξ_1 is the vector of the three unknown coordinate increments (δX_j , δY_j and δZ_j) of the rover receiver j ; ξ_2 is the vector of double-difference ionospheric delays (I_{ij}^{kl}); ξ_3 and ξ_4 are the vectors of double-difference integer ambiguities on L_1 ($N_{ij,1}^{kl}$) and L_w ($N_{ij,w}^{kl}$), respectively; e_{P_1} , e_{P_2} , e_{Φ_1} , e_{Φ_w} and e_0 are the error vectors of the double-difference observations ($\bar{P}_{ij,1}^{kl}$, $\bar{P}_{ij,2}^{kl}$, $\bar{\Phi}_{ij,1}^{kl}$ and $\bar{\Phi}_{ij,w}^{kl}$) and the double-difference ionospheric pseudo-observations ($I_{ij,0}^{kl}$); Σ_{P_1} , Σ_{P_2} , Σ_{Φ_1} , Σ_{Φ_w} and Σ_0 are the variance-covariance matrices of the error vectors (e_{P_1} , e_{P_2} , e_{Φ_1} , e_{Φ_w} and e_0); $\bar{P}_{ij,1}^{kl}$, $\bar{P}_{ij,2}^{kl}$, $\bar{\Phi}_{ij,1}^{kl}$ and $\bar{\Phi}_{ij,w}^{kl}$ are the double-difference code and carrier-phase pseudo-range observations after GPS error model reduction; $\rho_{ij,0}^{kl}$ is the computed double-difference geometric term using the coordinate of the reference receiver i and the approximate coordinate of the rover receiver j ; $\mathbf{u}_{ij}^{kl} = \left[\left(\mathbf{u}_{ij}^{kl} \right)_0 \quad \left(\mathbf{u}_{ij}^{kl} \right)_1 \quad \left(\mathbf{u}_{ij}^{kl} \right)_2 \right]^T$ is a 3-dimensional vector of the partial derivatives of the

double-difference geometric term (ρ_{ij}^{kl}) with respect to to the coordinate of the rover

receiver j evaluated at the approximate rover coordinate; $\beta = \frac{f_1^2}{f_2^2}$ and $\beta_1 = -\frac{f_1}{f_2}$; f_1 and

f_2 are the frequencies on L_1 and L_2 ; λ_1 and λ_w are the wavelengths on L_1 and L_w ; \mathbf{I}_n is the n -dimensional identity matrix.

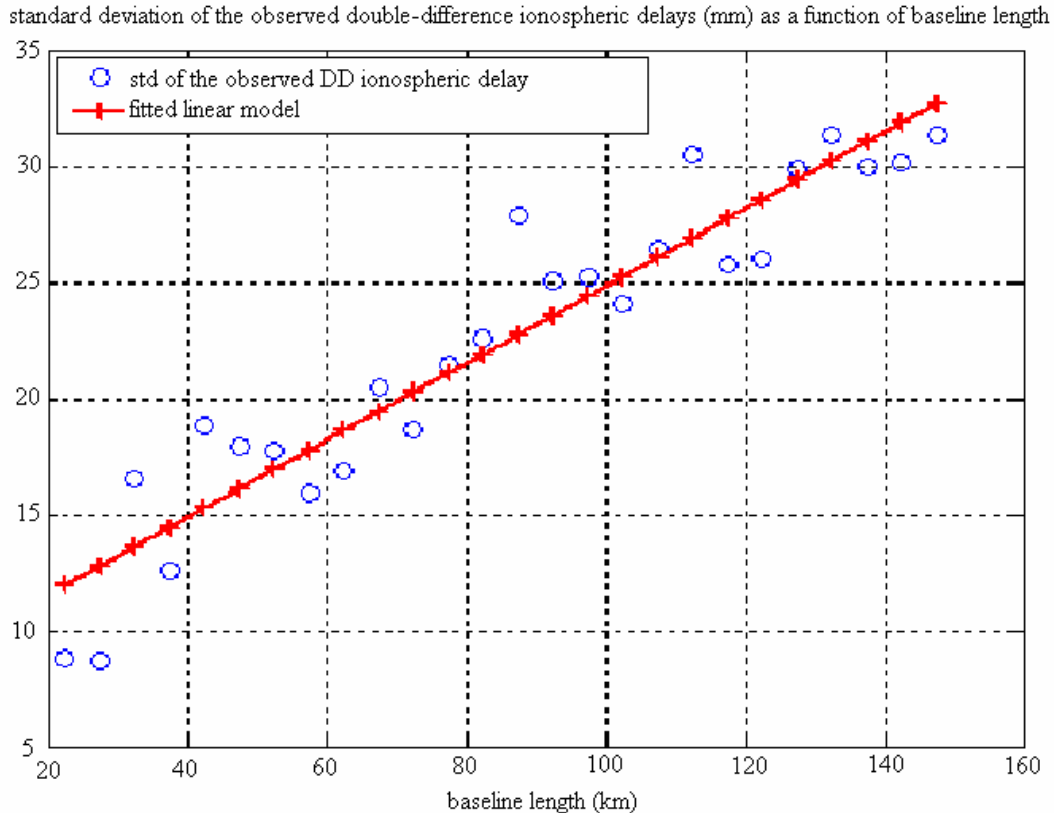


Figure 3.2. Standard deviation (std) of the observed vertical double-difference ionospheric delay as a function of baseline length (from a network located in Florida, USA, using data collected in Jan. 2007).

3.2.2 Single-epoch GPS ambiguity resolution

Equations (3.1-3.4) describe the GPS double-difference model for the instantaneous RTK positioning approach. Similarly to the traditional RTK positioning approach, which uses the Kalman filter or a sequential least-squares adjustment, the instantaneous RTK positioning approach also starts with a float GPS ambiguity resolution, and a double-difference integer ambiguity resolution is derived from it. In estimating the float

GPS N_1 and wide-lane N_w ambiguities, the least-squares adjustment is implemented here to solve for the three unknown rover coordinates and the float ambiguities (plus the double-difference ionospheric delays for longer baselines), using the code and carrier-phase pseudorange measurements (and incorporating double-difference slant ionospheric pseudo-observations for longer baselines) for the satellites above the elevation mask angle. In the double-difference integer ambiguity resolution stage, various algorithms can be used; the LAMBDA method of Teunissen (1993 & 1994) was implemented in this dissertation. The wide-lane N_w ambiguities are recommended to be fixed first, which will then facilitate the N_1 ambiguity resolution. For short baselines, the N_1 and N_w ambiguities can also be easily fixed in a single step. Also, both the N_1 and N_w ambiguities should be fixed in a single step while insufficient number of L_w measurements (the minimum is four) is available to fix the N_w ambiguities in a separate step, for example, when the rover receiver operates in kinematic mode with frequent losses of GPS lock on L_2 . After fixing the double-difference integer ambiguities, the high-accuracy carrier-phase measurements L_1 are directly used to solve the rover position for short baselines, whereas the ionospheric-free (L_3) linear combination is recommended to be used for longer baselines, even though the L_1 measurements combined with the double-difference ionospheric pseudo-observations, can also provide an equivalent solution for the longer baselines.

A number of factors will impact the performance of the single-epoch ambiguity resolution; for example, the base-rover separation, the number of available double-difference satellite pairs above the elevation mask angle, and the code measurement (P_1 and P_2) accuracy. A minimum of four double-difference satellite pairs with both (L_1 and L_2) carrier-phase measurements are recommended to be observed in order to assure the success of the double-difference integer ambiguity resolution. A code smoothing scheme, using the high-accuracy carrier-phase measurements (L_1 and L_2), such as, the Hatch filter shown in equations (3.3 and 3.4), can be used to improve the code measurement accuracy by filtering the multipath and the measurement noise of the code pseudo-range measurements (P_1 and P_2). Figure 3.3 presents an example of the code smoothing effects using carrier-phase measurements. The code-smoothing schema can be done for the one-way, single-difference or double-difference measurements.

$$\begin{aligned}\tilde{P}_{1,k} &= \frac{P_{1,k}}{n_1} + \frac{(\tilde{P}_{1,k-1} + \Phi_{1,k} - \Phi_{1,k-1} + 2\Delta I) \cdot (n_1 - 1)}{n_1} \\ \tilde{P}_{2,k} &= \frac{P_{2,k}}{n_2} + \frac{(\tilde{P}_{2,k-1} + \Phi_{2,k} - \Phi_{2,k-1} + 2\beta\Delta I) \cdot (n_2 - 1)}{n_2}\end{aligned}\tag{3.3}$$

$$\Delta I = I_k - I_{k-1} = \frac{(\Phi_{1,k} - \Phi_{2,k}) - (\Phi_{1,k-1} - \Phi_{2,k-1})}{\beta - 1} \quad (3.4)$$

Here, n_1 and n_2 are the numbers of continuous carrier-phase measurements, Φ_1 and Φ_2 , on L_1 and L_2 , respectively, without cycle slips; $\tilde{P}_{1,k}$ and $\tilde{P}_{2,k}$ are the smoothed code measurements on L_1 and L_2 at epoch k ; ΔI is the change of the ionospheric delays, I , between two epochs; $\beta = \frac{f_1^2}{f_2^2}$; f_1 and f_2 are the frequencies on L_1 and L_2 , respectively.

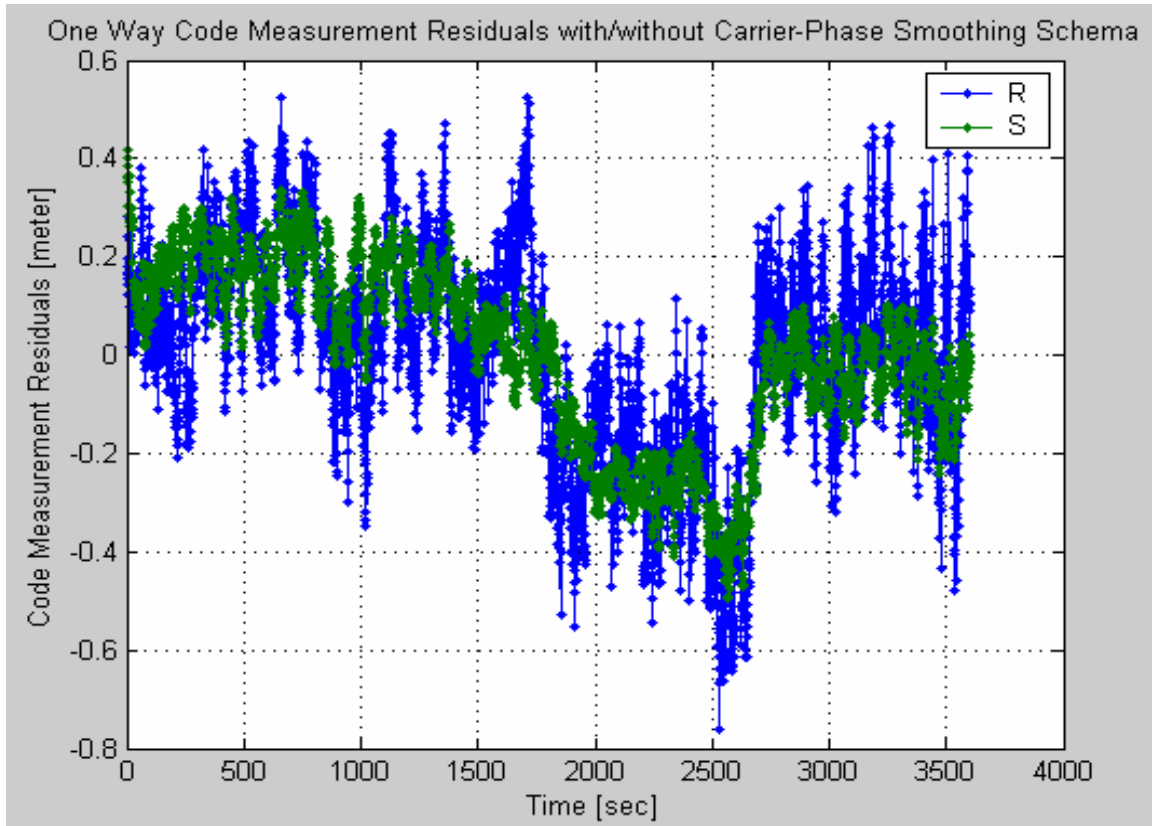


Figure 3.3. An example of the code smoothing effects using carrier-phase measurements. Note: R denotes the raw code measurement residuals (i.e., after the subtraction of the geometric term, receiver and satellite clocks, tropospheric and ionospheric error models), and S denotes the carrier-phase-smoothed code measurement residuals.

The quality control of the single-epoch integer ambiguity resolution provides an indication of the reliability of the instantaneous RTK positioning technique; see, for example, Han (1997c), as well as, Tiberius *et al.* (1997) for the performance and quality control of the kinematic positioning using the LAMBDA method. Another method to test the ambiguity using statistical testing technique was proposed by Euler & Schaffrin (1990). The quality control used here consists of checking the ratio of the squared norm of the ambiguity sets for the best and the second-best candidate from the LAMBDA method. The ambiguities are assumed to be fixed if the ratio is greater than a pre-defined value (a ratio cutoff of 3.0 is adopted in this dissertation). Figure 3.4 shows a one-hour example of the single-epoch L_w ambiguity ratio for a 16 km baseline with a double-difference ionospheric constraint for each double-difference satellite pair. The ionospheric constraint was selected here to be ± 1 mm of the vertical double-difference ionospheric delay per one-kilometer baseline. As will be shown in Section 3.2.3, a scale factor with respect to this pre-selected constraint level is estimated to accommodate the variation of the actual ionospheric conditions. The carrier-phase code smoother was turned off in this example, and 75 percent of epochs passed the L_w ratio test.

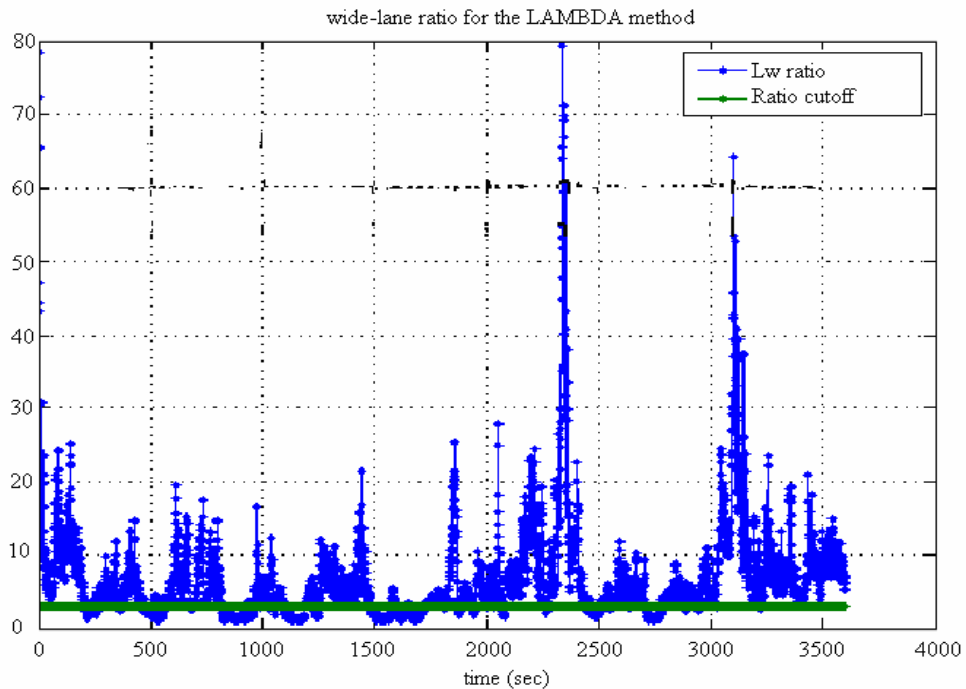


Figure 3.4. An example of the single-epoch wide-lane ratio from the LAMBDA method for a 16 km baseline during one hour (3600 epochs) (75 percent of epochs passed the ambiguity ratio test when applying $0 \text{ m} \pm 1 \text{ mm/km}$ ionospheric constraints and using raw code measurements without carrier-phase-based smoothing).

3.2.3 Stochastic model based on variance component model

The stochastic model of the instantaneous kinematic positioning plays a significant role in the success of the integer ambiguity resolution. The implementations of the stochastic model in this dissertation include: 1) an elevation-dependent measurement accuracy model, and 2) a variance component model (VCM) to estimate the code and carrier-phase measurement reference variances, and the reference variance of the double-difference ionospheric pseudo-observations. The generalized VCM for n types of measurements with n unknown reference variance components is shown in equation (3.5). The recursive solution of this nonlinear estimation for the unknown parameters and the unknown reference variance components is shown in equations (3.6 - 3.8), starting with a suitable initial reference variance components (Schaffrin, 2001b).

$$y = A\xi + e,$$

$$e \sim \left(0, \Sigma = \mathcal{G}_1 Q_1 + \mathcal{G}_2 Q_2 + \dots + \mathcal{G}_n Q_n = \sum_{i=1}^n \mathcal{G}_i Q_i \right), y \equiv [y_1^T \quad y_2^T \quad \dots \quad y_n^T]^T \quad (3.5)$$

$$\begin{bmatrix} tr(\hat{W}Q_1\hat{W}Q_1) & tr(\hat{W}Q_1\hat{W}Q_2) & \dots & tr(\hat{W}Q_1\hat{W}Q_n) \\ tr(\hat{W}Q_2\hat{W}Q_1) & tr(\hat{W}Q_2\hat{W}Q_2) & \dots & tr(\hat{W}Q_2\hat{W}Q_n) \\ \vdots & \vdots & \ddots & \vdots \\ tr(\hat{W}Q_n\hat{W}Q_1) & tr(\hat{W}Q_n\hat{W}Q_2) & \dots & tr(\hat{W}Q_n\hat{W}Q_n) \end{bmatrix} \begin{bmatrix} \hat{\mathcal{G}}_1 \\ \hat{\mathcal{G}}_2 \\ \vdots \\ \hat{\mathcal{G}}_n \end{bmatrix} = \begin{bmatrix} y^T \hat{W}Q_1 \hat{W}y \\ y^T \hat{W}Q_2 \hat{W}y \\ \vdots \\ y^T \hat{W}Q_n \hat{W}y \end{bmatrix} \quad (3.6)$$

$$\hat{W} = \hat{\Sigma}^{-1} - \hat{\Sigma}^{-1} A (A^T \hat{\Sigma}^{-1} A)^{-1} A^T \hat{\Sigma}^{-1} \quad (3.7)$$

$$\hat{\xi} = (A^T \hat{\Sigma}^{-1} A)^{-1} A^T \hat{\Sigma}^{-1} y \quad (3.8)$$

Here, y is the vector of the measurements including n types of measurement sub-vectors y_1, y_2, \dots, y_n ; A is the design matrix; ξ is the vector of the unknown parameters; e is the vector of the random errors with zero-mean, Σ is the unknown variance-covariance matrix, and \mathcal{G} is the vector of the unknown variance-covariance components; Σ with top and bottom limit values indicates the summation from the bottom limit value to the top limit value; the subscript i is the index starting from 1 to n (the dimension of the vector of the variance-covariance components); the variance-covariance component \mathcal{G}_i has the corresponding cofactor matrix Q_i ; tr represents the trace operator of a matrix; a variable with a hat (^) indicates that it has been estimated; W is called a reduced weight matrix.

The single-epoch RTK positioning implementation takes the three different measurement types: 1) double-difference code measurements, 2) double-difference

carrier-phase measurements, and 3) double-difference ionospheric delay pseudo-observations. Thus, the dimension of the variance component vector, \mathcal{G} , shown in equation (3.5), is three. Since predefined reference variances are used for each measurement type (i.e., the code measurements, the carrier-phase measurements and the double-difference ionospheric delay pseudo-observations), in the actual implementation of the variance-component model, the scale factors with respect to the predefined reference variances are estimated instead of the actual reference variances for each type of measurements. The detailed form of the variance component vector implemented in this dissertation is shown in equation (3.9). According to Han (1997c), estimating a scale factor of the nominal code measurement accuracy from the real-time GPS measurement residuals can improve the GPS integer ambiguity resolution. Having a better stochastic model will result in a better performance in the GPS integer ambiguity resolution and its corresponding positioning accuracy. An example of the scale factor with respect to the reference variance of the code measurements is shown in Figure 3.9 of the data analysis Section 3.3.1. The example analysis of the variance component estimation and the GPS ambiguity resolution can be found in (Tiberius & Kenselaar, 2003).

It should be noted that even if the ambiguity ratio test successfully passed, another global statistical test, in the parameter estimation procedure (i.e., when the rover position is obtained using the fixed double-difference integer ambiguities) is also applied. For details on the test implemented here, see, Schaffrin (2000 & 2001a).

$$\Sigma = s_P \begin{bmatrix} \Sigma_{P_1} & 0 & 0 & 0 & 0 \\ 0 & \Sigma_{P_2} & 0 & 0 & 0 \\ 0 & 0 & 0 & 0 & 0 \\ 0 & 0 & 0 & 0 & 0 \\ 0 & 0 & 0 & 0 & 0 \end{bmatrix} + s_L \begin{bmatrix} 0 & 0 & 0 & 0 & 0 \\ 0 & 0 & 0 & 0 & 0 \\ 0 & 0 & \Sigma_{L_1} & 0 & 0 \\ 0 & 0 & 0 & \Sigma_{L_2} & 0 \\ 0 & 0 & 0 & 0 & 0 \end{bmatrix} + s_I \begin{bmatrix} 0 & 0 & 0 & 0 & 0 \\ 0 & 0 & 0 & 0 & 0 \\ 0 & 0 & 0 & 0 & 0 \\ 0 & 0 & 0 & 0 & 0 \\ 0 & 0 & 0 & 0 & \Sigma_I \end{bmatrix} \quad (3.9)$$

Where, $\mathcal{G} = [s_P \sigma_P^2 \quad s_L \sigma_L^2 \quad s_I \sigma_I^2]^T$; s_P , s_L and s_I are the scale factors with respect to the nominal code and carrier-phase variance model and the a priori double-difference ionospheric information, respectively; Σ_{P_1} , Σ_{P_2} , Σ_{L_1} , Σ_{L_2} and Σ_I are the nominal variance-covariance models for double-difference code measurements (P_1 and P_2), double-difference carrier-phase measurement (L_1 and L_2), and the virtual double-difference ionospheric measurements; σ_P^2 , σ_L^2 and σ_I^2 are the predefined nominal reference variances for code and carrier-phase measurements and the a priori double-difference ionospheric information, respectively.

3.2.4 Partial integer ambiguity fixing strategy

Another data processing strategy employed in this dissertation is the partial fixing of the GPS ambiguities if all the available GPS ambiguities for observations above the elevation mask angle cannot be fixed, for example, due to the failure of the ratio test. The ambiguities of the double-difference satellite pairs with the lower elevation angles are more difficult to fix in comparison to these of the double-difference satellite pairs with higher elevation angles due to more uncertainties in the code and carrier-phase measurements. Therefore, if the ambiguity ratio test fails for all the available ambiguities, the lowest double-difference satellite pair will be removed, and this removal will continue until only four double-difference satellite pairs are left. As mentioned earlier, four is the minimum number of double-difference satellite pairs for the epoch-by-epoch RTK positioning technique implemented in this dissertation.

3.2.5 Integer ambiguity bridging between consecutive epochs

Even after adopting the above data processing strategies, the ambiguity ratio test of some epochs may still not be passed. In such cases, if the ambiguity resolution of the previous epoch is successful, the change of the ambiguities (i.e., the cycle slip) can easily be solved using the change of the measurements (ΔP_1 , ΔP_2 , ΔL_1 and ΔL_w) due to the almost identical error sources (mainly the identical double-difference ionospheric delays, i.e., $\Delta I \approx 0$) between two nearby epochs. The LAMBDA method is also applied in this case to fix the cycle slips. If the cycle slips are fixed, the ambiguities of the current epoch can be propagated from the previous epoch. Since this technique takes advantage of the measurements from the two nearby epochs, it is clearly contradictory to the proposed single-epoch RTK positioning procedure, which only uses the measurements of the current epoch. However, it can bridge the GPS ambiguities in the kinematic case, instead of discarding the current epoch due to the failure of the ambiguity ratio test. But, if the ambiguities were fixed to the wrong values in the previous epoch, such technique will pass the wrong ambiguities to the current epoch as the classical OTF may also do. Thus to minimize the risk of propagating the wrong ambiguities from the previous epoch, this technique should only be used as a last resort of the data processing. Figure 3.5 illustrates the workflow implemented according to the data processing strategies described above.

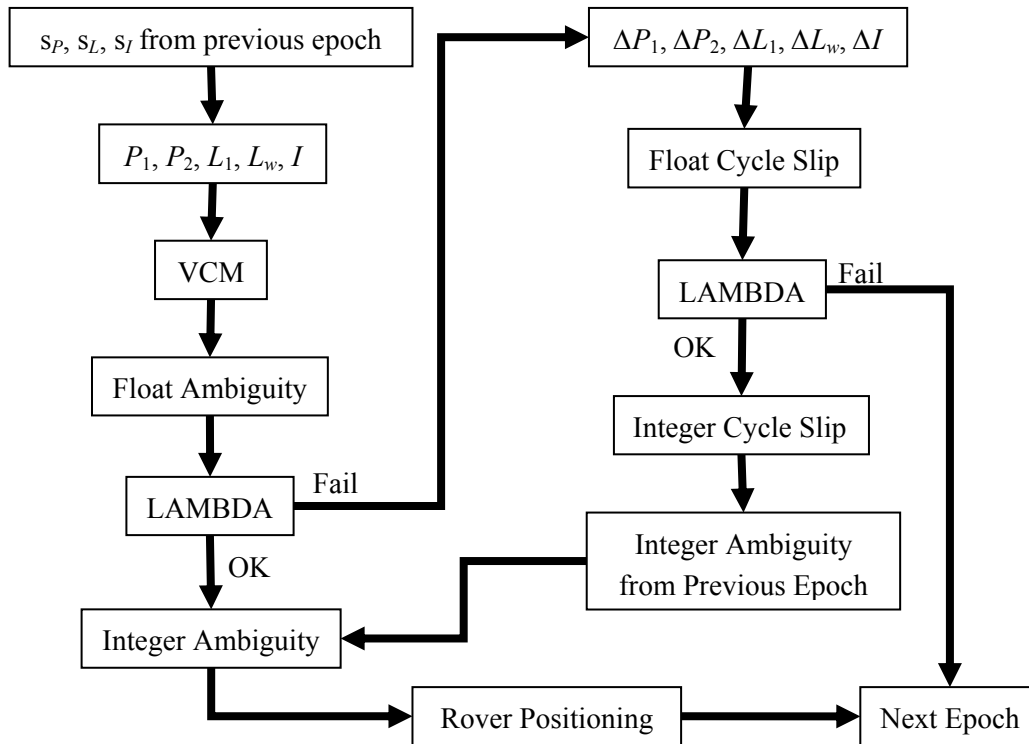


Figure 3.5. Workflow of the epoch-by-epoch RTK positioning approach (the a priori I can be based on the broadcast Klobuchar ionospheric model or the IGS published GIM, or the spatial prediction from a network-derived ionospheric model or the temporal prediction from the previously derived ionospheric model; s_P , s_L and s_I are the scale factors to the nominal variance component models for the code, carrier-phase, and virtual-ionospheric measurements).

3.3 Analysis of experimental static data

3.3.1 Baseline-by-baseline mode

In order to evaluate the performance of the implemented single-epoch positioning approach, several baselines with various lengths (16 km, 25 km, 50 km and 70 km) were processed using the software developed according to the algorithms presented earlier. Current implementation includes: 1) double-difference ionospheric pseudo-observations 2) carrier-phase-based code smoothing technique; 3) VCM-based stochastic model; 4) partial ambiguity fixing strategy, and 5) bridging the GPS ambiguities from the previous fixed epoch.

The tested baselines are from a local network located in Florida, and the data were acquired in Jan. 2007. Table 3.1 presents the statistics of the ambiguity fixing process for a 25 km baseline during one hour (3600 epochs) using the selected data process strategies listed above. Only 43.81% of 3600 epochs is fixed by using only the double-difference

ionospheric pseudo-observations (option 1). By turning on the estimation of the variance component (option 3), additional 11 epochs are fixed. The improvement due to the VCM is not significant, which indicates that the pre-defined stochastic error model already matches the data very well. By turning on the carrier-phase-based code measurement smoothing strategy (option 2), a relatively significant improvement can be found; namely, a total of 57.36% epochs can be fixed, as compared to 43.81% when using only option 1. The most significant improvement in the ambiguity fixing rate is caused by applying the partial ambiguity fixing strategy (option 4). Around 87.19% of epochs can be fixed by combining options 1 and 4. The integer fixing rate reaches 98.14% when options 1 through 4 are combined, and all epochs can be fixed if bridging the ambiguity from the previous epoch is also turned on (option 5). The detail statistics of the final solution for this baseline is shown later.

Options	1	1+3	1+2	1+4	1+3+4	1+2+3+4	1+2+3+4+5
Fixed Epochs	1577	1589	2065	3139	3156	3533	3600
Fixed Rate (%)	43.81	44.14	57.36	87.19	87.67	98.14	100.00

Table 3.1. Ambiguity fixing statistics for a 25 km baseline with one hour of data, using selected data process strategies.

Figure 3.6 illustrates an example of the single-epoch L_w and L_1 solutions for a static 70 km baseline processed in the kinematic mode, compared to the reference coordinates from the NGS OPUS (<http://www.ngs.noaa.gov/OPUS/>) solution (i.e., Figure 3.6 and the following Figures 3.7-3.9 illustrate the coordinate differences between the epoch-by-epoch solutions and the reference static OPUS coordinates). In Figure 3.6, the sub-plot at the top shows the L_w solution difference, the sub-plot in the middle shows the L_1 solution difference, and the sub-plot at the bottom shows the number of the fixed ambiguities on L_1 and L_w , respectively. As marked in Figure 3.6, there are some cases where the L_w ambiguity of the lowest double-difference satellite pair is fixed, while the corresponding L_1 ambiguity is not fixed. Figures 3.7 and 3.8 present the same information for baselines with lengths of 16 km and 25 km, respectively. The sub-plots at the top and in the middle of Figure 3.9 illustrate information comparable to these of Figures 3.6, 3.7 and 3.8, whereas the sub-plot at the bottom of Figure 3.9 shows an example of the scale factor with respect to the nominal variance model for the code measurements estimated from the VCM, where the carrier-phase-based code smoothing effects can be clearly observed. The reference variance of the code measurement accuracy (s_p) is 40 percent smaller after 500 epochs of smoothing and reaches 20 percent after 1000 epochs.

Table 3.2 presents the detailed statistics of the results in Figures 3.6, 3.7, 3.8 and 3.9. Both the mean and the standard deviation (std in Table 3.2) of the L_w and L_1 solutions are within centimeter-level, and the vertical component is a few centimeters weaker than the

horizontal component. The height component of the GPS RTK positioning is well-known to be weaker than the horizontal components. It should be noted that the tropospheric model uncertainties over the longer baselines also partially contribute to the weaker behavior of the vertical component, since the double-difference tropospheric delay residuals are ignored here. For example, relatively bigger height error in the 50 km baseline, as shown in Figure 3.9, may be caused by insufficiently modeled tropospheric effects. Figure 3.10 illustrates the mean and the standard deviation of the L_1 solutions for the four example baselines. As compared to the reference, the position errors of the 50 km baseline are a little worse than that of the other three baselines, even though all of them are of cm-level accuracy.

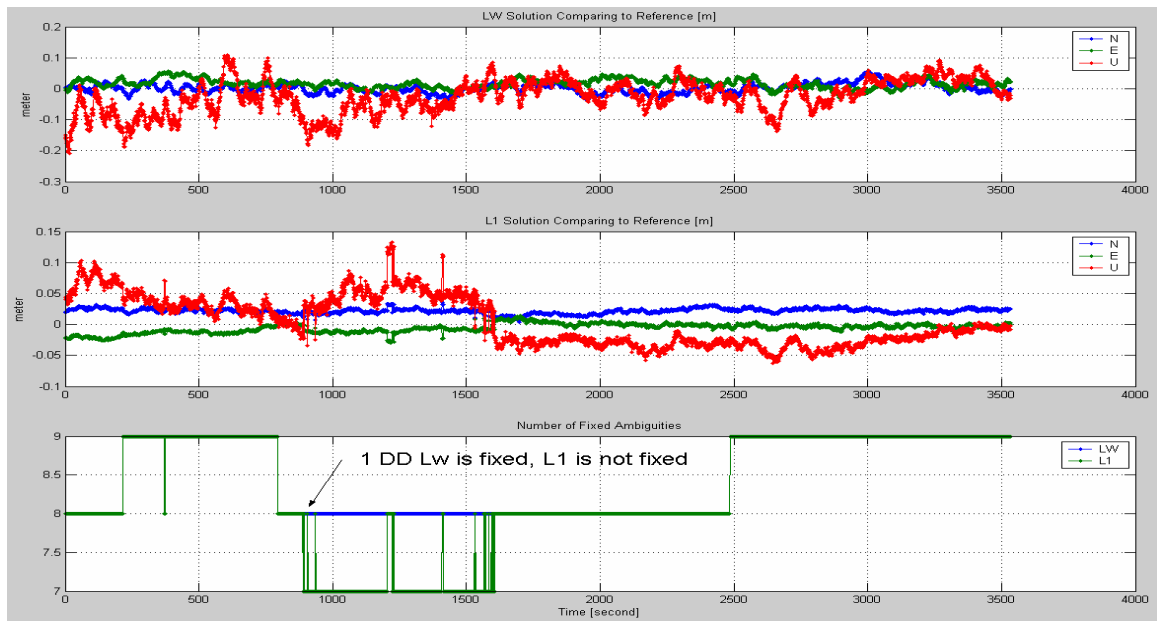


Figure 3.6. An example single-epoch L_w and L_1 solutions, as compared to a reference from NGS OPUS for a static 70 km baseline during one hour (3600 epochs) (mask elevation: 10°).

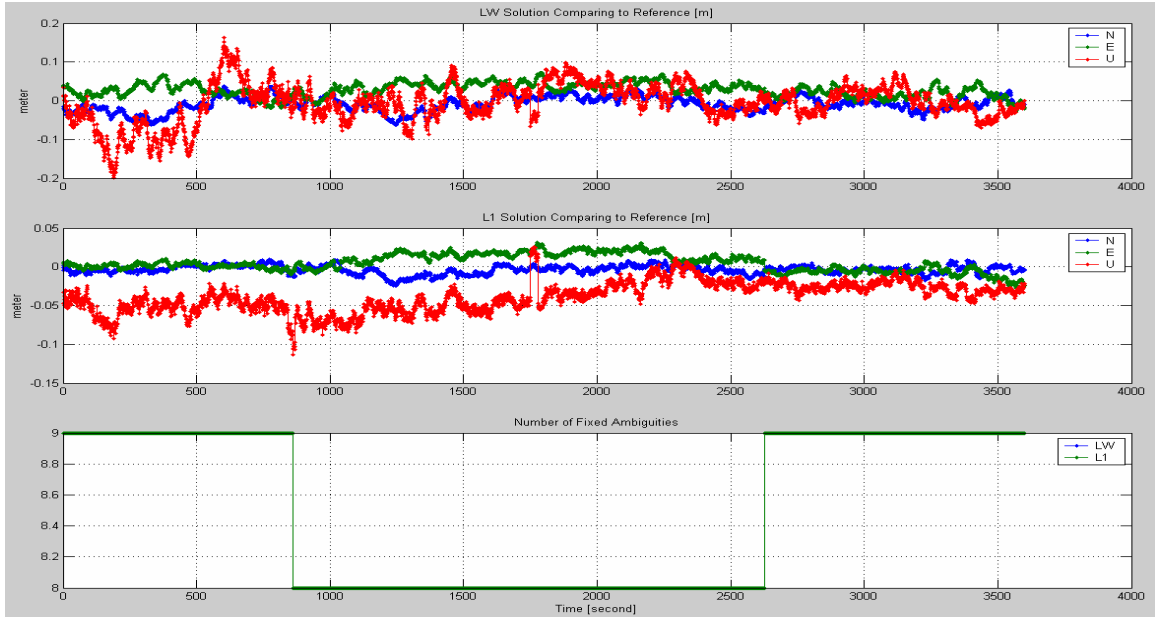


Figure 3.7. An example single-epoch L_W and L_1 solutions, as compared to a reference from NGS OPUS for a static 16 km baseline during one hour (3600 epochs) (mask elevation: 10°).

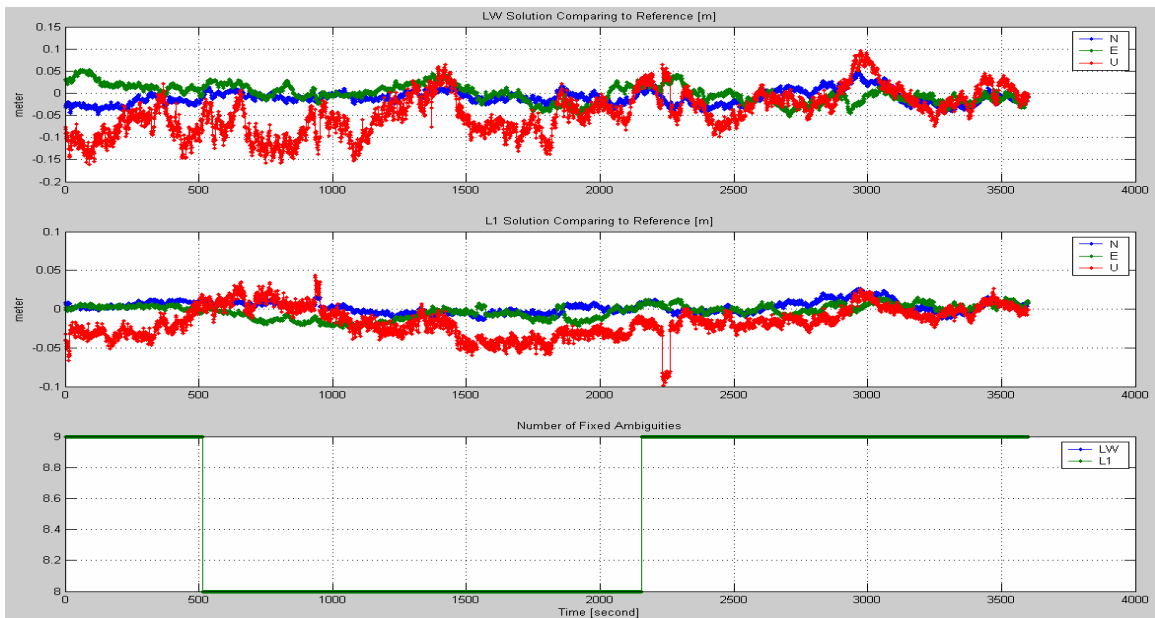


Figure 3.8. An example single-epoch L_W and L_1 solutions, as compared to a reference from NGS OPUS for a static 25 km baseline during one hour (3600 epochs) (mask elevation: 10°).

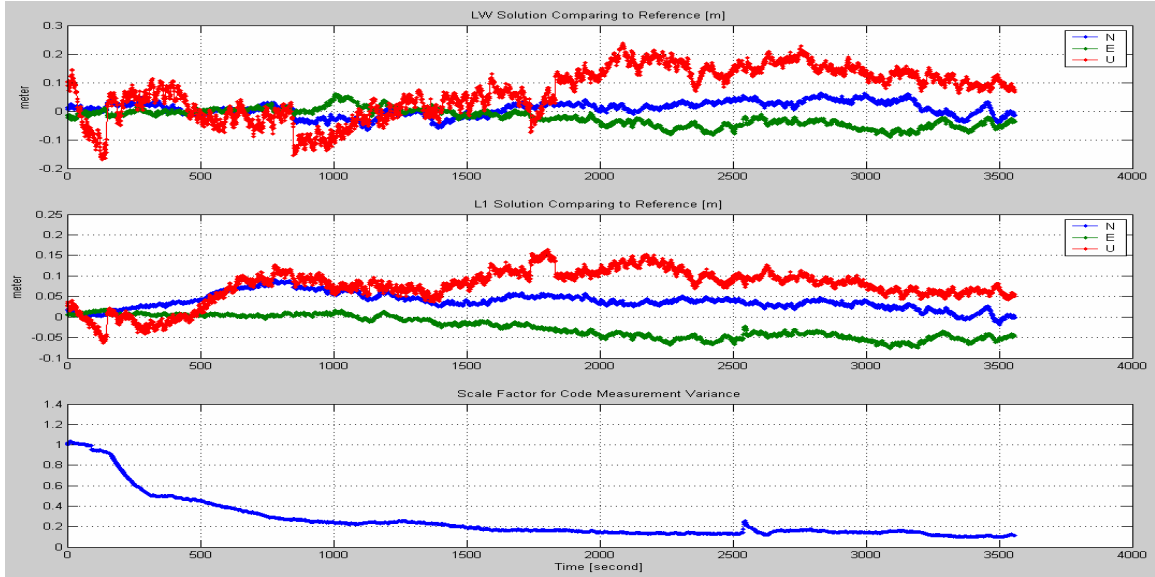


Figure 3.9. An example single-epoch L_w and L_1 solutions, as compared to a reference from NGS OPUS for a static 50 km baseline during one hour (3600 epochs) (mask elevation: 10°).

Baseline Length	Statistics Information	L_w solution			L_1 solution		
		N [cm]	E [cm]	U [cm]	N [cm]	E [cm]	U [cm]
16 [km]	Mean	-0.8	2.8	-0.6	-0.4	0.5	-3.9
	Std	± 2.0	± 1.8	± 5.0	± 0.6	± 1.1	± 1.9
	Max	3.8	7.2	16.3	1.0	3.1	2.6
	Min	-6.3	-3.0	-19.8	-2.5	-2.8	-11.4
25 [km]	Mean	-1.0	-0.0	-4.3	0.2	-0.3	-1.6
	Std	± 1.6	± 2.0	± 4.8	± 0.7	± 0.9	± 1.9
	Max	4.8	5.3	9.6	2.6	1.5	4.3
	Min	-4.8	-5.3	-16.1	-1.5	-2.4	-9.9
50 [km]	Mean	0.8	-2.3	6.7	3.8	-2.5	7.4
	Std	± 2.5	± 2.9	± 8.6	± 2.0	± 2.6	± 4.2
	Max	6.2	5.9	23.7	9.2	1.9	16.4
	Min	-6.6	-9.1	-17.0	-1.9	-7.6	-6.3
70 [km]	Mean	0.2	1.6	-2.6	2.2	-0.6	0.4
	Std	± 1.5	± 1.5	± 5.4	± 0.4	± 0.7	± 4.0
	Max	5.5	5.6	11.0	3.5	1.4	13.3
	Min	-3.5	-3.1	-20.8	0.4	-2.9	-6.3

Table 3.2. Statistics of single-epoch L_w and L_1 solutions, as compared to the references from NGS OPUS, using one-hour example data for baselines of 16, 25, 50 and 70 km.

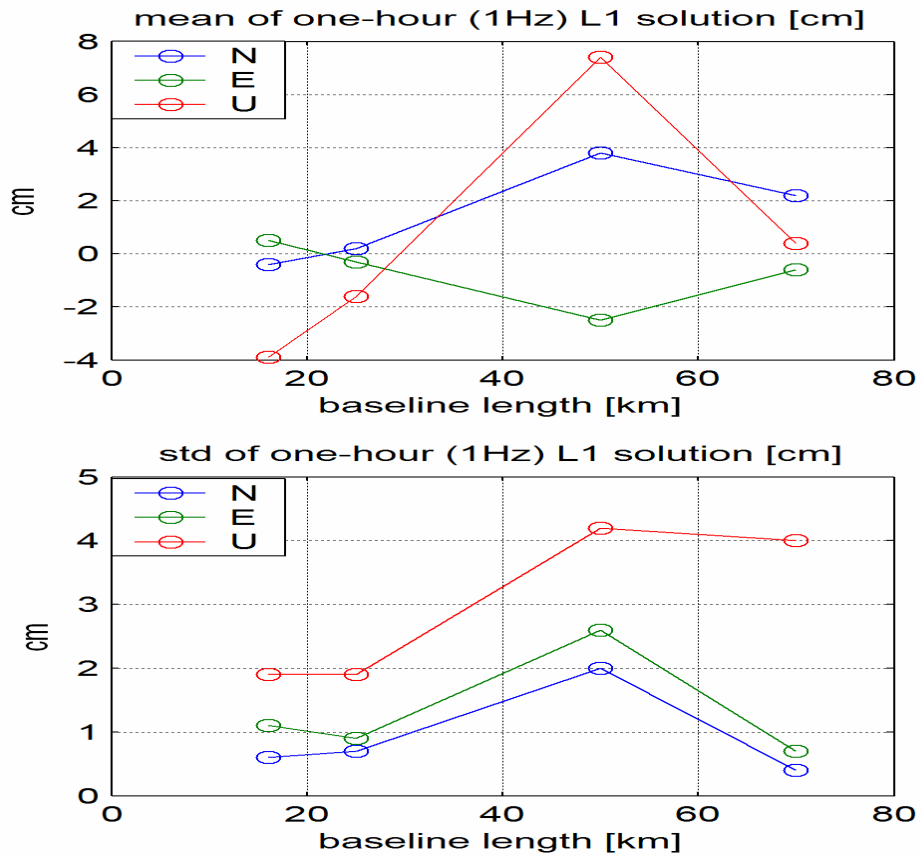


Figure 3.10. Statistics (mean and std) of single-epoch L_1 solutions, as compared to the references from NGS OPUS, using one-hour example data for baselines of 16, 25, 50 and 70 km.

3.3.2 Network mode

The solutions shown in Figures 3.6-3.10 and Table 3.2 were processed in a baseline-by-baseline mode, mainly to demonstrate the capability of the instantaneous RTK positioning approach with the double-difference ionospheric pseudo-observations from the a priori ionospheric model. The Klobuchar ionospheric model was used in the above tests. As explained earlier, the double-difference ionospheric pseudo-observations can also result from the spatial prediction of a network-derived ionospheric model. The details of the procedure of the double-difference ionosphere modeling with multiple reference stations can be found in Yi and Grejner-Brzezinska (2003). The results presented in Yi and Grejner-Brzezinska (2003) of the instantaneous multiple-base kinematic carrier-phase positioning, aided by double-difference ionosphere modeling, and the prediction in the spatial domain indicate that a few-centimeter accuracy can be achieved for the medium-length baselines (~ 100 km). Figure 3.11 demonstrates an

instantaneous L_1 carrier-phase fixed solution, aided by the ionosphere prediction in the spatial domain and a 5 second moving average in the temporal domain for a static ~ 121 km baseline, as compared to the reference coordinates published by NGS (a data set from OHIO CORS stations at GPS day 343, 2002).

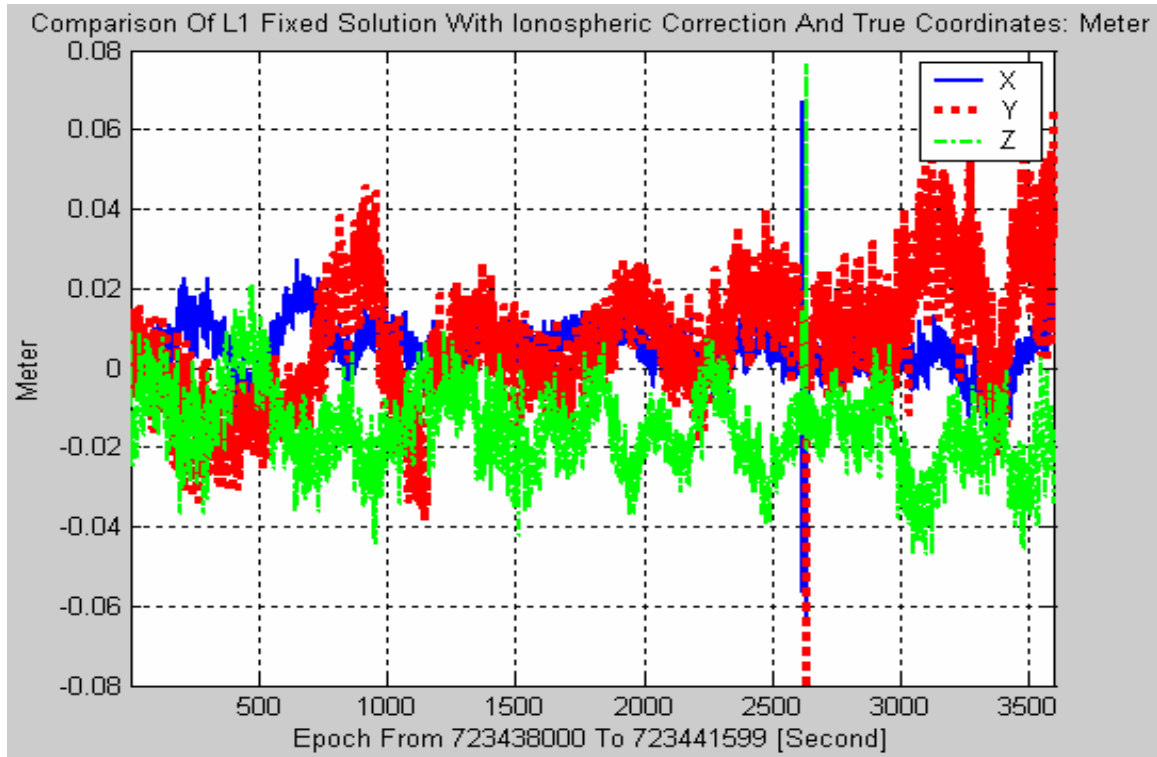


Figure 3.11. Difference with respect to the actual coordinates of the L_1 -fixed solution with ionospheric correction for the Colb-Leba baseline ~ 121 km; the spikes around epoch 2600 are caused by the wrong ambiguity resolution.

3.4 Analysis of experimental kinematic data

In order to evaluate the performance of the implemented single-epoch positioning approach under kinematic environments, an experimental kinematic data set was collected on Sept. 26, 2003, in Columbus, OH, with four GPS rover receivers (two Trimble 5700 GPS receivers with two Trimble Zephyr geodetic antennas, referred to as T1 and T2; one Topcon Legacy GPS receiver with a Topcon Legant antenna, referred to as J2; and one NovAtel OEM4 with a Topcon Legant antenna, referred to as N2) installed on the top of a van. Two GPS reference receivers (one Topcon Legacy, referred to as J1 and one NovAtel OEM4, referred to as N1) connected with a GPS600 antenna installed on the roof of the Center for Mapping (CFM), OSU. The GPS receivers used together with the antenna types according to NGS are listed in Table 3.3. The absolute antenna

calibration results from NGS (<http://www.ngs.noaa.gov/ANTCAL/>) were used in the following data processing. The hardware configuration installed on the vehicle is illustrated in Figure 3.12. The following analyses are based on the four rover receivers (T1, T2, J2 and N2), using the two reference receivers (J1 and N1) at CFM, together with another CORS reference receiver in Columbus (referred to as COLB), based on a 1 Hz sampling rate. The performance analysis based on the same dataset using an earlier version of the implemented software was reported to be better, as compared to a commercial GPS software package, in Yi & Grejner-Brzezinska (2004).

No.	Receiver Type	Antenna Type	Receiver Name	Sampling Rate	Base /Rover
1	TRIMBLE 5700	TRM29659.00 UNAV	COLB	1Hz	Base
2	TPS LEGACY	NOV600	J1	2Hz	Base
3	NovAtel OEM4	NOV600	N1	4Hz	Base
4	TPS LEGACY	TPSLEGANT3_UHF	J2	2Hz	Rover
5	TRIMBLE 5700	TRM41249.00	T1	1Hz	Rover
6	NovAtel OEM4	TPSLEGANT3_UHF	N2	4Hz	Rover
7	TRIMBLE 5700	TRM39105.00	T2	1Hz	Rover

Table 3.3. GPS hardware list.

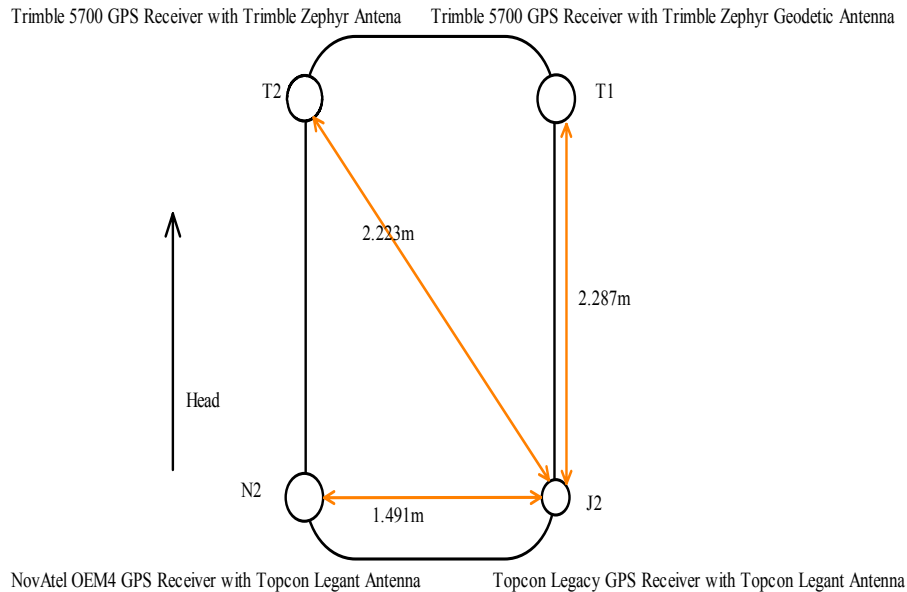


Figure 3.12. Rover receiver hardware configuration for the experimental data set.

In order to validate the positioning performance of the single-epoch RTK positioning approach, actual reference trajectories for this experiment must be provided for the rover receivers. However this information is not available for the kinematic data, unless some image-based photogrammetric method (including control points) is used simultaneously with the GPS data collection. In this experiment, however, there was no imaging component included. Therefore, a simple assumption utilizing the multiple roving antennas was used: the distance between the two antennas should be invariant, assuming that the antennas were firmly attached to the van. Thus, the differences in the position solutions between the various rover receivers can be examined. With the major focus on the performance of the epoch-by-epoch solution, the option to bridge the ambiguities from the previous epoch is turned off in this data process. Also the option for the network error modeling is also turned off, which indicates that each baseline is processed independently from each other, in this way, the comparison of the relative distances between two antennas can better reflect the actual performance of the single-epoch positioning approach implemented in this dissertation under kinematic environments.

The test started and ended at CFM and lasted about 1.5 hours with the distance to the reference station COLB ranging from 4 km to 20 km and from 0 km to 16 km to the reference stations (J1 and N1) located at CFM. As shown in Figure 3.13, the environment for this experimental data set included mainly urban setting, with both dense foliage and open areas (with the speed limit of: 15-45 miles per hour); the trajectory also includes some parts of a highway (speed limit of: 55-65 miles per hour). Therefore, the receivers experienced rather frequent losses of GPS lock during the experiment due to the environmental obstructions, possible high multipath, and interference (especially on the busy highway).

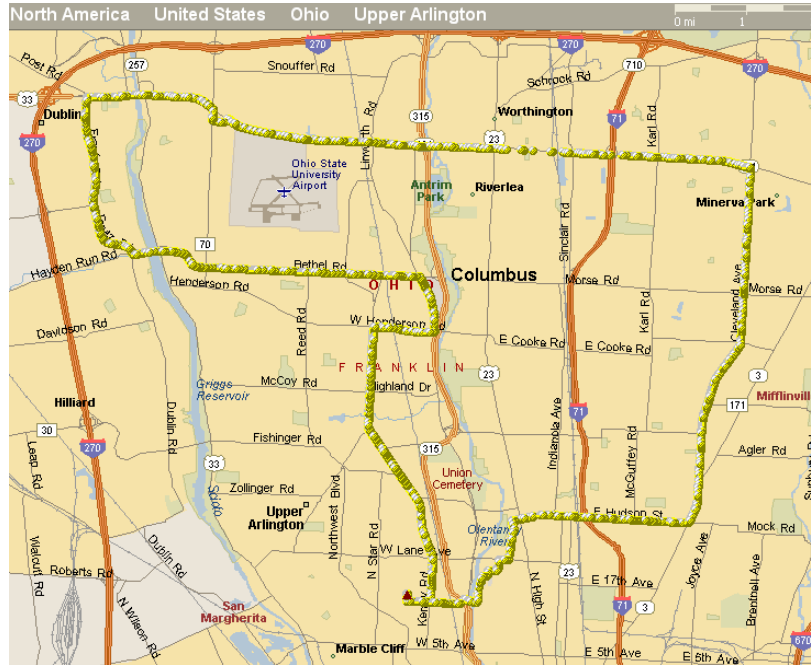


Figure 3.13. Test trajectory, Sept. 26, 2003.

The two static receivers, J1 and N1, were first treated as rover receivers and the COLB served as the reference receiver. The baselines COLB-J1 and COLB-N1 (both around four km in length) were processed in the epoch-by-epoch mode and the summary statistics for these solutions are listed in Table 3.4. For baselines COLB-J1 and COLB-N1, total of 8207 and 8236 epochs, respectively, have more than four double-differences (which is the minimum number needed for relative GPS positioning). For around 99.85% and 98.65% of the epochs, respectively, it was possible to achieve L_1 fixed solutions. Since they are static baselines, the outlier epochs were removed by checking the repeatability of the baselines; standard deviation of around 5 mm was achieved for both baselines. The percentages of the valid epoch with respect to the L_1 fixed epoch are around 99.93% and 99.75%, for COLB-J1 and COLB-N1, respectively. The final coordinates for the receiver J1 and N1 are based on the average solutions of baselines COLB-J1 and COLB-N1 after removing the outliers, and these coordinates were used as reference coordinates for the other baselines that involved receivers J1 and N1. Note that the two columns “Valid Epoch” and “Valid Rate” in Table 3.4 pertain to the static baselines 1 and 2. The values for these two columns cannot be provided for baselines 3-14 because they include the moving rover receivers, whose reference trajectories are not available.

BL No.	Base	Rover	Epoch (≥ 4 DDs)	L1 Fixed Epoch	Fixed Rate (%)	Valid Epoch	Valid Epoch (%)
1	COLB	J1	8207	8195	99.85	8189	99.93
2	COLB	N1	8236	8125	98.65	8105	99.75
3	COLB	J2	7136	6744	94.51		
4	COLB	T1	6981	6763	96.88		
5	COLB	N2	6842	6528	95.41		
6	COLB	T2	6858	6507	94.88		
7	J1	J2	14284	13701	95.92		
8	J1	T1	6980	6727	96.38		
9	J1	N2	13675	13053	95.45		
10	J1	T2	6857	6546	95.46		
11	N1	J2	14232	13498	94.84		
12	N1	T1	6968	6627	95.11		
13	N1	N2	27131	25635	94.49		
14	N1	T2	6812	6431	94.41		

Table 3.4. Baseline data processing statistics.

For the four rover receivers (marked as J2, T1, N2 and T2), a total of 12 baselines were processed using three reference stations COLB, J1 and N1. Table 3.4 lists the total epochs with at least four double-differences, the epochs with fixed L_1 ambiguities and the fixed rates, for the 12 baselines. Around 95% of fixed L_1 solution can be achieved for all the reference and rover combinations. It should be noted here that baselines 7, 9 and 11 were processed in 2Hz mode and baseline 13 was processed in 4 Hz mode, while other baselines were processed at 1Hz sampling rate. A closer inspection of the fixed rate in Table 3.4 indicates that the fixed rate of the rover receivers N2 and T2 are a little better than these of the rover receiver J2 and T1, no matter which reference receiver is used (with the exception of baseline 3); the reason could be that J2 and T1 were installed on the right side of the van, where they were was more likely to experience loss of lock due to the foliage on the right side of the road, as compared to the left side of the vehicle.

As mentioned earlier, the computed distances between two rover receivers determined from different baselines, as shown in Table 3.4, are used to verify the correctness of the position solutions. Table 3.5 provides the number of epochs used to estimate the distances between the pairs of different rover receivers, the number of valid epochs of the estimated distance (after removing the incorrect distances/epochs), the percentage of the valid epochs, the mean and std of the computed distances after removing the outliers. Around 8 mm accuracy (in terms of the standard deviation) in the estimation of the distance between two rover receivers from different baselines can be achieved, with the valid percentages of the epochs at more than 95% for most baselines,

except for baseline pairs (3 and 7) and (3 and 11) (91.85% and 90.74%, respectively). The computed distances agree with the actual distance within 1 cm accuracy. The actual distance between two antennas is determined from the data collected when the vehicle was in a stationary mode; see Yi & Grejner-Brzezinska (2004) for more details.

BL No.	BL No.	Total Epoch	Valid Epoch	Valid Epoch (%)	Mean [m]	Std [m]
3	4	6526	6354	97.36	2.287	0.007
3	5	6393	6093	95.31	1.491	0.005
3	6	6316	6091	96.44	2.223	0.005
3	7	6651	6109	91.85	0.015	0.008
3	8	6488	6342	97.75	2.287	0.009
3	9	6341	6203	97.82	1.490	0.008
3	10	6344	6199	97.71	2.221	0.007
3	11	6589	5979	90.74	0.017	0.009
3	12	6417	6285	97.94	2.288	0.009
3	13	6264	6124	97.77	1.490	0.008
3	14	6250	6111	97.78	2.223	0.007

Table 3.5. The statistics of the computed distances between two rover receivers determined from different baselines.

3.5 Summary and conclusions

The single-epoch RTK positioning technique in both baseline and network modes, implemented to extend the capability of GPS data processing from multiple reference and rover receivers was discussed in this chapter. The detailed data processing strategies were discussed, aimed at improving the ambiguity success rate and the quality control in the epoch-by-epoch solution. These strategies include: 1) the double-difference ionospheric pseudo-observations to extend the baseline length and to enable the epoch-by-epoch ambiguity resolution; 2) the carrier-phase-based code smoothing technique to improve the code measurement accuracy by lowering the multi-path and the measurement noise; 3) the VCM-based stochastic model, which can better reflect the actual GPS measurement stochastic characteristics; 4) a partial ambiguity fixing strategy, and 5) bridging the GPS ambiguities from the previous fixed epoch. The experimental results, based on static baselines processed in kinematic mode, indicate that a cm-level positioning accuracy can be achieved for baselines of around 16 km, 25 km, 50 km and 75 km, processed in baseline-by-baseline mode, and for a baseline around 120 km processed in the network mode. By comparing the relative distances computed from the position solutions, the experimental kinematic results indicate that in most of the cases more than 95% valid

solutions of around 95% fixed L_1 solutions can be achieved by using only the data processing strategies 1, 2, 3 and 4, as listed above.

Even though the system design of the implemented RTK positioning technique is intended to provide real-time RTK network-based positioning solution if more than two reference receivers are provided, more steps are needed for an actual operational product. In the current implementation of the network mode, the predicted double-difference ionospheric corrections from the network-derived ionospheric error model are directly removed from the double-difference measurements between the rover receivers and their closest reference receivers. However, for example, for a VRS product, given the rover receiver coordinates, the virtual GPS measurements from one reference station (normally the closest one from the rover coordinates) can be generated from the network-derived ionospheric and tropospheric error models; then the generated VRS measurements are broadcast in a specific data format (see, for example, Vollath *et al.*, 2000). This step has not been implemented here.

CHAPTER 4

EXTENDED INERTIAL-SENSOR STOCHASTIC ERROR IDENTIFICATION AND MODELING

In this chapter, an overview of the INS error sources, inertial sensor stochastic error identification and modeling techniques are introduced. The stochastic error is often referred to as the stochastic noise, thus the stochastic error identification is also referred to as stochastic noise identification. In the sequel, the stochastic noise and the stochastic error are used as synonyms. The stochastic error identification techniques, to be discussed here, include: 1) the Allan variance (AVAR) analysis in the time domain, and 2) the Power Spectral Density (PSD) method in the frequency domain. The stochastic error models are represented as random processes based on the identified stochastic error characteristics or manufacturer's error specifications. The static and relatively long data observation sessions (more than several hours) are recommended to perform the two noise identification techniques. The two noise identification techniques can also be used for kinematic data if the actual dynamics can be separated from the noise, which is practically impossible. Other noise identification techniques designed for kinematic datasets exist, for example, the adaptive Kalman filter, but will not be investigated in this dissertation. The analyses for the two noise identification techniques based on the experimental static datasets for four inertial sensors of different grades are presented here.

4.1 Primary INS error sources

As stated in Chapter 2, due to the time integration of inertial measurements which are contaminated by the deterministic (also referred to as systematic) and stochastic (also referred to as random) errors, the inertial navigation errors in position, velocity and orientation will accumulate with time, especially in the vertical components (i.e., height for position and heading for orientation), even if accurate initial position, velocity and orientation are available. Therefore, it is particularly important to understand the INS primary error sources and adopt the appropriate INS error models to control the drifts in the position, velocity and orientation. The most significant error sources of an inertial sensor are its instrumental errors, which dominate the inertial navigation performance in a major way. No matter what technologies are used in the inertial sensors, according to

IEEE Std 952, (1997), a general form of the inertial sensor measurement model should consist of the four components: 1) a mathematical statement of the physical model; 2) an error model consisting of a perturbation model and environmental sensitivities; 3) a stochastic model describing any stochastic error drift behavior; and 4) a measurement model consisting of a linear combination of the output and additive measurement noise. The physical model is normally described by the differential or algebraic equations that define the physics of the system's operation. This is the deterministic part of the model, normally determined by its dynamic description. The dynamic modeling of an optical gyro, for example, involves a scale factor, a constant bias, a misalignment, and other environment biases (IEEE Std 952, 1997). The part of the general model that is of interest here is the stochastic model, which should be optimized to allow the evaluation and the improvement of the system's performance through optimal filtering. Therefore, a careful identification of the INS stochastic error models is crucial, and should be performed to achieve the highest navigation accuracy. Equation (4.1) below describes the error model of an inertial sensor.

$$\delta \mathbf{s}_{ib}^b = \underbrace{(\delta \mathbf{C}_s^b \mathbf{s}_{ib}^s + \delta \mathbf{temp} + \delta \mathbf{nl} + \delta \mathbf{gs} + \dots)}_D + \underbrace{(\delta \mathbf{d}_F + (\delta \mathbf{d}_{RN} + \delta \mathbf{d}_{RB} + \delta \mathbf{d}_{RK} + \delta \mathbf{d}_{RR} + \delta \mathbf{d}_{RM} + \delta \mathbf{d}_{RS} + \dots) + \delta \mathbf{d}_Q)}_S \quad (4.1)$$

$$\delta \mathbf{C}_s^b = \begin{bmatrix} \delta \mathbf{sf}_1 & \delta \mathbf{ma}_{12} & \delta \mathbf{ma}_{13} \\ \delta \mathbf{ma}_{21} & \delta \mathbf{sf}_2 & \delta \mathbf{ma}_{23} \\ \delta \mathbf{ma}_{31} & \delta \mathbf{ma}_{32} & \delta \mathbf{sf}_3 \end{bmatrix} \quad (4.2)$$

Here, the subscripts and the superscripts i , b and s denote the inertial frame (i -frame), the IMU body frame (b -frame), and the sensor instrumental frame (s -frame), respectively; \mathbf{s}_{ib}^s represents a vector of inertial measurements in the b -frame, coordinated in the s -frame; $\delta \mathbf{s}$ represents a vector of the inertial sensor (i.e., accelerometer or gyroscope) errors in the b -frame for the vector of inertial measurements \mathbf{s}_{ib}^s in the b -frame, coordinated in the s -frame; $\delta \mathbf{C}$ represents the transformation error matrix from the respective sensor's own instrumental frame to the body-frame; the components of $\delta \mathbf{C}$ include three scale factor errors ($\delta \mathbf{sf}$) and six misalignment effects ($\delta \mathbf{ma}$); $\delta \mathbf{temp}$ is a vector of errors caused by the temperature variation; $\delta \mathbf{nl}$ contains the nonlinearity effects; $\delta \mathbf{gs}$ contains the G-sensitivity effects for the gyros only; $\delta \mathbf{d}_F$ is a vector of fixed biases; $\delta \mathbf{d}_{RN}$ is a vector of the rate white noise (also called angle/velocity random walk) term; $\delta \mathbf{d}_{RB}$ is a vector of the "flicker noise" (also called bias instability) term; $\delta \mathbf{d}_{RK}$ is a vector of the "rate random walk" terms; $\delta \mathbf{d}_{RR}$ is a vector of the trend (ramp) effects; $\delta \mathbf{d}_{RM}$ is a vector of the exponentially correlated (Markov) noise terms; $\delta \mathbf{d}_{RS}$ is a vector of the sinusoidal noise terms; $\delta \mathbf{d}_Q$ is a vector of the quantization noise terms.

The error sources in the aforementioned inertial measurement model, shown in equation (4.1), can be grouped into the deterministic errors (D) and the stochastic errors (S). The deterministic errors include: 1) the scale factor and misalignment effects; 2)

temperature-related variations due to the temperature changes, temperature ramps and gradients; 3) non-linearity errors; 4) G-sensitivity (for gyros only) effects, and 5) other minor environmental sensitivity errors, for example, the error caused by the magnetic effects. These errors are normally reduced using the regression techniques (some linear and/or non-linear function approximations), according to the a priori coefficients determined in the laboratory conditions. Normally, the outputs from most of the inertial sensors (i.e. the accelerometers and gyroscopes) are already compensated for such deterministic errors at the hardware level using the calibrated a priori coefficients. The inaccuracies of the deterministic errors can be further estimated, using the Kalman Filter technique, by augmenting these error terms via some random processes into the state vector of the position, velocity, and orientation, as shown in equation (2.22).

The stochastic errors (S) include: (1) the long-time correlated random ‘bias’, which is also called ‘turn-on bias’ which is different in each experiment; (2) random drifts containing, for example, the rate white noise, the ‘flicker noise’, the rate random walk and the rate ramp (trend), the exponentially correlated (Markov) noise, and the sinusoidal noise; and (3) the quantization noise. The stochastic errors of an inertial sensor are also normally modeled as some random processes in accordance with the manufacturers’ error specifications, or through the stochastic error identification procedures discussed here. Table 4.1 summarizes the descriptions and definitions of the stochastic errors according to IEEE Std 528, (2001), and Figure 4.1 demonstrates how these stochastic errors propagate into the direct accelerations and angular-rates (\mathbf{f}_{xyz} and $\boldsymbol{\omega}_{xyz}$) from the three accelerometers and gyroscopes, and into the accelerometer-integrated velocities and gyroscope-integrated angles ($\Delta\mathbf{V}_{xyz}$ and $\Delta\boldsymbol{\theta}_{xyz}$).

Due to the complexity and diversity of the inertial sensor instrumental errors, Table 2.1, shown in Chapter 2, presents only some examples describing the deterministic and stochastic errors of the inertial sensors used by the author of this dissertation throughout his doctoral studies, in accordance with the manufacturer’s error specifications.

Errors	Definition or description
Random ‘bias’	The average over a specified time of accelerometer and gyroscope outputs, measured at specified operating conditions that have no correlation with input acceleration or rotation.
Random drifts	Rate white noise Also called angle/velocity random walk for $\Delta\theta$ and ΔV , due to the white noise in angular rates and accelerations of the gyroscopes and accelerometers.
	Flicker noise Also named ‘bias instability’, defined as the ‘random’ variations in the biases as computed over a specified finite sample time and averaging time interval; it is a non-stationary (evolutionary) process characterized by a f^{-1} PSD (power spectral density).
	Random walk Defined as the drift rate error buildup with time that is due to the white noise in the jerks and angular accelerations of the accelerometers and gyroscopes.
	Rate ramp Defined as a behavior characterized by the quadratic growth with the average time of the rate Allan variance.
	Exponentially correlated (Markov) noise Characterized by an exponential decaying function with a finite correlation time.
	Sinusoidal noise The PSD of this noise is characterized by one or more distinct frequencies.
Quantization noise	Defined as the random variations in the digitized output signal, due to sampling and quantizing a continuous signal with a finite word length conversion, and the resulting incremental error sequence is a uniformly distributed random variable over the interval $\pm\frac{1}{2}$ least significant bit (LSB).

Table 4.1. Inertial sensor random errors.

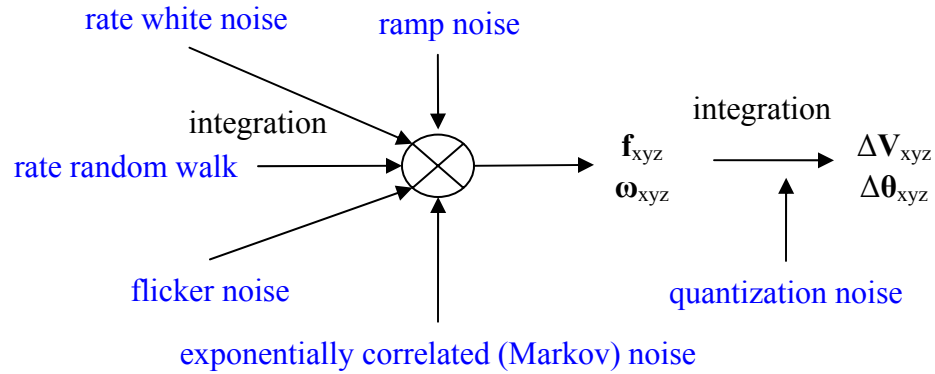


Figure 4.1. Random error contributions to the measurements of the inertial sensors.

4.2 INS dynamic modeling

The INS error model of the inaccuracies of the deterministic errors is referred to as the INS dynamic model. The three scale factor errors and the misalignment errors form the error of the transformation matrix from the instrument's own coordinate frame (*s*-frame) to the body frame (*b*-frame). The temperature-related variations can be compensated by using a polynomial fitting function. As an example, a 2nd order polynomial fitting function with six (3×2) coefficients for three accelerometers and three gyroscopes can be used. If considering the 2nd order non-linearity effects, a total of 18 (3×6) coefficients is needed to model the non-linearity effects for three accelerometers and three gyroscopes, respectively. For some gyroscopes, other cross-coupling effects with accelerometer measurements, called G-sensitivity effects, need to be modeled; a total of 27 (3×9) coefficients must be included if the 1st and 2nd order G-sensitivity effects of gyros to accelerations are considered. Traditionally, these errors together with their coefficients are normally augmented into the state vector as x_f and x_ω sub-vectors and are modeled as some random processes to be estimated together with the other state sub-vectors by using the Kalman filter technique (Jekeli 2001; Farrell and Barth 1999; Titterton and Weston 1997; Siouris 1993). Table 4.2 summarizes the typical number of coefficients to model the possible inaccuracies of the deterministic errors. Due to the different technologies used in inertial sensors, not all the inertial deterministic errors listed in Table 4.2, will be evidenced in all types of accelerometers and gyroscopes.

Inertial sensor errors	Acceleration	Gyroscope
Scale factor	3	3
Misalignment	6	6
1 st order temperature variation	3	3
2 nd order temperature variation	3	3
2 nd order nonlinearity	18 (=3×6)	18 (=3×6)
G-sensitivity	–	27 (=3×9)
Total coefficients	33	60

Table 4.2. Components of the state vector for the deterministic errors of the inertial sensors (Note: the number of the misalignment components of the state vector will be three instead of six in case of a symmetric system.).

4.3 INS stochastic error identification and modeling

The INS error modeling of the stochastic components is referred to as the INS stochastic error modeling. It includes two steps: (1) the stochastic error identification, and (2) the stochastic error model. Several methods in the frequency and time domains have been devised for the stochastic error identification. Two most commonly used techniques are: (1) the Allan variance approach in the time domain, see, for example, Annex C (pp. 65-76) of IEEE Std 647, (1995), and (2) the PSD (power spectral density) approach in the frequency domain, see, for example, Annex I (pp. 166-182) of IEEE Std 1293, (1998). Other frequently used approaches are the adaptive Kalman filtering, and the correlation method. The correlation approach analyzes the auto-covariance sequence, computed from the output data to derive stochastic error model parameters. In this case, the auto-covariance can be (1) modeled as a sum of the exponentials and damped sinusoids, or (2) expressed by the coefficients of a differential equation, or (3) expressed as an autoregressive moving average (ARMA) process. According to IEEE Std 952, (1997), the correlation approach is considered to be very model-sensitive, and is not suited to handling odd power processes, higher-order processes, or wide dynamic ranges. According to IEEE, Std 952, (1997), the Allan variance analysis and the PSD method are the preferred ones for the INS stochastic error identification.

The stochastic errors are normally modeled as some stochastic random processes, according to their stochastic error characteristics from the error identification techniques, or directly from the manufacturer's error specifications. And they are augmented with other state sub-vectors into the Kalman Filter to approximate their spectrum of inertial measurements. Having correct stochastic error models in the inertial navigation system will result in a better performance of the calibration, alignment and navigation Kalman Filters.

sample interval of the averaged grouped data \bar{y} , formed using k consecutive original data points; $N = \text{round}(\frac{n}{k})$ is the maximum number of group data for a selected k ; E is called the percentage accuracy of the Allan variance estimation.

In general, any combination of these stochastic errors, as listed in Table 4.1 regardless of other types of errors that are not shown, but may exist, can be present in the experimental inertial data. In most cases, different noise contributions appear in different regions of averaging time, τ . Thus, this allows an easy identification of various stochastic errors that exist in the data, using the regression technique. Figure 4.2 from the IEEE Std 647, (1995) illustrates a sample noise characteristic for a gyroscope using Allan variance analysis. The quantization noise has the slope -1 in the log-log Allan variance plot. The rate white noise, flicker noise, rate random walk, and rate ramp will have the slopes $-\frac{1}{2}$, 0 , $+\frac{1}{2}$, and $+1$, respectively, in the log-log Allan variance plot. The Markov noise and the sinusoidal noise have varying slopes in the log-log Allan variance plot. If not considering the Markov and sinuous noises, the random drift coefficients R , K , B , N and Q for the rate ramp, rate random walk, flicker noise, rate white noise and quantization noise, as listed in the Table 4.3, can be estimated directly from the rigorous equation (4.5), or from the approximate equation (4.6) using the regression technique. The regression technique is normally implemented using the least-squares adjustment with the percentage error determining the weights. The coefficients can also be separately estimated by using the simple linear fitting in the log-log plots (R , K , B , N , and Q) shown in the third column of Table 4.3. According to Figure 4.1, the quantization noise will not be evidenced in the direct accelerations and angular rates (\mathbf{f}_{xyz} and $\boldsymbol{\omega}_{xyz}$) of the accelerometers and gyroscopes, since the quantization noise is only introduced during the integration from accelerations and angular rates to accelerometer-integrated velocities and gyroscope-integrated angles ($\Delta\mathbf{v}_{xyz}$ and $\Delta\boldsymbol{\theta}_{xyz}$). After the coefficients R , K , B , N and Q were estimated using the aforementioned regression method, they can be used to compensate the stochastic error sources, which will be discussed later.

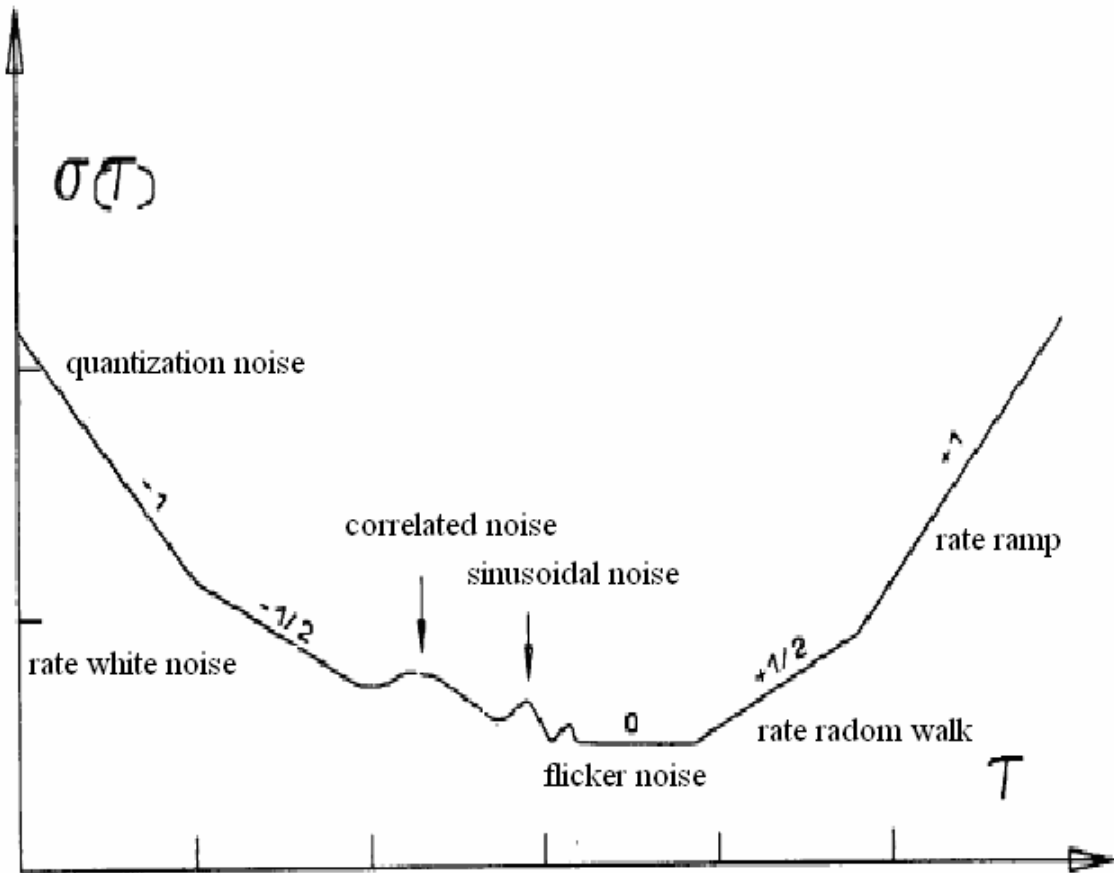


Figure 4.2. Sample noise characterizations in log-log plot using the Allan variance analysis (from IEEE 647, (1995)).

Rigorous equation
$$\sigma^2(\tau) = \frac{R^2 \tau^2}{2} + \frac{K^2 \tau}{3} + \frac{B^2 2 \ln 2}{\pi} + \frac{N^2}{\tau} + \frac{3Q^2}{\tau^2} \quad (4.5)$$

Simplified equation
$$\sigma(\tau) \approx \frac{R}{\sqrt{2}} \tau^{\frac{2}{2}} + \frac{K}{\sqrt{3}} \tau^{\frac{1}{2}} + B \sqrt{\frac{2 \ln 2}{\pi}} + N \tau^{-\frac{1}{2}} + Q \sqrt{3} \tau^{-\frac{2}{2}} \quad (4.6)$$

Here: $\sigma(\tau)$ denotes the Allan variance; R unit \cdot s $^{-1}$, K unit \cdot s $^{-1/2}$, B unit, N unit \cdot s $^{1/2}$ and Q unit \cdot s are the coefficients for the rate ramp, the rate random walk, the flicker noise, the rate white noise, and the quantization noise, respectively; unit \equiv m/s 2 for the accelerations and unit \equiv rad/s for the angular rates.

Noise name	Allan variance	Log-log model	Coefficients
Quantization noise	$\sigma^2(\tau) = \frac{3Q^2}{\tau^2}$	$y = -x + b$	$Q = \sqrt{\frac{e^{2b}}{3}} = \frac{e^b}{\sqrt{3}}$
Rate white noise	$\sigma^2(\tau) = \frac{N^2}{\tau}$	$y = -\frac{1}{2}x + b$	$N = \sqrt{e^{2b}} = e^b$
Flicker noise		$y = b$	$B = \frac{e^b}{0.664}$
Rate random walk	$\sigma^2(\tau) = \frac{K^2\tau}{3}$	$y = \frac{1}{2}x + b$	$K = \sqrt{3e^{2b}} = \sqrt{3}e^b$
Rate ramp	$\sigma^2(\tau) = \frac{R^2\tau^2}{2}$	$y = x + b$	$R = \sqrt{2e^{2b}} = \sqrt{2}e^b$

Table 4.3. Stochastic noise contributions for the estimation of the Allan variance analysis.

4.3.1.2 Power spectral density (PSD) method

The PSD method in the frequency domain, which takes the advantage of the Fast Fourier Transform (FFT) technique for the numerical evaluation, is the most commonly used data analysis technique for the discrete inertial measurements. Two kinds of inertial measurements exist for various inertial sensors, the accelerations and angular rates directly from the accelerometers and gyroscopes, and the accelerometer-integrated velocities and gyroscope-integrated angles. The PSD transformation between the two types of measurements can be expressed as $\text{PSD}(\text{derivative of data}) = [(2\pi)^2 f^2] \cdot \text{PSD}(\text{data})$, where f is the spectral frequency in Hz. Since the PSD function of a process is an even function, the PSD is normally referred to as the two-sided PSD, which is two times of the one-sided PSD. The two-sided PSD is often used in the mathematical proof relating to the PSD, while the one-sided PSD is often used in the actual data analysis since it requires working only with positive frequency. According to the definition, the rate white noise has a constant power at all frequencies, and is represented by a zero slope line parallel to the frequency axis; the integration of white noise results in a random walk process, whose PSD is represented by a slope of -2 in the log-log plot. The so-called flicker noise will often be seen in the experimental data with a slope of -1 in the log-log plot. If the outputs of the sensors are the accelerometer-integrated velocities and gyroscope-integrated angles, the quantization noise will be evident with a log-log PSD slope of $+2$. Figure 4.3 shows the typical noise characteristics of the accelerometer and gyroscope PSD in the rate domain (accelerations or angular rates). The gradient transitions in the slopes will replace

the sharp transitions in the log-log plot for the real experimental data, also the slopes will be slightly different from the theoretical slopes (-2 , -1 , 0 , and 2) due to the uncertainty of the measured PSD. Similarly to the Allan variance analysis, the noise coefficients can also be fitted using a log-log model or a least-squares adjustment based on equation (4.7). The log-log fitting can also be done according to the 2nd column shown in Table 4.4. The PSD method cannot distinguish between the rate random walk and the rate ramp whose log-log models are both $y = -2x + b$. Thus, the rate ramp must be removed before applying the PSD method. However, the Allan variance analysis in the time domain can distinguish between the rate random walk and the rate ramp.

$$\text{PSD} \quad \Phi(f) = (2\pi f)^2 Q^2 \Delta t + N^2 + \frac{B^2}{2\pi f} + \frac{K^2}{(2\pi f)^2} \quad (4.7)$$

Error Sources	Error Model	Log-log Model	Coefficients
Quantization noise	$\Phi_{\text{RQ}}(f) = (2\pi f)^2 Q^2 \Delta t$	$y = +2x + b$	$Q = \frac{1}{2\pi\sqrt{\Delta t}} \sqrt{e^b}$
Rate white noise	$\Phi_{\text{RN}}(f) = N^2$	$y = b$	$N = \sqrt{e^b}$
Flicker noise	$\Phi_{\text{RB}}(f) = \frac{B^2}{2\pi f}$	$y = -x + b$	$B = \sqrt{2\pi} \sqrt{e^b}$
Rate random walk	$\Phi_{\text{RK}}(f) = \frac{K^2}{(2\pi f)^2}$	$y = -2x + b$	$K = 2\pi \sqrt{e^b}$

Table 4.4. Random noise contributions for the PSD method.

Here, Δt is the sampling interval; Φ is the PSD; f is the spectral frequency in Hz; Q , N , B , K and R are the stochastic error coefficients for the stochastic errors in form of: (1) the quantization noise, (2) the rate white noise, (3) the flicker noise, (4) the rate random walk, where y is expressed as a linear log-log fitting function of x , with a const term b used to estimate the coefficients Q , N , B and K .

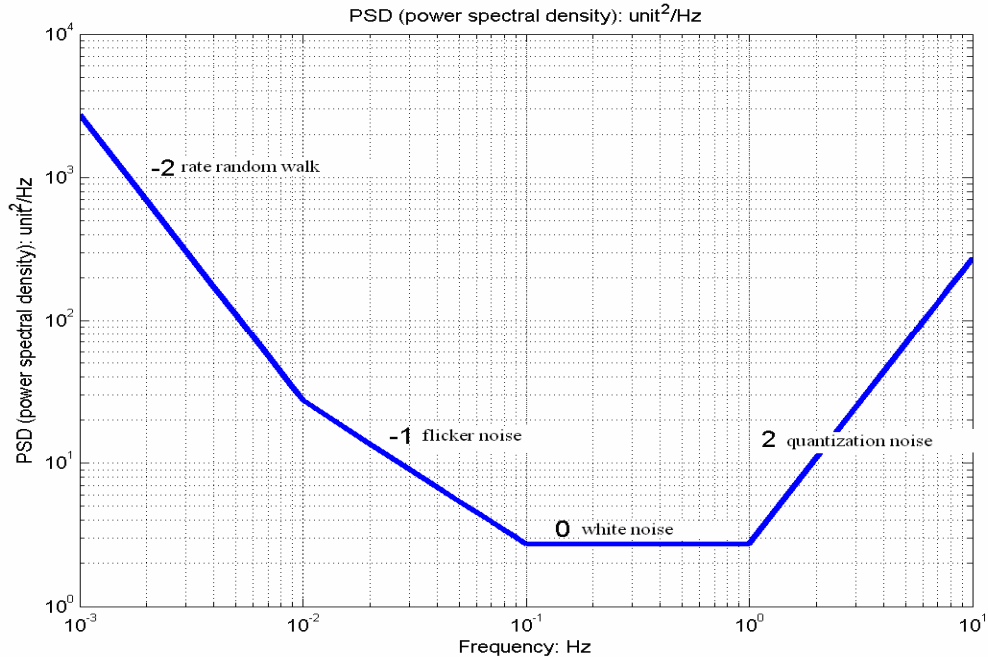


Figure 4.3. Typical slopes in log-log plot of one-sided PSD vs. frequency for accelerations or angular rates.

4.3.1.3 Numerical examples

In order to demonstrate the aforementioned noise identification techniques and to investigate the stochastic noise characteristics of inertial sensors in comparison to the manufacturer's specifications, several static datasets were collected using various grade inertial sensors. These inertial sensors include: (1) two navigation grade H764G; (2) one navigation-grade LN100; (3) one tactical grade HG1700; and (4) one consumer grade Crossbow MEMS IMU400CC. The two noise identification techniques discussed were applied to these static datasets. Two experiments were conducted on June 26, 2004 (Day of Year: DOY 178, referred to as DOY 178, 2004) and Oct. 20, 2004 (DOY: 294, 2004), respectively. The first experiment on DOY 178, 2004 collected ~8 hours of static data for three inertial sensors H764G, HG1700, and IMU400CC. The experiment on DOY, 294, 2004 collected two static segments (referred to as 294₁ and 294₂). All four types of the inertial sensors were included in the second experiment. The raw inertial output from HG1700 and IMU400CC include the temperature, which may indicate the absence of the temperature compensation in the raw inertial measurements. Thus, a 2nd-order polynomial fitting function $f(T)=a_0+a_1T+a_2T^2$, where T is the measured temperature, was used to fit the raw inertial measurements, and then to remove the temperature-related trends. Table 4.5 shows two examples of the fitted coefficients (a_0 , a_1 and a_2) for temperature compensation to remove the deterministic error sources from inertial measurements for

the HG1700 and IMU400CC test datasets. Coefficient a_0 is a constant term of the inertial measurements, and a_1 and a_2 indicate the relationship between the inertial measurement and temperature. Both a_1 and a_2 of the IMU400CC x and y accelerometers and gyroscopes are of comparable magnitudes, while these coefficients for the IMU400CC z accelerometer and gyroscope are much bigger. The a_1 and a_2 coefficients of the HG1700 x and z accelerometers are very similar, and both are smaller than these of the HG1700 y accelerometer. Similarly to the temperature relationship of the IMU400CC gyroscopes, the a_1 and a_2 coefficients of the HG1700 x and y gyroscopes are similar, and much smaller than these of the HG1700 z gyroscope. Overall, the temperature dependency of the IMU400CC inertial measurements is much stronger than that of the HG1700, except for the y accelerometer.

	a_0 unit	a_1 unit·C ⁻¹	a_2 unit·C ⁻²		a_0 unit	a_1 unit·C ⁻¹	a_2 unit·C ⁻²
\mathbf{f}_x	-0.1205590	0.0031942	-0.0000488	$\Delta\mathbf{v}_x$	0.1812791	0.0011339	-0.0000123
\mathbf{f}_y	-0.3494839	-0.0041194	0.0000662	$\Delta\mathbf{v}_y$	-1.0330649	-0.0204334	0.0002917
\mathbf{f}_z	-9.6776737	0.0093617	-0.0001517	$\Delta\mathbf{v}_z$	-9.7609339	-0.0016558	0.0000217
$\boldsymbol{\omega}_x$	-0.0350548	0.0026017	-0.0000475	$\Delta\boldsymbol{\theta}_x$	-0.0003935	0.0000201	-0.0000003
$\boldsymbol{\omega}_y$	-0.0552294	0.0038179	-0.0000641	$\Delta\boldsymbol{\theta}_y$	-0.0004730	0.0000235	-0.0000003
$\boldsymbol{\omega}_z$	0.0192663	-0.0019009	0.0000341	$\Delta\boldsymbol{\theta}_z$	-0.0012132	0.0000634	-0.0000008
	IMU400CC on DOY 178				HG1700 on DOY 178		

Table 4.5. Temperature de-trending coefficients, using a 2nd-order polynomial fitting function $f(T)=a_0+a_1T+a_2T^2$ (unit≡m·s⁻² for the accelerometer measurement and unit≡rad·s⁻¹ for the gyroscope measurement).

Figure 4.4 shows an example of the Allan variance estimation for one of the H764G instruments, using three datasets (one from the experiment on DOY 178, 2004, and two static segments from the experiment on DOY 294, 2004) with different lengths. It clearly indicates that the longer static dataset will result in a more stable and reliable Allan variance estimation. Thus, the final Allan variance coefficients are estimated from the longest dataset on DOY 178, 2004, which is around 8 hours. According to Figure 4.4, the quantization noise dominates the gyroscope measurements up to around ten seconds and accelerometer measurements around a few seconds. The gyroscope measurements exhibit a rate white noise in the time domain from 20-100 seconds. The accelerometer measurements experience a short-time rate white noise around tens of seconds, continuing with a flicker noise up to a few hundreds of seconds. Then, they end with the rate random walk in the x and z directions, and with a combination of the rate random walk and rate ramp in the y direction. The rate ramp effects shown in Figure 4.4 obviously indicate that some deterministic error sources exist in the accelerometer

measurements; this is because no deterministic error sources were removed from the H764G datasets. Table 4.6 shows the Allan variance error characteristics and coefficients, estimated from the Allan variance log-log models for H764G sensor. As can be seen in Table 4.6 (after appropriate unit conversion), the quantization noise for the gyroscope measurements, is around 0.8 arcsec, and $0.00015 \text{ m}\cdot\text{s}^{-1}$. The angle random walk is $0.008 \text{ }^\circ\cdot\text{h}^{-\frac{1}{2}}$, and the velocity random walk is $0.3 \text{ }\mu\text{g}\cdot\text{h}^{\frac{1}{2}}$. Figure 4.5 shows the Allan variance estimations for LN100, HG1700 and IMU400CC. The detailed noise characteristics for H764G, LN100, HG1700 and IMU400CC using the Allan variance analysis and the PSD are provided in Appendix B.

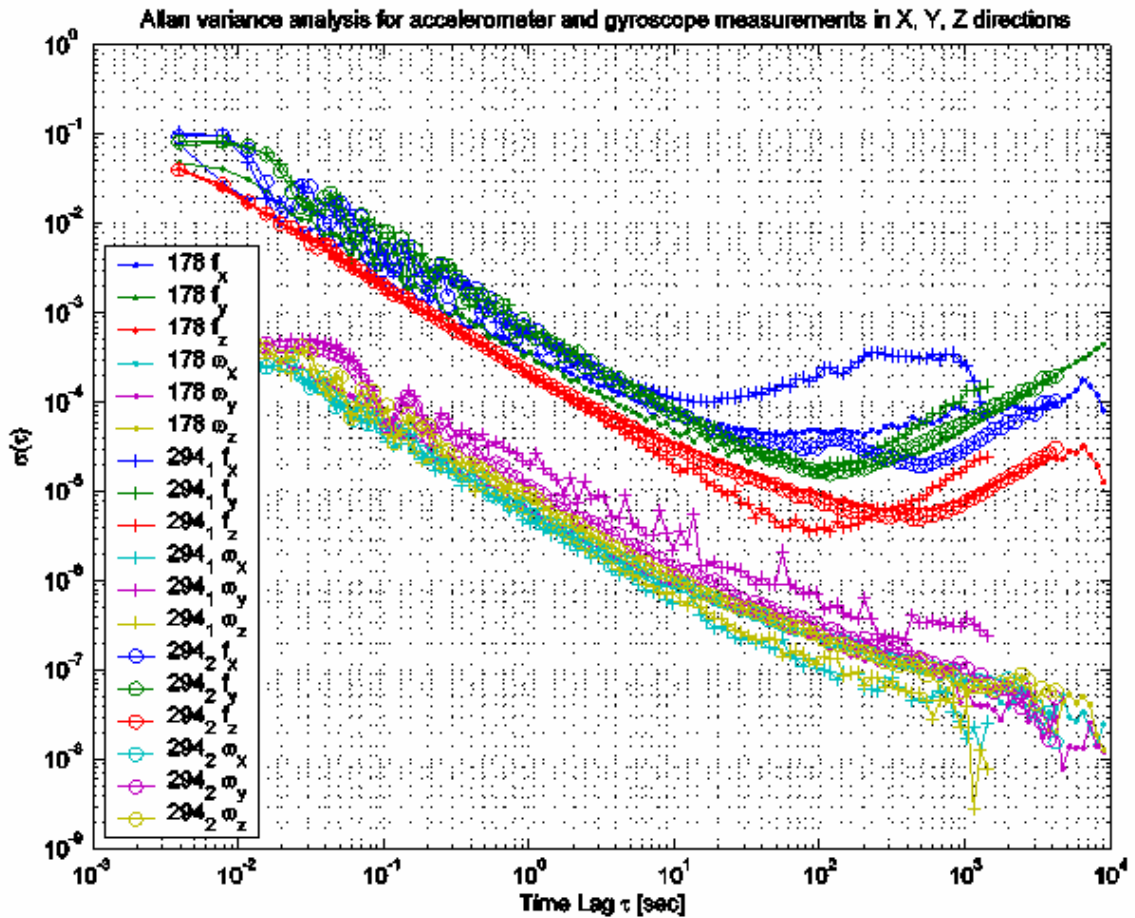


Figure 4.4. Allan variance estimation for H764G using three different datasets: 1st dataset collected on DOY 178, 2004, marked as 178 (8h35m50s at 256Hz sampling rate); 2nd dataset collected on DOY 294, 2004, marked as 294₁ (0h49m10s at 256Hz sampling rate); 3rd dataset collected on DOY 294, 2004, marked as 294₂ (2h35m30s at 256Hz sampling rate).

		Q	N	B	K	R
Error characteristics	f_X	<1 s	1~10 s	20~200 s	200~10000 s	
	f_Y	<1 s	4~20 s	50~200 s	200~500 s	500~10000 s
	f_Z	<1 s	10~80 s	200~700 s	500~5000 s	
	ω_X	<5 s	20~100 s			
	ω_Y	<5 s	20~100 s			
	ω_Z	<5 s	20~100 s			
		Q unit·s	N unit·s ^{1/2}	B unit	K unit·s ^{-1/2}	R unit·s ⁻¹
Error coefficients	f_X	0.0001611	0.0002786	0.0000714	0.0000037	
	f_Y	0.0001846	0.0001609	0.0000277	0.0000022	0.0000000703
	f_Z	0.0001153	0.0000961	0.0000096	0.0000005	
	ω_X	0.0000033	0.0000023			
	ω_Y	0.0000036	0.0000023			
	ω_Z	0.0000045	0.0000026			

Table 4.6. Allan variance error characteristics, and estimated coefficients for H764G using static dataset of DOY 178, 2004 (unit≡m·s⁻² for the accelerometer measurement and unit≡rad·s⁻¹ for the gyroscope measurement).

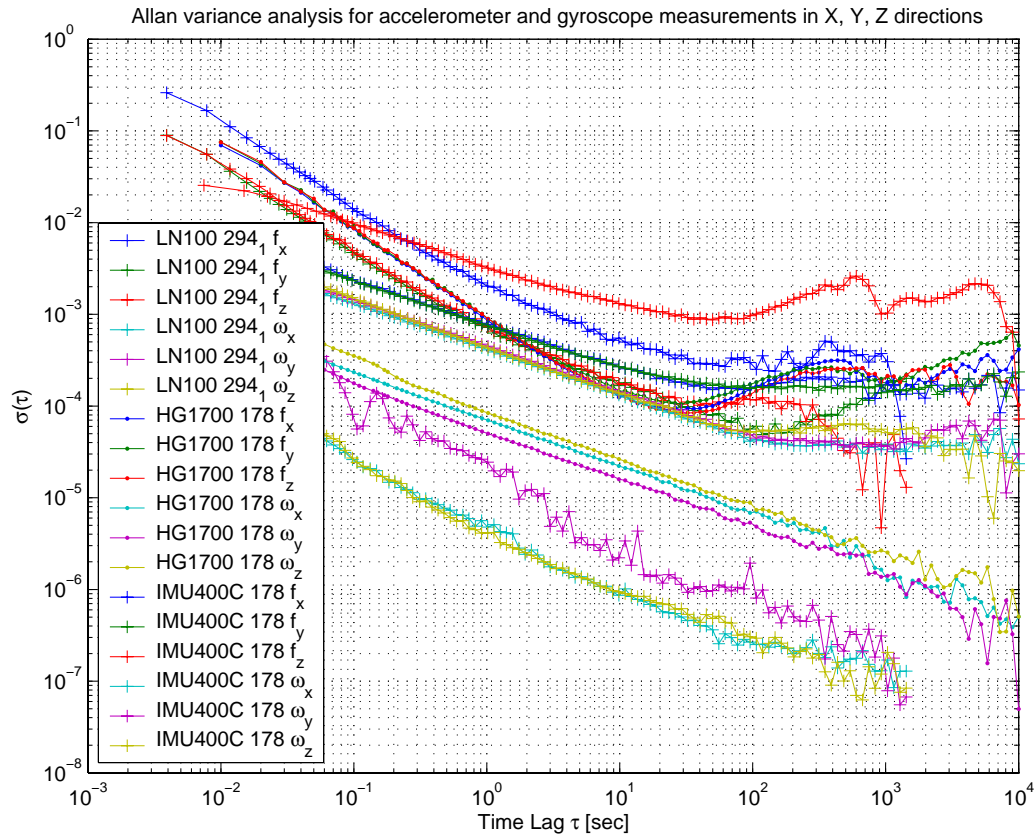


Figure 4.5. Allan variance estimations for LN100, using 1st static dataset of DOY 294, 2004 (marked as LN100 294₁), and for HG1700 and IMU400CC, using static datasets of DOY 178, 2004 (marked as HG1700 178 and IMU400CC 178).

One example of the PSD estimation for H764G using the static dataset of DOY 178, 2004, is shown in Figure 4.6. The PSD estimates shown in Figure 4.6 represent the combinations of the environmental noise and intrinsic noise in the inertial sensors. For example, in the accelerometer measurements, the seismic environmental noise might cause discrete spikes, typically above 1 Hz, due to resonances in the local geology and the test platform. The H764G is a navigation-grade inertial sensor, which is very sensitive to environmental noise; thus, several spikes are present in the high frequency areas of the PSD spectrum of all three accelerometers and three gyroscopes, as shown in Figure 4.6. A quantization noise appears in the high frequencies (higher than around 2 Hz) of all accelerometers and gyroscopes. The rate white noise shows in the low frequencies (up to around 2 Hz) for the three gyroscopes. However, the three accelerometers have a flicker noise in the frequencies lower than 0.003 Hz, and a rate white noise in the frequencies between 0.003 Hz and ~2 Hz. Detailed PSD stochastic error characteristics and the

respective coefficients are listed in Table 4.7. The rate white noise present in the y accelerometer has more variations than the other two directions. Also the spikes shown in the high frequencies of different axes of different inertial measurement units are different, which indicates that each axis of the inertial sensor experience different environmental noise. Differently from the results obtained with the Allan variance analysis, no obvious effect of the rate random walk is evident in the accelerometers.

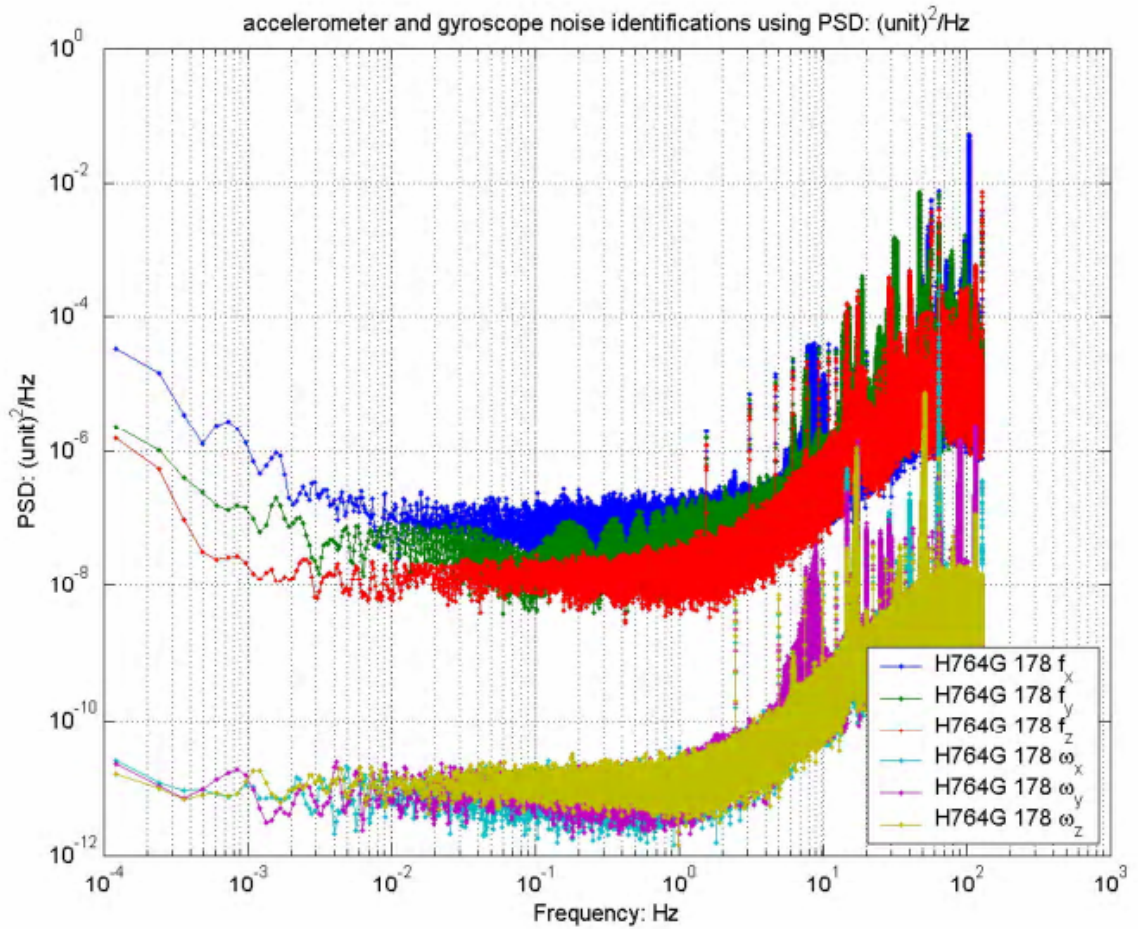


Figure 4.6. PSD estimations for H764G, using the dataset of DOY 178, 2004.

		Q	N	B	K	R
Error characteristics	f_X	>3 Hz	0.003~3 Hz	<0.003 Hz		
	f_Y	>2 Hz	0.003~2 Hz	<0.003 Hz		
	f_Z	>2 Hz	0.003~2 Hz	<0.003 Hz		
	ω_X	>2 Hz	<2 Hz			
	ω_Y	>2 Hz	<2 Hz			
	ω_Z	>2 Hz	<2 Hz			
		Q unit·s	N unit·s ^{1/2}	B unit	K unit·s ^{-1/2}	R unit·s ⁻¹
Error coefficients	f_X	0.0000801	0.0001940	0.0000544		
	f_Y	0.0000993	0.0001292	0.0000213		
	f_Z	0.0000676	0.0000843	0.0000097		
	ω_X	0.0000017	0.0000020			
	ω_Y	0.0000022	0.0000021			
	ω_Z	0.0000018	0.0000024			

Table 4.7. Example PSD stochastic error characteristics, and coefficients for H764G using the static dataset of DOY 178, 2004 (unit≡m·s⁻² for the accelerometer measurement and unit≡rad·s⁻¹ for the gyroscope measurement).

4.3.1.4 Summary of the INS stochastic error identification using the Allan variance analysis and the PSD method

Table 4.8 summarizes the stochastic error coefficients for H764G, LN100, HG1700 and IMU400CC identified by using the Allan variance analysis and the PSD method described above. The estimated coefficients for the three orthogonal accelerometers and the three gyroscopes for the same inertial sensor using the same noise identification technique are averaged. The cross-comparison of these stochastic error coefficients using the Allan variance analysis and the PSD method indicates that both results match very well except for some coefficients marked in red in Table 4.8. The differences between the two methods (marked in red) are found in: (1) the quantization noise and the rate random walk of the accelerometers of H764G, and (2) the flicker noise and rate random walk of the accelerometers of HG1700. Based on the common sensor stochastic error characteristics identified using the Allan variance analysis and using the PSD method, the following conclusions are drawn:

- ✓ Rate white noise is found in all accelerometers and gyroscopes of H764G, LN100, HG1700 and IMU400CC.
- ✓ Quantization noise is found in the accelerometers of H764G, LN100 and HG1700, and in the gyroscopes of H764G and LN100.
- ✓ Flicker noise is found in the accelerometers of H764G, LN100, HG1700 and IMU400CC, and in the gyroscopes of IMU400CC.

Sensor	Data	Method	Q unit·s	N unit·s ^{1/2}	B unit	K unit·s ^{-1/2}	R unit·s ⁻¹
H764G	f_{XYZ}	AVAR	0.0001537	0.0001785	0.0000359	0.0000017	
		PSD	0.0000823	0.0001358	0.0000285		
	ω_{XYZ}	AVAR	0.0000038	0.0000024			
		PSD	0.0000019	0.0000022			
LN100	f_{XYZ}	AVAR	0.0002781	0.0006137	0.0001370		
		PSD	0.0001959	0.0006053	0.0001276		
	ω_{XYZ}	AVAR	0.0000016	0.0000031			
		PSD	0.0000011	0.0000032			
HG1700	f_{XYZ}	AVAR	0.0005020	0.0004426	0.0001360	0.0000252	
		PSD	0.0005221	0.0002271	0.0000170		
	ω_{XYZ}	AVAR		0.0000691			
		PSD	0.0000038	0.0000635			
IMU400 CC	f_{XYZ}	AVAR		0.0007656	0.0002501		
		PSD		0.0007279	0.0002782		
	ω_{XYZ}	AVAR		0.0004388	0.0000707		
		PSD		0.0004371	0.0000630		

Table 4.8. The stochastic error coefficients identified by using the Allan variance (AVAR) analysis and the PSD method (unit≡m·s⁻² for the accelerometer measurement and unit≡rad·s⁻¹ for the gyroscope measurement). Significant noise differences between the Allan variance analysis and the PSD method are marked in red.

The stochastic error coefficients, combining both the Allan variance analysis and the PSD method, are listed in Table 4.9. The rate random walk shown in the accelerometers of H764G and HG1700 are ignored and the final adopted coefficient B for the accelerometers of HG1700 is from the Allan variance analysis. All other coefficients are averaged to obtain the final coefficients listed in this table. In this table, the quantization noise in the accelerometers of H764G is smaller than that of LN100, while the quantization noise in the gyroscope of H764G is bigger than that of LN100. The quantization noise in the accelerometers of both navigation-grade INS (i.e. H764 and LN100) is smaller than that of the tactical-grade HG1700. The magnitude of the rate white noise in all accelerometers and gyroscopes is increasing from H764G, to LN100, to HG1700 and to IMU400CC, with the exceptions in the accelerometers of LN100, whose accelerometer rate white noise coefficient is bigger than that of HG1700. The flicker noise in the accelerometers of these sensors also follows the order: H764G (smallest), LN100, HG1700 and IMU400CC (largest).

Sensor	Data	Q unit·s	N unit·s ^{1/2}	B unit
H764G	\mathbf{f}_{XYZ}	0.0001180	0.0001572	0.0000322
	$\boldsymbol{\omega}_{XYZ}$	0.0000028	0.0000023	
LN100	\mathbf{f}_{XYZ}	0.0002370	0.0006095	0.0001323
	$\boldsymbol{\omega}_{XYZ}$	0.0000014	0.0000031	
HG1700	\mathbf{f}_{XYZ}	0.0005121	0.0003349	0.0001360
	$\boldsymbol{\omega}_{XYZ}$		0.0000663	
IMU400CC	\mathbf{f}_{XYZ}		0.0007468	0.0002642
	$\boldsymbol{\omega}_{XYZ}$		0.0004379	0.0000668

Table 4.9. The final estimated coefficients of the stochastic error models combining both the Allan variance analysis and the PSD method (unit= $\text{m}\cdot\text{s}^{-2}$ for the accelerometer measurement and unit= $\text{rad}\cdot\text{s}^{-1}$ for the gyroscope measurement).

4.3.2 INS random error modeling

Among the noise contributors shown in Figure 4.1, the random bias, $\delta\mathbf{d}_F$, can be modeled as a random constant, and the rate white noise, $\delta\mathbf{d}_{RN}$, can be treated as a measurement noise for the raw measurements of accelerations and angular rates (\mathbf{f}_{xyz} and $\boldsymbol{\omega}_{xyz}$), while it will be modeled as angle and velocity random walk for the integrated measurements of the accelerometer-integrated velocities and gyroscope-integrated angles ($\Delta\mathbf{V}_{xyz}$ and $\Delta\boldsymbol{\theta}_{xyz}$). The flicker noise, $\delta\mathbf{d}_{RB}$, is very complex, and a very comprehensive review of this 1/f noise can be found in Edoardo (2002) while, according to Keshner (1982), the flicker noise over a given bandwidth can be modeled as the combination of a sum of the exponentially correlated Markov noise states. Also, according to Stockwell (2005), the flicker noise can as well represent the best achievable bias stability with the fully modeled inertial sensors. The rate random walk, $\delta\mathbf{d}_{RK}$, is modeled as a random walk process in the rate (acceleration and angular rate) domain (Ford & Evans, 2000). The rate ramp can be modeled as a 2nd order differential equation driven by the ramp noise. Equation (4.8) presents a possible stochastic noise model of the inertial sensors, assuming that if the inertial measurements are the accelerations and angular rates (\mathbf{f}_{xyz} and $\boldsymbol{\omega}_{xyz}$), the corresponding noise component of the measurement equation is (4.9), while if given are the inertial integrated observables ($\Delta\mathbf{V}_{xyz}$ and $\Delta\boldsymbol{\theta}_{xyz}$), the corresponding noise component of measurement equation is shown in equation (4.10), with an additional quantization noise serving as the white measurement noise according to IEEE Std 1293, (1998).

$$\begin{cases} \dot{\mathbf{d}}_F = 0 \\ \mathbf{d}_{RN} = N \cdot \mathbf{v} \\ \dot{\mathbf{d}}_{RB} = -\beta_{RB} \mathbf{d}_{RB} + \beta_{RB} B \cdot \mathbf{v} \\ \dot{\mathbf{d}}_{RK} = K \cdot \mathbf{v} \\ \ddot{\mathbf{d}}_{RR} = R \cdot \mathbf{v} \\ \dot{\mathbf{d}}_{RM} = -\beta_{RM} \mathbf{d}_{RM} + \beta_{RM} M \cdot \mathbf{v} \end{cases} \quad (4.8)$$

$$e_k = \mathbf{d}_F + \mathbf{d}_{RN} + \mathbf{d}_{RB} + \mathbf{d}_{RK} + \mathbf{d}_{RR} + \mathbf{d}_{RM} \quad (4.9)$$

$$e_k = (\mathbf{d}_F + \mathbf{d}_{RN} + \mathbf{d}_{RB} + \mathbf{d}_{RK} + \mathbf{d}_{RR} + \mathbf{d}_{RM}) \cdot \Delta t + Q \cdot \mathbf{n} \quad (4.10)$$

Here, \mathbf{d}_F is the random ‘bias’ error; \mathbf{d}_{RN} is the rate white noise; \mathbf{d}_{RB} is the flicker noise; \mathbf{d}_{RK} is the rate random walk; \mathbf{d}_{RR} is the rate ramp; \mathbf{d}_{RM} is the exponentially correlated Markov noise; z_k is the measurement; β is the correlation time; Δt is the sample interval; and \mathbf{v} and \mathbf{n} is the independent white Gaussian noise with zero mean and unit variance; e_k are the measurement noise component for the inertial measurements.

In contrast to the stochastic noise model shown in equation (4.8), modeled as random processes using the differential equations, an equivalent ARMA model representation has been reported in Seong *et al.* (2000). The equivalent ARMA models for the mixed combination of the rate white noise, the rate random walk, the quantization noise, and the 1st order Gaussian-Markov correlated noise are shown in Table 4.10. Then a state-space vector representation of the noise contributions can be easily implemented based on the ARMA representation with difference Auto-Regressive order and the Moving Average order. AMRA model order (i, j) shown in Table 4.10 represents the i -order Auto-Regressive processes and j -order Moving Average processes.

Noise contributions	AMRA model order
rate white noise + quantization noise	(0,1)
rate white noise + rate random walk	(0,1)
rate white noise + first-order Markov noise	(1,1)
rate random walk + quantization noise	(0,2)
quantization noise + first-order Markov noise	(1,2)
rate white noise + rate random walk + quantization noise	(0,2)
rate white noise + quantization noise + first-order Markov noise	(1,2)
rate random walk + first-order Markov noise	(1,1)
rate white noise + rate random walk + first-order Markov noise	(1,2)
rate random walk + quantization noise + first-order Markov noise	(1,3)
rate white noise + rate random walk + quantization noise + first-order Markov noise	(1,3)

Table 4.10. Equivalent ARMA models for the noise contributions identified using the Allan variance analysis or the PSD method.

4.3.3 Performance comparisons of the customized error model as compared to the default error model from manufacturer's error specifications

In Grejner-Brzezinska *et al.* (2005b), a tactical-grade inertial sensor HG1700 integrated with the GPS was used as an example to validate the navigation performance of the customized inertial sensor error model, shown in Table 4.9, as compared to the default inertial sensor error model from the manufacturer's error specification, shown in Table 2.1. Figure 4.7 illustrates the free inertial navigation horizontal position drifts of HG1700, using the aforementioned inertial sensor error models (i.e., the customized error model v.s. default error model), as compared to the GPS/INS reference solution from a high-end inertial sensor LN100. Around 30 percent navigation improvement in the horizontal position component based on the example shown in Figure 4.7 can be evidenced for the tactical-grade inertial sensor HG1700, after a 600-second free inertial navigation using the customized error model. Another example based on a low-cost customer-grade MEMS inertial sensor is shown in Chapter 5.

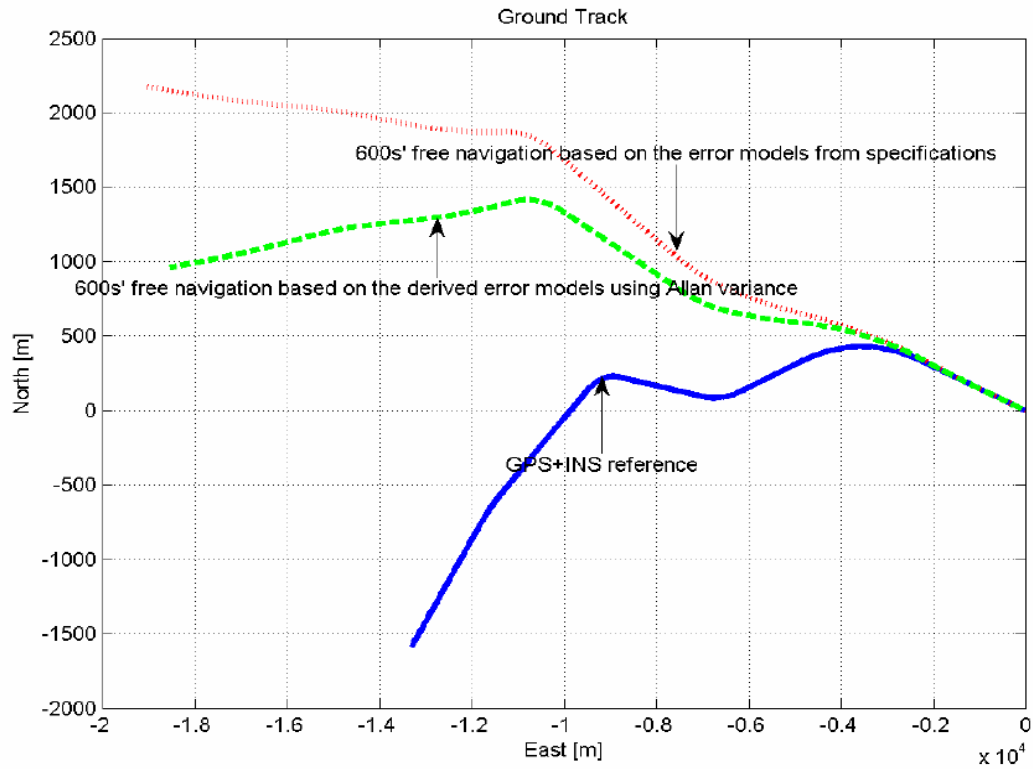


Figure 4.7. The free inertial navigation error drifts of a tactical-grade inertial sensor HG1700, as compared to the GPS/INS reference solution from a navigation-grade inertial sensor LN100, using the customized inertial sensor error model derived using Allan variance analysis and the default error model from the manufacturer's error specifications.

CHAPTER 5

WAVELET-BASED SIGNAL DE-NOISING TECHNIQUE

5.1 Wavelet-based signal de-noising technique for a low cost MEMS IMU

With the emergence of the low-cost MEMS IMUs, assessing their applicability to land-based and/or airborne direct sensor orientation is attracting a lot of interest in the mobile mapping and remote sensing communities. However, the relatively high measurement noise of these sensors degrades the overall navigation performance of the integrated system, especially during the losses of GPS lock. In general, the inertial measurements consist of the motion dynamics, vehicle vibration disturbances, sensor dither disturbances (for example, the Ring Laser Gyro), and inertial sensor errors. As explained in Chapter 4, the inertial sensor errors include the deterministic and the stochastic components. The stochastic errors can be further classified as colored (or time correlated) noise and the measurement noise. The deterministic errors and the colored noise can be accounted for by using INS dynamic and stochastic error modeling, as explained in Chapter 4. Thus, the goal of signal de-noising is to reduce the measurement noise as well as the dithering effects and vibrations, while preserving the spectrum of the true motion dynamics, the sensor's deterministic error and the colored noise. The commonly used signal de-noising techniques include the moving average technique and low-pass filtering.

In recent years, the wavelet signal de-noising technique has been proposed to smooth the raw inertial measurements, and efforts to improve the navigation performance of inertial navigation have been reported; see, for example (Nassar, 2003; Grejner-Brzezinska *et al.*, 2005; Yi *et al.*, 2005). The wavelet signal de-noising technique is also found in other applications; see for example (Schaffrin & Pan, 1999; Sardy *et al.*, 2001; Chi *et al.*, 1999). The fundamental principle of the wavelet-based signal de-noising technique, as shown in equation (5.1) is to decompose the signal (here, the inertial measurements that are contaminated with the noise) into: 1) *approximations*, i.e., the high-resolution, low-frequency components of the original signal, and 2) the so-called *details* that correspond to the low-resolution, high-frequency components, using several levels of two complementary filters (i.e., high and low pass filters), referred to as the multiple level wavelet decomposition; see, for example, Daubechies (1992). Figure 5.1 illustrates an example of the wavelet-based signal decomposition into a five-level wavelet

decomposition (also referred to as level of wavelet de-noising or level of de-noising) of the output of a MEMS accelerometer (here, Crossbow MEMS IMU400CC) in the kinematic mode. It clearly indicates that the decomposed component, labeled as \mathbf{a}_5 , after the five-level wavelet decomposition, contains an *approximation* of the raw signal, labeled as \mathbf{s} . The removed components at different levels of the wavelet decomposition, labeled as \mathbf{d}_1 , \mathbf{d}_2 , \mathbf{d}_3 , \mathbf{d}_4 and \mathbf{d}_5 , are the *details* of this MEMS accelerometer output. The wavelet de-noising algorithm used in this dissertation to analyze the Crossbow MEMS IMU400CC was derived from the Matlab wavelet toolbox, based on the Symlet wavelets, which are considered near-symmetrical, linear phase filters (Matlab, 2007).

$$\mathbf{s}(t) = \mathbf{a}_k(t) + \sum_{i=1}^{i=k} \mathbf{d}_i(t) \quad (5.1)$$

Here, $\mathbf{s}(t)$ represents the original signal. After an optimal k level of decomposition, $\mathbf{s}(t)$ can be decomposed into the approximation $\mathbf{a}_k(t)$, representing the majority of the deterministic errors and stochastic colored noise, and the summation of the k -level $\mathbf{d}_i(t)$, containing the details for each level of the wavelet decomposition.

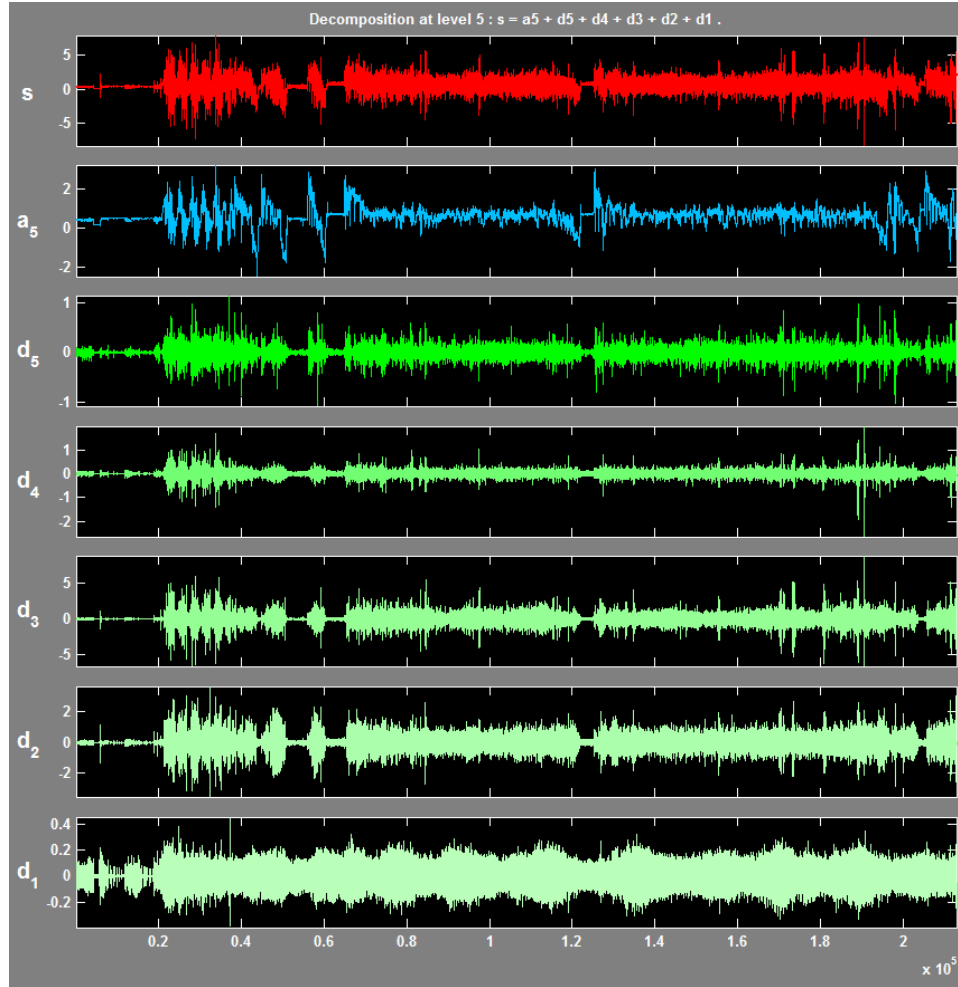


Figure 5.1. An example of the wavelet signal decomposition for an accelerometer output of MEMS IMU400CC in the kinematic mode.

As mentioned earlier, the *details* from the wavelet decomposition of the inertial measurements should only contain the high-frequency measurement noise and some vehicle vibration disturbance. Some of the vehicle dynamics as well as sensor systematic and temporally correlated error sources may also be included in the *details*, which indicates that an over-smoothing might have occurred. The main concern of the over-smoothing is the possible partial removal of some motion dynamic of the vehicle. The over-smoothing effects could be reduced by a careful selection of the allowable level of de-noising, which is a function of the motion dynamics, the data sampling rate, the type of inertial sensor, etc. (Grejner-Brzezinska *et al.*, 2005b; Yi *et al.*, 2005). To prevent the possibility of the actual motion dynamics removal from the signal, the bandwidth of the actual motion dynamics must be carefully analyzed together with the spectrum characteristics of the wavelet de-noising algorithm. The maximum allowable level of

de-noising is normally determined by examining the statistics (mean, standard deviation, autocorrelation sequence, power spectrum, etc.) of the removed noise (Grejner-Brzezinska *et al.*, 2005a & 2005b; Yi *et al.*, 2005).

Figure 5.2 illustrates an example of how to determine the allowable level of de-noising by examining the statistics of the removed noise for a static MEMS IMU dataset. The allowable level of de-noising is ~ 11 for both the gyroscope and accelerometer signals. The allowable level of de-noising is smaller for the kinematic dataset to prevent the partial removal of the dynamic signals. Different motion dynamics will have a corresponding allowable level of de-noising. Shown in Figure 5.3, a signal with medium dynamics will allow a four-level de-noising for the raw acceleration and gyroscope measurements. Figure 5.4 shows the auto-correlation sequence (ACS) and the power spectral density (PSD) of the removed details, using the four-level de-noising for the same kinematic MEMS IMU dataset as in Figure 5.3. Compared to the original signal, the approximation at level four is smoother, while the ACS and PSD of the removed details both indicate a white noise property. However, since the level of de-noising is a function of motion dynamics, the actual allowable level of de-noising should be verified by the true kinematic dataset.

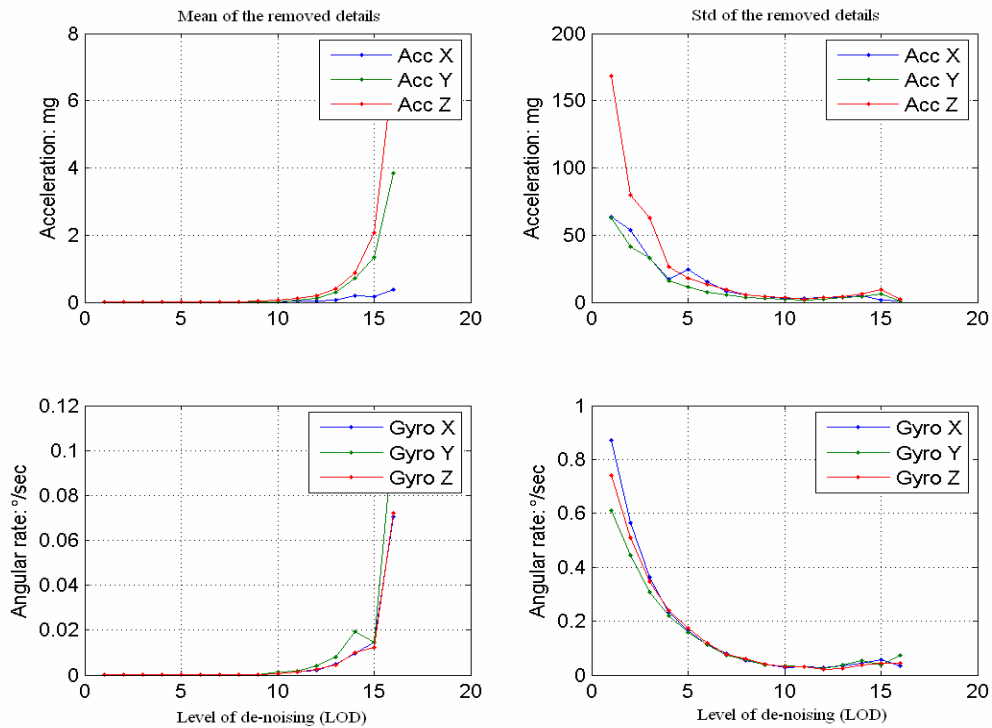


Figure 5.2. Statistics of the removed details for different levels of de-noising for a static dataset of MEMS IMU400CC.

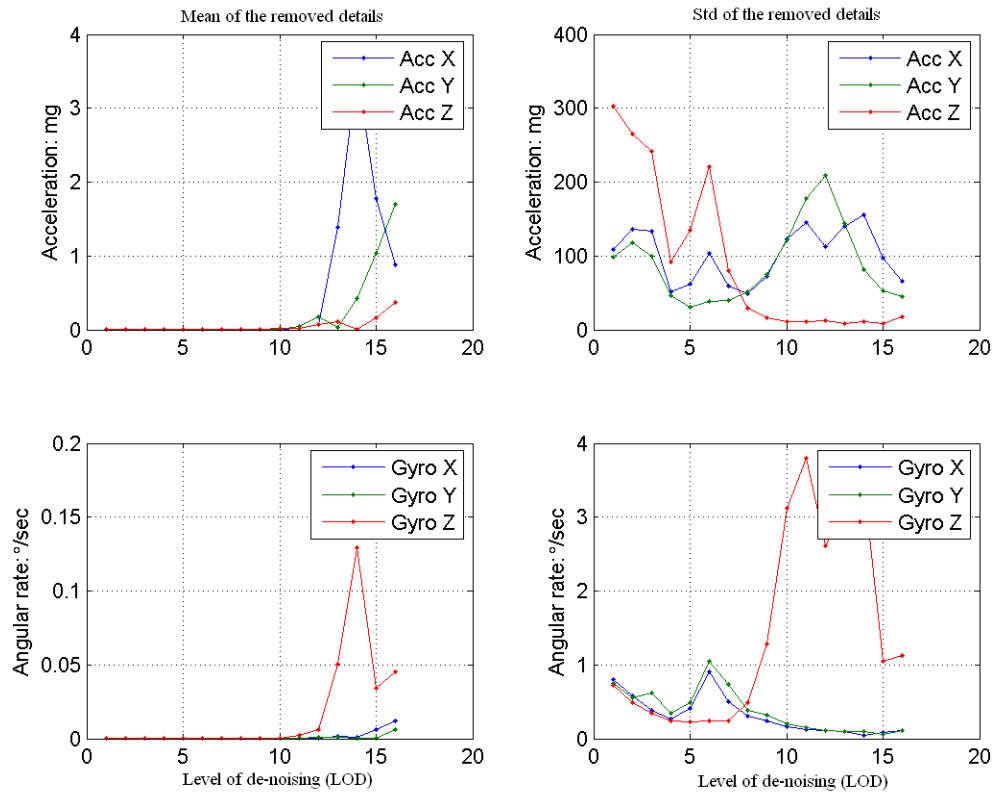


Figure 5.3. Statistics of the removed details for different levels of de-noising for a kinematic land-based trajectory (mild dynamics, i.e., velocity of around 60 km/hour including several large, mild-turn loops around the OSU west campus; refer to Yi *et al.* (2005) for details on the trajectory of this data set) of MEMS IMU400CC.

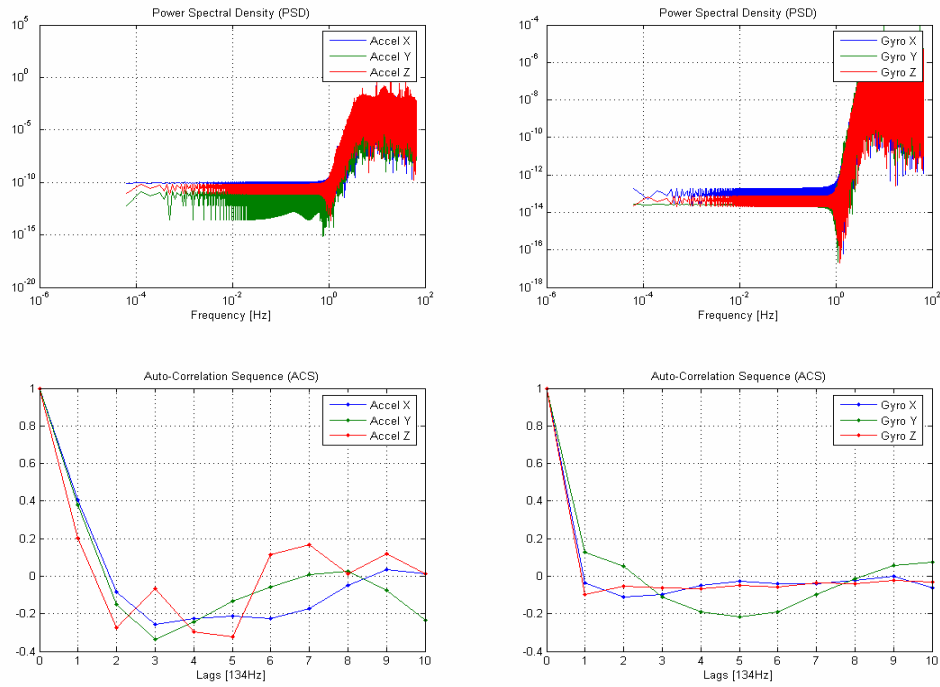


Figure 5.4. The Power spectral density (PSD) and the auto-correlation sequence of the removed details using a four-level de-noising for a kinematic dataset of MEMS IMU400CC.

The outputs of a stationary IMU (theoretically) contain only the sensor systematic and stochastic errors; thus the Allan variance analysis technique, described in Chapter 4, can be applied to the outputs of a stationary IMU to illustrate how different levels of de-noising affect the Allan variance characteristics of the systematic and stochastic errors. Figure 5.5 illustrates the Allan variance characteristics of the output of a stationary accelerometer in x -direction of MEMS IMU400CC as a function of different levels of de-noising. As discussed in Chapter 4, in the original signal, referred to as ‘Level 0’ in Figure 5.5, the rate white noise dominates in the time scale up to 100 seconds. After the fourth-level of de-noising (referred to as ‘Level 4’), the rate ramp (i.e., the trend of the original signal) replaces the rate white noise in the time resolution up to 0.3 seconds, and the rate white noise dominates in the time scale from 0.3 to 100 seconds. If the level of de-noising increases to 13, the rate white noise is almost smoothed out, leaving the clearly identified trends. With the level of de-noising changing, the characteristics of the corresponding smoothed signals also change; Table 5.1 lists the rate ramp (R) characteristics of the accelerometer and gyroscope outputs of MEMS IMU400CC as a function of different levels of de-noising. A consistent stochastic error characteristics and

level of de-noising should be used. Figure 5.6 presents the actual smoothed effects of the x -acceleration of MEMS IMU400CC as a function of different levels of de-noising; the same data were used in Figure 5.2.

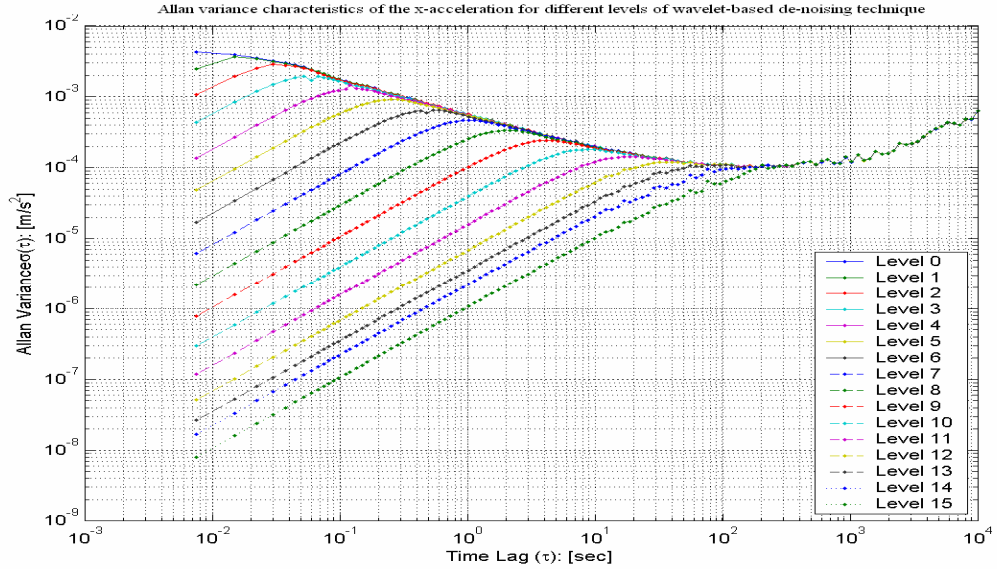


Figure 5.5. The Allan variance characteristics of the x -acceleration of MEMS IMU400CC in stationary mode as a function of different levels of de-noising.

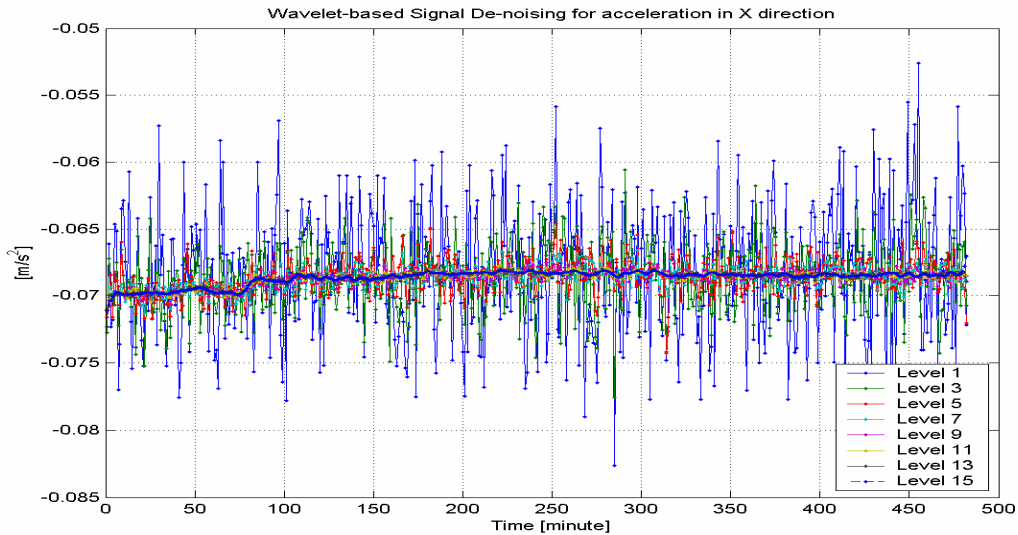


Figure 5.6. The x -acceleration of MEMS IMU400CC in stationary mode as a function of different levels of de-noising.

Level No.	f_x [unit/s]	f_y [unit/s]	f_z [unit/s]	ω_x [unit/s]	ω_y [unit/s]	ω_z [unit/s]
Level 1	0.2737191	0.3270140	0.5194367	0.2006140	0.2398238	0.2638552
Level 2	0.1723866	0.1988566	0.3151786	0.1195368	0.1385335	0.1506296
Level 3	0.0780233	0.0845559	0.1182690	0.0500663	0.0559692	0.0597116
Level 4	0.0245568	0.0296756	0.0415258	0.0177413	0.0197430	0.0201920
Level 5	0.0087875	0.0107016	0.0150089	0.0063592	0.0070526	0.0069316
Level 6	0.0032082	0.0039337	0.0056081	0.0023030	0.0025631	0.0024707
Level 7	0.0011560	0.0014081	0.0019711	0.0008174	0.0009087	0.0008642
Level 8	0.0004191	0.0005073	0.0007086	0.0002884	0.0003238	0.0003082
Level 9	0.0001498	0.0001830	0.0002666	0.0001057	0.0001139	0.0001085
Level 10	0.0000560	0.0000686	0.0000991	0.0000392	0.0000402	0.0000381
Level 11	0.0000223	0.0000276	0.0000394	0.0000158	0.0000147	0.0000137
Level 12	0.0000097	0.0000114	0.0000160	0.0000073	0.0000053	0.0000053
Level 13	0.0000050	0.0000049	0.0000069	0.0000032	0.0000021	0.0000019
Level 14	0.0000032	0.0000025	0.0000033	0.0000019	0.0000010	0.0000010
Level 15	0.0000015	0.0000013	0.0000021	0.0000011	0.0000005	0.0000006

Table 5.1. The rate ramp (R) characteristics of the accelerometer and gyroscope outputs of MEMS IMU400CC as a function of different levels of de-noising.

5.2 The effects of the wavelet-based de-noising on the initial static coarse alignment

The low-cost and low-accuracy MEMS gyro suffers from a relatively high measurement noise, and the earth rotation signal is buried in the high measurement noise, which indicates that it is almost impossible to recover the initial heading (yaw) from the raw inertial measurements using the gyro-compassing technique (Jekeli, 2001). However, with the aid of the signal de-noising technique, based on the wavelet method discussed earlier, and combined with a moving average technique applied to the epoch-by-epoch gyro data, about $\pm 10^\circ$ heading accuracy of MEMS IMU400CC can be achieved, as compared to the reference orientation of the collocated high-end IMU sensor (Grejner-Brzezinska *et al.*, 2005a & 2005b). Figure 5.7 shows the example statistics of the initial orientation, determined from 1600 seconds of experimental static MEMS IMU400CC data, as a function of the level of wavelet de-noising combined with the one-second moving average technique applied to the raw gyro data. In fact, the raw inertial measurements were first de-noised using different levels (up to 15 levels, see Figure 5.7); then the de-noised inertial measurements, collected at a 134 Hz rate, were averaged over 1-second intervals and passed to the coarse self-alignment algorithm. It can be observed in Figure 5.7 that an accuracy of better than $\pm 1^\circ$ (in terms of the standard deviation) can be achieved for the horizontal components (roll and pitch) regardless of the level of de-noising, while the orientation accuracy for the vertical component reaches the accuracy of $\pm 10^\circ$ after 12 levels of de-noising of the vertical gyro measurements.

These orientation accuracies were validated by comparing the solution from the gyros of the MEMS IMU400CC with the solution from another high-end INS (LN100 used here), mounted in the same platform and collocated with MEMS IMU400CC axes. Three mis-alignment orientation angles between three gyro axes of MEMS IMU400CC and those of LN100 can be modeled as random “constants” and estimated in the Kalman filtering combining the inertial measurements of MEMS IMU400CC and the high-accuracy GPS/INS solution of position, velocity and orientation from LN100.

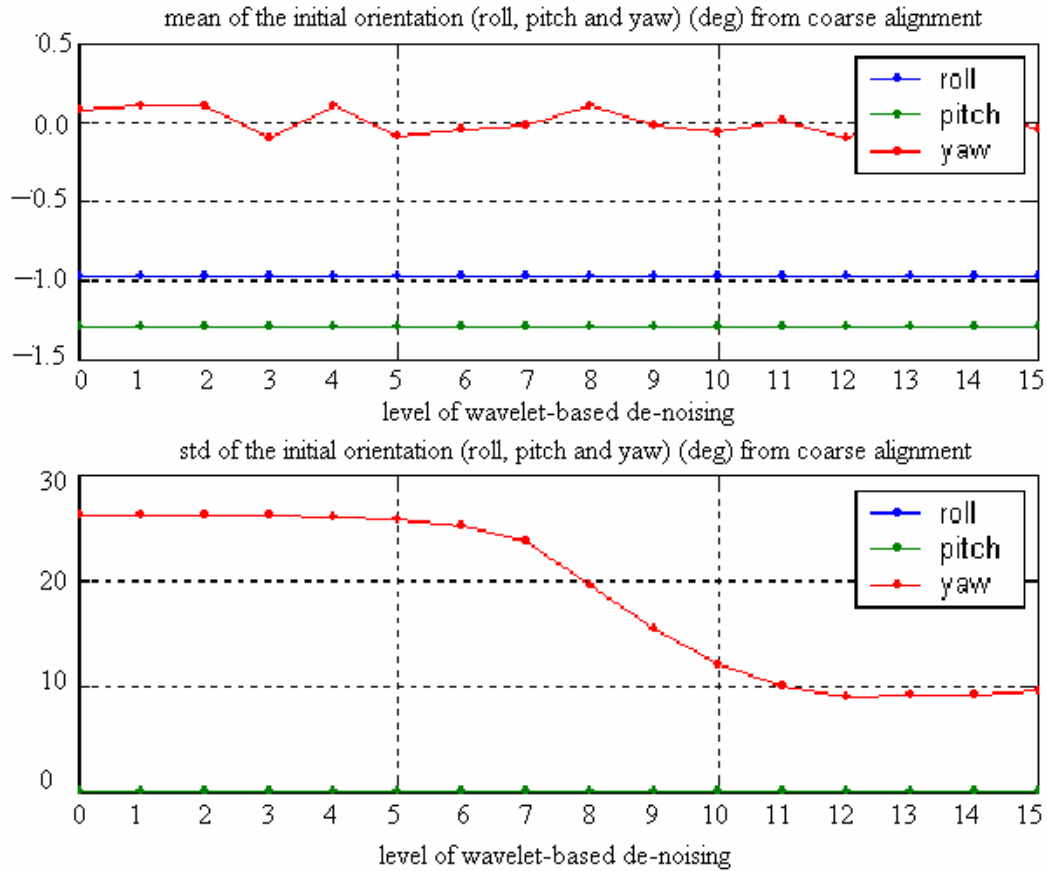


Figure 5.7. Initial orientation determination from the coarse self-alignment for MEMS IMU400CC, using wavelet-based de-noised gyro-measurements combined with the one-second moving average technique.

5.3 The effects of the wavelet-based de-noising on the kinematic navigation solutions

In order to investigate the effect of the wavelet de-noising technique and to determine the allowable level of de-noising for the real kinematic experiments of the land-based mobile mapping system, a total of five free inertial navigation solutions, using a kinematic MEMS IMU400CC dataset after *zero*, *one*, *two*, *three* and *four* levels of

wavelet de-noising were performed, by simulating the GPS gaps after sufficient initial calibration of the inertial errors using GPS signals (Yi *et al.*, 2005). Table 5.2 lists the horizontal and vertical position deviations of these free inertial navigation solutions with different durations of the free inertial navigation periods, comparing the results to a high-end reference GPS/INS integrated solution without GPS gaps. The solution after *one* level of de-noising was obviously improved, compared to the solution without wavelet de-noising (i.e., *zero* level of de-noising), and the solution after *two* levels of wavelet de-noising was worse than that after *one* level of de-noising, while still being better than that for the raw data. No obvious performance improvements of the solutions after *three* and *four* levels of de-noising were found, as compared to the solution using raw data. Thus, the optimal level of de-noising for this experiment is *one*.

Level		10sec [m]		30sec [m]		60sec [m]	
		mean	std	mean	std	mean	std
0	N	5.42	5.03	47.70	44.75	168.89	142.52
	E	2.96	2.75	32.20	33.17	201.44	218.67
	U	0.34	0.40	2.08	1.43	2.30	1.47
1	N	0.45	0.29	0.66	0.46	32.31	48.15
	E	0.13	0.16	4.00	4.14	16.92	18.81
	U	0.29	0.36	1.22	0.91	14.85	18.35
2	N	3.29	2.99	34.59	36.09	225.36	243.78
	E	1.22	1.10	6.67	4.84	59.66	93.48
	U	0.30	0.36	1.44	1.02	2.30	2.20
3	N	5.77	5.17	43.71	39.12	113.84	78.69
	E	1.68	1.75	32.16	37.43	276.40	322.15
	U	0.17	0.22	1.03	0.76	3.65	6.35
4	N	5.99	5.53	52.66	49.55	193.90	167.42
	E	1.93	1.71	19.90	20.67	136.17	151.53
	U	0.18	0.23	0.95	0.76	5.16	5.19

Table 5.2. Position deviation of the free inertial navigation solutions with different durations of the free inertial navigation periods with respect to the reference GPS/INS trajectory without GPS gaps, for different levels of de-noising applied to MEMS IMU400CC data.

5.4 The effects of the wavelet de-noising, combined with the customized stochastic error model on kinematic navigation solution

As already mentioned, the free inertial navigation performance of the low-cost MEMS IMU can be improved by means of: 1) the customized stochastic error model, derived by using the Allan-variance analysis and/or PSD method, as described in Chapter

4, and 2) the wavelet signal de-noising technique discussed here. In order to assess the effects of the two proposed approaches on the kinematic navigation solutions, a total of five 60-second GPS gaps were intentionally introduced to a kinematic land-based dataset at five different locations, and five free inertial navigation solutions were computed. These five free inertial navigation solutions in four scenarios (referred to as R1, R2, S1_2, and S2_2, and shown in Table 5.3) were analyzed as gaps of different durations and shown in Table 5.4 and 5.5) (Yi *et al.*, 2005). They are compared to the corresponding reference GPS/INS solution obtained under the same conditions, that is, the same inertial measurements, identical error model parameters, and the same Kalman filter initial states as well as the corresponding error covariance matrix.

Scenario name	Description
R1	Raw measurements + manufacturer's error model
R2	Raw measurements + customized error model
S1_2	Smoothed measurements based on <i>one</i> level of de-noising + customized error model
S2_2	Smoothed measurements based on <i>two</i> level of de-noising + customized error model

Table 5.3. Four scenarios of the free inertial navigation solutions.

Tables 5.4 and 5.5 present the position and orientation deviations from the reference GPS/INS position and orientations as a function of GPS gap duration. The comparison of the R1 and R2 solutions indicates that when the customized error model is used instead of the manufacturer's error specification, significant navigation improvements can be achieved. Namely, a reduction of around 60% and 15% in the 3D position and orientation deviations from the reference position and orientation solutions, respectively, can be achieved for 10-second GPS gaps in the R2 solution, as compared to the R1 solution; 50% and 17% reduction, respectively, of these deviations is achieved for the 30-second GPS gaps. Around 50% and 12% reduction, respectively, in these deviations is achieved for the 60-second GPS gaps. This implies the importance of the *customized* error model on a sensor-by-sensor basis.

Further improvements in both position and orientation were achieved by combining the wavelet-based de-noising technique with the *customized* error model, as can be observed by a comparison of S1_2 and S2_2 with the R1 solution. This comparison indicates that more improvements with *one* level of de-noising can be achieved, in contrast to the higher levels of de-noising that may over-smooth the actual dynamics or time-correlated errors (i.e., invalidate the stochastic error model). It should be pointed out that not all components/sensors are equally affected, as shown in Tables 5.4 and 5.5, which indicate that the performance improvements of wavelet de-noising is also a

function of the trajectory dynamics. The real-time implementation of the wavelet-based de-noising may need to adaptively adjust the level of de-noising, according to the trajectory dynamics to achieve better navigation performance.

Level		10sec [m]		30sec [m]		60sec [m]	
		mean	std	mean	std	mean	std
R1	N	0.22	0.15	9.15	11.20	106.34	96.77
	E	2.28	3.82	48.05	81.51	342.90	577.82
	U	0.18	0.10	4.11	6.31	54.86	102.70
R2	N	0.59	0.72	16.68	16.42	123.96	110.23
	E	0.80	0.85	17.48	20.38	130.23	149.59
	U	0.15	0.13	1.34	1.10	9.82	11.00
S1_2	N	0.58	0.77	16.07	16.44	120.66	108.54
	E	0.73	0.78	15.93	18.95	118.87	138.85
	U	0.14	0.11	1.27	1.05	9.20	10.50
S2_2	N	0.51	0.58	15.07	14.36	112.29	97.57
	E	0.94	1.11	20.17	25.85	148.51	185.41
	U	0.14	0.14	1.42	1.21	11.22	14.02

Table 5.4. Free inertial navigation position error (with respect to the reference GPS/INS trajectory) as a function of the GPS gap duration.

Level		10sec [°]		30sec [°]		60sec [°]	
		mean	std	mean	std	mean	std
R1	R	0.18	0.05	1.78	2.18	4.41	5.74
	P	1.17	1.79	3.31	4.87	5.99	8.76
	H	2.90	2.75	9.55	8.29	19.58	18.87
R2	R	0.21	0.07	1.32	1.20	2.08	1.54
	P	0.39	0.34	1.14	1.07	2.48	2.37
	H	2.70	2.59	8.29	7.10	18.21	18.41
S1_2	R	0.21	0.08	1.29	1.17	1.99	1.47
	P	0.35	0.31	1.04	0.95	2.31	2.20
	H	2.60	2.50	8.11	6.92	17.81	18.01
S2_2	R	0.20	0.07	1.36	1.28	2.18	1.71
	P	0.44	0.43	1.28	1.22	2.70	2.77
	H	2.77	2.64	8.57	7.32	18.72	18.67

Table 5.5. Free navigation orientation error (with respect to the reference GPS/INS trajectory) as a function of the GPS gap duration.

Figure 5.8 illustrates an example comparison of a 90-second free inertial navigation for case R1 (with *zero* level of de-noising and the manufacturer’s error model) and case S1_2 (with *one* level of de-noising and the customized error model) with the GPS/INS reference. The R1 solution drifted around 696 m in horizontal position from the reference after the 90-second period of free inertial navigation; around 29 percent of this drift is reduced by using *one* level of de-noising and the customized error model, as can be seen in Figure 5.8. The statistics of the free navigation performance, shown in Tables 5.4 and 5.5, indicate that short GPS losses of lock may still meet the position and horizontal orientation accuracy for some mobile mapping applications using the tested MEMS IMU400CC. More demanding applications cannot use a sensor of this grade/performance, as position and orientation errors grow rather fast with time. Namely, around 1 m, 22 m, and 169 m of the 3D position drift after 10 s, 30 s, and 60 s, respectively, of the free inertial navigation can be observed; around 0.5°, 1.6°, and 3.0°, respectively, of the 2D orientation (roll and pitch) error drift after 10 s, 30 s, and 60 s, respectively, of the free inertial navigation is observed. The worst accuracy is in the heading component, which suffers from more than 2° drift after 10 s of free inertial navigation. Therefore, additional sensors, for example multiple GPS antenna systems, a magnetometer, or a digital compass, should be investigated to aid the vertical orientation component (i.e., heading or yaw) while using this low-cost MEMS IMU.

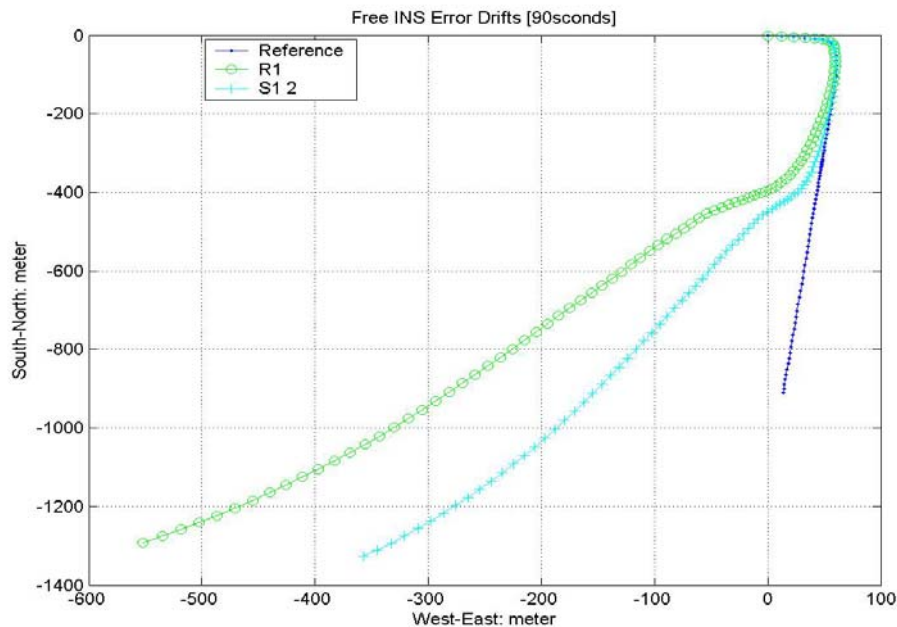


Figure 5.8. The free inertial navigation solutions, R1 and S1_2 compared to the reference GPS/INS solution.

CHAPTER 6

ALTERNATIVES TO THE EXTENDED KALMAN FILTER

Due to the nonlinearity of the state-space model (i.e., system and measurement models) involved in the GPS/INS-based multi-sensor integrated systems, the well-known Extended Kalman Filter (EKF) is predominantly used in a number of GPS/INS implementations, under the assumption that the states behave as Gaussian Random Variables (GRV). The EKF also works for nonlinear systems with a non-Gaussian distribution, although it may experience difficulties with heavily skewed nonlinear systems. In addition, due to first-order linearization, the EKF is only reliable for these nonlinear systems that are almost linear in the time scale of the update intervals; otherwise, if the assumption of local linearity is violated, it may introduce significant errors in the predicted estimates and the error covariance of the state vector transformed through nonlinear systems, resulting in a suboptimal performance or even filter divergence (see, for example, Julier and Uhlmann, 1997).

In the last few decades, several algorithms have been developed to improve the performance of the EKF. For example, the predicted state estimates using the EKF in the prediction stage can be evaluated from the direct nonlinear system model, instead of the linearized system model. It provides a better approximation to the actual predicted state estimates; however, the state error covariance matrix may still not reflect the actual error characteristics of the predicted state estimates. The higher-order EKF and iterated EKF (IEKF) can also improve the performance. While the higher-order EKF is more complicated, as it requires deriving the higher-order linearized state-space model, the IEKF is less flexible for real-time implementations since it requires iterative refining of the state estimates by re-evaluating the filter around the updated state estimates in one filter cycle. One unconventional alternative approach, called wave filter, was proposed by Salychev & Schaffrin (1992). It can provide some compensation to the linearization errors by using wave functions. The common feature of the aforementioned KF variants is that they are best described as trying to transform the nonlinear filtering to a sequence of optimal linear Kalman Filters, and the major difference in the filters lies in the methods on how the linearization errors are handled.

Two alternative nonlinear filters will be investigated in the next section. They are theoretically different from the aforementioned filters, and summarized in a probabilistic

framework; thus, they are referred to as nonlinear Bayesian filtering techniques. The KF variants can also be treated as special cases of the nonlinear Bayesian filtering, even though they had not originally been derived from the probabilistic framework.

6.1 Nonlinear Bayesian filtering

The primary objective of a multi-sensor integrated system is to infer the unknown quantities (i.e., the position, velocity and orientation of the platform, together with the sensor errors, system and environmental parameters), based on the system model, using noisy measurements. Given a priori probability density function (density for short), inferring the state of a dynamic model from the noisy measurements is called Bayesian inference; see, for example, Ristic *et al.* (2004). The input includes the system model with a prior density and a measurement sequence, while the output is the state posterior density based on all available information. The state posterior density is usually *non-Gaussian*, if either the system model or the measurement model is nonlinear. The real-time Bayesian inference of the most recent state is called Bayesian filtering. It recursively provides sequential updates of the previous estimates, and allows for faster real-time data processing with lower storage requirements. Such a recursive Bayesian filter consists of two steps, namely, prediction and update. In the prediction step, the state posterior density is predicted forward from the previous epoch to the current epoch according to the system model. Due to the involvement of random errors, the state posterior density is actually translated, deformed and widened after the prediction procedure. The update step is to modify (usually to tighten) the predicted state posterior density incorporating the latest noisy measurements according to the measurement model. The basic principle of Bayesian filtering is the Bayes theorem (see, for example, Ristic *et al.*, 2004). Given the state posterior density, a number of state estimates (for example, the mean, mode, median, confidence level, kurtosis, etc.) can be calculated.

6.1.1 Conceptual solution

Following the notation of Ristic *et al.* (2004), the probability state-space model includes a state transition density (or probability) shown in equation (6.1) and a marginal density shown in equation (6.2). The transition density (also referred to as transition prior), $p(x_k | x_{k-1})$, is equivalent to the well-known system model shown in equation (2.36)

of Chapter 2, and the marginal density, $p(z_k | x_k)$, is equivalent to the well-known measurement model shown in equation (2.37) of Chapter 2. Let $X_k \equiv \{x_j\}_{j=0}^{j=k}$ denote the state sequence up to epoch k , and X_0 is the set of state initial estimates. Let

$Z_k \equiv \{z_j\}_{j=0}^{j=k}$ denote the measurement sequence available up to time k , and Z_0 is the set

of zero or no measurements. The joint state posterior density is represented as $p(X_k|Z_k)$, and the marginal state posterior density is called filtering density, $p(x_k|Z_k)$. The objective of the nonlinear Bayesian filtering is to filter the state estimates, x_k , from the measurement sequence, Z_k , and a given state initial density, $p(x_0) = p(x_0|z_0)$. From the Bayesian perspective, it can be transformed into a recursive process by obtaining the filtering density using the aforementioned two steps: prediction and update, with the given initial state density. In the prediction step, the state predicted density (also referred to as prior density), $p(x_k|Z_{k-1})$, at epoch k can be obtained, as shown in equation (6.4), from the state posterior density, $p(x_{k-1}|Z_{k-1})$, at epoch $k-1$, and the state transition density, $p(x_k|x_{k-1})$. Following the Bayes' rule, as shown in equations (6.4) and (6.5), the update procedure is to modify the state predicted density to obtain the state posterior density, $p(x_k|Z_k)$, at current epoch k , once a measurement, z_k , is available. After the state posterior density, $p(x_k|Z_k)$, has been obtained, using the recursive equations (6.4) and (6.5), the state estimates can be computed from the filtering density, $p(x_k|Z_k)$. For example, the minimum mean square error (MMSE) estimate, as shown in equation (6.7), is the conditional mean of x_k , given Z_k . In the aforementioned prediction and update steps, two basic assumptions are made for the state-space model, shown in equations (6.1) and (6.2): 1) the state is the following first-order Markov process, i.e., $p(x_k|x_{k-1}, \dots, x_0) = p(x_k|x_{k-1})$; and 2) the measurements are independent of the given state, implying $p(z_k|x_k, Z_{k-1}) = p(z_k|x_k)$.

$$\text{Transition density} \quad x_k = f_{k-1}(x_{k-1}, v_k) \Leftrightarrow p(x_k|x_{k-1}) \quad (6.1)$$

$$\text{Marginal density} \quad z_k = h_k(x_k, n_k) \Leftrightarrow p(z_k|x_k) \quad (6.2)$$

$$\text{State initial density} \quad p(x_0) = p(x_0|Z_0) \Leftrightarrow (\hat{x}_0 - x_0) \sim (0, P_0) \quad (6.3)$$

$$\text{State predicted density} \quad p(x_k|Z_{k-1}) = \int p(x_k|x_{k-1}) \cdot p(x_{k-1}|Z_{k-1}) \cdot dx_{k-1} \quad (6.4)$$

$$\begin{aligned} & p(x_k|Z_k) \\ &= p(x_k|z_k, Z_{k-1}) \\ \text{State updated density} \quad &= \frac{p(z_k|x_k, Z_{k-1}) \cdot p(x_k|Z_{k-1})}{p(z_k|Z_{k-1})} \quad (6.5) \\ &= \frac{p(z_k|x_k) \cdot p(x_k|Z_{k-1})}{p(z_k|Z_{k-1})} \end{aligned}$$

$$\text{Evidence} \quad p(z_k|Z_{k-1}) = \int p(z_k|x_k) \cdot p(x_k|Z_{k-1}) \cdot dx_k \quad (6.6)$$

$$\text{MMSE state estimate} \quad \hat{x}_{k|k}^{\text{MMSE}} \equiv E\{x_k|Z_k\} = \int x_k \cdot p(x_k|Z_k) \cdot dx_k \quad (6.7)$$

$$\text{MMSE state error covariance} \quad P_{k|k}^{\text{MMSE}} \equiv \int (x_k - \hat{x}_{k|k}^{\text{MMSE}})(x_k - \hat{x}_{k|k}^{\text{MMSE}})^T \cdot p(x_k|Z_k) \cdot dx_k \quad (6.8)$$

$$\text{Structure of update equation} \quad \text{posterior} = \frac{\text{likelihood} \times \text{prior}}{\text{evidence}} \quad (6.9)$$

Here, the subscripts 0, $k-1$, k , and $k+1$ denote the discrete time epochs; x , v , z and n are the state vector, the process noise vector, the measurement vector and the measurement noise vector, respectively; p represents the probability density function (density); the process noise, v , and the measurement noise, n , are assumed to be white, with known densities. v and n are independent, and both v and n are independent of the state density of x ; $v_k \sim (0, Q_k)$ and $n_k \sim (0, R_k)$; f_{k-1} is the nonlinear system function to describe the probabilistic model of the state evolution, leading to the transitional density, i.e., $p(x_k|x_{k-1})$; h_k is the nonlinear measurement function, necessary to describe the likelihood (or marginal) density, i.e., $p(z_k|x_k)$.

In general, the state posterior density of the Bayesian filtering is a non-Gaussian density, thus the described conceptual solution, i.e., the recursive formation shown in equations (6.4) and (6.5), cannot be solved analytically except for some specific cases, such as, for example, the KF for linear systems. For the nonlinear state-space model, shown in equations (6.1) and (6.2), there exist several practical approximate approaches to the conceptual solution of the Bayesian filtering. One suboptimal approach is to approximate both the nonlinear system model and the measurement model by linear models. An optimal solution can then be provided to the linearized model. The EKF family (including the EKF, the higher-order EKF, and the IEKF) is formed by following

this kind of a sub-optimal approach; see, for example, (Kalman, 1960; Jazwinski, 1970). Another suboptimal approach is based on direct approximation of the non-Gaussian density. The Unscented Kalman Filter (UKF) and the Particle Filter (PF), discussed later, belong to this type of suboptimal approach; see, for example, Doucet *et al.* (2001).

If both the system and the measurement models are linear, as well as the process and the measurement noises are drawn from Gaussian densities with known parameters (mean and covariance), the state posterior density at each epoch is also Gaussian and can be completely represented by the mean and the covariance of the state posterior density. In this case, the nonlinear Bayesian filtering changes to an optimal Kalman filtering. For the nonlinear system, the linearization procedure converts the nonlinear Bayesian filtering into Linear Kalman filtering, resulting in a suboptimal EKF family. As mentioned earlier, the EKF family also works for non-Gaussian systems, even though they may experience difficulties for heavily skewed nonlinear systems.

Except for the conventional EKF, two other approximate algorithms of the nonlinear Bayesian filtering have been investigated widely in the last few years, and are explored here as alternatives that can eliminate the drawbacks of the EKF, namely the UKF (see, for example, Julier and Uhlmann, 1997; Wan and van der Merwe, 2001) and the PF (see, for example, Doucet *et al.*, 2001; Arulampalam *et al.*, 2002; Ristic *et al.*, 2004).

6.1.2 Unscented Kalman Filter

Unlike the EKF, the UKF does not approximate the nonlinear functions f and h in equations (6.1) and (6.2) using the first-order linearization approximation. Instead, it approximates the state posterior density $p(x_k|Z_k)$ by a Gaussian density using a minimal set of *deterministically* selected samples (referred to as sigma points). These samples can better capture the mean and the covariance of a density than the EKF. A set of transformed samples is generated from the selected samples directly through the nonlinear systems using a so-called Unscented Transformation (UT). The transformed samples can capture the mean and the covariance of the transformed density accurately up to third-order for a Gaussian density (or second-order for a non-Gaussian density) in terms of the Taylor series expansion for any nonlinear systems; see the prove by (Wan & van der Merwe, 2001). The idea of representing the density by using a set of samples is referred to as statistical linearization (Gelb, 1974), as compared to the analytical linearization of the EKF. The whole class of nonlinear filtering using the statistical linearization is referred to as the family of the Linear Regression Kalman Filters (LRKF) (see, for example, Lefebvre *et al.*, 2002), with the major difference in the selection of the samples. Also, the fact that no derivative is involved in the state-space model results in a high tolerance to substantial initial state errors. For example, it is possible for the UKF to eliminate the initial coarse and fine alignments for the inertial sensors, translating to a rapid deployment and operational readiness of the multi-sensor integrated systems.

6.1.2.1 The implementation using the UKF

Given the nonlinear state-space model shown in equations (6.1-6.3), the implementation using the UKF approach is as follows:

1. To generate samples from the state estimate, \hat{x}_{k-1} , and the state error covariance matrix, P_{k-1} , from the previous epoch (the initial state estimate, \hat{x}_0 , and the initial state error covariance, P_0 , will be used for the first epoch, where $k=1$):

To represent the state posterior density, $p(x_{k-1}|Z_{k-1})$, using N samples χ_{k-1}^i and their weights, $\{W_{k-1}^i\}_{i=0}^{N-1}$, where χ denotes the sample of the state vector.

2. To predict the state estimates, $\hat{x}_{k|k-1}$, and the state error covariance, $P_{k|k-1}$, from the previous epoch to the current epoch:

$$\hat{x}_{k|k-1} = \sum_{i=0}^{N-1} W_{k-1}^i \cdot f_{k-1}(\chi_{k-1}^i), \quad (6.10)$$

$$P_{k|k-1} = Q_{k-1} + \sum_{i=0}^{N-1} W_{k-1}^i \cdot \left(f_{k-1}(\chi_{k-1}^i) - \hat{x}_{k|k-1} \right) \left(f_{k-1}(\chi_{k-1}^i) - \hat{x}_{k|k-1} \right)^T. \quad (6.11)$$

3. To generate samples from the state predicted estimate, $\hat{x}_{k|k-1}$, and the state predicted error covariance matrix, $P_{k|k-1}$, from the current epoch:

To represent the state predicted density $p(x_k|Z_{k-1})$ using N samples $\chi_{k|k-1}^i$ and their weights, $\{W_{k|k-1}^i\}_{i=0}^{N-1}$.

4. To generate the updated state estimate, $\hat{x}_{k|k}$, and the updated state error covariance matrix, $P_{k|k}$, from the current epoch based on the available measurements:

$$\hat{z}_{k|k-1} = \sum_{i=0}^{N-1} W_{k|k-1}^i \cdot h_k(\chi_{k|k-1}^i) \quad (6.12)$$

$$\hat{x}_{k|k} = \hat{x}_{k|k-1} + K_k \left(z_k - \hat{z}_{k|k-1} \right) \quad (6.13)$$

$$P_{k|k} = P_{k|k-1} - K_k (R_k + P_{zz}) K_k^T \quad (6.14)$$

$$K_k = P_{xz} (R_k + P_{zz})^{-1} \quad (6.15)$$

$$P_{xz} = \sum_{i=0}^{N-1} W_{k-1}^i \cdot (\chi_{k|k-1}^i - \hat{x}_{k|k-1}) (h_k(\chi_{k|k-1}^i) - \hat{z}_{k|k-1})^T \quad (6.16)$$

$$P_{zz} = \sum_{i=0}^{N-1} W_{k-1}^i \cdot (h_k(\chi_{k|k-1}^i) - \hat{z}_{k|k-1}) (h_k(\chi_{k|k-1}^i) - \hat{z}_{k|k-1})^T \quad (6.17)$$

The key step in the UKF is to construct the samples from the current state estimates, \hat{x} , and the state error covariance matrix, P . A common approach to construct the samples is the following:

$$\chi^i = \hat{x} \quad W^i = \frac{\kappa}{(\dim(x) + \kappa)} \quad i = 0 \quad (6.18)$$

$$\chi^i = \hat{x} + L_i \quad W^i = \frac{\kappa}{2(\dim(x) + \kappa)} \quad i = 1, \dots, \dim(x) \quad (6.19)$$

$$\chi^i = \hat{x} - L_i \quad W^i = \frac{\kappa}{2(\dim(x) + \kappa)} \quad i = \dim(x) + 1, \dots, \dim(x) + \dim(x) \quad (6.20)$$

$$L^T \cdot L = (\dim(x) + \kappa) P \quad (6.21)$$

Here, κ is the sigma point selection scaling parameter, such that $\dim(x) + \kappa \neq 0$; according to (Julier and Uhlmann, 1997), κ is used to provide an extra degree-of-freedom to “fine-tune” the higher-order moments of the approximation, thus to reduce the overall predicted errors. If the state density of x is assumed Gaussian, the recommended choice of κ is $\dim(x) + \kappa = 3$; a different choice of κ may be more appropriate for a different state density of x ; the index i represents the index of the deterministically chosen sigma points; L is the square root matrix of the error covariance matrix, P ; L_i is the i -th column of matrix L .

6.1.3 Particle Filter

Another alternative to EKF, the Particle Filter, is a technique to implement the recursive nonlinear Bayesian filter, described in equations (6.4) and (6.5), by performing Sequential Monte Carlo (SMC) estimation according to the sample-based representation of the state posterior density (Doucet *et al.*, 2001; Arulampalam *et al.*, 2002; Ristic *et al.*, 2004). The advantage of the PF, as compared to the UKF and the EKF, is that with sufficient samples to represent the state posterior density, the PF will approach the optimal estimate of the nonlinear Bayesian filter. Thus, theoretically, the PF is more accurate than the UKF and the EKF, even though the UKF, the PF and the EKF are all suboptimal filters.

6.1.3.1 Monte Carlo approximation

As mentioned earlier, the PF is a sample-based approach. If it is possible to draw N independent samples, $\{x^i\}_{i=1}^N$, from a density $p(x)$, then, as shown in equation (6.23), the expectation of a nonlinear function, $f(x)$, can be approximated by the sample average, which should be an unbiased estimate of $f(x)$. With the increasing number of the samples, the sample average will converge to $f(x)$ according to the law of large numbers (see, for example, Ristic *et al.*, 2004).

$$p(x) \approx \frac{1}{N} \sum_{i=1}^N \delta(x - x^i) \quad (6.22)$$

$$E\{f(x)\} = \int f(x) \cdot p(x) \cdot dx \approx \int f(x) \cdot \left[\frac{1}{N} \sum_{i=1}^N \delta(x - x^i) \right] \cdot dx = \frac{1}{N} \sum_{i=1}^N f(x^i) \quad (6.23)$$

Here, $\delta(\)$ denotes the Dirac delta function.

6.1.3.2 Importance sampling

Ideally, if samples can be generated directly from $p(x)$, then, as shown earlier, the sample average, computed from equation (6.23), using samples $\{x^i\}_{i=1}^N$, is an unbiased estimate of the nonlinear function, $f(x)$. Unfortunately, it is never possible to sample

from the actual density. However, if samples can be drawn from another known density, $q(x)$, which is similar to $p(x)$, then an unbiased estimate can be provided from the corrected weighted sample average by using the samples associated with weights, as shown in equation (6.24). The density $q(x)$ is referred to as the *importance* or *proposal* density, the procedure to sample from the importance density is referred to as importance sampling, and the weight for each sample is called the importance weight. The normalized importance weights, $w(x^i)$, shown in equation (6.25) are normally used for the samples:

$$\begin{aligned}
& E\{f(x)\} \\
&= \int f(x) \cdot p(x) \cdot dx \\
&= \int f(x) \cdot \frac{p(x)}{q(x)} \cdot q(x) \cdot dx \leftarrow p(x) = \frac{p(x)}{q(x)} \cdot q(x) \\
&= \int f(x) \cdot \tilde{w}(x) \cdot q(x) \cdot dx \leftarrow \tilde{w}(x) = \frac{p(x)}{q(x)} \\
&\approx \frac{1}{N} \sum_{i=1}^N [f(x^i) \cdot \tilde{w}(x^i)] \leftarrow q(x) \approx \frac{1}{N} \sum_{i=1}^N \delta(x - x^i) \\
&= \sum_{i=1}^N [f(x^i) \cdot w(x^i)] \leftarrow \text{normalization} \quad w(x^i) \leftarrow \frac{\tilde{w}(x^i)}{\sum_{j=1}^N \tilde{w}(x^j)}
\end{aligned} \tag{6.24}$$

$$\sum_{i=1}^N w(x^i) = 1 \tag{6.25}$$

6.1.3.3 Sequential importance sampling

If the importance sampling is used in the Bayesian framework to approximate the integration shown in equations (6.4-6.8) using discrete sums of the weighted samples, as shown in equation (6.24), then the state posterior density, $p(x_k|Z_k)$, is the density mentioned in Section 6.1.3.2. Equation (6.26) shows the detailed corresponding form of equation (6.24) for the state posterior density, $p(x_k|Z_k)$, with a known and easy-to-sample importance density, $q(x_k|Z_k)$. The Bayes rule is used in equation (6.26).

By drawing samples from the importance density, $q(x_k|Z_k)$, the expectation of a

nonlinear function can be approximated by samples with weights, $\{x_k^i, w_k^i\}_{i=1}^N$, according to equation (6.28). Given the assumptions of the state-space model shown in Section 6.1.1 (i.e., $p(x_k|x_{k-1}, \dots, x_0) = p(x_k|x_{k-1})$ and $p(z_k|x_k, Z_{k-1}) = p(z_k|x_k)$), the importance weights can be recursively estimated, as shown in equation (6.30); for the proof see De Freitas *et al.* (1998). The sequential importance sampling (SIS) forms the basis of the sequential Monte Carlo estimation, which is also known as bootstrap filtering, the condensation algorithm, particle filtering, interacting particle approximations, and the “survival of the fittest”; see, for example, Ristic *et al.* (2004). The key idea to implement the nonlinear Bayesian filter via the SIS is to represent the state posterior density by a set of random samples with associated weights and to compute the estimates based on direct sums of the weighted random samples. Given a set of random samples with weights $\{x_{k-1}^i, w_{k-1}^i\}_{i=1}^N$ at epoch $k-1$, a programming pseudo-code, using the filter via the SIS to obtain the samples with weights $\{x_k^i, w_k^i\}_{i=1}^N$ at epoch k , is given in Table 6.1.

$$\begin{aligned}
& E\{f(x_k)\} \\
&= \int f(x_k) \cdot p(x_k|Z_k) \cdot dx_k \\
&= \int \frac{p(x_k|Z_k)}{q(x_k|Z_k)} \cdot f(x_k) \cdot q(x_k|Z_k) \cdot dx_k \leftarrow p(x_k|Z_k) = \frac{p(x_k|Z_k)}{q(x_k|Z_k)} \cdot q(x_k|Z_k) \\
&= \int \frac{p(Z_k|x_k) \cdot p(x_k)}{p(Z_k) \cdot q(x_k|Z_k)} \cdot f(x_k) \cdot q(x_k|Z_k) \cdot dx_k \leftarrow p(x_k|Z_k) = \frac{p(Z_k|x_k) \cdot p(x_k)}{p(Z_k)} \\
&= \int \frac{\tilde{w}_k(x_k)}{p(Z_k)} \cdot f(x_k) \cdot q(x_k|Z_k) \cdot dx_k \leftarrow \tilde{w}_k(x_k) = \frac{p(Z_k|x_k) \cdot p(x_k)}{q(x_k|Z_k)} \\
&= \frac{\int \tilde{w}_k(x_k) \cdot f(x_k) \cdot q(x_k|Z_k) \cdot dx_k}{p(Z_k)} \tag{6.26}
\end{aligned}$$

$$\begin{aligned}
&= \frac{\int \tilde{w}_k(x_k) \cdot f(x_k) \cdot q(x_k|Z_k) \cdot dx_k}{\int p(Z_k|x_k) \cdot p(x_k) \cdot \frac{q(x_k|Z_k)}{q(x_k|Z_k)} \cdot dx_k} \\
&= \frac{\int \tilde{w}_k(x_k) \cdot f(x_k) \cdot q(x_k|Z_k) \cdot dx_k}{\int \tilde{w}_k(x_k) \cdot q(x_k|Z_k) \cdot dx_k} \\
&= \frac{E\{\tilde{w}_k(x_k) \cdot f(x_k)\}_{q(x_k|Z_k)}}{E\{\tilde{w}_k(x_k)\}_{q(x_k|Z_k)}}
\end{aligned}$$

$$\tilde{w}_k(x_k) = \frac{p(Z_k|x_k) \cdot p(x_k)}{q(x_k|Z_k)} \tag{6.27}$$

$$\begin{aligned}
& E\{f(x_k)\} \\
&\approx \frac{\frac{1}{N} \sum_{i=1}^N [\tilde{w}_k(x_k^i) \cdot f(x_k^i)]}{\frac{1}{N} \sum_{i=1}^N [\tilde{w}_k(x_k^i)]} \tag{6.28}
\end{aligned}$$

$$\begin{aligned}
&= \sum_{i=1}^N [w_k^i \cdot f(x_k^i)] \\
&w_k^i \equiv w_k(x_k^i) = \frac{\tilde{w}_k(x_k^i)}{\sum_{j=1}^N \tilde{w}_k(x_k^j)} \tag{6.29}
\end{aligned}$$

$$w_k^i = w_{k-1}^i \cdot \frac{p(z_k | x_k^i) \cdot p(x_k^i | x_{k-1}^i)}{q(x_k^i | x_{k-1}^i, z_k)} \quad (6.30)$$

$$\left\{ \{x_k^i, w_k^i\}_{i=1}^N \right\} = SIS \left[\left\{ \{x_{k-1}^i, w_{k-1}^i\}_{i=1}^N, z_k \right\} \right]$$

✓ For $i=1, \dots, N$

■ Draw $x_k^i \sim q(x_k^i | x_{k-1}^i, z_k)$

■ Evaluate the importance weights $w_k^i = w_{k-1}^i \cdot \frac{p(z_k | x_k^i) \cdot p(x_k^i | x_{k-1}^i)}{q(x_k^i | x_{k-1}^i, z_k)}$

✓ End For

✓ Compute the total weight $t = \sum_{i=1}^N w_k^i$

✓ For $i=1, \dots, N$

■ Normalize $w_k^i \leftarrow \frac{w_k^i}{t}$

✓ End For

Table 6.1. A programming pseudo-code using filtering via the SIS.

6.1.3.4 Sequential importance resampling

The SIS Particle Filter has a problem, referred to as degeneracy problem, which means that, after a certain number of recursive filter steps, all but one samples will have negligible normalized weights. One strategy to overcome the degeneracy of samples in SIS is resampling, which will eliminate samples with low importance weights and multiply samples with high importance weights. The SIS filter combined with a resampling scheme is referred to as sampling importance resampling (SIR) filter, proposed by Gordon *et al.* (1993). The SIR filter is a very commonly used Particle Filter; it maps the N unequally weighted samples, $\{x_k^i, w_k^i\}_{i=1}^N$, into a new set of N equally weighted samples, $\{x_k^j, N^{-1}\}_{j=1}^N$.

The procedure of a SIR filter is the following:

1 Initiation: $\{x_0^i, w_0^i\}_{i=1}^N$

A set of initial random samples $\{x_0^i, w_0^i\}_{i=1}^N$ is drawn from the initial assumed density, $p(x_0)$.

- 2 Sequential importance sampling (SIS) procedure: $\left[\{x_{k-1}^i, w_{k-1}^i\}_{i=1}^N, z_k \right] \rightarrow \{x_k^i, w_k^i\}_{i=1}^N$

These samples are propagated through the existing nonlinear system model (also including the process noise). The weights of the samples are re-evaluated (or updated) according to the nonlinear measurement model (also including the measurement noise) once a measurement is available (shown in equation 6.30); then, the weights are normalized.

- 3 State estimation procedure

The state estimates can be computed using the samples associated with weights, as shown in equation (6.28)

- 4 Re-sampling (also called particle depletion)

The samples with small weights, as compared to the threshold, are eliminated. The remaining samples are re-sampled with weights to generate N independent and identically distributed (i.i.d.) random particles to approximate the state posterior density, $p(x_k | Z_k)$.

6.1.3.5 Choice of importance density

The performance of the SIR algorithm is dependent on the adopted importance density, and the choice of the importance density plays a significant role in the design of a Particle Filter, since the samples are directly drawn from the importance density and the importance weights are evaluated from the importance density. Different choices of the importance density exist, and the most popular one is the transition prior, $q(x_k^i | x_{k-1}^i, z_k) = p(x_k^i | x_{k-1}^i)$, since it is easier to draw samples, and easier to perform the subsequent importance weight computations, as shown in equation (6.31).

$$w_k^i = w_{k-1}^i \cdot p(z_k | x_k^i) \quad (6.31)$$

However, since the Particle Filter with transition prior as the importance density does not incorporate the most recent observations, its performance is not comparable with other Particle Filters incorporating the newest observations. For example, the SIR Particle Filters with the importance density generated from the EKF (see, for example, De Freitas *et al.*, 1998) and the UKF (see, for example, van der Merwe *et al.*, 2000) are shown to be better than the generic SIR Particle Filter with the importance density using the transition prior. In this dissertation, the PF with the EKF importance proposal distribution

(EKF+PF for short) was implemented. In the EKF+PF, the EKF allows the PF to incorporate the latest measurements into the a priori updating routine, and to generate the proposal distributions that match the actual posterior distribution more closely; it has the capability of generating heavier-tailed distributions, as compared to the generic PF (see, for example, van der Merwe *et al.*, 2000)

6.1.4 Computational aspects of the UKF, the PF and the EKF

Due to the underlying model differences and, consequently, the related significant implementation differences when using the UKF, the EKF+PF and the EKF, the computational loads of these approaches also vary significantly. The analytical solution (i.e., the corresponding linear error model) of the state-space model is required, using the first-order linearization approximation, for the implementation using the EKF. Currently, the psi-angle error model (Bar-Itzhack and Berman, 1988), shown in Chapter 2, is the most commonly used GPS/INS linear error model adopted for the implementation using the EKF. Once the linear error model is derived, it is only evaluated once to predict 1) the state estimates and the corresponding error covariance matrix in the time update step, and 2) the measurements and the corresponding error covariance in the measurement update step.

There is no need to derive such a linear error model for the implementation using the UKF. Instead, in the time update step, the predicted state estimates and the error covariance matrix of the state vector are computed from the transformed samples through the direct nonlinear system model. As a result of the introduction of the sigma points, there is a more accurate approximation of the prediction of the estimate and error covariance of the transformed states after the nonlinear function propagation. However, a heavier computation load is introduced due to multiple evaluations (equal to the number of sigma points) of the nonlinear function. The number of sigma points used to describe a nonlinear function in the UKF is a function of the number of unknown variables. For example, the number of sigma points in the time update procedure is $2 \cdot \dim(x) + 1$, where x is the state vector.

The computational load using a generic Particle Filter is significantly heavier than that using the UKF and the EKF, due to the involvement of a large number of particles. But the PF offers a better representation to the state posterior density. The hybrid Particle Filters, such as EKF+PF implemented here, require a relatively small number of particles, which may vary as a function of the IMU sensor quality. In comparison with the EKF, the ratio of the computational loads using the PF and the EKF is approximately equal to the number of the particles used. This ratio does not change too much with the variation of the dimension of the state vector, unlike using the UKF, where the computational load is almost a linear function of the state vector dimension.

Figure 6.1 shows an example of the computational loads using the UKF, the EKF+PF and the EKF as a function of the state dimension in the GPS/INS integration.

The computational time using the EKF with 9 states (i.e., three position components, three velocity components and three orientation angles) is scaled to 1.0 (i.e., treated as a reference), and the processing times using the EKF (with more than 9 states), the UKF and the EKF+PF are then compared to this reference time. In the UKF implementation used here for the testing of the computational loads, we assume an additive process and measurement noise, and the measurement model is adopted as linear (i.e., using GPS position components). Thus, the required computational time will be, in this case, less than the UKF implemented with non-additive process and measurement noises as well as a nonlinear measurement model. In the EKF+PF implementation, its computational load is a function of the number of particles, and the number of particles, $N = 25$, is used here as an example for the comparison of the computational loads. As shown in Figure 6.1, with the increase of the state dimension, the larger computational load of the UKF (in comparison to the EKF) is obvious, while the ratio of the required computational time of the EKF+PF vs. the EKF is relatively constant, namely approximately equal to the number of particles (N). However, the computational load in the UKF, the EKF and the EKF+PF may be reduced with a careful inspection of the nonlinear function in the filter implementation, as addressed in the next section.

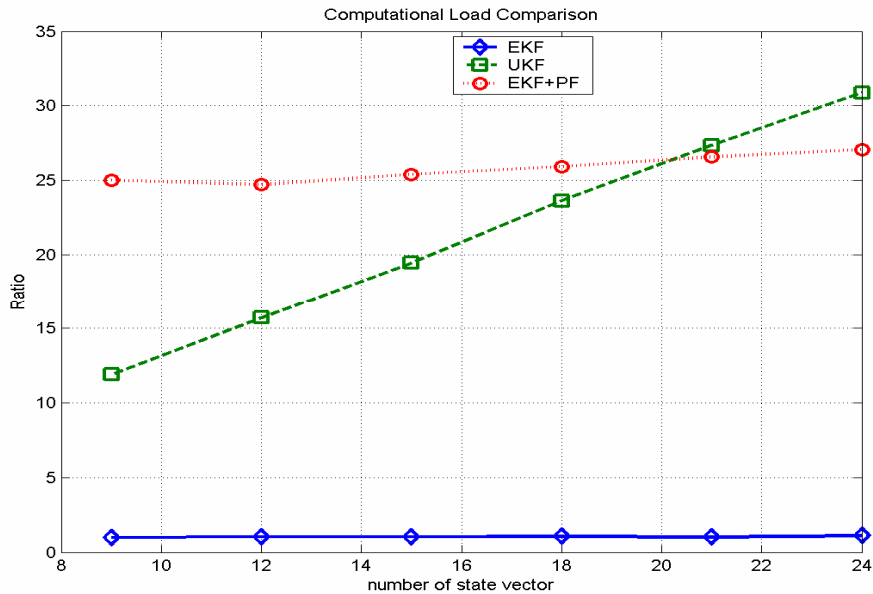


Figure 6.1. The comparison of the computational loads using the UKF, the EKF+PF and the PF, as a function of the state vector dimension; the computational time for reference EKF with 9 states is assumed a unity; the vertical axis shows the ratio of the processing time with respect to the reference EKF processing time.

6.1.5 Computational optimization for the UKF, the PF and the EKF

As discussed in the previous section, the computational loads of the UKF and the EKF+PF will be more significant than that of the EKF. Thus, the practical applications of the alternative nonlinear filters have been limited due to the extra computational load, as compared to that of the EKF. Now when the computers become more and more powerful, the argument about the extra computational loads becomes less significant. Nevertheless, any possible computational optimization will still be helpful. In order to reduce the extra computational loads introduced by the multiple evaluations of samples (i.e., deterministically selected sigma points for the UKF and the random selected particles for the PF) of the state vector through the nonlinear system and measurement models, a close examination of the system and measurement models of the GPS/INS integration should be performed.

The system model includes nine navigation differential equations and the error modeling for the inertial sensor errors (such as the accelerometer and gyroscope biases and drifts, etc.) and the environmental parameters (such as the lever arm offsets, tropospheric and ionospheric delay residuals). The error models for the state vector other than the nine navigation parameters (i.e., position, velocity and orientation) are normally linear, leaving the nine nonlinear differential equations, whose nonlinearities are functions of system dynamics (for example, the velocity, shape and direction of the trajectory, etc.). Thus, an implementation can be carried out to reduce the computational load of the adopted nonlinear filtering techniques (i.e., EKF, UKF and PF) in the GPS/INS integration. The basic idea is to group the whole state vector into several state sub-vectors according to the nonlinearities of each sub-vector. Then, the UKF or the PF are applied only to the sub-vector with strongest nonlinearity, while the linearized EKF is adopted for the other state sub-vectors with weak nonlinearities. According to the above analysis, the strongest nonlinearity in the GPS/INS integration lies in the system model of the navigation parameters, as show in equations (2.25 and 2.26).

In the loosely-coupled GPS/INS integration, the measurements are the direct positions and velocities from GPS (and the orientation, if multiple GPS antenna are used), thus, the measurement model is linear. In the tightly-coupled GPS/INS integration, the measurements are the code and carrier-phase pseudo-ranges, which indicates that the measurement model is nonlinear; however, the nonlinearity of such a measurement model is not very strong. Therefore, there is no significant advantage in the measurement models of both loosely-coupled and tightly-coupled GPS/INS integrations for the UKF and the PF, as compared to the EKF approach. Thus, the evaluation of the measurement model in both the UKF and the PF implementations can be based on the same linearized measurement model as that of the EKF, which reduces the extra computational load.

The state vector, x , can be grouped into two state sub-vectors, x_1 and x_2 (i.e., $x = \begin{bmatrix} x_1^T & x_2^T \end{bmatrix}^T$), and the corresponding process noise vector, v , is also grouped into two

process noise sub-vectors, v_1 and v_2 (see, equation (6.33)). The two process noise sub-vectors, v_1 and v_2 , are assumed to be un-correlated. For the linear dynamic model, shown in equation (6.32), the transition matrix Φ (equation (6.34)) is an upper-triangular matrix, and the propagation of the components of the error covariance matrix, P (equation (6.35)), from $k-1$ to k is shown in equations (6.36-6.42). In such implementation, the UKF or the PF will only apply to the state sub-vector, x_1 , which means that only $\Phi_{1,1}P_{k-1,1,1}\Phi_{1,1}^T$ in equation (6.38) and $x_{k,1}$ are computed from the samples of the state sub-vector, x_1 , and the other error covariance matrix components and state sub-vector, $x_{k,2}$, are computed from a linearized error model. As shown in Chapter 2, in the GPS/INS integration, the possible state sub-vectors of the state vector x can be the navigation parameters (x_{nav}), the accelerometer errors (x_{acc}), the gyroscope errors (x_{gyro}), the gravity disturbance (x_{grav}), the antenna offset between GPS antenna with respect to the IMU body center (x_{ant}) and the environmental parameters (for example, tropospheric and/or ionospheric errors) (x_{gps}). The state vector, x , can be the augmented form of the above state sub-vectors (i.e., $x=[x_1 \ x_2 \ x_3 \ x_4 \ x_5 \ x_6]^T=[x_{nav} \ x_{acc} \ x_{gyro} \ x_{grav} \ x_{ant} \ x_{gps}]^T$). The transition matrix follows the pattern shown in equation (6.43); then the propagation of the error covariance matrix components is shown in equations (6.44-6.47), except for the component $\Phi_{1,1}P_{k-1,1,1}\Phi_{1,1}^T$ of the navigation parameters (position, velocity and orientation), which is evaluated based on samples of the sub-vector x_1 , as explained earlier. In such a way, the maximum number of evaluations of the nonlinear system function using the UKF is 19 ($=2 \times 9 + 1$) and will not change as the state dimension changes. Due to taking into consideration the special pattern of the transition matrix in equation (6.43), the computational load of the EKF is also reduced; and thus, for the EKF+PF it is also reduced, while the UKF and the EKF+PF still require more computational load than the EKF.

$$x_k = \Phi_{k,k-1}x_{k-1} + \Gamma_k v_k, \quad x_{k-1} - \hat{x}_{k-1} \sim (0, P_{k-1}), \quad v_k \sim (0, Q_k) \quad (6.32)$$

$$x = \begin{bmatrix} x_1^T & x_2^T \end{bmatrix}^T, \quad v = \begin{bmatrix} v_1^T & v_2^T \end{bmatrix}^T \quad (6.33)$$

$$\Phi_{k,k-1} = \begin{bmatrix} \Phi_{1,1} & \Phi_{1,2} \\ 0 & \Phi_{2,2} \end{bmatrix}, \quad \Gamma_k = \begin{bmatrix} \Gamma_{1,1} & 0 \\ 0 & \Gamma_{2,2} \end{bmatrix} \quad (6.34)$$

$$P_{k-1} = \begin{bmatrix} P_{k-1,1,1} & P_{k-1,1,2} \\ P_{k-1,2,1} & P_{k-1,2,2} \end{bmatrix}, \quad Q_k = \begin{bmatrix} Q_{1,1} & 0 \\ 0 & Q_{2,2} \end{bmatrix} \quad (6.35)$$

$$P_k = \Phi_{k,k-1} P_{k-1} \Phi_{k,k-1}^T + \Gamma_k Q_k \Gamma_k^T \quad (6.36)$$

$$\Phi_{k,k-1} P_{k-1} \Phi_{k,k-1}^T = \begin{bmatrix} \Phi_{1,1} & \Phi_{1,2} \\ 0 & \Phi_{2,2} \end{bmatrix} \begin{bmatrix} P_{k-1,1,1} & P_{k-1,1,2} \\ P_{k-1,2,1} & P_{k-1,2,2} \end{bmatrix} \begin{bmatrix} \Phi_{1,1}^T & 0 \\ \Phi_{1,2}^T & \Phi_{2,2}^T \end{bmatrix} \quad (6.37)$$

$$\Gamma_k Q_k \Gamma_k^T = \begin{bmatrix} \Gamma_{1,1} & 0 \\ 0 & \Gamma_{2,2} \end{bmatrix} \begin{bmatrix} Q_{1,1} & 0 \\ 0 & Q_{2,2} \end{bmatrix} \begin{bmatrix} \Gamma_{1,1}^T & 0 \\ 0 & \Gamma_{2,2}^T \end{bmatrix} = \Gamma_{1,1} Q_{1,1} \Gamma_{1,1}^T + \Gamma_{2,2} Q_{2,2} \Gamma_{2,2}^T \quad (6.38)$$

$$P_{k,1,1} = \Phi_{1,1} P_{k-1,1,1} \Phi_{1,1}^T + \Phi_{1,2} P_{k-1,2,1} \Phi_{1,1}^T + \Phi_{1,1} P_{k-1,1,2} \Phi_{1,2}^T + \Phi_{1,2} P_{k-1,2,2} \Phi_{1,2}^T + \Gamma_{1,1} Q_{1,1} \Gamma_{1,1}^T \quad (6.39)$$

$$P_{k,1,2} = \Phi_{1,1} P_{k-1,1,2} \Phi_{2,2}^T + \Phi_{1,2} P_{k-1,2,2} \Phi_{2,2}^T \quad (6.40)$$

$$P_{k,2,1} = \Phi_{2,2} P_{k-1,2,1} \Phi_{1,1}^T + \Phi_{2,2} P_{k-1,2,2} \Phi_{1,2}^T \quad (6.41)$$

$$P_{k,2,2} = \Phi_{2,2} P_{k-1,2,2} \Phi_{2,2}^T + \Gamma_{2,2} Q_{2,2} \Gamma_{2,2}^T \quad (6.42)$$

$$\Phi = \begin{bmatrix} \Phi_{11} & \Phi_{12} & \Phi_{13} & 0 & 0 & 0 \\ 0 & \Phi_{22} & 0 & 0 & 0 & 0 \\ 0 & 0 & \Phi_{33} & 0 & 0 & 0 \\ 0 & 0 & 0 & \Phi_{44} & 0 & 0 \\ 0 & 0 & 0 & 0 & \Phi_{55} & 0 \\ 0 & 0 & 0 & 0 & 0 & \Phi_{66} \end{bmatrix} \quad (6.43)$$

$$\begin{aligned} P_{k,1,1} &= \Phi_{1,1} P_{k-1,1,1} \Phi_{1,1}^T \\ &+ \Phi_{1,2} P_{k-1,2,1} \Phi_{1,1}^T + \Phi_{1,3} P_{k-1,3,1} \Phi_{1,1}^T \\ &+ \Phi_{1,1} P_{k-1,1,2} \Phi_{1,2}^T + \Phi_{1,1} P_{k-1,1,3} \Phi_{1,3}^T \\ &+ \Phi_{1,2} P_{k-1,2,2} \Phi_{1,2}^T + \Phi_{1,3} P_{k-1,3,2} \Phi_{1,2}^T + \Phi_{1,2} P_{k-1,2,3} \Phi_{1,3}^T + \Phi_{1,3} P_{k-1,3,3} \Phi_{1,3}^T \\ &+ \Gamma_{1,1} Q_{1,1} \Gamma_{1,1}^T \end{aligned} \quad (6.44)$$

$$P_{k,1,2} = \text{Diag} \left(\begin{bmatrix} \Phi_{1,1} P_{k-1,1,2} \Phi_{2,2}^T \\ \Phi_{1,1} P_{k-1,1,3} \Phi_{3,3}^T \\ \Phi_{1,1} P_{k-1,1,4} \Phi_{4,4}^T \\ \Phi_{1,1} P_{k-1,1,5} \Phi_{5,5}^T \\ \Phi_{1,1} P_{k-1,1,6} \Phi_{6,6}^T \end{bmatrix} \right) + \text{Diag} \left(\begin{bmatrix} \Phi_{1,2} P_{k-1,2,2} \Phi_{2,2}^T + \Phi_{1,3} P_{k-1,3,2} \Phi_{2,2}^T \\ \Phi_{1,2} P_{k-1,2,3} \Phi_{3,3}^T + \Phi_{1,3} P_{k-1,3,3} \Phi_{3,3}^T \\ \Phi_{1,2} P_{k-1,2,4} \Phi_{4,4}^T + \Phi_{1,3} P_{k-1,3,4} \Phi_{4,4}^T \\ \Phi_{1,2} P_{k-1,2,5} \Phi_{5,5}^T + \Phi_{1,3} P_{k-1,3,5} \Phi_{5,5}^T \\ \Phi_{1,2} P_{k-1,2,6} \Phi_{6,6}^T + \Phi_{1,3} P_{k-1,3,6} \Phi_{6,6}^T \end{bmatrix} \right) \quad (6.45)$$

$$P_{k,2,1} = P_{k,1,2}^T \quad (6.46)$$

$$P_{k,2,2} = \text{Diag} \left(\begin{array}{c} \Phi_{2,2} P_{k-1,2,2} \Phi_{2,2}^T + \Gamma_{2,2} Q_{2,2} \Gamma_{2,2}^T \\ \Phi_{3,3} P_{k-1,3,3} \Phi_{3,3}^T + \Gamma_{3,3} Q_{3,3} \Gamma_{3,3}^T \\ \Phi_{4,4} P_{k-1,4,4} \Phi_{4,4}^T + \Gamma_{4,4} Q_{4,4} \Gamma_{4,4}^T \\ \Phi_{5,5} P_{k-1,5,5} \Phi_{5,5}^T + \Gamma_{5,5} Q_{5,5} \Gamma_{5,5}^T \\ \Phi_{6,6} P_{k-1,6,6} \Phi_{6,6}^T + \Gamma_{6,6} Q_{6,6} \Gamma_{6,6}^T \end{array} \right) \quad (6.47)$$

6.2 Navigation performance analysis

6.2.1 Previously reported performance analysis

The preliminary navigation performance analysis of the UKF and PF, in comparison to that of the EKF, was reported in (Yi and Grejner-Brzezinska, 2005; Yi and Grejner-Brzezinska, 2006a & 2006b) based on three different kinematic datasets, under various dynamics using both the loosely-coupled and the tightly-coupled integrated modes for a high-end inertial sensor, H764G, and a low-cost MEMS inertial sensor, IMU400CC. These preliminary results indicate that small differences can be found between the free navigation mode solutions using the UKF and EKF for H764G, and the solution using the UKF is slightly better than the EKF solution; the improvements in the position components are more obvious with the increase of the GPS gap duration. The high consistency of the solutions using the UKF and the EKF for H764G, when GPS is available, or during short GPS gaps may be contributed to the high sampling rate of H764G, which indicates weak nonlinearity of the system model in the time scale of the update intervals, and to slow drifts of H764G. In contrast to the high-end H764G, more significant differences were found in the low-cost MEMS IMU400CC. When GPS is available, the differences between the solutions using the UKF and the EKF can reach dm-level in position, 1-2° in pitch and roll and around 10° in heading. Even more significant differences between the solutions using the UKF and the EKF were found during GPS gaps. This is mainly caused by the large inertial sensor noise level. Due to the high-tolerance to large initial errors using the UKF, the orientation converges faster by 10-15% when using the UKF instead of the EKF.

With a small number of particles is used ($N=25$ in the previous publications), the position differences of the GPS/INS solutions using the EKF+PF and the EKF are at the cm-level for both H764G and IMU400CC. The free inertial navigation performance using the EKF+PF is slightly better than using the UKF and the EKF for H764G. Around 6-cm (corresponding to 3%) improvement in the 3-dimensional position drifts of the solution using the EKF+PF was identified for the high-end sensor after a simulated 60-second GPS gap, in comparison with the drifts of the solutions using the UKF or the EKF.

During the GPS blockage, after the filter convergence was reached, an 8-arcsec (corresponding to 80%) orientation drift improvement in heading component could be found in the solutions using the EKF+PF vs. the EKF after a 120-second GPS gap, while no significant orientation drift differences can be found between the solutions using the UKF and the EKF for H764G. However, the solution using the EKF+PF behaves worse than the solutions using the UKF and the EKF for IMU400CC, which may indicate that the number of particles used in the EKF+PF was insufficient for IMU400CC.

Overall, no significant differences were found in the position and orientation solutions obtained on the EKF, the UKF and the EKF+PF for the high-end inertial sensor, H764G, even though some differences do exist amongst the solutions. Therefore, the following analysis is focused on the performance comparison using different filters for the low-cost MEMS inertial sensor, IMU400CC.

6.2.2 Performance analysis for the low-cost MEMS IMU400CC

In the following navigation performance analysis of the UKF and the EKF+PF (referred to as the EPF), as compared to the EKF, the same dataset, as used in Yi and Grejner-Brzezinska (2006b) is used. The loosely-coupled integrated mode of the EKF, the UKF, the EPF implementations is used here, with nine navigation states (three positions, three velocities and three orientations) and up to 15 sensor errors and system parameters (three accelerometer biases, three gyro biases, three accelerometer scale factor errors, three gyro scale factor errors and three lever arm offsets). Two inertial sensors, H764G and IMU400CC, are used, where GPS/H764G provides the orientation reference for IMU400CC performance. The initial error covariance of the inertial sensor errors is based on the corresponding customized error model derived in Chapter 4 and listed in Table 6.2 together with other information for the state and noise vectors. The GPS position solution, derived by the single-epoch GPS RTK (here, post-processed) positioning technique described in Chapter 3, was used as the measurement update to the loosely-coupled GPS/INS integration implemented using the EKF, the UKF and the EPF. The lever arm offsets between the IMU body center of H764G and IMU400CC with respect to the GPS antenna phase center were estimated iteratively using the EKF-based GPS/INS integration until the convergence was reached; they were treated as fixed and removed from the navigation estimation procedure in the tested filters. The focus of the analysis presented here is on the navigation performance of the low-cost MEMS IMU400CC as a function of trajectory dynamics and filter type (i.e., the EKF, the UKF and the EPF). The previous results indicated that 25 particles may not be enough to properly handle this low-cost MEMS inertial sensor; thus, the following results are based on a 50-particle PF. The resulting position components are compared to the actual GPS positions, and the resulting orientation components (mainly the vertical component, i.e., heading or yaw) are compared to the EKF-based GPS/INS orientation solutions from H764G that was collocated with the MEMS sensor. In the data processing for

IMU400CC, all the initial conditions, GPS and inertial measurements are identical for all three filters.

	No.	Sigma (δ)		Noise (q)	
		H764G	IMU400CC	H764G	IMU400CC
Position (XYZ)	3	± 1.0 m	± 1.0 m	–	
Velocity (NED)	3	± 0.01 m/s	± 0.01 m/s	–	
Orientation (RP)	3	$\pm 0.015^\circ$	2.0°	–	
Orientation (Y)		$\pm 0.045^\circ$	6.0°		
Accelerometer biases	3	$3.28\mu\text{g}$	8.5mg	$16.0\mu\text{g}/\text{Hz}^{1/2}$	
Gyroscope biases	3	$0.0035^\circ/\text{h}$	$1^\circ/\text{sec}$	$0.008^\circ/\text{h}^{1/2}$	
Accelerometer scale factor	3	100ppm	0.01	–	
Gyroscope scale factor	3	5ppm	0.01	–	
Accelerometer measurement noise	3	–	–	–	0.0007468 $\text{m}/\text{s}^{1/2}$
Gyroscope measurement noise	3	–	–	–	0.0004379 $\text{rad}/\text{s}^{1/2}$
Lever arm	3	0.1 m	0.1 m		

Table 6.2. State, noise and system parameter vector information for H764G and IMU400CC.

Figure 6.2 shows the trajectories of the EKF-based GPS/INS integrated position solutions from H764G and IMU400CC. The number with an arrow in Figure 6.2 denotes the epoch index at the corresponding location of the ground trajectory. There is a 49-second GPS gap after 144-second calibration (75-second static alignment and 69-second kinematic alignment). After the 49-second GPS gap, about 414 m and 0.5 m 3-dimensional position errors can be found for IMU400CC and H764G, respectively, as compared to the reference GPS solution available at epoch 194 after the GPS signal was reacquired. The segments marked with red in Figure 6.2 indicate that no actual GPS solutions exist at these periods due to the loss of GPS lock or a failure of the carrier-phase double-difference ambiguity resolution.

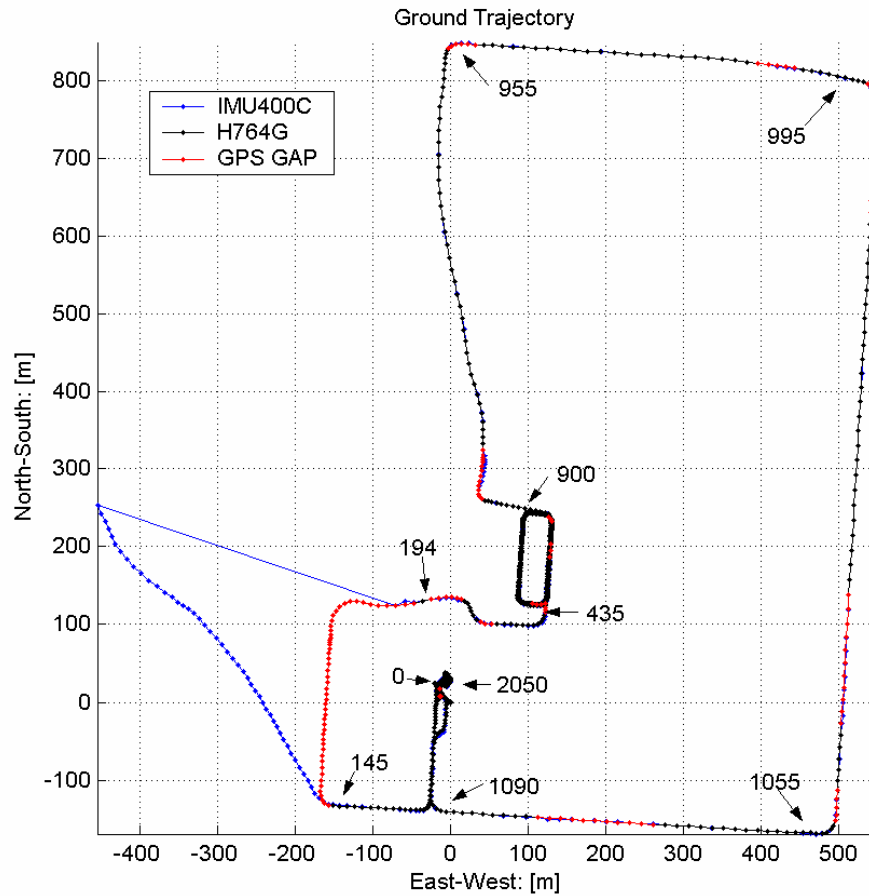


Figure 6.2. Trajectory of the kinematic experiment on July 20, 2005 (the number with an arrow indicate the epoch index at the corresponding location).

6.2.2.1 Orientation performance using the EKF, the UKF and the EPF

Figure 6.3 illustrates the heading variations of this experiment from the EKF-based GPS/INS solutions of H764G and IMU400CC. The average error in the heading component from IMU400CC is 8.0° and the corresponding standard deviation is $\pm 13^\circ$, as compared to that from H764G. As can be seen in Figure 6.3, as compared to the reference, the IMU400CC heading error is a function of vehicle dynamics, shape and direction of the trajectory. According to these components, the entire experiment can be separated into eight segments. Segments 1, 3, 6, and 8 were the stationary periods, and the heading component in all these periods drifts visibly, where, as shown next, the drift rate of the heading error during stationary periods is better controlled with longer prior kinematic calibration prior to the stationary period. Segment 2 starts in the south direction, then turns west, then north, and ends going east according to Figures 6.2 and 6.3; large

heading errors can be found in this segment. Segment 4 was a maneuvering stage including several (around 10) small loops at the parking lot of the OSU west campus. For this segment, the heading component from the low-cost MEMS IMU matched the high-end H764G heading reference at degree-level accuracy.

The trajectory of segment 5 was a loop around the OSU west campus, starting in the north direction, then going east, south, and finally west, and ended at the OSU CFM parking lot. Due to the kinematic calibration of segment 4, the heading component still matched the reference heading during segment 5 with the accuracy of around 1.0° . Segment 7 was also a maneuvering period with irregular trajectory (the trajectory is shown in Figure 6.6, insert). Starting with already drifted heading from the static segment 6, the heading error during segment 7 gradually becomes smaller due to more epochs of kinematic calibration using precise GPS positions; still, these errors are relatively significant.

Overall, the performance in the heading component of the MEMS inertial sensor is of very low quality, especially in the stationary mode when heading drifts rapidly. Despite the limited heading performance of IMU400C, the following analysis will demonstrate how the implemented filter types affect the heading accuracy during various trajectory dynamics shown in Figure 6.3.

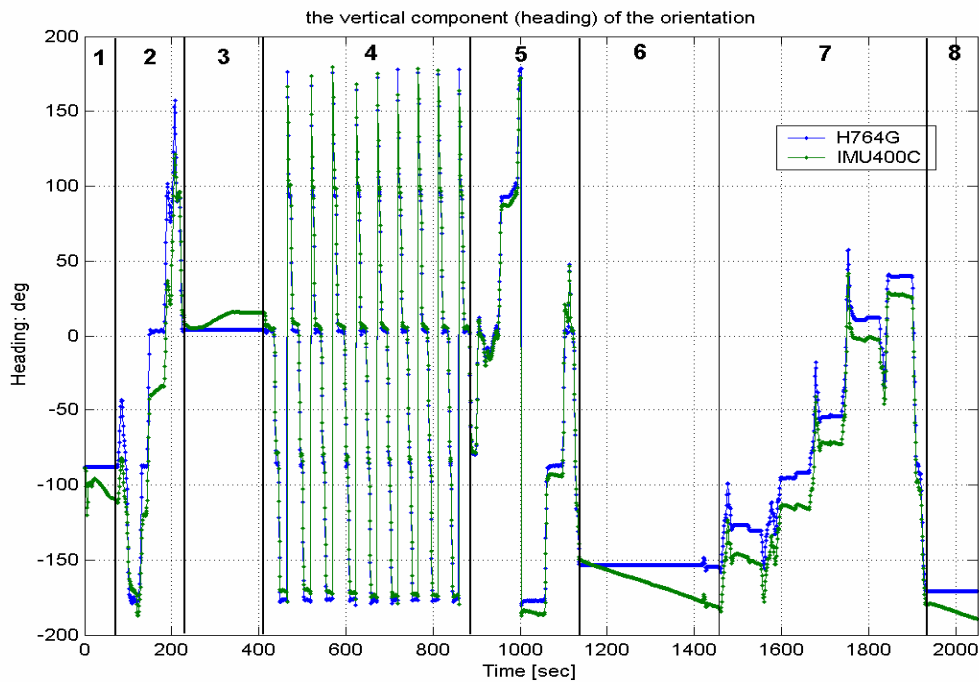


Figure 6.3. Heading variation of the kinematic experiment on July 20, 2005, EKF solution.

In this experiment, the first 75 seconds (segment 1) are stationary (see Figure 6.4) and the next 69 seconds are in motion, followed by a 49-second GPS gap. During the first two periods, the IMU400CC is calibrated continuously using the carrier-phase fixed GPS position (cm-level position accuracy). Figure 6.4 shows the GPS/INS integrated heading solution (up to 194 epochs) from IMU400CC using the EKF, the UKF and the EPF, and the reference heading solution from H764G. The heading component of MEMS inertial sensor drifts very fast for all three filters in the stationary period even with accurate GPS position measurement update; around $0.2\text{--}0.4^\circ/\text{s}$ heading drift rate for the stationary period can be found for all tested filters, according to Figure 6.4, as compared to $1.0^\circ/\text{s}$ according to the manufacturer's specification, shown in Chapter 2. The poor heading performance of IMU400CC should be the results of the high measurement noise of the gyroscopic measurements. Even though heading drifts very fast for all three filters in the stationary period, the heading drift rate using the EPF is the slowest one (around $0.23^\circ/\text{s}$) and that of the UKF is the fastest one (around $0.36^\circ/\text{s}$). The heading drift rate during a static period will be better controlled after longer calibration, which will be shown next.

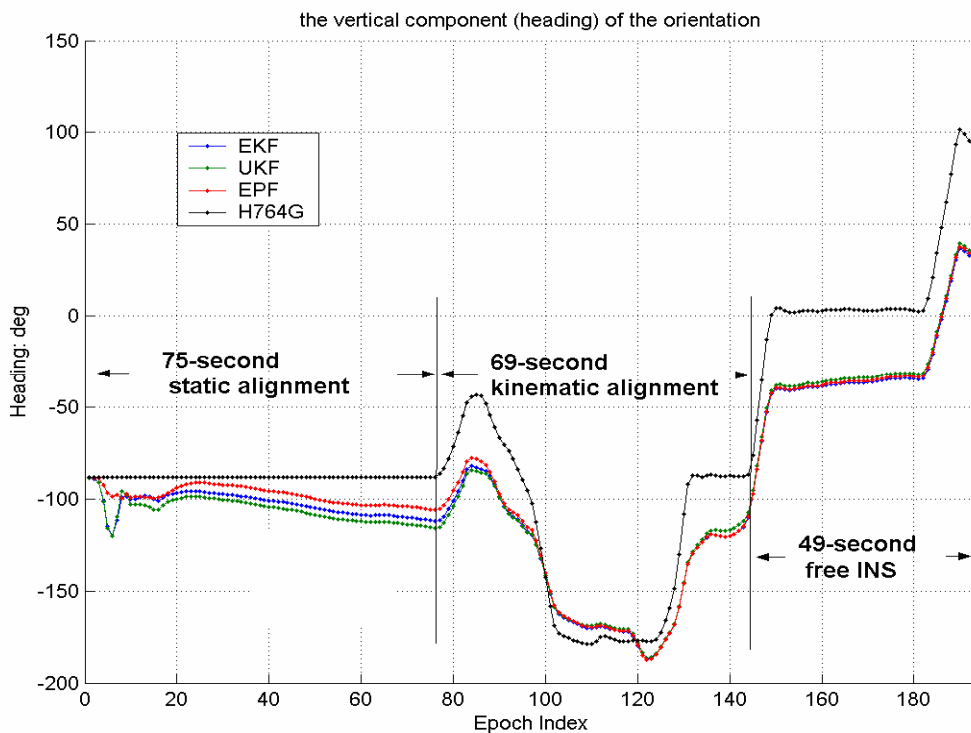


Figure 6.4. The heading solutions from IMU400CC using the EKF, the UKF and the EPF, and from H764G using the EKF during the first 194 seconds, including a 75-second static alignment, a 69-second kinematic alignment and a 49-second free inertial navigation mode due to the loss of GPS lock.

Table 6.3 lists the detailed statistics of the orientation errors from IMU400CC using the EKF, the UKF and the EPF, as compared to the reference from H764G during the analyzed 194-second period. In the first 75 seconds of this period, the heading solution using the EPF outperforms these from the EKF and the UKF in terms of the mean, the standard deviation and the maximum of the differences with respect to the reference solution, and the EKF heading solution is better than the UKF heading solution. In the kinematic alignment period (next 69 seconds), the EPF is still the best in terms of the mean and the standard deviation of the heading errors, while the maximum of the absolute heading errors using the UKF is the smallest (around -15.76°). In the static and kinematic alignment periods (from epoch 1 to 145), no significant differences can be found in the roll and pitch solutions, as compared to the reference from H764G. However, after the 145-second static and kinematic alignment, the orientation components in roll, pitch and heading using the UKF is better than these using the EKF and the EPF in the free navigation mode (from epoch 146 to 194). The heading component from the EPF is still better than that using the EKF in terms of the mean, the standard derivation and the maximum of the heading errors, as compared to the reference. The absolute heading error, defined as the absolute value of the difference between each solution obtained from alternative filter and the reference solution, is similar for all filters tested. For example, the relative improvement of the EPF, as compared to the EKF in the actual heading errors during the kinematic alignment of the second period, shown in Figure 6.4, is only around 8%. The relative improvement of the UKF, as compared to the EKF, in the actual heading errors during the free inertial navigation period is only around 6%. During the first static period, the relative improvement of the EPF, as compared to the EKF, in the actual heading errors is better, reaching around 33%.

The actual heading errors shown in Figure 6.4 and in Table 6.3, indicate that none of the three filters is able to provide sufficient calibration to bound the heading (the weakest orientation component) errors for the 75-second static calibration and the 69-second kinematic calibration. The kinematic alignment under longer maneuvering conditions can provide better calibration to control the orientation errors, as shown next. In Table 6.3 (and the following tables), a special attention should be paid to the values marked in red, which indicate the improvements found.

		EKF	UKF	EPF	EKF	UKF	EPF	EKF	UKF	EPF
Mean	R [°]	-0.64	-0.62	-0.64	-0.54	-0.55	-0.55	-1.56	-1.53	-1.61
	P [°]	1.13	1.10	1.09	0.88	0.86	0.86	0.73	0.64	0.72
	H [°]	-14.50	-17.57	-9.61	-17.19	-16.91	-15.76	-43.17	-40.67	-42.33
Std	R [°]	0.24	0.23	0.23	0.79	0.78	0.80	1.00	0.98	1.02
	P [°]	0.16	0.18	0.21	0.71	0.74	0.71	0.78	0.76	0.80
	H [°]	6.13	6.52	4.75	17.78	18.22	17.24	9.04	8.92	8.88
Max	R [°]	1.45	1.51	1.19	1.96	2.01	1.98	3.19	3.12	3.27
	P [°]	1.51	1.50	1.50	2.79	2.86	2.77	2.35	2.23	2.36
	H [°]	31.72	32.05	17.45	43.03	42.09	43.03	64.94	62.06	63.72
		static alignment (epochs: 1–75)			kinematic alignment (epochs: 76–145)			free inertial navigation (epochs: 146–193)		

Table 6.3. The statistics of the orientation errors from IMU400CC using the EKF, the UKF and the EPF, as compared to the reference EKF-based GPS/INS solution from H764G during periods of the first static alignment (epoch from 1 to 75), kinematic alignment (epoch from 76 to 145) and a free inertial navigation mode due to the loss of GPS lock.

Two maneuvering periods were included in this experimental dataset. Maneuver 1 starts at epoch 435 and ends at epoch 900, and includes a total of 10 loops at the OSU west campus parking lot. The second maneuvering period ranges from epoch 1415 to epoch 1920. Figure 6.5 shows the heading solutions using different filtering techniques, as compared to the reference solution for the first maneuvering period. Table 6.4 presents the detailed orientation errors, as compared to the reference for both maneuvering periods. A closer inspection of Figure 6.5 and Table 6.4 indicates that the heading solution using the UKF is much better than these from the EKF and the EPF in terms of the mean heading errors (-1.0° for the UKF and around -4.1° for the EKF and the EPF). The average roll and pitch errors using the UKF are also smaller than these using the EKF and the EPF. The relative improvement of the UKF, as compared to the EKF, in the actual heading errors during the first maneuvering period can reach around 75%. The relative improvement of the UKF, as compared to the EKF, in the actual roll and pitch errors during the first maneuvering period is around 52% and 14%, respectively. No obvious orientation differences can be found between the EKF and the EPF during the first maneuvering period.

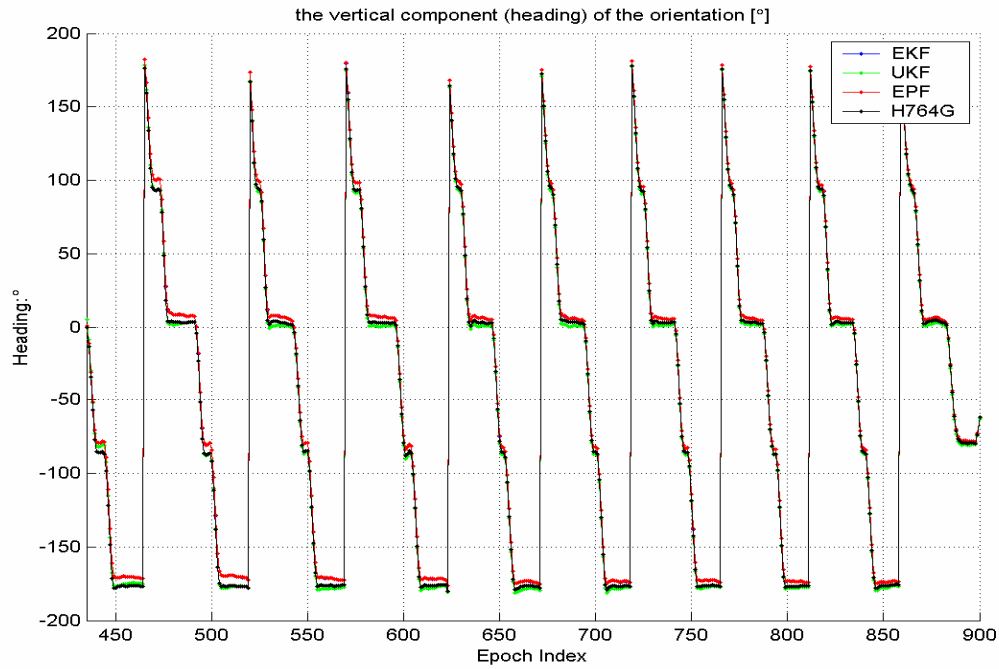


Figure 6.5. The heading solutions from IMU400CC using the EKF, the UKF and the EPF, and the reference heading from H764G using the EKF during the maneuver 1.

		Maneuver No.1 (epochs: 435–900) Re: Figure 6.5			Maneuver No.2 (epochs: 1415–1920) Re: Figure 6.6		
		EKF	UKF	EPF	EKF	UKF	EPF
Mean	R [°]	-0.73	-0.35	-0.73	0.72	0.82	0.72
	P [°]	0.56	0.48	0.56	0.60	0.73	0.59
	H [°]	4.12	-1.01	4.16	-18.64	-8.73	-18.95
Std	R [°]	0.30	0.42	0.30	0.41	0.36	0.41
	P [°]	0.43	0.43	0.43	0.43	0.39	0.43
	H [°]	1.81	1.39	1.83	4.72	2.91	4.77
Max	R [°]	2.03	2.16	2.02	1.50	1.57	1.49
	P [°]	1.85	1.73	1.85	1.63	1.71	1.62
	H [°]	11.20	6.25	11.28	27.19	15.11	27.61

Table 6.4. The statistics of the orientation errors from IMU400CC using the EKF, the UKF and the EPF, as compared to the reference EKF-based GPS/INS solution from H764G during two maneuvering periods from epochs 435 to 900 and from epochs 1415 to 1920.

Figure 6.6 (insert) illustrates the trajectory of the second maneuvering period and the heading solutions using the EKF, the UKF and the EPF together with the reference heading during this period. Figure 6.6 also shows the comparison of the heading solutions for a stationary segment. A drift rate of $0.10^{\circ}/s$, $0.06^{\circ}/s$ and $0.10^{\circ}/s$ for heading solutions for the EKF, the UKF and the EPF, respectively, can be found, even after 1136 epochs of static and kinematic alignments with high accuracy GPS position measurement update. Such drift rate during the static period is better controlled if longer prior kinematic calibration is used, as compared to the $0.3^{\circ}/s$ drift rate at the beginning of the experimental trajectory with short calibration time, shown earlier. In the second maneuvering period, the heading solution using the UKF is still better than these using the EKF and the EPF in terms of the mean and standard deviation of the errors, as compared to the reference, while the EKF and the EPF behave a little better than the UKF in the roll and the pitch components. The EKF and the EPF behave very similarly in all three orientation components.

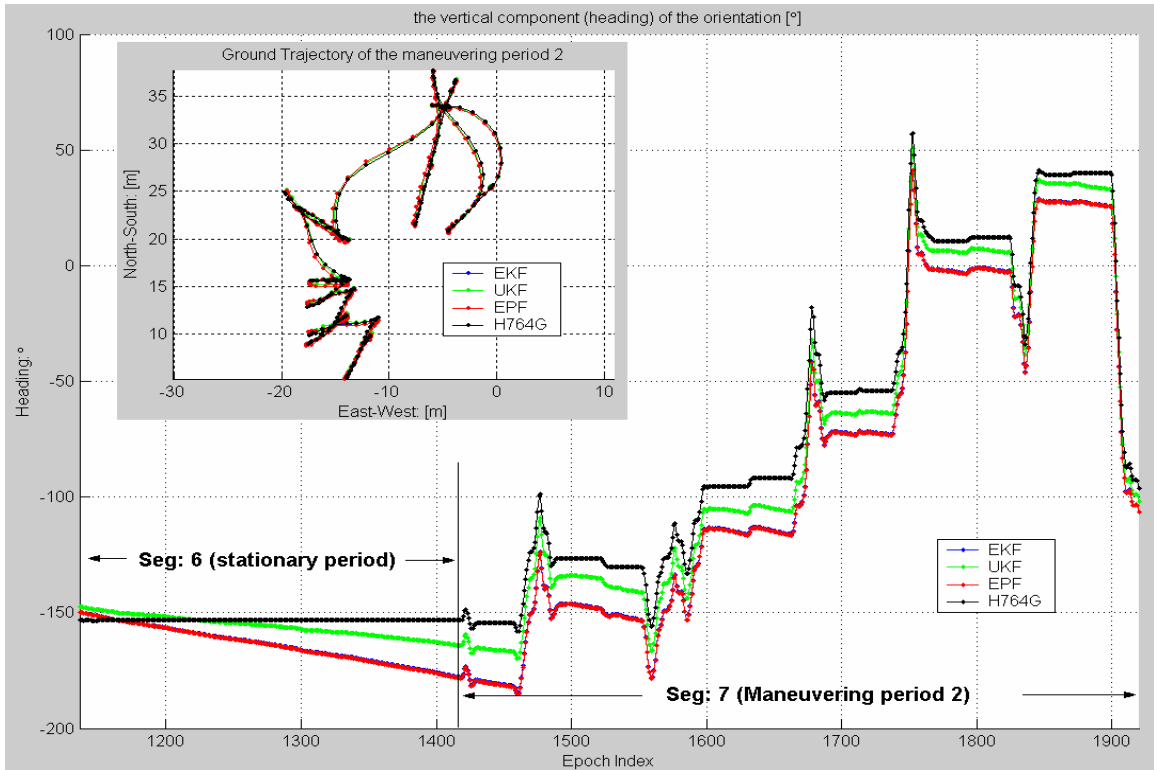


Figure 6.6. The heading solutions for IMU400CC using the EKF, the UKF and the EPF, as compared to the reference heading solution from H764G during a stationary period (epochs 1136 to 1414) and the second maneuvering period (epoch 1415 to 1920); the upper-left subplot illustrates the corresponding ground trajectory of the second maneuvering period.

After the first maneuvering period (Segment 4, in Figure 6.3) and before the second maneuvering period (Segment 7), there is a 190-second trajectory (refer to Figure 6.2 and Figure 6.3) segment 5, where the vehicle first went north (from epoch 900 to 955), then went east (from epoch 955 to 995), then went south (from epoch 995 to 1055), then went west (from 1055 to 1090). Table 6.5 lists the statistics of the orientation errors using the EKF, the UKF and the EPF, as compared to the reference during the aforementioned portions of the trajectory. The orientation solution in the roll, pitch and heading components from the UKF behaves better than these from the EKF and the EPF, and the EPF behaves very similarly to the EKF. Around 87%, 22% and 90% of relative improvement can be found in the actual errors of the roll, pitch and heading components, respectively, using the UKF, as compared to these of the EKF during the period of going north, and better than 0.5° orientation errors (in absolute term) for all three components can be achieved in such scenario (the actual errors are -0.07° , 0.39° and -0.28° in the roll, pitch and heading components for the UKF, as compared to the reference orientation solutions from H764G). This good orientation accuracy for the low-cost MEMS IMU can be attributed to the 465-second maneuvering period (i.e., Segment 4) with loops just before the straight portion going north. Similar relative improvements in the roll, pitch and heading components can be found in the other parts of the trajectory (i.e., going east, south and west); refer to Table 6.5 for the actual errors and relative improvements for the UKF, as compared to the EKF. It should be noted that the kinematic calibration along these straight trajectories cannot bound the heading error drifts, even with the precise cm-level GPS position measurement updates. The actual average heading error drifted from -0.28° during the “going north” trajectory, to 0.97° during the “going east” trajectory, to 1.51° during the “going south” segment, and ended with 1.65° during the “going west” segment. But these drifts are obviously smaller when the vehicle is moving as compared to those when the vehicle is stationary, as shown earlier.

		Going North (epochs: 900–955)			Going East (epochs: 955–995)		
		EKF	UKF	EPF	EKF	UKF	EPF
Mean	R [°]	-0.53	-0.07	-0.54	-0.46	-0.08	-0.47
	P [°]	0.50	0.39	0.50	0.53	0.37	0.53
	H [°]	-2.92	-0.28	-3.02	-5.92	0.97	-6.09
Std	R [°]	0.33	0.21	0.34	0.37	0.19	0.38
	P [°]	0.46	0.40	0.46	0.32	0.19	0.32
	H [°]	1.28	0.58	1.31	0.36	0.47	0.37
Max	R [°]	1.09	0.51	1.11	1.04	0.58	1.06
	P [°]	1.22	1.18	1.23	1.28	0.70	1.30
	H [°]	6.25	1.08	6.42	6.77	1.89	6.97

		Going South (epochs: 995–1055)			Going West (epochs: 1055–1090)		
		EKF	UKF	EPF	EKF	UKF	EPF
Mean	R [°]	-0.42	-0.18	-0.42	-0.54	-0.30	-0.54
	P [°]	0.42	0.31	0.42	0.61	0.35	0.62
	H [°]	-7.64	1.51	-7.86	-6.83	1.65	-7.04
Std	R [°]	0.24	0.17	0.24	0.53	0.24	0.54
	P [°]	0.41	0.24	0.42	0.62	0.35	0.63
	H [°]	1.19	0.27	1.22	1.37	0.45	1.39
Max	R [°]	0.95	0.57	0.96	1.72	0.94	1.75
	P [°]	1.34	0.71	1.36	2.15	0.76	2.18
	H [°]	9.39	2.22	9.65	9.84	2.76	10.08

Table 6.5. The statistics of the orientation errors from IMU400CC using the EKF, the UKF and the EPF, as compared to the reference EKF-based GPS/INS solution from H764G during four straight motion periods.

The UKF demonstrated a faster convergence in the heading component in kinematic alignment than the EKF, based on the simulated example for the navigation-grade H764G (Yi and Grejner-Brzezinska, 2005). Figure 6.7 shows a heading convergence example as a function of the tested filter type for the low-cost MEMS IMU400CC during the static alignment. Even when starting with the actual heading from the reference and using 1-second measurement updates of the high accuracy (cm level) GPS position solution, the correct heading solution still cannot be maintained due to the low quality of the inertial measurements and less coupling between the position components and the heading component no matter which filter is used. The EPF behaves the best, and the UKF is the weakest in maintaining the correct heading in such scenario. Around 23°, 26° and 17°

drifts from the actual heading for the solutions using the EKF, the UKF and the EPF, respectively, were found. Figure 6.8 illustrates another example of the heading convergence errors, as compared to the reference heading during the first maneuvering period (Segment 4, in Figure 6.3), and the corresponding trajectory is shown in the upper-right subplot. The UKF starts with a heading biased by 60° , while the EKF and the EPF begin with the heading biased by around 12° . After a 24-second kinematic calibration, starting at epoch 437, the UKF began to converge closer to the reference heading, as compared to the EKF and the EPF. It is noted that the biased heading for each filter is caused by the heading drift during the static period (i.e., Segment 3 shown in Figure 6.3) before the tested maneuvering period shown in Figure 6.8.

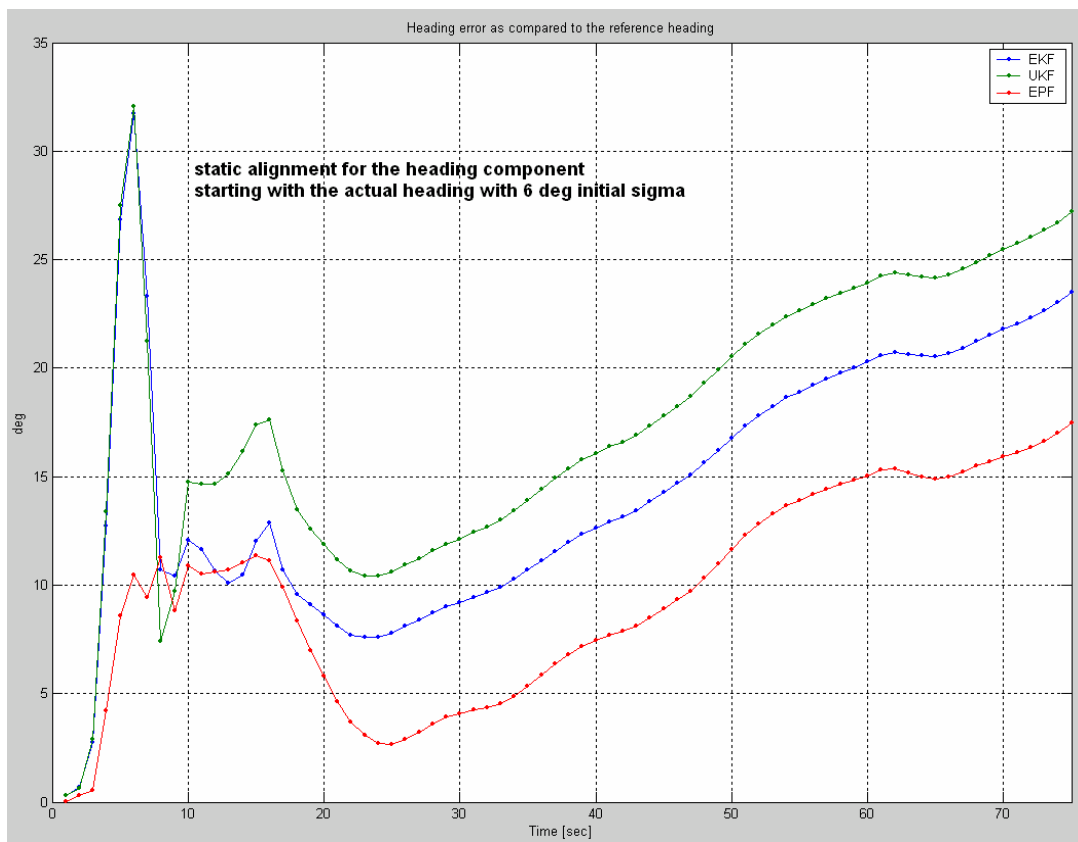


Figure 6.7. The heading convergence errors during the static alignment period for IMU400CC using the EKF, the UKF and the EPF, as compared to the reference heading from H764G.

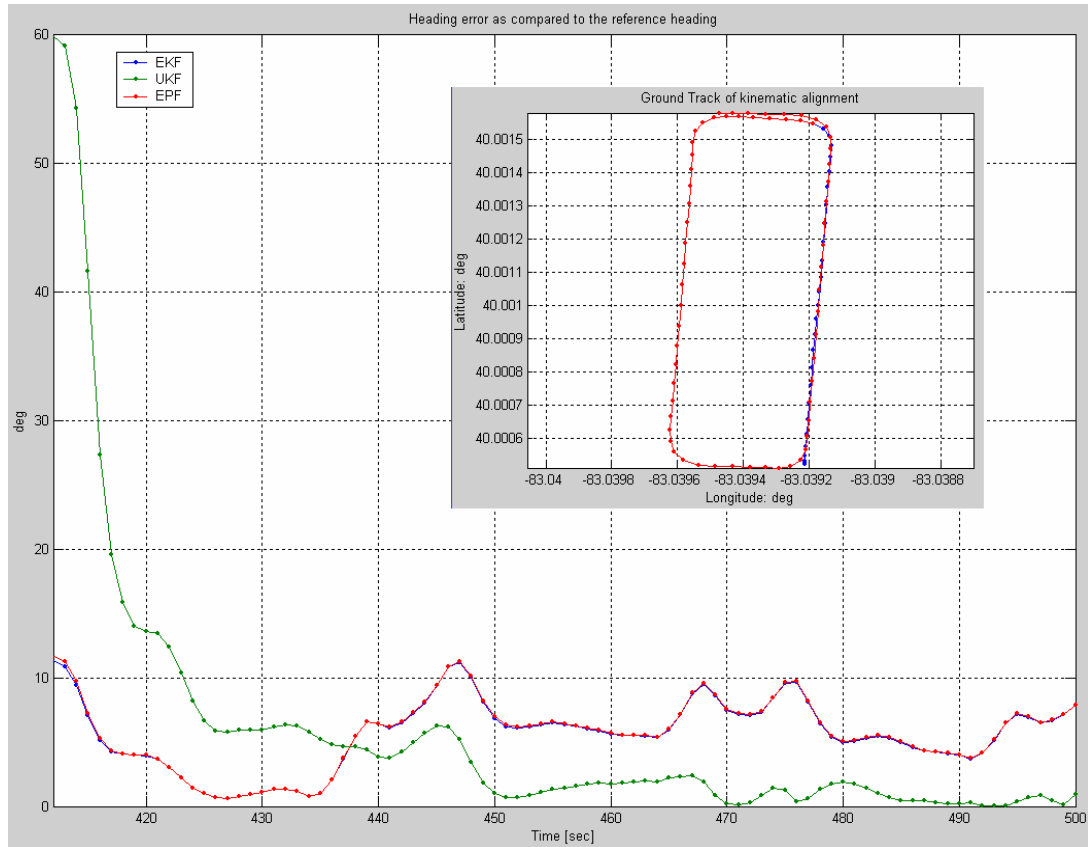


Figure 6.8. The heading convergence errors during the first maneuvering period (Segment 4 in Figure 6.3, starting at epoch 413) for IMU400CC using the EKF, the UKF and the EPF, as compared to the reference heading from H764G.

6.2.2.2 Position performance using the EKF, the UKF and the EPF

As marked in Figure 6.2 with red color, several actual GPS gaps exist in this experimental dataset either due to the loss of GPS lock or a failure of the double-difference ambiguity resolution. Table 6.6 presents the 3-dimensional position error drifts for the EKF, the UKF and the EPF solutions, during these gaps, as compared to the reference GPS solutions at the end of each gap. A total of 10 gaps with various lengths appear in the entire trajectory. The UKF is better than the EKF for four of the 10 gaps, and the EPF is better than the EKF for five of the 10 gaps. However, as can be observed in Table 6.6, the three filters behave, generally, similarly in the 3-dimensional position error drifts. In order to get more reliable statistical information for these filters in terms of the tolerance to GPS gaps, a total of 1919 samples of the 3-dimensional position error drifts for 1-second GPS gaps, as compared to the GPS reference, were collected, and the statistics are listed in Table 6.7. The UKF has the smallest mean (0.969 m) and the smallest standard deviation (1.447 m), as compared to the EKF and the EPF. Around

11% of relative improvement can be found in the average 3-dimensional position error for 1-second GPS gaps using the UKF, as compared to this using the EKF. The EPF has the comparable mean (1.092 m) and standard deviation (1.483 m) to these of the EKF, while it has the smallest maximum (16.940 m) and the smallest minimum (0.050 m), in comparison to these of the EKF and the UKF.

No.	Start epoch index	Gap length [sec]	EKF [m]	UKF [m]	EPF [m]
1	94	3	1.738	1.747	1.722
2	145	49	414.289	419.629	417.639
3	900	13	4.122	4.974	4.103
4	953	5	3.955	2.872	4.039
5	1002	3	0.819	1.489	0.834
6	1005	3	0.924	1.551	0.909
7	1037	10	7.083	6.672	7.074
8	1053	4	1.764	1.131	1.802
9	1078	10	4.569	3.996	4.546
10	1948	3	1.457	2.091	1.457

Table 6.6. Free inertial navigation 3-D position error drifts of the actual GPS gaps for IMU400CC using the EKF, the UKF and the EPF, as compared to the actual GPS reference positions at the end of the GPS gaps.

	EKF	UKF	EPF
Mean	1.092	0.969	1.092
Std	1.483	1.447	1.483
Max	16.942	16.966	16.940
Min	0.060	0.060	0.050

Table 6.7. Statistics of the 1-second free inertial navigation 3-dimensional position error drifts for IMU400CC using the EKF, the UKF and the EPF, as compared to the GPS reference positions.

Another eight 16-second GPS gaps were simulated; the horizontal position error drifts using the three filters are illustrated in Figure 6.9, together with the actual vehicle trajectory. The comparison of the position error drifts is shown in Table 6.8. The UKF is better than the EKF for six of the eight 16-second gaps, and the EPF is better than the EKF for one of the 10 gaps. The EKF is better than the UKF for two of the eight 16-second gaps, and better than the EPF for seven of the eight 16-second gaps.

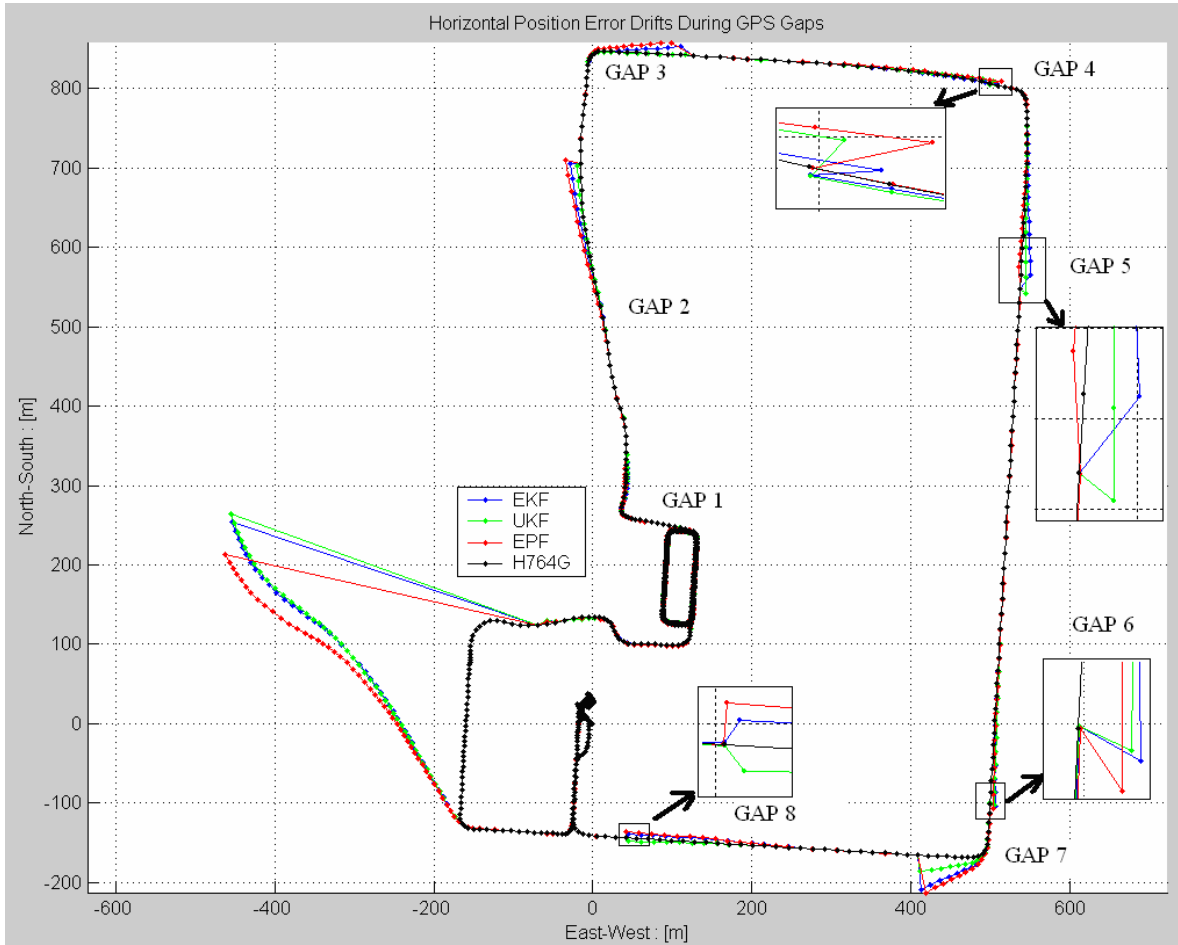


Figure 6.9. Horizontal position error drifts using the EKF, the UKF and the EPF during the simulated 16-second GPS gaps, as listed in Table 6.8.

Gap No.	Start epoch index		EKF	UKF	EPF
1	900	N [m]	4.296	-7.079	13.468
		E [m]	0.100	-0.575	2.523
		D [m]	-2.077	-2.717	-1.363
		3-D [m]	4.773	7.604	13.770
2	925	N [m]	-19.687	-16.826	-25.056
		E [m]	15.646	6.138	22.313
		D [m]	-2.461	-2.217	-3.055
		3-D [m]	25.267	18.047	33.690
3	950	N [m]	-12.644	-0.317	-18.075
		E [m]	0.540	-7.436	14.151
		D [m]	0.246	-2.712	0.797
		3-D [m]	12.658	7.922	22.969
4	975	N [m]	2.948	-0.835	-0.925
		E [m]	-22.886	-17.385	-29.762
		D [m]	-1.668	-2.359	-0.736
		3-D [m]	23.135	17.564	29.786
5	1000	N [m]	1.206	27.242	-9.931
		E [m]	-14.049	-7.804	2.638
		D [m]	1.143	-2.481	-0.106
		3-D [m]	14.147	28.446	10.276
6	1037	N [m]	19.814	18.490	23.172
		E [m]	-6.965	-5.453	-4.703
		D [m]	-2.367	-2.005	-1.828
		3-D [m]	21.135	19.381	23.715
7	1053	N [m]	49.756	23.012	53.660
		E [m]	9.913	11.658	1.416
		D [m]	-0.259	-2.559	-0.084
		3-D [m]	50.734	25.923	53.679
8	1078	N [m]	-4.955	4.476	-8.447
		E [m]	12.853	12.034	15.290
		D [m]	0.773	-0.667	0.532
		3-D [m]	13.796	12.857	17.476

Table 6.8. Free inertial navigation 3-dimensional position error drifts of the simulated 16-second GPS gaps for IMU400CC using the EKF, the UKF and the EPF, as compared to the actual GPS reference positions at the end of the GPS gaps.

6.2.3 Summary of alternative nonlinear filters

- ✓ The concept of the nonlinear Bayesian filters was introduced and reviewed.
- ✓ Two alternative nonlinear Bayesian filters, namely UKF and PF, were discussed in detail.
- ✓ The example analyses, with the focus on the orientation and position performance of a low-cost MEMS IMU as a function of different filter implementation were provided.
- ✓ A computational optimization scheme for the UKF, the PF and the EKF was presented.
- ✓ During the stationary period (Segment 1 in Figure 6.3), without sufficient prior kinematic calibration using the precise cm-level GPS position measurement update, the heading component drifts very fast, reaching $0.31^\circ/\text{s}$, $0.35^\circ/\text{s}$ and $0.23^\circ/\text{s}$ for the EKF, the UKF and the EPF, respectively. These drifts are better than the manufacturer's error specification ($1.0^\circ/\text{s}$). Under such scenario, around 26% improvement in the drift rate of the heading component was found for the EPF, as compared to the standard EKF, while the UKF is worse than the EKF in terms of the heading drift rate by around 13%.
- ✓ During the stationary period (Segment 6 in Figure 6.3), with static and kinematic calibration for around 1139 epochs using the precise cm-level GPS position measurement update, the heading drift rate was better controlled than in the above scenario without prior kinematic calibration, reaching around $0.10^\circ/\text{s}$, $0.06^\circ/\text{s}$ and $0.10^\circ/\text{s}$ for the EKF, the UKF and the EPF, respectively. Under such scenario, around 40% improvement in the heading drift rate was found for the UKF, as compared to the standard EKF and the EPF.
- ✓ The high heading drift rate, even with precise cm-level GPS positioning measurement update, is the result of the high gyro measurement noise and less coupling between the position and the heading components.
- ✓ With a short prior kinematic calibration (around 69 second), the actual heading errors increased to more than 40° for a 49-second GPS gap for the EKF, the UKF and the EPF; still, during this gap, around 6% and 2% of relative improvement was found for the UKF and the EPF, respectively, as compared to the EKF, in terms of the actual heading errors.
- ✓ In the maneuvering period (Segment 4 in Figure 6.3) with loops, around 1° accuracy in the heading component can be achieved using the UKF, and around 75% of relative improvement was found in the UKF solution, as compared to that for the EKF. Around 53% of relative improvement in the heading component for the UKF was found, in another maneuvering period (Segment 7 in Figure 6.3) with irregular trajectory, as compared to that of the EKF.
- ✓ With long-period kinematic calibration, the UKF is significantly better than the EKF in terms of the actual heading error. Around 90%, 116%, 120% and 124%,

respectively, of relative improvement in the actual UKF heading errors can be found, as compared to these of the EKF during the four straight portions of the trajectory after a 465-second maneuvering period (Segment 4 in Figure 6.3) with loops.

- ✓ As compared to the reference from H764G, the actual roll and pitch errors of the EKF, the UKF and the EPF are a little better than 0.5° . During the kinematic calibration periods, the UKF is always better than the EKF, and the EPF is at the same accuracy level as the EKF.
- ✓ As for the heading convergence error, the EPF is the best if only static alignment is applied; if the kinematic calibration is involved, the UKF can provide better convergence performance than the EKF, and the EPF behaves similarly to the EKF.
- ✓ Similarly to the orientation performance of the three filters, in most cases, the UKF is better than the EKF and the EPF in terms of the position error drifts. The EPF behaves very similarly to the EKF, while in some cases, the EPF is better than the EKF, for example, in static cases with insufficient kinematic alignment.
- ✓ Based on the total of 1919 1-second free inertial navigation samples, around 11% of relative improvement can be found in the average 3-dimensional position error for 1-second GPS gap using the UKF, as compared to that of the EKF, and the EPF behavior is very comparable to that of the EKF.

CHAPTER 7

CONCLUSIONS, CONTRIBUTIONS AND RECOMMENDATIONS

7.1 Conclusions

As discussed in Chapter 1, the three primary objectives of this dissertation were 1) to further improve the accuracy and reliability of the GPS/INS integrated systems designed for mobile mapping applications, especially in confined environments causing frequent losses of GPS lock and lower positioning accuracy due to long GPS baselines; 2) to extend the applicability of the low-end MEMS inertial sensor to direct sensor georeferencing and 3) to test selected nonlinear filter designs, as alternatives to the Extended Kalman Filter in GPS/INS integration. The following conclusions recapitulate the findings supporting the three objectives listed above; the detailed conclusions were provided in the end of each chapter.

- ✓ The epoch-by-epoch positioning approach supporting baseline and network modes with several special data processing techniques to improve the success rate of the ambiguity resolution and the quality control of the RTK systems demonstrated.
 - Cm-level positioning accuracy for the tested static baselines up to 70 km in baseline-by-baseline mode, and 120 km in the network mode with 100% L_1 ambiguity fixed rate.
 - Cm-level positioning accuracy for the tested kinematic baselines varying from 4 km to 20 km with more than 95% valid solutions of around 95% fixed L_1 solutions using only selected special data processing techniques.
- ✓ Significant improvements (around 30%) in position and orientation of free inertial navigation can be achieved by the “customized” sensor-by-sensor error model derived from the Allan variance analysis and/or PSD method, as compared to the manufacturer’s default error model.
 - This indicates some possible inaccuracies of the manufacturer’s error model and different behavior of the IMU sensor in x , y , z directions.
- ✓ Wavelet-based signal de-noising improves the position and orientation accuracy and the initial coarse alignment accuracy of the low-cost MEMS inertial sensor.
- ✓ The alternative filter, UKF, for low-cost MEMS IMU400CC
 - Can speed up the heading convergence and improve the heading accuracy.

- ◆ Around 75% of relative improvement in the UKF heading component was found, as compared to that for the EKF in a maneuvering period with loops.
- Slightly improves the tolerance to GPS gaps.
 - ◆ Around 11% of relative improvement was found in the average 3-dimensional position error for 1-second GPS gaps using the UKF, as compared that using the EKF, based on 1919 samples.
- ✓ The alternative filter, EPF (EKF+PF), for low-cost MEMS IMU400CC
 - During the stationary period, without sufficient prior kinematic calibration using the precise cm-level GPS position measurement update, provides around 26% improvement in the drift rate of the heading component, as compared to the standard EKF. In other cases, both filters provide comparable heading accuracy.
 - Behaves similarly to the EKF in terms of tolerance to GPS gaps.
- ✓ The low-cost MEMS inertial sensor investigated in this dissertation provides limited position and orientation accuracy for mobile mapping applications.
 - Careful IMU error modeling, signal de-noising technique, and alternative nonlinear filter can improve the performance. Still only low-accuracy mobile mapping applications may consider this sensor.

7.2 Contributions

The contributions of this dissertation can be summarized as follows:

- ✓ The AIMSTM (Airborne Integrated Mapping System) capability was extended from the EKF-only solution, based on high-end inertial sensor and single baseline GPS solution.
 - to support both baseline and network GPS RTK modes
 - to support various grade inertial sensors
 - to use alternative nonlinear filters
- ✓ An effective and reliable epoch-by-epoch GPS positioning technique supporting multiple reference and rover receivers with several special data processing strategies to improve the ambiguity success rate and the quality control was implemented.
- ✓ A comprehensive analysis of the stochastic error characteristics for four inertial sensors and a “customized” sensor-by-sensor error model for each sensor using two techniques, the Allan variance analysis and the Power Spectral Density method, in time and spectral domains, respectively, was provided.
- ✓ The performance comparison of two nonlinear Bayesian filters and the traditional Extended Kalman Filter using a high-end inertial sensor, H764G, and a low-cost MEMS inertial sensor, IMU400CC, was provided and discussed.
- ✓ A computational optimization scheme for nonlinear filtering according to the special structure of GPS/INS integration was provided and implemented.

7.3 Recommendations

As mentioned in Chapter 3, numerous global and local GPS ionospheric error models have been developed. For example, the global ionospheric model can be 1) the broadcast Klobuchar ionospheric model included in the GPS navigation message, or 2) the Global Ionospheric Maps from CODE (<http://www.aiub.unibe.ch/ionosphere.html>) or JPL (http://iono.jpl.nasa.gov/latest_rti_global.html). The local and/or regional ionospheric models are provided by, for example, Real-Time US-Total Electron Content (US-TEC, <http://www.sec.noaa.gov/ustec/index.html>), Wide Area Augmentation System (WAAS, http://www.faa.gov/about/office_org/headquarters_offices/ato/service_units/techops/navservices/gnss/waas/), the European Geostationary Navigation Overlay Service (EGNOS, <http://www.esa.int/esaNA/egnos.html>), and numerous local continuously tracking GPS networks. Some of the existing models do not provide any accuracy assessment for their ionospheric corrections. Therefore, it is necessary to develop a uniform validation technique for the quality control of the GPS ionospheric error models, coming from various sources. Such validation technique can be based, for example, on statistical testing procedures, especially for the local network-derived GPS ionospheric error models with few GPS stations, as compared to global or regional ionospheric models from relatively large GPS networks.

The sensor noise identification techniques discussed in Chapter 4 of this dissertation, i.e., the Allan-variance analysis and the PSD method can provide complete understanding of the sensor error characteristics. While the relatively long (normally several hours) static experiments are required, for short static or kinematic experiments, the adaptive Kalman filter can be used for online identification of the inertial sensor noise model by assuming some random processes for the sensor noise model (for example, an ARMA model can be used). The adaptive Kalman filter approach can also be used to provide a cross-comparison for the sensor noise models identified by the Allan-variance analysis and the PSD method.

The current implementation of the wavelet-based signal de-noising technique discussed in Chapter 5, is based on the Matlab implementation, and the level of de-noising is selected by an experimental basis and remains unchanged for the entire trajectory. As pointed out in Chapter 5, the level of de-noising is a function of the sensor type, system dynamics and the geometry of the vehicle trajectory. Therefore, the adaptive wavelet-based signal de-noising technique should be considered in the real scenarios for better navigation performance.

As shown in Chapters 5 and 6, the low-cost MEMS inertial sensor, IMU400CC, has very limited navigation performance, due primarily to the low accuracy of the heading component. The heading component can drift very quickly, even if supported by 1) the advanced “customized” inertial sensor error modeling, 2) wavelet-based signal de-noising technique, and 3) advanced nonlinear Bayesian filter, such as, UKF. In order to further extend the applicability of low-cost MEMS inertial sensors for mobile mapping

applications, it is necessary to fuse additional sensors such as, for example, magnetometer, to aid the heading components.

As shown in Chapter 6, the Particle Filter demonstrated a better than the EKF navigation performance and was also in some cases, better than the UKF. To further investigate this characteristics, the PF may still need fine tuning, for example, in terms of, the number of particles, the choice of the importance density function, etc. In the current implementation, the proposed density is based on the EKF-generated posterior density. It is believed that the proposed density generated by the UKF-based posterior density can provide better performance with fewer particles than the EKF-based posterior density. The UKF-based PF could be tested against the EKF-based PF implemented in this dissertation.

Currently, the so-called, knowledge systems, based on the adaptive learning techniques, for example, the artificial neural networks, fuzz logic control, etc., are being introduced to support multi-sensor integration, especially in GPS-denied environments where navigation in dead reckoning (DR) mode is needed. The impact of such systems in accuracy and continuity of DR navigation should be investigated for possible navigation improvements of the integrated systems, such as that, presented here.

APPENDIX A

INERTIAL DATA PREPROCESSING

A total of six inertial systems are available at The Ohio State University (OSU) Satellite Positioning and Inertial Navigation (SPIN) Laboratory. They are (1) two navigation-grade H764G; (2) one navigation-grade LN100; (3) one tactical-grade HG1700; (4) one tactical-grade LN200; and (5) one consumer-grade MEMS IMU400CC. The 2005 hardware configuration is illustrated in Figure 2.4, and the manufacturer specifications of these systems are listed in Table 2.1. This chapter provides a brief introduction to the raw data conversion procedure, inertial sensors orientation alignment and time calibration.

A.1 Raw inertial measurement conversion and inertial data formats

The raw inertial measurements are stored in the binary formats. Each inertial sensor has different internal binary data format. These formats should be converted to a uniform data format, which is easily accessible by the post-processing software. Also, the inertial measurements, except for the two H76G, need to be synchronized with the external accurate GPS time. H764G has a built-in GPS receiver to synchronize the inertial measurements with the accurate GPS time. The raw data conversion and the time synchronization can be done using a software module called “*preimu*”. Figure A.1 shows the interface of this data conversion program. The inertial sensors orientation alignment and the time correction between different inertial sensors with respect to one of the H764G used as a reference, as described in the next section, can also be done by this software. The final data formats of the raw inertial measurements and INS navigation solutions for the INS data post-processing are listed in Table A.1 and Table A.2. In Table A.1, the ΔV and $\Delta\omega$ represent the three accelerometer-integrated velocities and three gyroscope-integrated angles, and the \mathbf{f} and ω represent the direct accelerations from three orthogonal accelerometers and angular rates from the three orthogonal gyroscopes. The H764G outputs a navigation solution from an internal GPS/INS Kalman filter using GPS code measurements, and LN100 outputs a free inertial navigation solution. These INS navigation solutions, whose formats are listed in Table A.2, serve as the initial conditions for our highly accurate GPS/INS data post-processing. HG1700 and MEMS IMU400CC

do not provide their own INS solutions, thus an initial coarse alignment procedure must be done for further data post-processing.

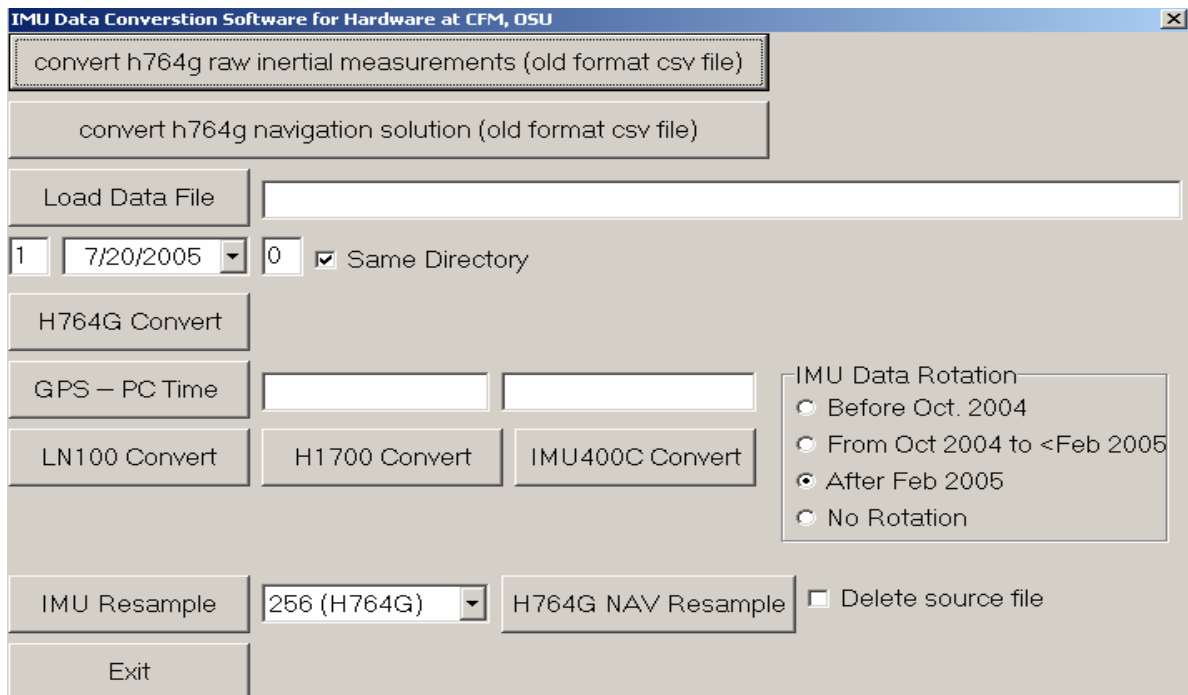


Figure A.1. Interface of the data conversion program.

No.	H764G	LN100	HG1700	IMU400CC	Name	Precision	Units
1	√	√	√	√	Time Tag	Double	[s]
2	√	√	√	×	$\Delta \mathbf{V}_x$	Double	$[\text{m}\cdot\text{s}^{-1}]$
3	√	√	√	×	$\Delta \mathbf{V}_y$	Double	$[\text{m}\cdot\text{s}^{-1}]$
4	√	√	√	×	$\Delta \mathbf{V}_z$	Double	$[\text{m}\cdot\text{s}^{-1}]$
5	√	√	√	×	$\Delta \boldsymbol{\omega}_x$	Double	[rad]
6	√	√	√	×	$\Delta \boldsymbol{\omega}_y$	Double	[rad]
7	√	√	√	×	$\Delta \boldsymbol{\omega}_z$	Double	[rad]
8	×	×	×	√	\mathbf{f}_x	Double	$[\text{m}\cdot\text{s}^{-2}]$
9	×	×	×	√	\mathbf{f}_y	Double	$[\text{m}\cdot\text{s}^{-2}]$
10	×	×	×	√	\mathbf{f}_z	Double	$[\text{m}\cdot\text{s}^{-2}]$
11	×	×	×	√	$\boldsymbol{\omega}_x$	Double	$[\text{rad}\cdot\text{s}^{-1}]$
12	×	×	×	√	$\boldsymbol{\omega}_y$	Double	$[\text{rad}\cdot\text{s}^{-1}]$
13	×	×	×	√	$\boldsymbol{\omega}_z$	Double	$[\text{rad}\cdot\text{s}^{-1}]$
14	×	×	√	√	Temp	Double	[°C]

Table A.1. The binary data format of inertial measurements (√ represents that the corresponding data listed in the “Name” column is available for the sensor listed from column two to four; × indicates that the data listed in the “Name” column is not available for the sensor listed from two to four); \mathbf{f} and $\boldsymbol{\omega}$ represent the acceleration and angular rate from an accelerometer and a gyroscope, while $\Delta \mathbf{V}$ and $\Delta \boldsymbol{\omega}$ are the accelerometer-integrated velocity and gyroscope-integrated angle.

No.	Name	Precision	Units
1	GPS Time	Double	[s]
2	Latitude	Double	[rad]
3	Longitude	Double	[rad]
4	Height	Double	[m]
5	Vn	Double	$[\text{m}\cdot\text{s}^{-1}]$
6	Ve	Double	$[\text{m}\cdot\text{s}^{-1}]$
7	Vd	Double	$[\text{m}\cdot\text{s}^{-1}]$
8	Heading (Yaw)	Double	[rad]
9	Roll	Double	[rad]
10	Pitch	Double	[rad]

Table A.2. The binary INS navigation data format for H764G and LN100.

A.2 Inertial sensors orientation alignment and time calibration

The sensor orientations of the three orthogonal accelerometers and the three orthogonal gyroscopes are different for each inertial sensor. In order to be able to provide a platform for performance cross-comparison amongst these inertial sensors, their inertial measurements should be rotated to the same orientation after identifying the relationship of the axis orientation of these sensors. Amongst these inertial sensors, each of the two H764G is equipped with its own built-in GPS sensor. Thus, the GPS time of the measurements from the two H764G can be assumed to be known; in other words, the IMU measurements are properly time-tagged by the GPS time. The time tags of the measurements from the other inertial sensors are maintained by using the CPU time in combination with an OEM timer board that maintains the GPS time (synchronized with the 1PPS event output from an external GPS sensor). Note that the time-tags are assigned to the inertial measurement records upon receiving them at the PC interface and therefore depending on the communication channel speed could represent a time that is later by a significant amount time; this offset or lag should be measured and a correction should be applied to obtain the correct (or optimal) GPS time-tags. Figure A.2 presents an example illustration of the time synchronization of the hardware components, including one MEMS IMU, one barometric altimeter and one compass, with the accurate 1 PPS output from a GPS sensor. Since the H764G measurements are properly time-tagged, they can be used for calibrating of the time delay or lag of other IMU sensors simply by comparing the measurements from two rigidly connected sensors and identifying the correlation of the various acceleration data (details are discussed later).. In summary, besides rotating these inertial measurements to the same orientations, the time of the measurements should be corrected to the same reference time system (here, the H764G GPS time). The time of the built-in GPS sensor in H764G will also contain errors due to the GPS receiver clock bias, which is less than 0.5 millisecond.

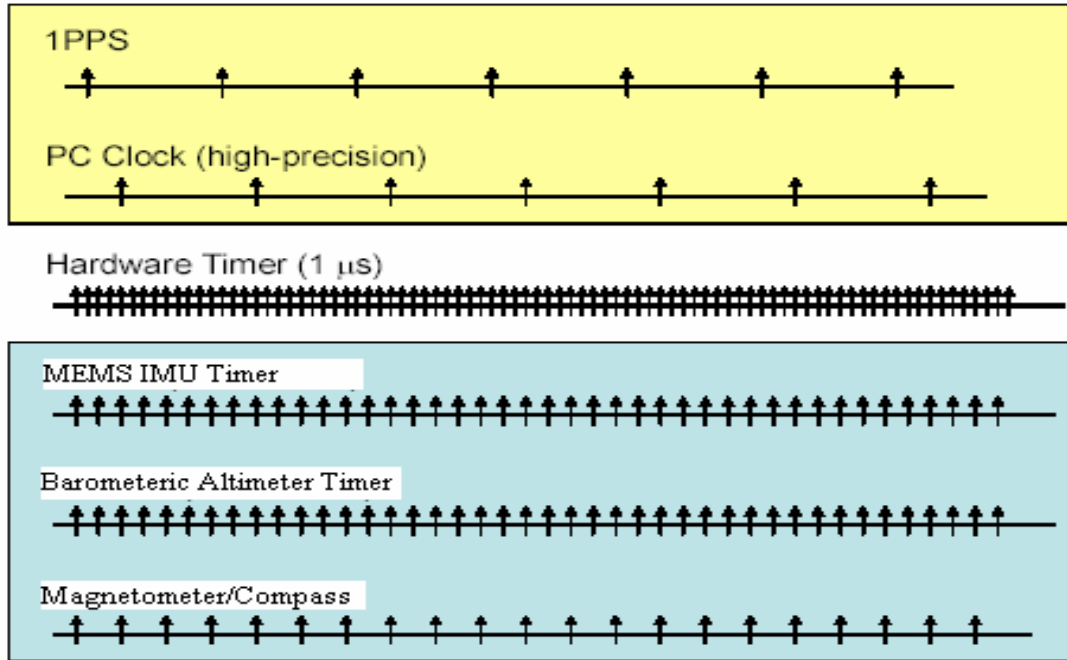


Figure A.2. Example illustration of the time synchronization of the hardware components (a MEMS IMU, a barometric altimeter and a compass) with the accurate 1 PPS output from GPS sensor (Note: ^[1] the time scales for the sensors are for demonstration only, not representing the actual sampling rate for the sensors; ^[2] The Barometric altimeter and compass sensors are not discussed here, even though they were implemented in the OSU hardware configuration).

The sensors orientation alignment and time lag calibration can be determined using the cross-correlation technique. If two inertial sensors are physically and closely fixed in the same platform, they will experience similar vehicle dynamics. This fact makes it possible to calibrate the time lag of inertial measurements from different inertial sensors, and identify the relationships of the sensor orientation using the cross-correlation technique. The discrete cross-correlation can be computed according to equation (A.1) for two discrete time series, x and y . Two datasets are re-sampled to 512Hz (i.e. twice of 256Hz, sampling rate of H764G), then the cross-correlation between each accelerometer axis and gyroscope axis is computed, and the maximum cross-correlation and its corresponding lag are located. Figure A.3 illustrates an example the cross-correlation of the IMU400CC accelerometer outputs in x , y and z directions (f_x , f_y and f_z) with respect to H764G₁ x accelerometer output (f_x), using the datasets collected on July 22, 2005. The maximum cross-correlation can be easily found between IMU400CC f_x and H764G₁ f_x with around $9/512 \approx 17.6$ millisecond delay in the negative direction. The complete sensor orientation alignment and time lag calibration using the above dataset, is listed in Table

A.3 and a summary of sensor orientation alignment and time calibration of different sensors is listed in Table A.4.

$$\phi_{xy}(\tau) = \frac{\sum_i [(x_i - \bar{x})(y_{i-\tau} - \bar{y})]}{\sqrt{\sum_i (x_i - \bar{x})^2} \sqrt{\sum_i (y_{i-\tau} - \bar{y})^2}} \quad (\text{A.1})$$

Where: x and y are two discrete time series; $\phi_{xy}(\tau)$ is the cross-correlation at the time lag τ , subscript i is the epoch index; \bar{x} and \bar{y} are the means of x and y .

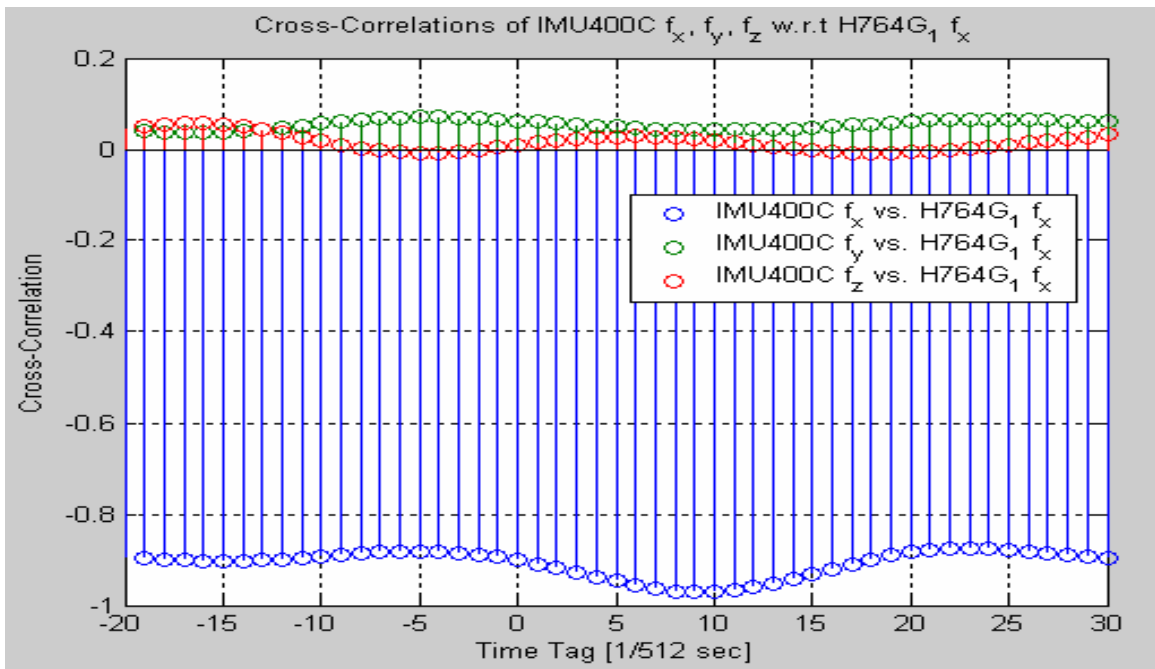


Figure A.3. Example cross-correlation of with respect to IMU400CC three accelerometer outputs in x , y , z directions (\mathbf{f}_x , \mathbf{f}_y and \mathbf{f}_z) with respect to H764G₁ outputs from x accelerometer (\mathbf{f}_x).

		H764G ₁		
		f_x	f_y	f_z
H764G ₂	f_x	0.99 (0)	0.02(1)	-0.11(-26)
	f_y	-0.03(14)	0.99 (0)	-0.17(-1)
	f_z	-0.10(28)	-0.08(3)	0.90 (0)
LN100	f_x	0.94 (4)	-0.34(-284)	-0.08(-26)
	f_y	-0.35(289)	0.95 (3)	-0.15(91)
	f_z	-0.13(8)	-0.18(-84)	0.89 (3)
HG1700	f_x	0.06(26)	0.13(-495)	0.93 (2)
	f_y	0.10(1)	0.94 (2)	0.14(493)
	f_z	-0.89 (3)	-0.21(3)	-0.12(28)
IMU400CC	f_x	-0.97 (9)	0.13(496)	0.06(-17)
	f_y	0.13(-500)	-0.97 (9)	0.10(8)
	f_z	0.13(35)	0.19(9)	-0.96 (9)
		ω_x	ω_y	ω_z
H764G ₂	ω_x	1.00 (0)	-0.13(-47)	-0.04(448)
	ω_y	-0.13(47)	1.00 (0)	0.07(270)
	ω_z	-0.04(-447)	0.07(-270)	1.00 (0)
LN100	ω_x	1.00 (2)	0.28(322)	-0.11(378)
	ω_y	-0.28(-500)	0.99 (2)	0.16(-500)
	ω_z	-0.14(-373)	0.10(500)	1.00 (0)
HG1700	ω_x	0.07(500)	0.06(396)	1.00 (1)
	ω_y	-0.06(165)	0.99 (2)	0.06(-392)
	ω_z	-1.00 (1)	0.06(-164)	-0.07(-500)
IMU400CC	ω_x	0.92 (11)	-0.11(10)	-0.08(500)
	ω_y	-0.11(58)	0.94 (11)	0.09(247)
	ω_z	-0.10(-500)	0.10(-223)	1.00 (11)

Table A.3. Example of sensor orientation and time lag calibration using cross-correlation technique based on datasets of July 22, 2005 (Note: a Matlab macro function ‘*imutimeoffset.m*’ was developed to process the data using the cross-correlation technique described above; the numbers shown in parentheses indicate the time lags in the unit of 1/512[Hz]; the number marked in red color indicates the location of the maximum cross-correlation; the first part of the table lists the cross-correlations of IMU400CC x , y , and z accelerometers (labeled as f_x , f_y and f_z) comparing to H764G₁ accelerometers in x , y and z directions (f_x , f_y and f_z) and the second shaded part presents the cross-correlations of IMU400CC gyroscopes in x , y and z directions (ω_x , ω_y and ω_z) comparing to H764G₁ gyroscopes in x , y and z directions (ω_x , ω_y and ω_z).

Sensor	Accelerometers			Gyroscopes			Lag [ms]
H764G ₁	+fx	+fy	+fz	+ωx	+ωy	+ωz	Reference
H764G ₂	+fx	+fy	+fz	+ωx	+ωy	+ωz	0.0
LN100	-	-	-	-	-	-	-
HG1700	+fy	-fz	-fx	+ωy	-ωz	-ωx	3.9
IMU400CC	+fx	+fy	-fz	-ωx	-ωy	+ωz	18.8
Valid for the data collected before Nov. 2004 using data of July 4, 2004							
H764G ₂	+fx	+fy	+fz	+ωx	+ωy	+ωz	0.0
LN100	+fx	+fy	+fz	+ωx	+ωy	+ωz	6.6
HG1700	+fy	-fz	-fx	+ωy	-ωz	-ωx	3.2
IMU400CC	+fx	+fy	-fz	-ωx	-ωy	+ωz	18.3
Valid data collected from Nov. 2004 to Fe2. 2005 using data of Nov. 19, 2004							
H764G ₂	+fx	+fy	+fz	+ωx	+ωy	+ωz	0.0
LN100	+fx	+fy	+fz	+ωx	+ωy	+ωz	4.5
HG1700	+fz	+fy	-fx	+ωz	+ωy	-ωx	3.9
IMU400CC	-fx	-fy	-fz	+ωx	+ωy	+ωz	19.2
Valid data collected after Feb 2005 using data of July 22, 2005							

Table A.4. Hardware assembly orientation alignment and time lag calibration of different sensors with respect to H764G₁.

APPENDIX B

INS STOCHASTIC ERROR IDENTIFICATION AND MODELING

This chapter provides the complete example analysis of the INS stochastic error identification using the Allan-variance (AVAR) analysis and the Power Spectral Density (PSD) method for all the six inertial systems as explained in Appendix A. The detailed Allan-variance and PSD analysis techniques, together with a brief version of the example analysis, are presented in Chapter 4.

Two static experiments conducted on June 26, 2004 (Day of Year: DOY 178, 2004) and Oct. 20, 2004 (DOY 294, 2004) respectively, were used here. The ~8-hour datasets on DOY 178, 2004 are available for three types of inertial sensors: H764G, HG1700 and IMU400CC. Two static segments (referred to as DOY 294₁, 2004 and DOY 294₂, 2004) in the experiment on DOY 294, 2004 are separated by one dynamic dataset. All four types of inertial sensors (i.e. H764G, LN100, HG1700 and IMU400CC) were included in the second experiment on DOY 294, 2004. The stochastic error analyses for H764G, HG1700 and IMU400CC are from the first experiment on DOY 178, 2004. The analysis for LN100 is from the first segment of the second experiment on DOY 294, 2004. The temperature-correlated trends of the raw inertial measurements from HG1700 and IMU400CC in both experiments are compensated using a second-order polynomial fitting function $f(T)=a_0+a_1T+a_2T^2$ of the sensed temperature, T , with coefficients a_0 , a_1 and a_2 .

The output of an inertial sensor can be expressed in the rate domain (i.e., the rate output) or in the integrated domain (i.e., the integrated output). For example, the rate output of an accelerometer is the acceleration and the integrated output is the accelerometer-integrated velocity; the rate output of a gyroscope is the angular rate and the integrated output is the gyroscope-integrated angle. Five basic noise terms present in the output of an inertial sensor are (1) quantization noise, (2) rate white noise, (3) flicker noise, (4) rate random walk and (5) rate ramp (Annex C of IEEE Std 647, 1995; Annex C of IEEE Std 952, 1997; Annex I of IEEE Std 1293, 1998). Table B.1 lists the Allan variance and Power Spectral Density (PSD) representations together with the log-log fitted models to estimate corresponding coefficients of the five basic noise terms of the rate output of an inertial sensor (refer to Annex C of IEEE Std 647, 1995 or Annex C of IEEE Std 952, 1997 for more information). The Allan variance and PSD representations of the integrated output of an inertial sensor will be different from Table B.1. The rate

white noise is also called angle random walk (ARW) for the gyroscope measurements, and the velocity random walk (VRW) for the accelerometer measurements. The flicker noise is also referred to as the bias instability, which indicates the bias fluctuations in the data. The rate ramp is actually a systematic (or deterministic) trend and it is caused by the imperfection of the INS dynamic error modeling. The PSD method in the frequency domain, cannot distinguish between the rate random walk and the rate ramp whose slopes of the PSD log-log plots both are -2 . Thus, the rate ramp must be removed before applying the PSD method. However, the Allan variance analysis in the time domain can distinguish between the rate random walk and the rate ramp, the slope of the Allan variance log-log plot of the rate ramp is $+1$ while that of the rate random walk is $+\frac{1}{2}$.

	Noise terms	Error Model	Log-log Model	Coefficients
Allan variance analysis	Quantization noise	$\sigma^2(\tau) = \frac{3Q^2}{\tau^2}$	$y = -x+b$	$Q = \sqrt{\frac{e^{2b}}{3}} = \frac{e^b}{\sqrt{3}}$
	Rate white noise	$\sigma^2(\tau) = \frac{N^2}{\tau}$	$y = -1/2x+b$	$N = \sqrt{e^{2b}} = e^b$
	Flicker noise	$\sigma^2(\tau) = \frac{B^2 2 \ln 2}{\pi}$	$y = b$	$B = \frac{e^b}{0.664}$
	Rate random walk	$\sigma^2(\tau) = \frac{K^2 \tau}{3}$	$y = 1/2x+b$	$K = \sqrt{3e^{2b}} = \sqrt{3}e^b$
	Rate ramp	$\sigma^2(\tau) = \frac{R^2 \tau^2}{2}$	$y = x+b$	$R = \sqrt{2e^{2b}} = \sqrt{2}e^b$
Power Spectral Density (PSD) method	Quantization noise	$\Phi_{\text{RQ}}(f) = (2\pi f)^2 Q^2 \Delta t$	$y = 2x+b$	$Q = \frac{1}{2\pi\sqrt{\Delta t}} \sqrt{e^b}$
	Rate white noise	$\Phi_{\text{RN}}(f) = N^2$	$y = b$	$N = \sqrt{e^b}$
	Flicker noise	$\Phi_{\text{RB}}(f) = \frac{B^2}{2\pi f}$	$y = -x+b$	$B = \sqrt{2\pi} \sqrt{e^b}$
	Rate random walk	$\Phi_{\text{RK}}(f) = \frac{K^2}{(2\pi f)^2}$	$y = -2x+b$	$K = 2\pi \sqrt{e^b}$
	Rate ramp	$\Phi_{\text{RR}}(f) = \frac{R^2}{(2\pi f)^3}$		

Table B.1. Inertial sensor stochastic noise representations of the Allan variance analysis and the PSD method.

Where: σ is the Allan variance; τ is the time lag for the Allan variance analysis; Δt is the sampling interval; Φ is the PSD; f is the frequency; Q , N , B , K and R are the stochastic error coefficients for the stochastic errors (1) Quantization noise, (2) Rate white noise, (3) Flicker noise, (4) Rate random walk and (5) Rate ramp; y is expressed as

a linear log-log fitting function of x with a const term b used to estimate the coefficients Q , N , B , K and R .

Except for the five basic noise terms, other noise terms, for example, the exponentially correlated (Markov) noise and the sinusoidal noise, may also exhibit in the data of an inertial sensor (Annex C of IEEE Std 647, 1995; Annex C of IEEE Std 952, 1997). The exponentially correlated noise is characterized by a noise amplitude parameter and a finite correlated time parameter to form an exponentially decaying function. The slope of the Allan variance log-log plot of the exponentially correlated noise transits from $+1/2$ to $-1/2$; and it will converge to $+1/2$ ($-1/2$) if the time lag τ for the Allan variance analysis is much smaller (longer) than the correlated time parameter. The exponentially correlated (Markov) noise can be easily identified using the Allan variance and PSD methods, while its parameters (the noise amplitude and the correlated time) are not easily estimated using the Allan variance and PSD log-log fitted models, other approaches can be used to recover its relating coefficients, for example, Maximum likelihood estimation (Ash and Skeen, 1995) and ARX models (see, for example, Ljung, 1999). The PSD of the sinusoidal noise is characterized by several distinct frequencies (Annex C of IEEE Std 647, 1995; Annex C of IEEE Std 952, 1997).

Typically, all the aforementioned noise terms may be present in the real data of an actual inertial sensor. The Allan variance and PSD log-log plots for the real output of an inertial sensor include the combined effects of these noise terms (and Figure B.1 illustrates an example Allan variance and PSD log-log plots (from IEEE Std 647, 1995 and IEEE Std 1293, 1998). Experiments indicate that in most of the case these noise terms are statistically independent and appear in different regions of time lag τ and frequency f , thus it is possible to recover the noise characteristics of different noise terms using the Allan variance and PSD methods (IEEE Std 647, 1995).

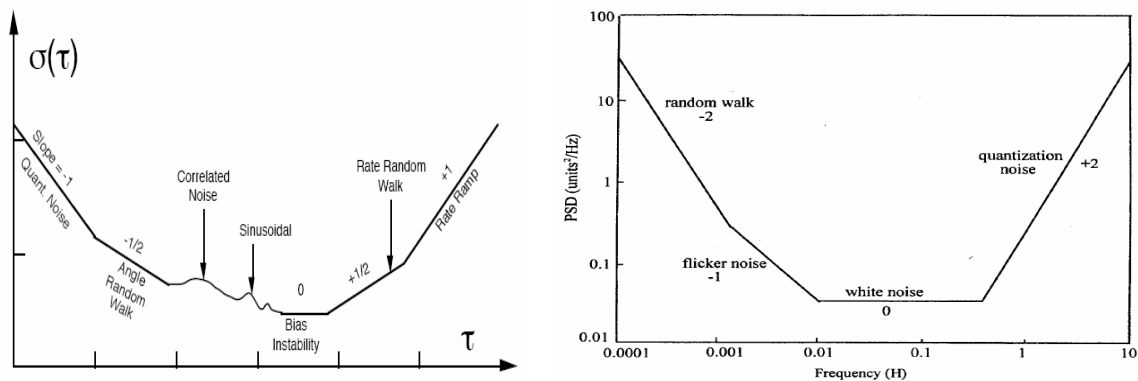


Figure B.1. The sample Allan variance (left) and PSD (right) log-log plots for the noise terms of an inertial sensor (Note: The PSD log-log plot (right) does not list the rate ramp, correlated and sinusoidal noises).

B.1 Static data analysis using the Allan variance analysis

The Allan variance estimation, according to equation 4.3 in Chapter 4, requires a relatively heavy computation burden if all lags τ up to half size of the dataset are computed. Thus, a set of lags τ is pre-selected by choosing the logarithmically equally spaced points between decades 10^{-3} and 10^4 . The number of spaced points, 100, 150, 200, 250, 500, 1000, 2000, 3000, 4000 and 5000, were tested, and 150 spaced points could balance the computational load, and the visualized effects of the calculated Allan variance $\sigma(\tau)$. The following Allan variance computations are based on 150 pre-selected points, and done by a C++ program called “*Allanvarest*”. The Allan variance stochastic error coefficients are estimated using the log-log models shown in the third column of Table B.1, which could be (not necessarily) done with the aid of some visualized tools. Thus, several Matlab™ script functions are implemented to interactively estimate the error coefficients of the noise terms using their log-log fitted models in the Matlab™ environment.

B.1.1 Allan variance analysis of H764G static data

The long dataset (~ 8 hours) of H764G collected on DOY 178, 2004 is used here as an example analysis to investigate the Allan variance analysis for H764G. Figure B.2 presents the Allan variance estimation for the three orthogonal accelerometers and the three orthogonal gyroscopes. The Allan variance estimations for the three gyroscopes are very similar, and each starts with a quantization noise up to 5 [sec] and ends with a rate white noise (angular random walk). The three accelerometers behave very similarly in the short time range, while they differ in the tail time areas. Each accelerometer starts with the short-time quantization noise up to 1 [sec], then switches to the rate white noise (velocity random walk), followed by a period of flicker noise. The tails of the three accelerometers differ significantly. The accelerometer in the x direction has a slope less than $+\frac{1}{2}$ around the tail time region, the best log-log fitting function for the accelerometer x direction at the tail (200-10000 [sec]) is $f(x) = +0.2567x - 11.3$, shown in Figure B.3. The accelerometers in the y and z directions both have $+\frac{1}{2}$ slopes in the tail of the time scale, but the accelerometer in y direction ends with a $+1$ slope. Figures 2.3-2.8 show the Allan variance log-log plots of the fitted error models for the three accelerometers and the three gyroscopes, and the Allan variance error characteristics and estimated error coefficients are listed in Table B.2.

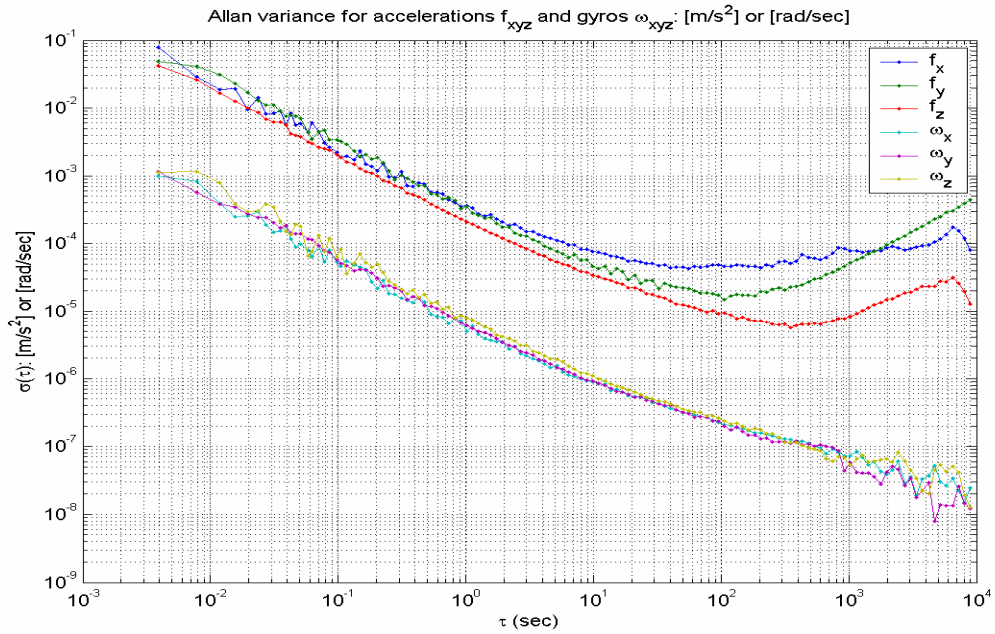


Figure B.2. The Allan variance log-log plot for H764G using dataset of DOY 178, 2004.

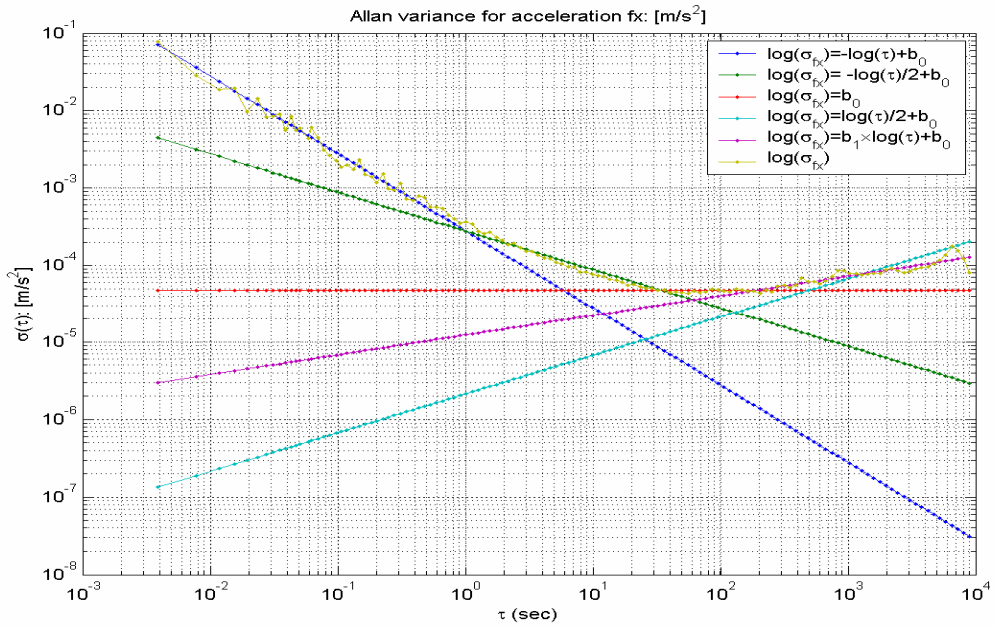


Figure B.3. The Allan variance log-log plot of the fitted error models for H764G x accelerometer using dataset of DOY 178, 2004.

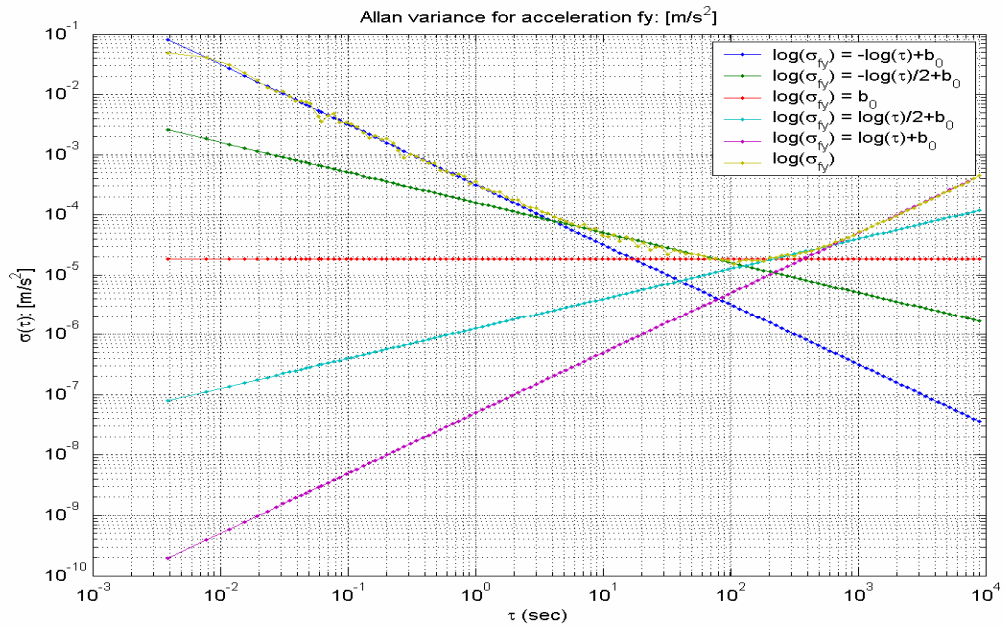


Figure B.4. The Allan variance log-log plot of the fitted error models for H764G *y* accelerometer using dataset of DOY 178, 2004.

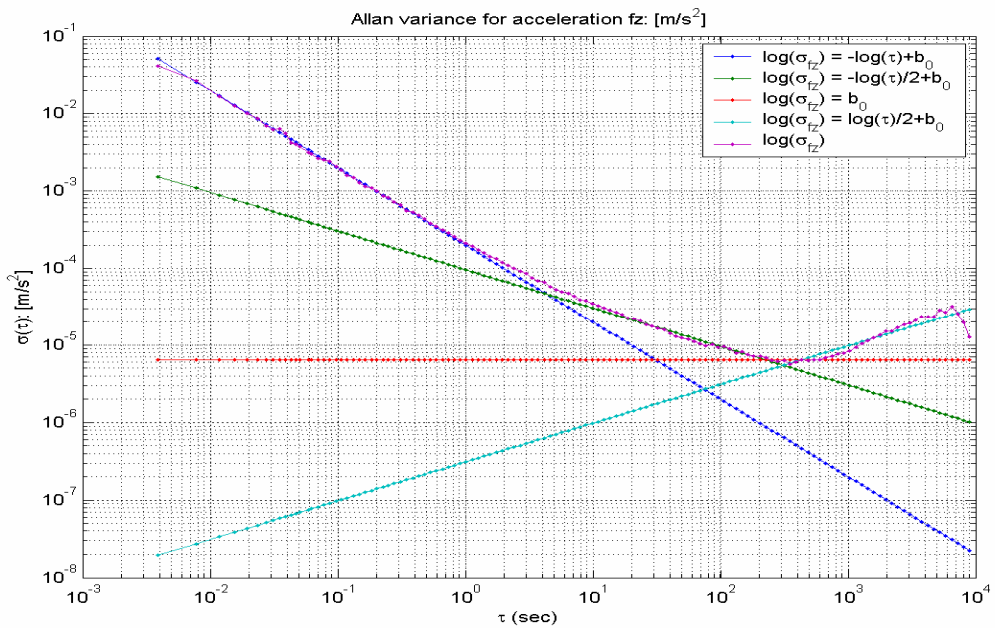


Figure B.5. The Allan variance log-log plot of the fitted error models for H764G *z* accelerometer using dataset of DOY 178, 2004.

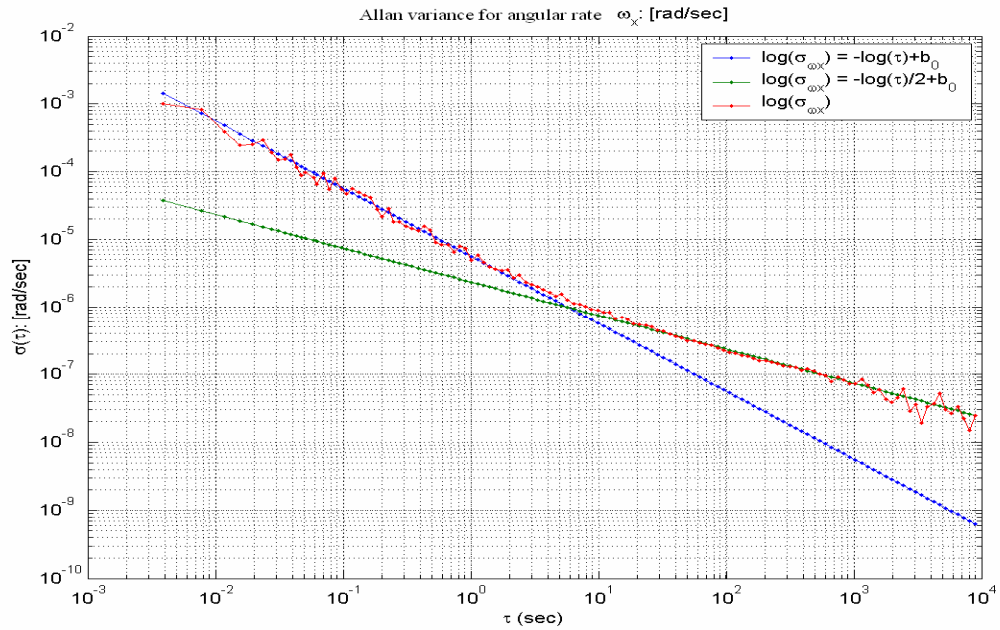


Figure B.6. The Allan variance log-log plot of the fitted error model for H764G x gyroscope using dataset of DOY 178, 2004.

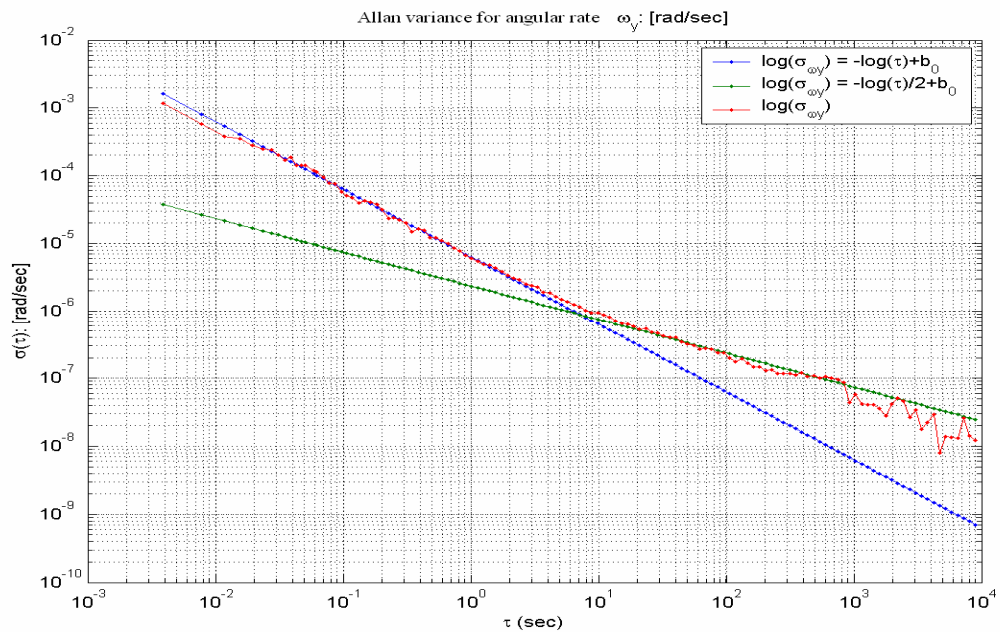


Figure B.7. The Allan variance log-log plot of the fitted error model for H764G y gyroscope using dataset of DOY 178, 2004.

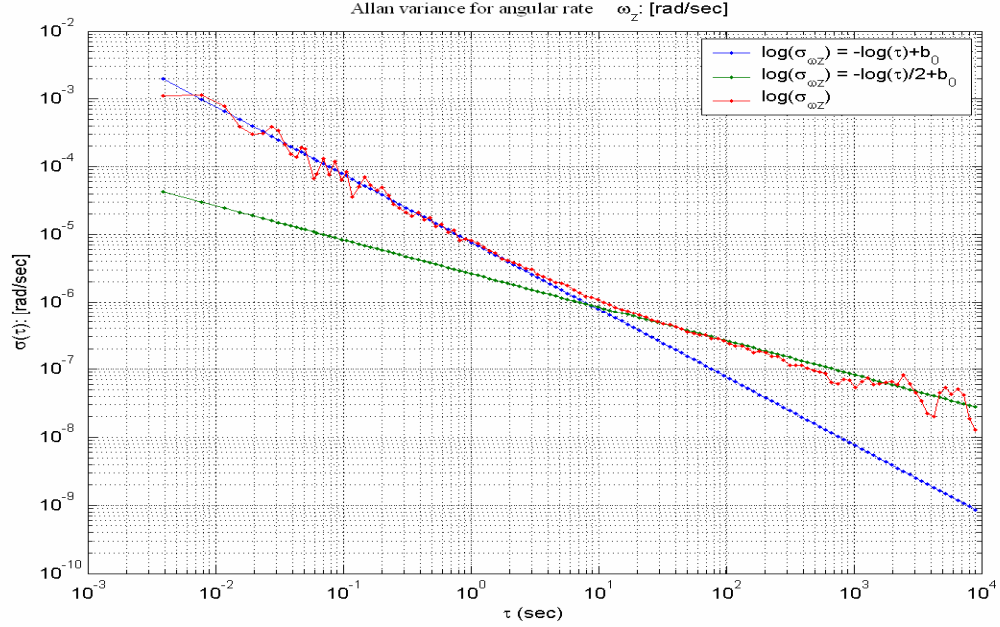


Figure B.8. The Allan variance log-log plot of the fitted error models for H764G z gyroscope using dataset of DOY 178, 2004.

		Q [-1]	N [-1/2]	B [0]	K [1/2]	R [1]
Error characteristics	f_X	<1 [s]	1~10 [s]	20~200 [s]	200~10000 [s]	—
	f_Y	<1 [s]	4~20 [s]	50~200 [s]	200~500 [s]	500~10000 [s]
	f_Z	<1 [s]	10~80 [s]	200~700 [s]	500~5000 [s]	—
	ω_X	<5 [s]	20~100 [s]	—	—	—
	ω_Y	<5 [s]	20~100 [s]	—	—	—
	ω_Z	<5 [s]	20~100 [s]	—	—	—
		Q [unit•s]	N [unit•s ^{1/2}]	B [unit]	K [unit/s ^{1/2}]	R [unit/s]
Error coefficients	f_X	0.0001611	0.0002786	0.0000714	0.0000037	—
	f_Y	0.0001846	0.0001609	0.0000277	0.0000022	0.0000000703
	f_Z	0.0001153	0.0000961	0.0000096	0.0000005	—
	ω_X	0.0000033	0.0000023	—	—	—
	ω_Y	0.0000036	0.0000023	—	—	—
	ω_Z	0.0000045	0.0000026	—	—	—

Table B.2. The Allan variance error characteristics and estimated error coefficients for H764G using dataset of DOY 178, 2004 (Note: unit = $m \cdot s^{-2}$ for the accelerometer measurement and unit = $rad \cdot s^{-1}$ for the gyroscope measurements).

Table B.2 and Figure B.3 indicate that a trend (rate ramp) is evident in the y accelerometer. This effect can be clearly identified in the de-noised raw inertial measurements using, for example, the wavelet de-noising technique described in chapter 5. Such trends may be caused by the environmental variations, for example, temperature. the wavelet de-noising technique was applied to this dataset, and a first-order polynomial function $f(t)=a_0+a_1t$ with respect to the time index t was fitted to remove the time-correlated trends in H764G dataset of DOY 178, 2004. The fitted polynomial coefficients (a_0 and a_1) are listed in Table B.3 and illustrated in Figure B.9. The log-log fitting procedure for the error coefficients was applied to the decorrelated H764G dataset in the time domain, and the results are listed in Table B.4. Comparing to Table B.2, the trend in the y accelerometer disappeared, and also some of other estimated coefficients have slightly changed.

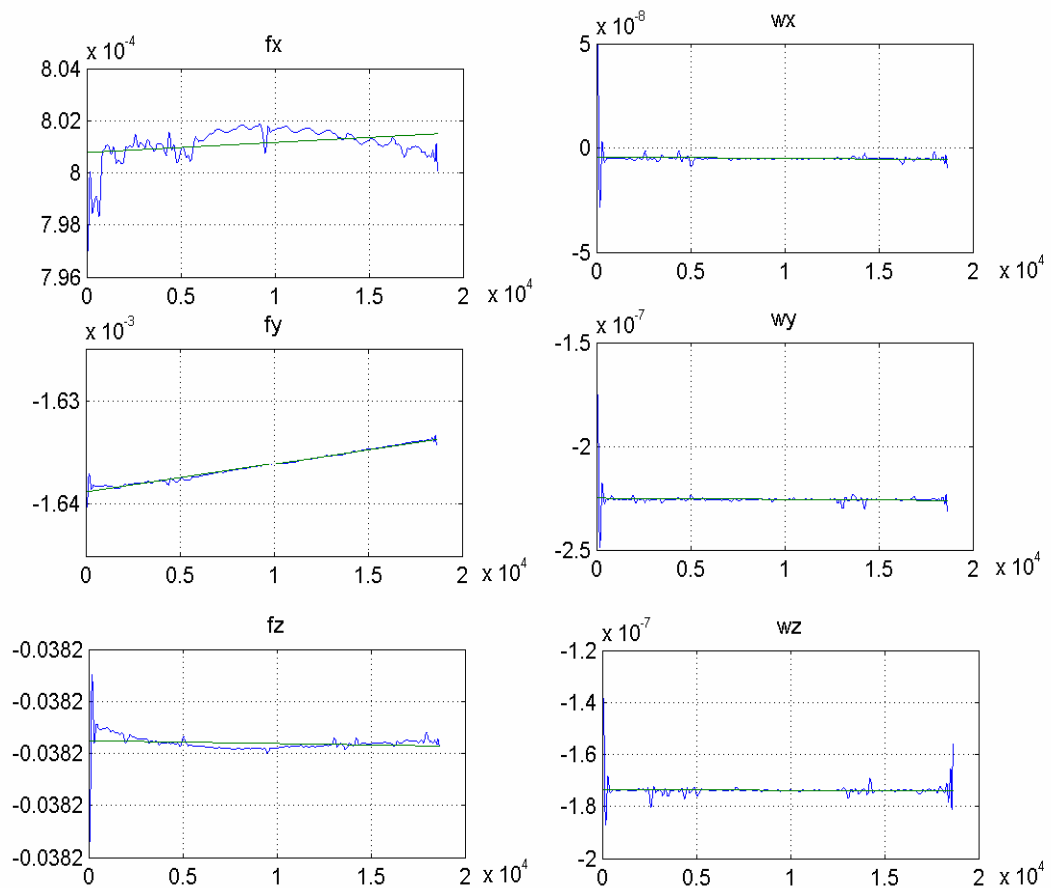


Figure B.9. The de-noised H764G dataset on DOY 178, 2004 using the wavelet de-noising technique.

	$\mathbf{a}_1[\text{unit}\cdot\text{s}^{-1}]$	$\mathbf{a}_0[\text{unit}]$
\mathbf{f}_X	1.500e-013	8.008e-004
\mathbf{f}_Y	1.076e-012	-1.639e-003
\mathbf{f}_Z	-2.175e-014	-3.824e-002
$\boldsymbol{\omega}_X$	-2.572e-016	-4.312e-009
$\boldsymbol{\omega}_Y$	-2.268e-016	-2.251e-007
$\boldsymbol{\omega}_Z$	-5.497e-017	-1.736e-007

Table B.3. Estimated first-order polynomial coefficients to detrend the H764G dataset on DOY 178, 2004 with time.

	Q [-1] [unit•s]	N [-½] [unit•s½]	B [0] [unit]	K [½] [unit/s½]	R [1] [unit/s]
\mathbf{f}_X	0.0001611	0.0002786	0.0000714	0.0000033	
\mathbf{f}_Y	0.0001846	0.0001608	0.0000267	0.0000012	
\mathbf{f}_Z	0.0001153	0.0000961	0.0000095	0.0000005	
$\boldsymbol{\omega}_X$	0.0000033	0.0000023			
$\boldsymbol{\omega}_Y$	0.0000036	0.0000023			
$\boldsymbol{\omega}_Z$	0.0000045	0.0000026			

Table B.4. The estimated Allan variance error coefficients for H764G using dataset of DOY 178, 2004 after removing the trend using a first-order polynomial function with time (Note: unit = $\text{m}\cdot\text{s}^{-2}$ for the accelerometer measurement and unit = $\text{rad}\cdot\text{s}^{-1}$ for the gyroscope measurements).

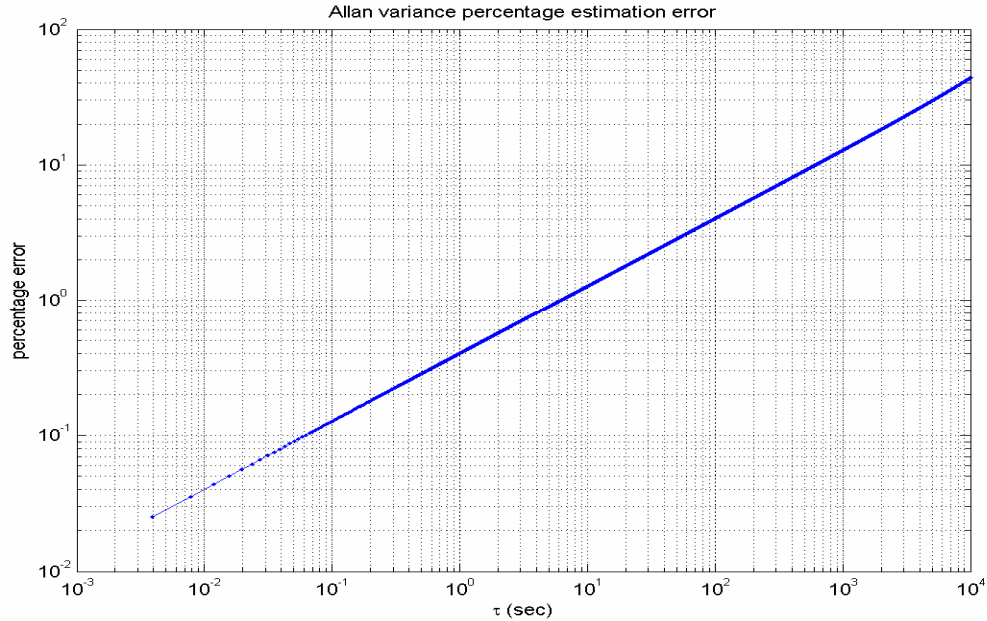


Figure B.10. The Allan variance percentage estimation error.

Following the explanation in chapter 4 of Yi (2007) and equation (4.4), the Allan variance percentage estimation errors are plotted in Figure B.10 to illustrate the Allan variance estimation accuracy. This kind of accuracy assessment is a function of the size of the available static dataset and its sampling rate. From Figure B.10, one can determine that the estimation accuracy is ~ 10 percent at the time $\tau = 600$ [sec]. With the increasing time (i.e., at the tail in the time domain), the coefficients at that time scales will not be reliable. Therefore, the identified stochastic error characteristics at the tail in the time domain will not be used, since they are not reliable, and they are less significant for the applications with frequent external measurement updates (normally a few seconds).

B.2.1 Allan variance analysis of LN100 static data

The long datasets of DOY 178, 2004 does not include the LN100 inertial sensor. The dataset used here to investigate the stochastic error characteristics for LN100 is collected on DOY 294, 2004 (Oct. 20, 2004). This dataset is relatively shorter than the H764G dataset. According to the aforementioned Allan variance estimation percentage error, the Allan variance estimation is only reliable for a short time (up to 100 [sec], with ~ 10 percent error, as shown in Figure B.11). The Allan variance log-log plot for this dataset is shown in Figure B.12, and its percentage error is illustrated in Figure B.11. All three accelerometers behave very similarly, except for the x accelerometer, which has an obvious offset comparing to the y and z accelerometers. The three accelerometers start with the quantization noise (up to 1 [sec]), and follow with the rate white noises, ending

with flicker noises with some variations. All three gyroscopes start with the quantization noise and end with the rate white noise. The y gyroscope behaves worse than the x and z gyroscopes, which may indicate malfunctioning of the y gyroscope. Figures 2.13-2.18 show the detailed log-log fitted error models for the three accelerometers and gyroscopes, and Allan variance stochastic error characteristics in the time domain together with their coefficients are listed in Table B.5.

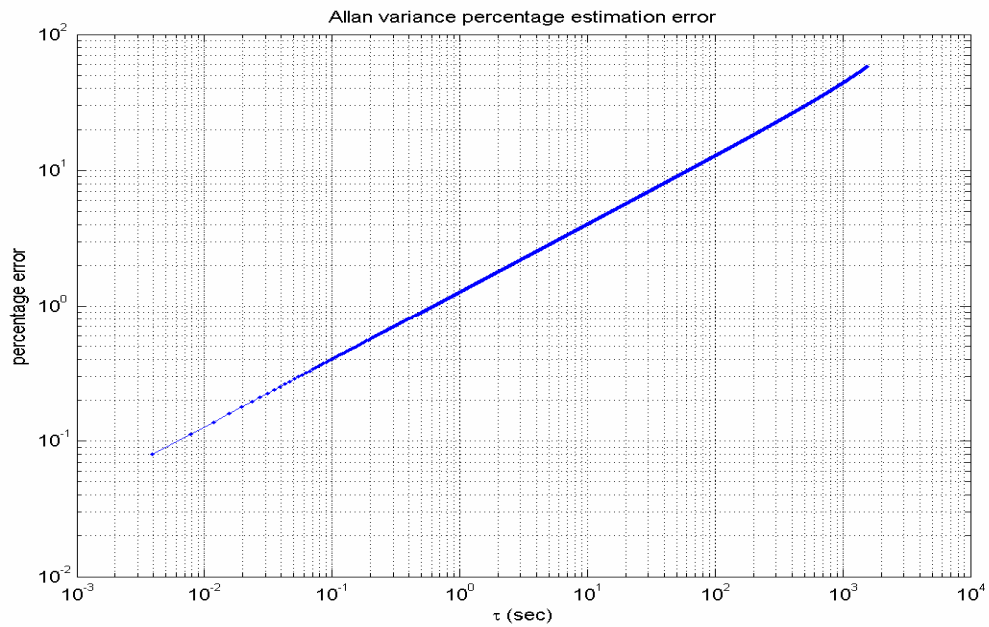


Figure B.11. The Allan variance percentage estimation error for LN100 using dataset of DOY 294, 2004.

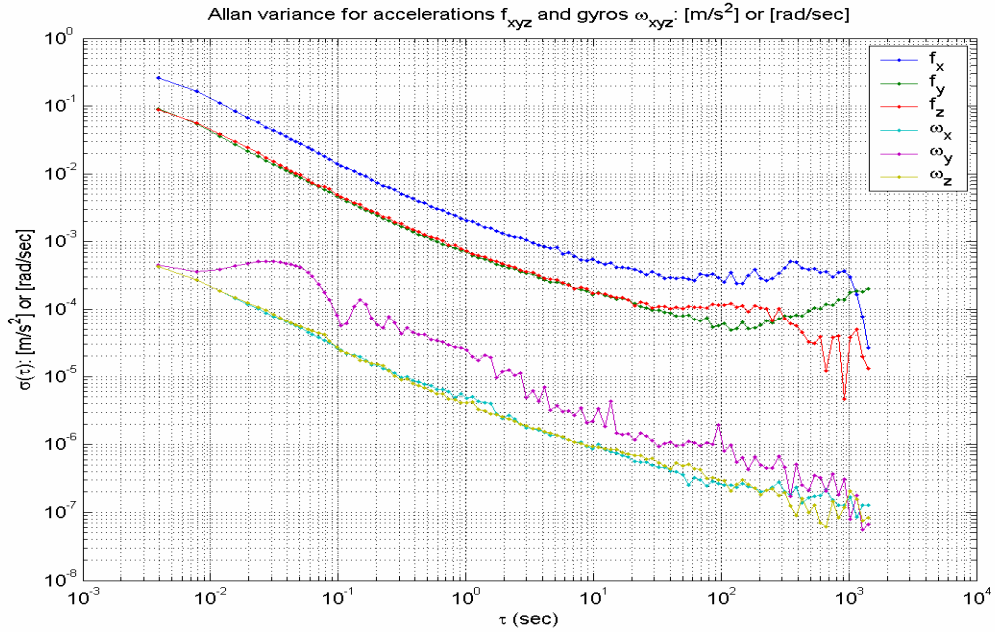


Figure B.12. The Allan variance log-log plot for LN100 using dataset of DOY 294, 2004.

	Q [-1]	N [-1/2]	B [0]	K [1/2]	R [1]
Error characteristics	f_X	<0.4 [s]	1~10 [s]	20~200 [s]	
	f_Y	<0.4 [s]	1~10 [s]	20~200 [s]	
	f_Z	<0.4 [s]	1~10 [s]	20~200 [s]	
	ω_X	<0.4 [s]	1~100 [s]		
	ω_Y	<0.4 [s]	1~100 [s]		
	ω_Z	<0.4 [s]	1~100 [s]		
	Q [unit*s]	N [unit*s ^{1/2}]	B [unit]	K [unit/s ^{1/2}]	R [unit/s]
Estimated error coefficients	f_X	0.0008288	0.0017987	0.0004672	
	f_Y	0.0002684	0.0005969	0.0001085	
	f_Z	0.0002878	0.0006305	0.0001655	
	ω_X	0.0000015	0.0000031		
	ω_Y	0.0000075	0.0000097		
	ω_Z	0.0000016	0.0000032		

Table B.5. The Allan variance stochastic error characteristics and the estimated error coefficients for LN100 using dataset of DOY 294, 2004.

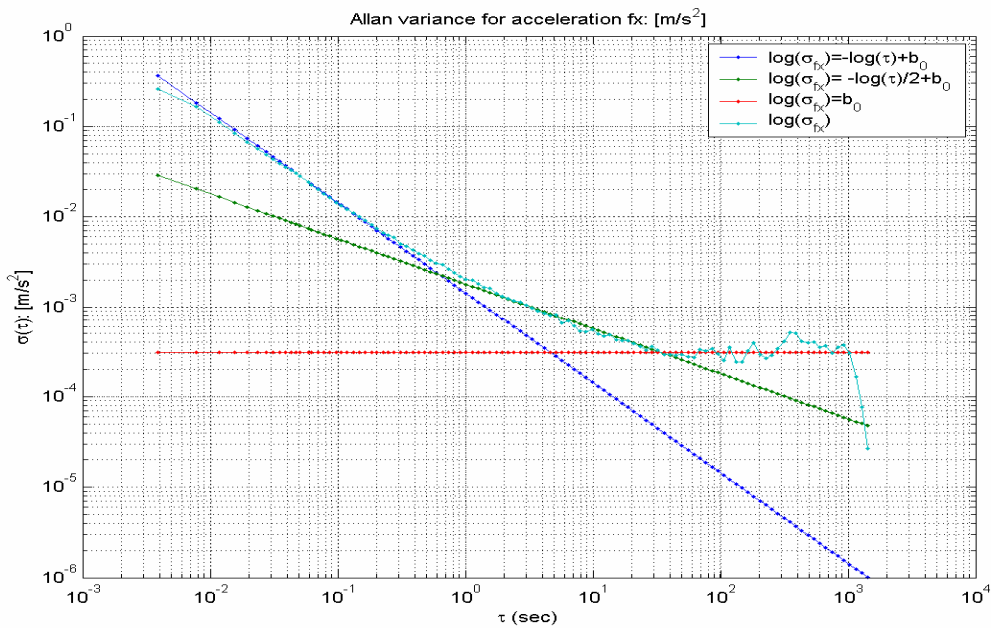


Figure B.13. The Allan variance log-log fitted plot of the x acceleration for LN100 using dataset of DOY 294, 2004.

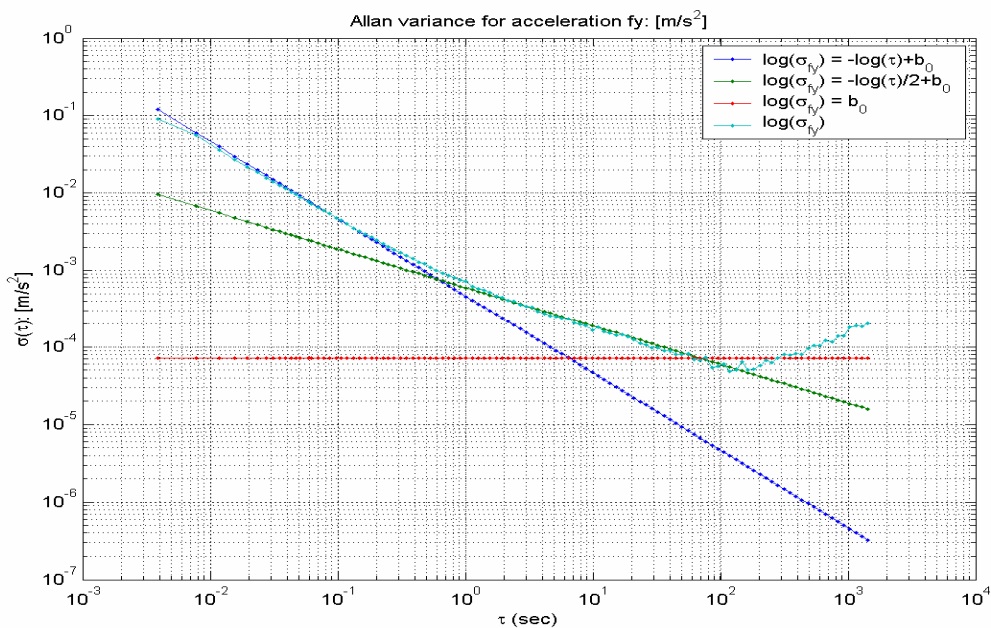


Figure B.14. The Allan variance log-log fitted plot of the y acceleration for LN100 using dataset of DOY 294, 2004.

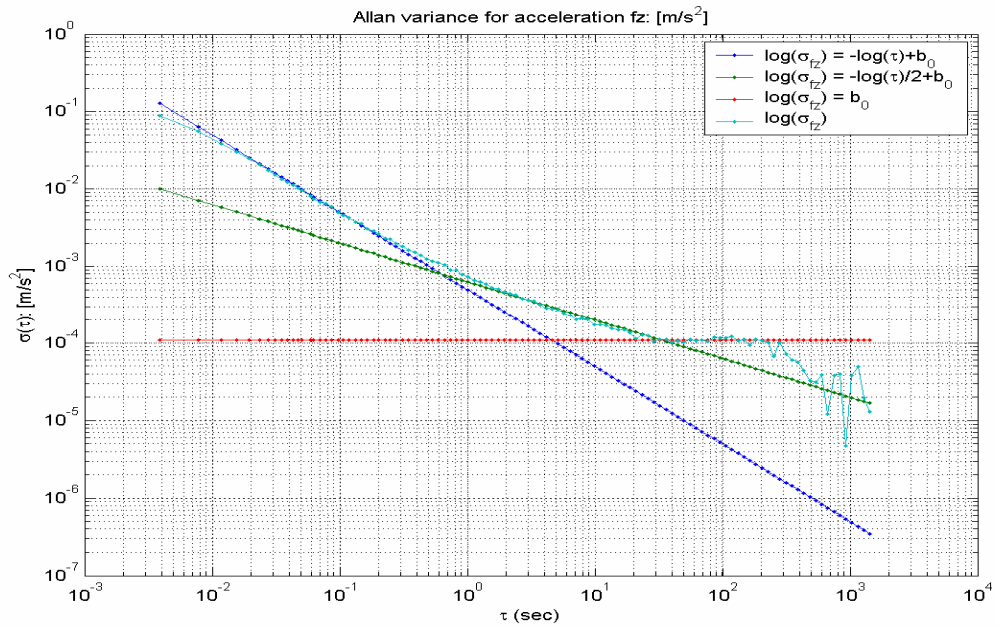


Figure B.15. The Allan variance log-log fitted plot of the z acceleration for LN100 using dataset of DOY 294, 2004.

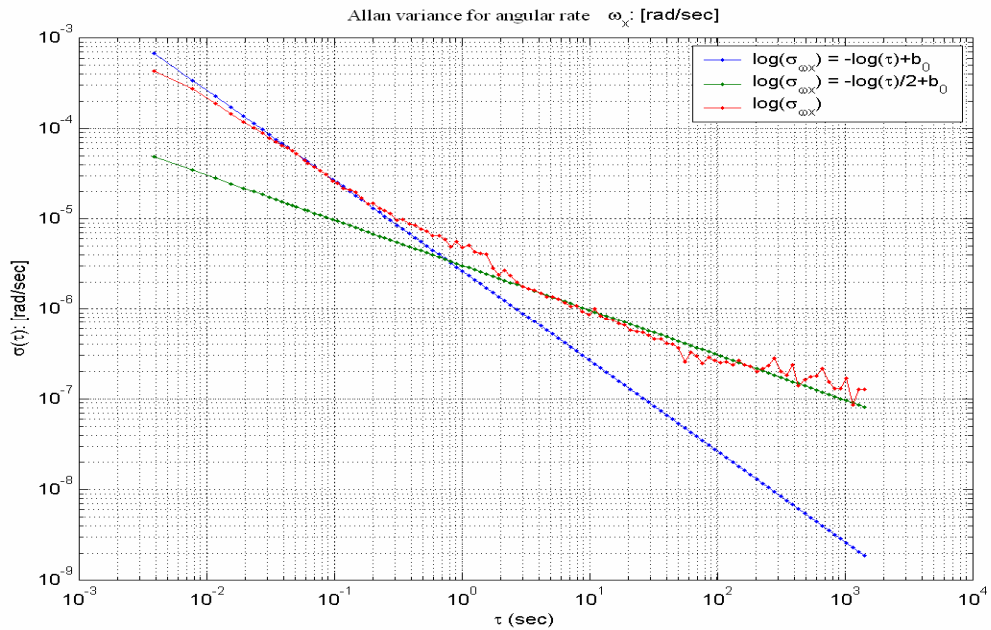


Figure B.16. The Allan variance log-log fitted plot of the x angular rate for LN100 using dataset of DOY 294, 2004.

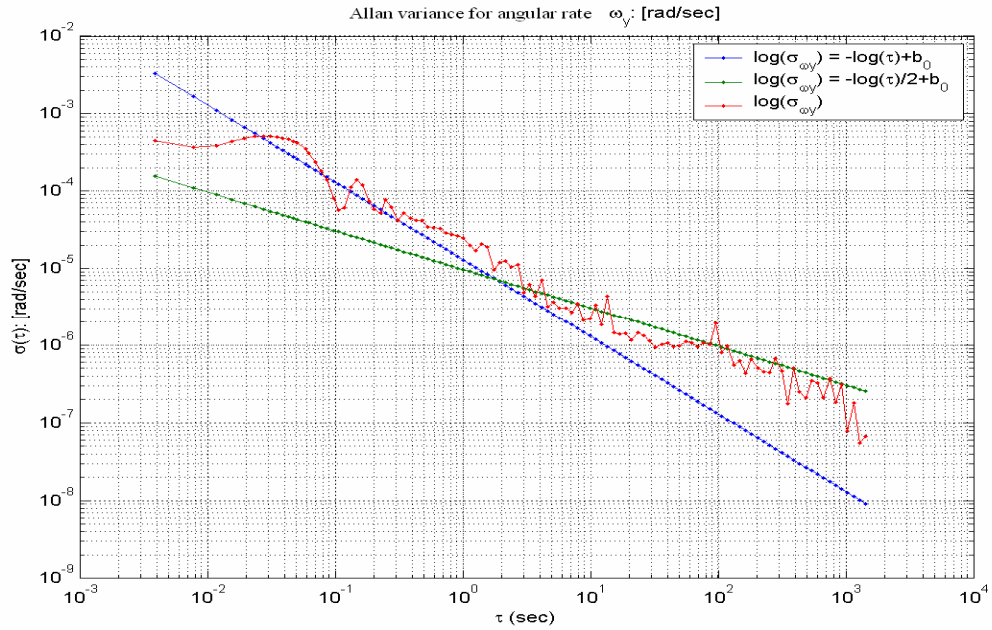


Figure B.17. The Allan variance log-log fitted plot of the y angular rate for LN100 using dataset of DOY 294, 2004.

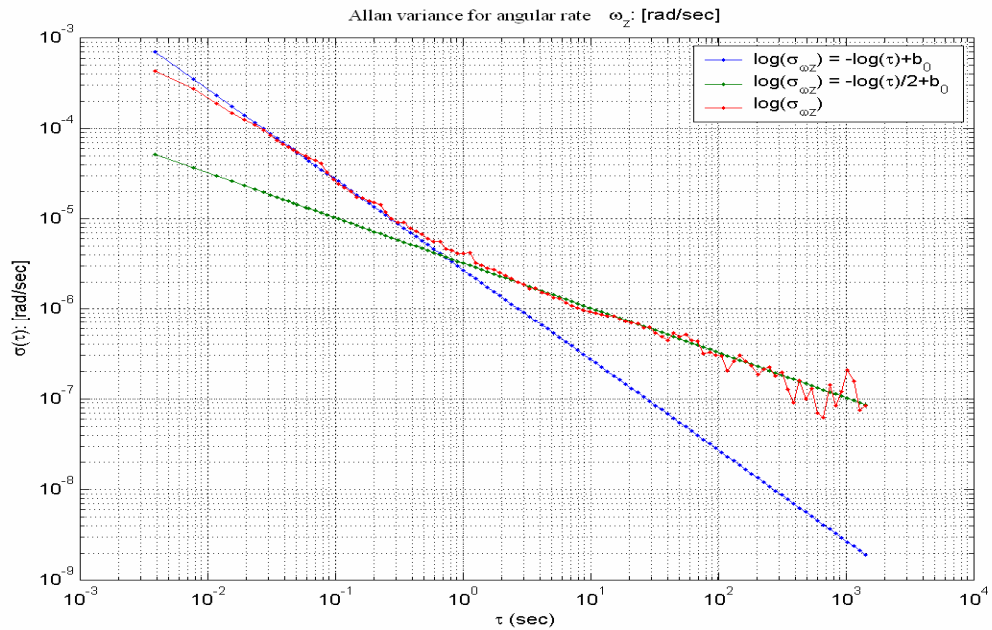


Figure B.18. The Allan variance log-log fitted plot of the z angular rate for LN100 using dataset of DOY 294, 2004.

B.3.1 Allan variance analysis of HG1700 static data

The data of HG1700 include two kinds of inertial measurements (i.e. the accelerometer-integrated velocities, $\Delta\mathbf{V}_{XYZ}$, and the gyroscope-integrated angles, $\Delta\boldsymbol{\theta}_{XYZ}$; and raw accelerations, \mathbf{f}_{XYZ} , and angular rates, $\boldsymbol{\omega}_{XYZ}$) as well as the temperature, T . The dataset ~ 8 -hour long on DOY 178, 2004 is used here to investigate the stochastic error characteristics of HG1700. The temperature-correlated trends existing in the data were first removed using a second-order polynomial function $f(T) = a_0 + a_1T + a_2T^2$ with respect to the sensed temperature, T ; the fitted coefficients (a_0 , a_1 and a_2) are listed in Table B.6. The accelerometer-integrated velocities $\Delta\mathbf{V}_{XYZ}$ and the gyroscope-integrated angles, $\Delta\boldsymbol{\theta}_{XYZ}$, were used in the following analysis.

	a_0 [unit]	a_1 [unit \cdot C $^{-1}$]	a_2 [unit \cdot C $^{-2}$]	a_0 [unit]	a_1 [unit \cdot C $^{-1}$]	a_2 [unit \cdot C $^{-2}$]
\mathbf{f}_X	0.1874908	0.0008166	-0.0000083	0.2061036	-0.0001150	0.0000032
\mathbf{f}_Y	-0.3108470	-0.0063897	0.0000904	-0.3034674	-0.0066903	0.0000935
\mathbf{f}_Z	-9.7935810	0.0000730	-0.0000011	-9.9221986	0.0070796	-0.0000963
$\boldsymbol{\omega}_X$	-0.0000947	0.0000048	-0.0000001	-0.0007429	0.0000414	-0.0000006
$\boldsymbol{\omega}_Y$	-0.0002328	0.0000096	-0.0000001	-0.0003806	0.0000187	-0.0000003
$\boldsymbol{\omega}_Z$	-0.0002798	0.0000124	-0.0000002	-0.0018777	0.0001004	-0.0000014
	$\Delta\mathbf{V}_{XYZ}$ and $\Delta\boldsymbol{\theta}_{XYZ}$			\mathbf{f}_{XYZ} and $\boldsymbol{\omega}_{XYZ}$		

Table B.6. The temperature-correlated bias compensation using a second order polynomial fitting $f(T) = a_0 + a_1T + a_2T^2$ for HG1700 using dataset of DOY 178, 2004 (Note: unit= $\text{m}\cdot\text{s}^{-2}$ for the accelerometer measurements and unit= $\text{rad}\cdot\text{s}^{-1}$).

The Allan variance log-log plot for this dataset is shown in Figure B.19, and its percentage error is illustrated in Figure B.20. The Allan variance estimation percentage error reaches up to 10 [%] around τ of 600 [sec]. All three accelerometers and the three gyroscopes behave very similarly. The three gyroscopes have some slight differences in different directions. The three accelerometers start with the quantization noise (up to around 2 [sec]), and follow with the rate white noise (from around 2 [sec] to 20 [sec]). The flicker noise is from 20 to 40 [sec] and the rate random walk noise is longer than 40 [sec]. The quantization noise in the gyroscopes is not obvious and the rate white noise almost dominates all the time ranges of the gyroscopic measurements. Figures 2.21-2.26 show the detailed log-log fitting for the three accelerometers and gyroscopes, and the Allan variance stochastic error characteristics in the time domain together with their coefficients are listed in Table B.7.

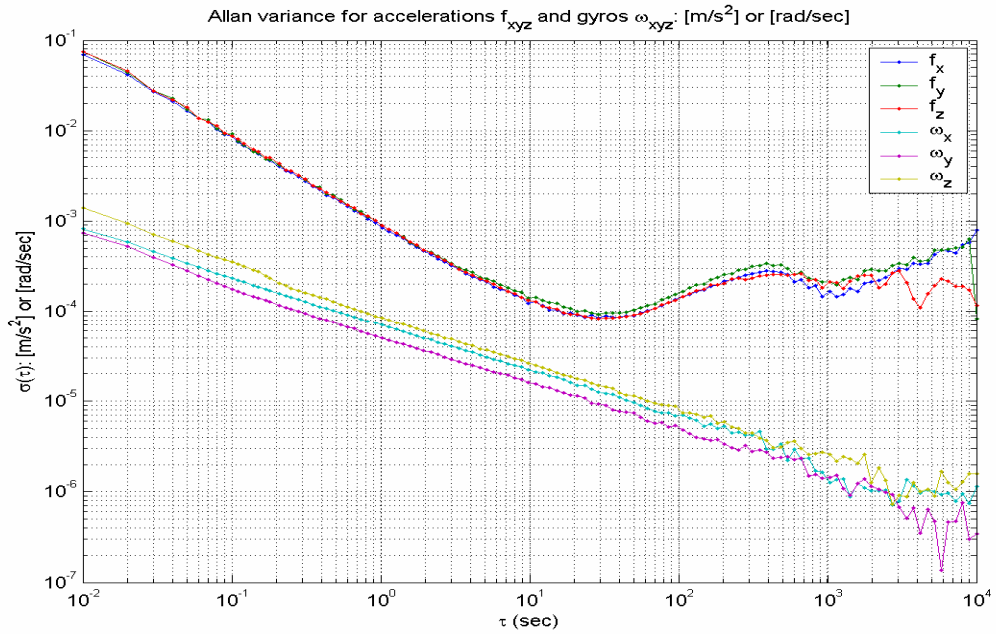


Figure B.19. Allan variance log-log plot for HG1700 using dataset of DOY 178, 2004.

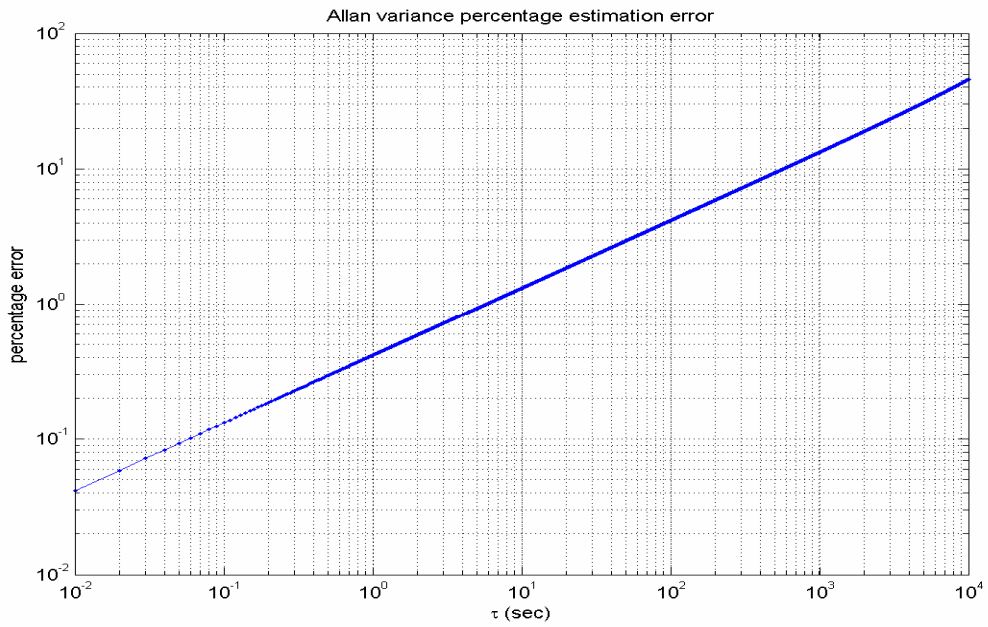


Figure B.20. Allan variance percentage estimation error for HG1700 using dataset of DOY 178, 2004.

		Q [+2]	N [0]	B [-1]	K [-2]	R [-2]
Error characteristics	f_X	<2 [s]	2~20 [s]	20~40 [s]	40~200 [s]	[2]
	f_Y	<2 [s]	2~20 [s]	20~40 [s]	40~200 [s]	[2]
	f_Z	<3 [s]	3~20 [s]	20~40 [s]	40~200 [s]	[2]
	ω_X	–	All time range	–	–	–
	ω_Y	–	All time range	–	–	–
	ω_Z	–	All time range	–	–	–
		Q [+2] [unit•s]	N [0] [unit•s ^{1/2}]	B [-1] [unit]	K [-2] [unit/s ^{1/2}]	R [-2] [unit/s]
Error coefficients	f_X	0.0004881	0.0004202	0.0001320	0.0000239	
	f_Y	0.0005061	0.0004781	0.0001462	0.0000278	
	f_Z	0.0005119	0.0004295	0.0001299	0.0000240	
	ω_X		0.0000693			
	ω_Y		0.0000517			
	ω_Z		0.0000864			

Table B.7. Allan variance stochastic error characteristics and coefficients for HG1700 using dataset of DOY 178, 2004.

HG1700 accelerometers in these time ranges slightly behave as the temporal-correlation errors (i.e. Gaussian-Markov errors). But Allan variance estimation percentage errors in those time ranges are around 10 [%], as shown in Figure B.20, thus they may also be caused by the Allan variance estimation errors.

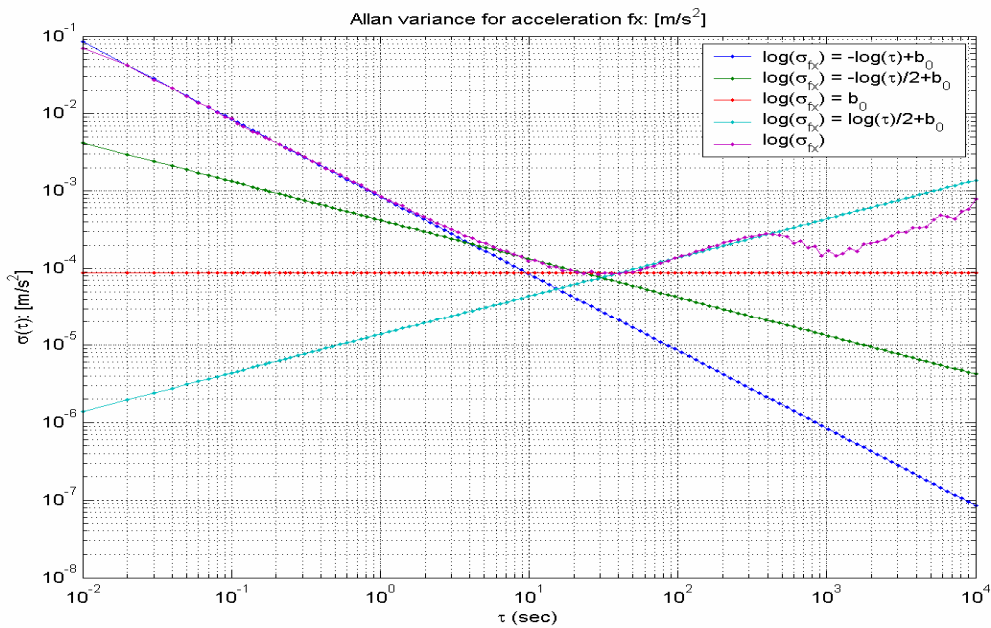


Figure B.21. Allan variance log-log plot fitting of the x acceleration for HG1700 using dataset of DOY 178, 2004.

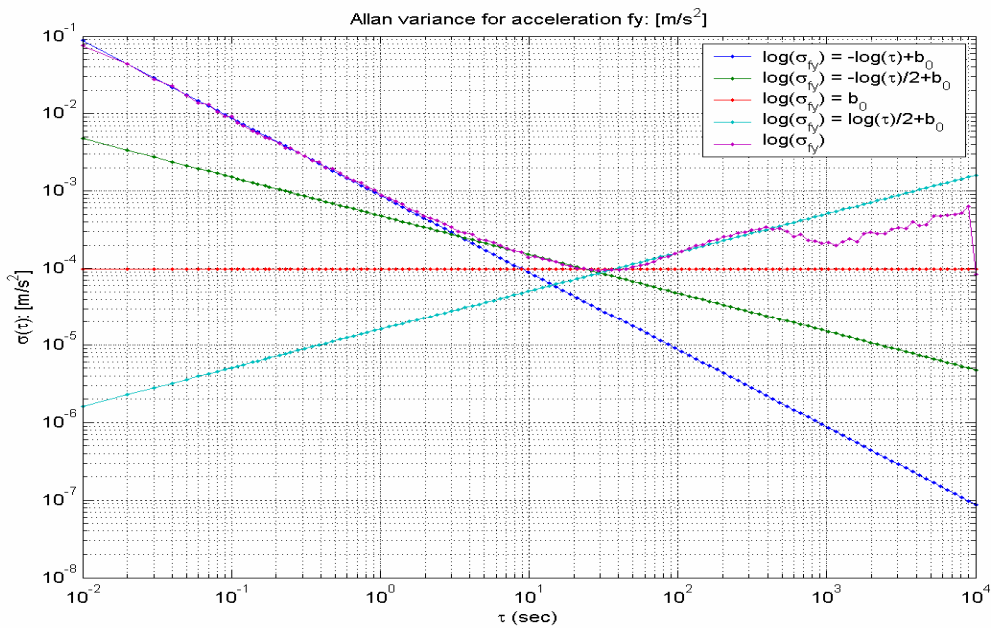


Figure B.22. Allan variance log-log plot fitting of the y acceleration for HG1700 using dataset of DOY 178, 2004.

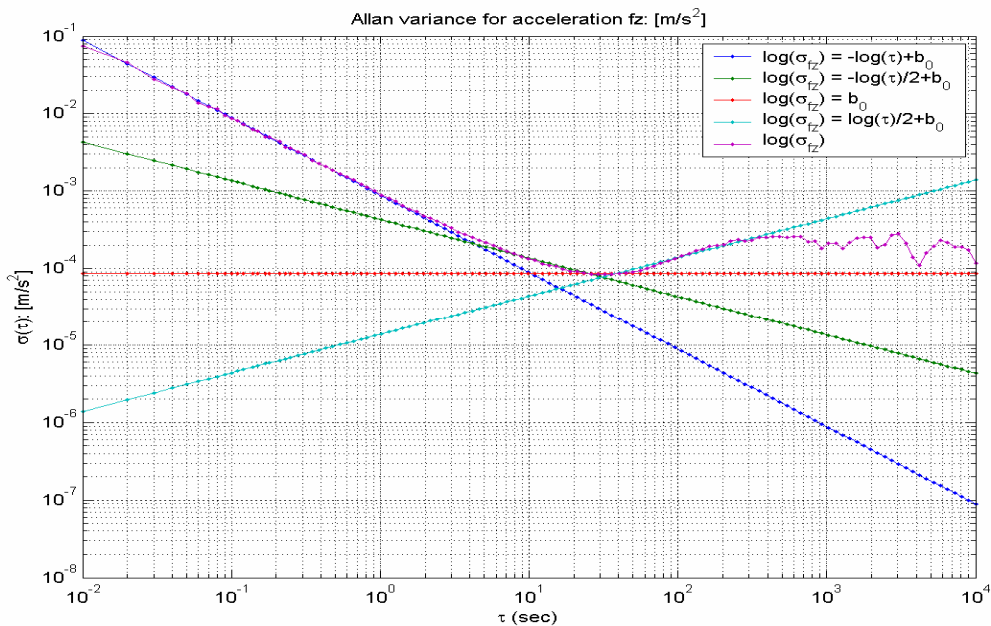


Figure B.23. Allan variance log-log plot fitting of the z acceleration for HG1700 using dataset of DOY 178, 2004.

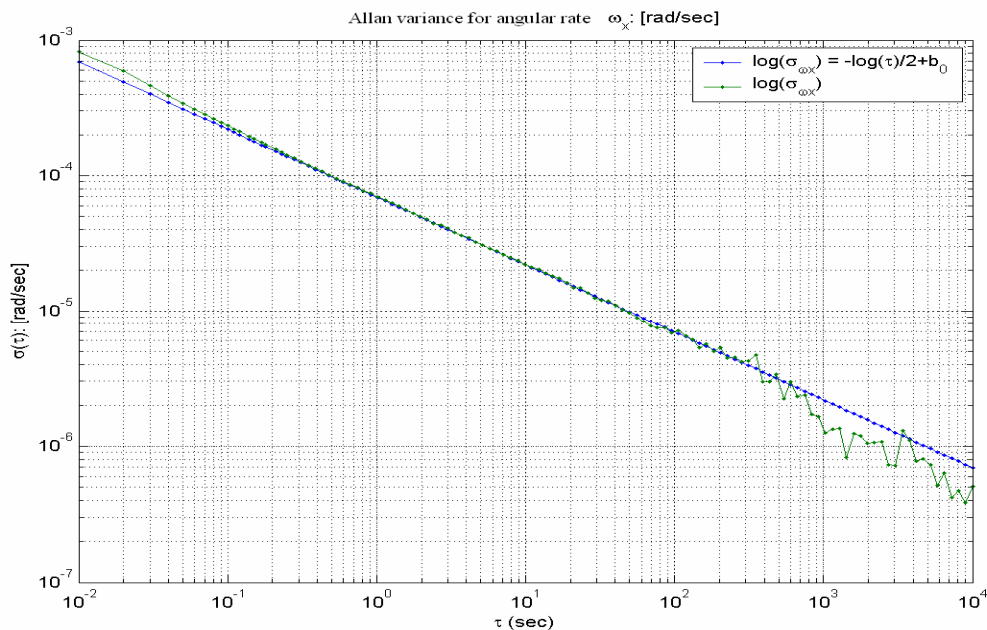


Figure B.24. Allan variance log-log plot fitting of the x angular rate for HG1700 using dataset of DOY 178, 2004.

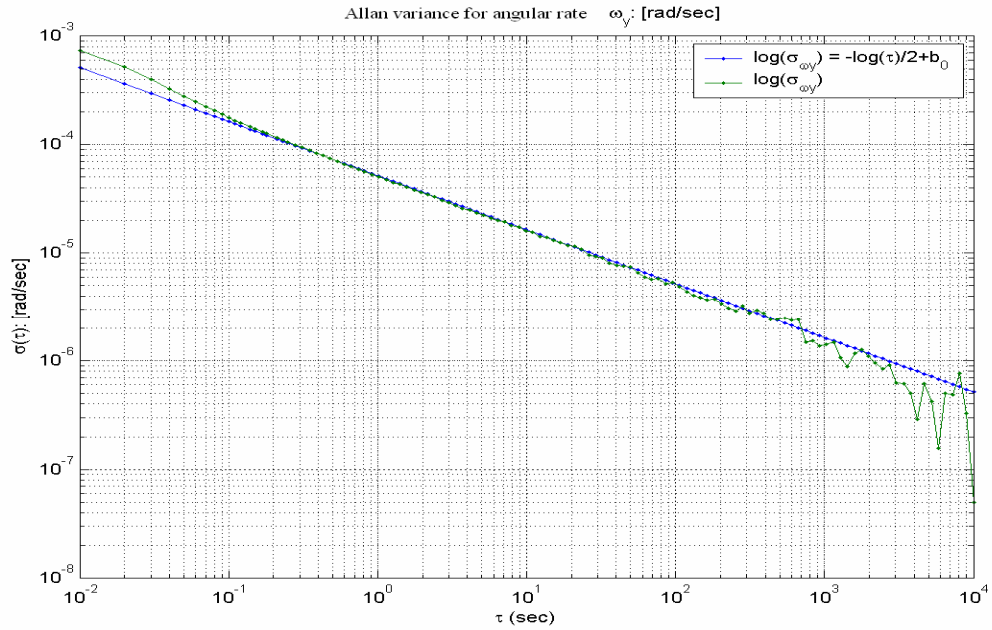


Figure B.25. Allan variance log-log plot fitting of the y angular rate for HG1700 using dataset of DOY 178, 2004.

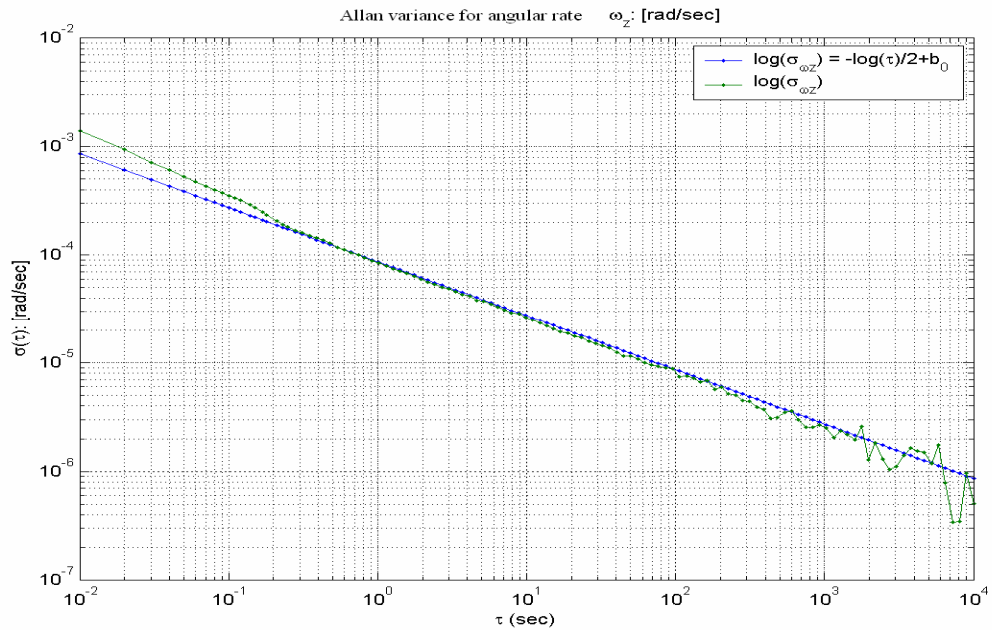


Figure B.26. Allan variance log-log plot fitting of the z angular rate for HG1700 using dataset of DOY 178, 2004.

B.4.1 Allan variance analysis of MEMS IMU400CC static data

Different from the three inertial sensors analyzed above (i.e. H764G, LN100 and HG1700), whose Allan variance analysis are based on the accelerometer-integrated velocities, $\Delta\mathbf{V}_{XYZ}$, and gyroscope-integrated angles, $\Delta\boldsymbol{\theta}_{XYZ}$, the inertial measurements from the MEMS IMU400CC are the direct raw accelerations, \mathbf{f}_{XYZ} , and angular rates, $\boldsymbol{\omega}_{XYZ}$, as well as the temperature, T . The dataset ~ 8 -hour in length of DOY 178, 2004 is used here to investigate the stochastic error characteristics of MEMS IMU400CC. A stronger temperature correlation can be found in this low-cost inertial sensor, comparing to HG1700; thus the temperature-correlated trend must be removed using, for example, a second-order polynomial function $f(T) = a_0 + a_1T + a_2T^2$ with respect to the sensed temperature, T . The fitted coefficients are listed in Table B.8. The z accelerometer has a much stronger temperature correlation than the other two sensors. Due to the stronger temperature correlation in the data of MEMS IMU400CC, the data before and after the temperature compensation are analyzed to compare the trend effects in the raw data using the Allan variance analysis. Similarly to the example shown in Figure B.8, such polynomial function fitting will remove the rate trends shown at the tail of the Allan variance plots.

	$a_0[\text{unit}]$	$a_1[\text{unit}\cdot\text{C}^{-1}]$	$a_2[\text{unit}\cdot\text{C}^{-2}]$
\mathbf{f}_X	-0.1147975	0.0028128	-0.0000425
\mathbf{f}_Y	-0.3547928	-0.0037804	0.0000608
\mathbf{f}_Z	-9.7049829	0.0112242	-0.0001836
$\boldsymbol{\omega}_X$	-0.0384758	0.0028094	-0.0000507
$\boldsymbol{\omega}_Y$	-0.0542311	0.0037562	-0.0000631
$\boldsymbol{\omega}_Z$	0.0145822	-0.0015856	0.0000288

Table B.8. The temperature-correlated bias compensation using second order polynomial fitting $f(T) = a_0 + a_1T + a_2T^2$ for MEMS IMU400CC using dataset of DOY 178, 2004.

Figures 2.27 and 2.28 present the Allan variance estimations for the inertial measurements (i.e. accelerations and angular rates) before and after removing the temperature correlated trends. Their cross-comparisons indicate that their short time (up to 100 [sec]) stochastic error characteristics are not affected by the removal of the trends, and the tails (starting from 100 [sec] to 10^4 [sec]) behave differently, especially in the z accelerometer, which has large variations at the tail of the Allan variance estimations. The rate white noise dominates all the inertial measurements of this sensor in the short time periods (up to 100 [sec]) and then the flicker noise is followed. Even the Allan variance estimations of the accelerometer in z direction are significantly different from these of the accelerometers in the x and y directions, a flicker noise with larger variations can still be approximated for it. The Allan variance estimation percentage error is very

similar to that of HG1700 shown in Figure B.20 due to the similar data size (both ~8-hour length) and sampling rate (134 [Hz] for MEMS IMU400CC and 100 [Hz] for HG1700); thus it is not shown here. The log-log model fitting plots for the stochastic error coefficients are shown in Figure B.29-2.34 and are listed in Table B.9.

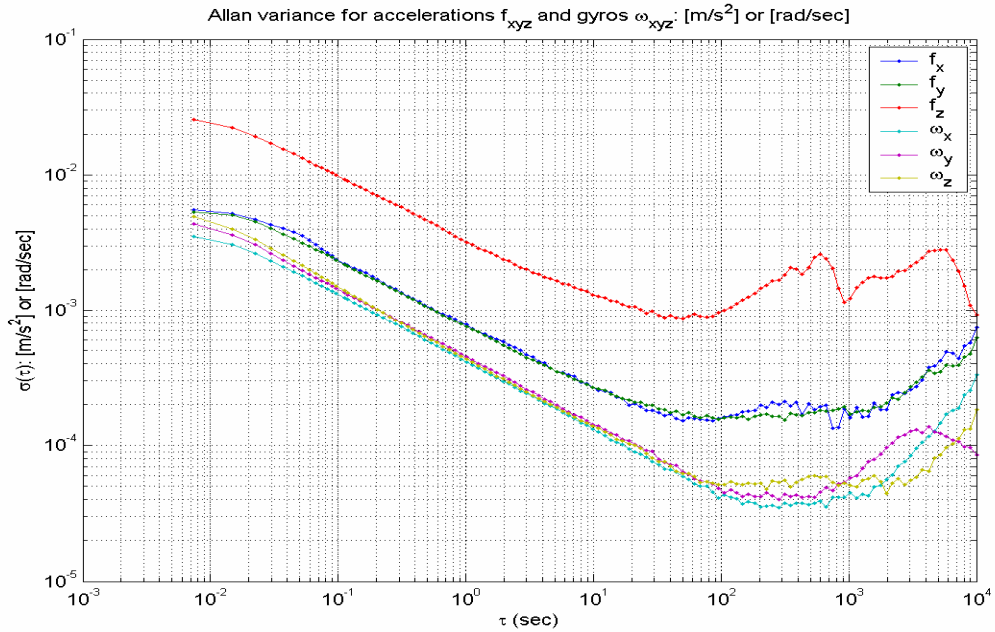


Figure B.27. Allan variance log-log plot for IMU400CC using dataset of DOY 178, 2004 before removing the temperature correlated trends.

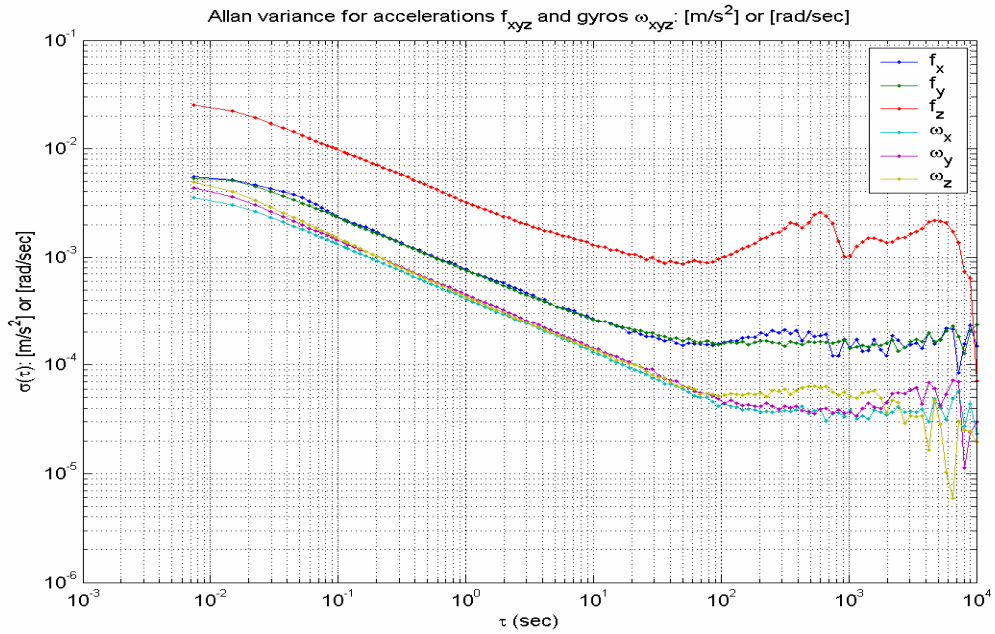


Figure B.28. The Allan variance log-log plot for IMU400CC using dataset of DOY 178, 2004 after removing the temperature correlated trends.

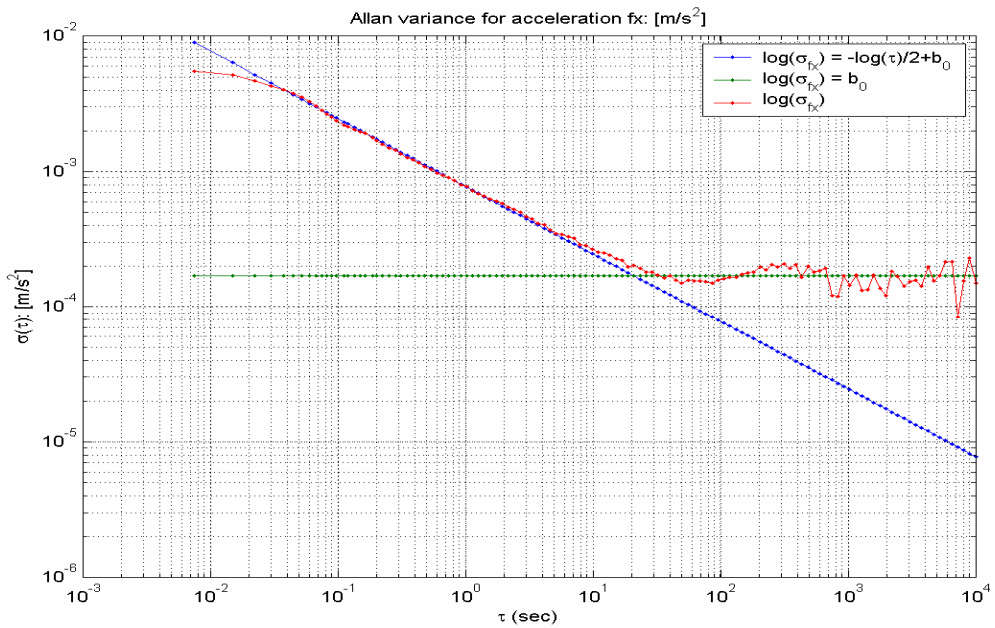


Figure B.29. Allan variance log-log plot fitting of the x acceleration for IMU400CC using dataset of DOY 178, 2004.

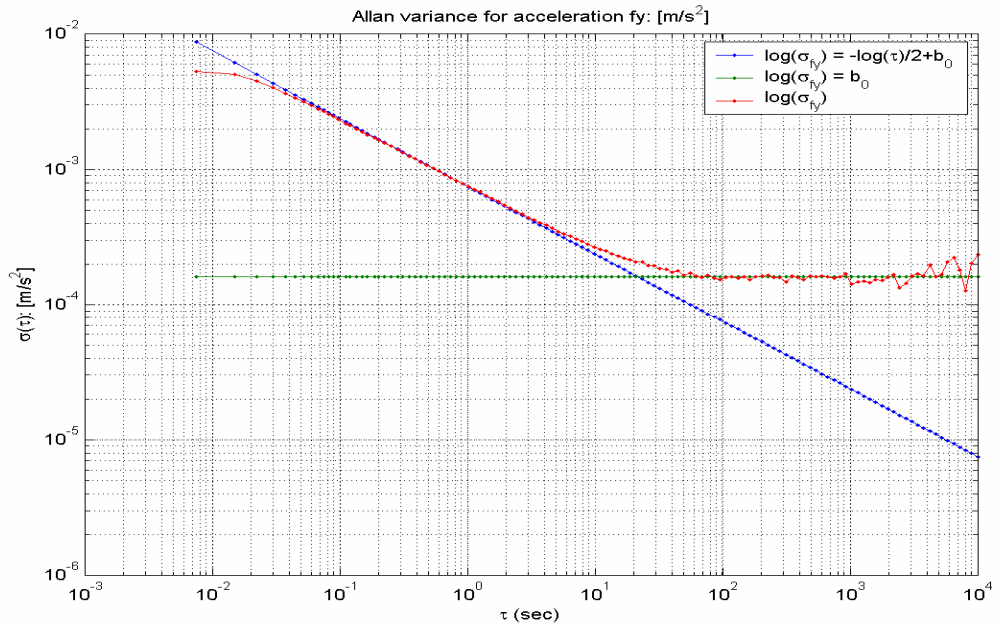


Figure B.30. Allan variance log-log plot fitting of the y acceleration for IMU400CC using dataset of DOY 178, 2004.

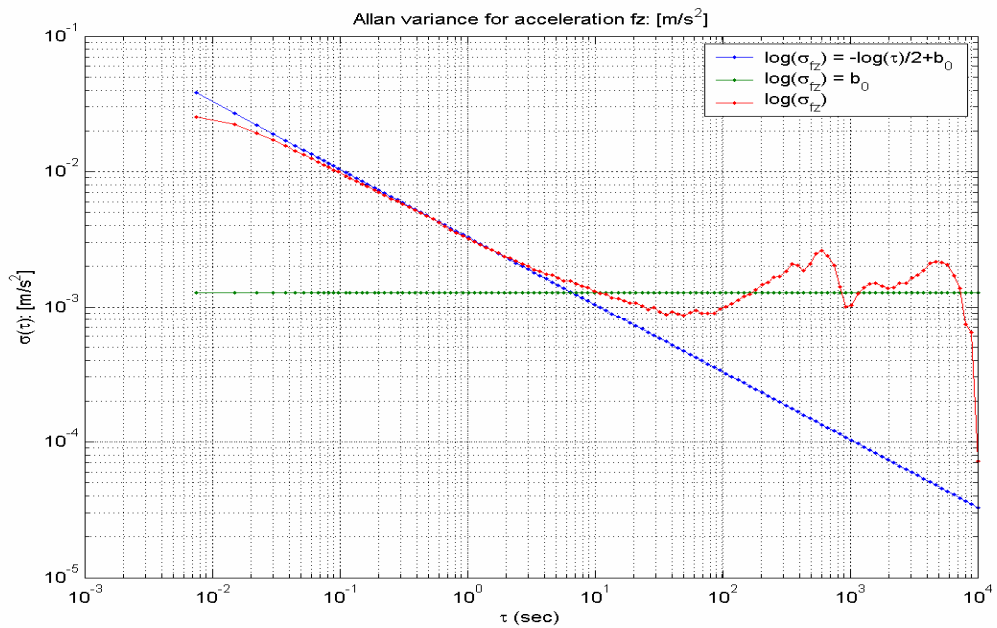


Figure B.31. Allan variance log-log plot fitting of the z acceleration for IMU400CC using dataset of DOY 178, 2004.

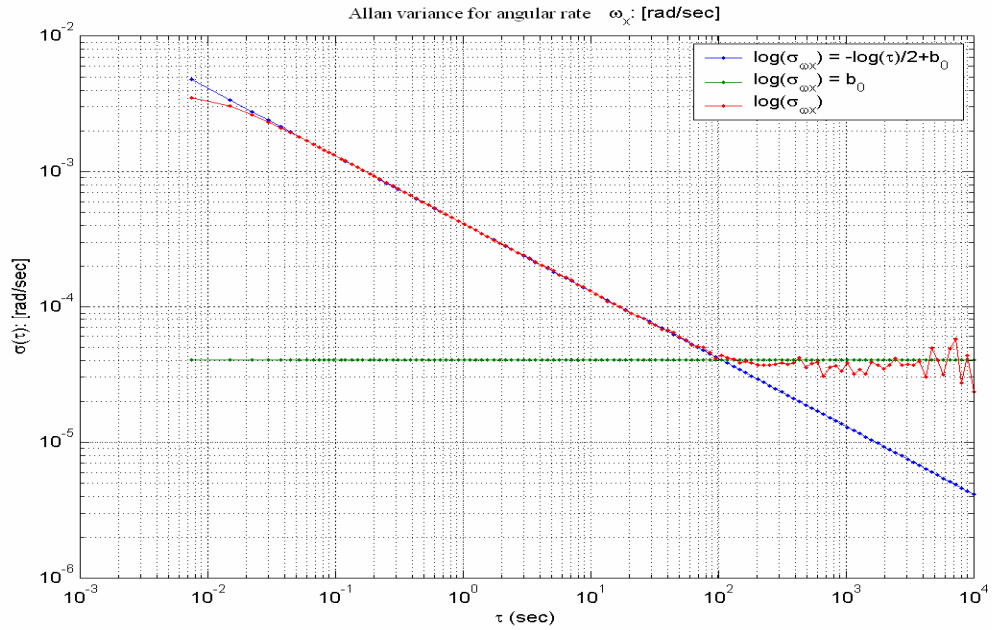


Figure B.32. Allan variance log-log plot fitting of the x angular rate for IMU400CC using dataset of DOY 178, 2004.

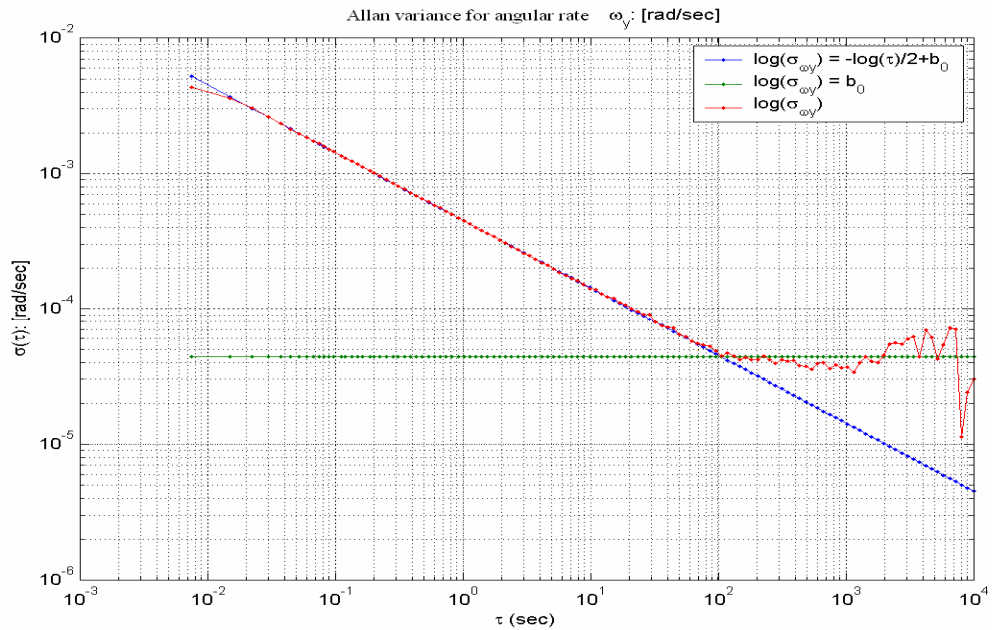


Figure B.33. Allan variance log-log plot fitting of the y angular rate for IMU400CC using dataset of DOY 178, 2004.

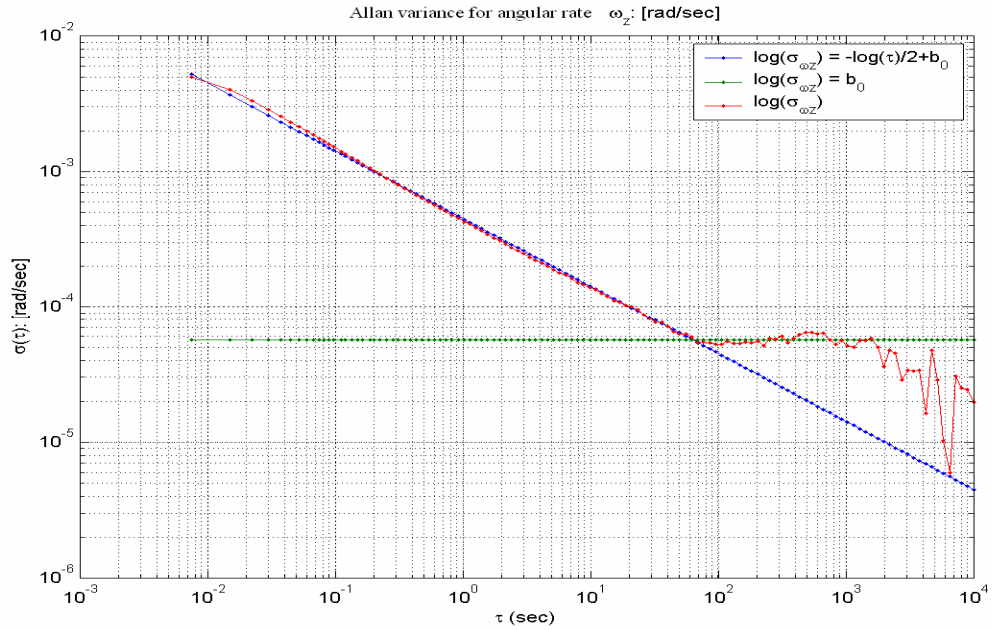


Figure B.34. Allan variance log-log plot fitting of the z angular rate for IMU400CC using dataset of DOY 178, 2004.

		Q [+2]	N [0]	B [-1]	K [-2]	R [-2]
Error characteristics	f_X		<40 [s]	>40 [s]		
	f_Y		<40 [s]	>40 [s]		
	f_Z		<10 [s]	>10 [s]		
	ω_X		<100 [s]	>100 [s]		
	ω_Y		<100 [s]	>100 [s]		
	ω_Z		<100 [s]	>100 [s]		
		Q [+2] [unit•s]	N [0] [unit•s ^{1/2}]	B [-1] [unit]	K [-2] [unit/s ^{1/2}]	R [-2] [unit/s]
Error coefficients	f_X		0.0007786	0.0002571		
	f_Y		0.0007527	0.0002430		
	f_Z		0.0032906	0.0019150		
	ω_X		0.0004144	0.0000609		
	ω_Y		0.0004521	0.0000659		
	ω_Z		0.0004499	0.0000852		

Table B.9. Allan variance stochastic error characteristics and coefficients for IMU400CC using dataset of DOY 178, 2004.

B.2 Static data analysis using the Power Spectral Density (PSD) method

Differently from the Allan variance analysis in the time domain, the PSD method identifies the INS stochastic error characteristics in the frequency domain. With the aiding of advanced computational techniques, for example, the Fast Fourier Transform (FFT), the spectrum of the signals (here, inertial measurements) can be easily estimated. Several spectral estimation methods exist, for example, (1) Nonparametric methods; (2) Parametric methods and (3) Subspace methods (Djuric & Kay, 1998). The *nonparametric methods* directly estimate the PSD from the signal itself, for example, (1) the simplest *periodogram* method, (2) the improved version of *periodogram method* called *Welch's method*; and (3) the modern *multi-taper method* (MTM). In the *parametric methods*, the signal is treated as a random process, whose coefficients are directly estimated first from the signal, and the PSD of the signal is obtained from the PSD of the random process. Example techniques include the *Yule-Walker autoregressive (AR) method* and *Burg method*. The parametric methods work better than the nonparametric methods for a relatively small data size. The *subspace methods* are also known as *high-resolution methods* or *super-resolution methods*. Such methods estimate the PSD of a signal using *eigenanalysis* or *eigendecomposition* of the correlation matrix. The example methods of this category are the *multiple signal classification (MUSIC) method* or the *eigenvector (EV) method*. All the aforementioned PSD methods are implemented in the Matlab software package. Here the Matlab function “*pwelch*”, which implements a *Welch's method*, is used to estimate the PSD of the inertial measurements. The Matlab function “*pwelch*”, can estimate both the “*one-sided*” and “*two-sided*” PSDs, and the log-log models shown in Table B.1 are based on the “*two-sided*” PSD estimation.

B.1.2 PSD analysis of H764G static data

The data used here are the same as that used in the Allan variance analysis, which is based on the long H764 dataset of DOY 178, 2004. Figures 2.35-2.40 show the PSD estimations and their log-log error fitted models. The PSD estimations shown in Figure B.35-2.40 (also the figures shown later for H764G, HG1700 and IMU400CC) represent the combinations of the environmental noise to the inertial sensors and the intrinsic noise in the inertial sensors. For example, in the inertial measurements from the accelerometers, the seismic environmental noise might cause discrete spikes, typically above 1 [Hz], due to the resonances in the local geology and test vehicle. H764G is a navigation-grade inertial sensor, which is very sensitive to the environmental noise, thus several spikes are present in the high frequency areas of PSD estimations of all the three accelerometers and three gyroscopes, shown in Figure B.35-2.40. A quantization noise exhibits itself in the high frequencies (higher than around 2 [Hz]) of all the accelerometers and gyroscopes. The rate white noise shows in the low frequencies (up to around 2 [Hz]) for the three gyroscopes. However, the three accelerometers have a flicker noise in the frequencies lower than 0.003 [Hz] and a rate white noise in the frequencies between 0.003 [Hz] with

around 2 [Hz]. The detailed PSD stochastic error characteristics and the coefficients are listed in Table B.10. The rate white noise present in the y accelerometer has more variations than the other two directions. Also, the spikes shown in the high frequencies of different axis of different inertial measurement units are different, which indicate that each axis of the inertial sensors experience various environmental noise. Different from the technique shown in the Allan variance analysis in section 1.1, no obvious effects of the rate random walk is evident in the accelerometers.

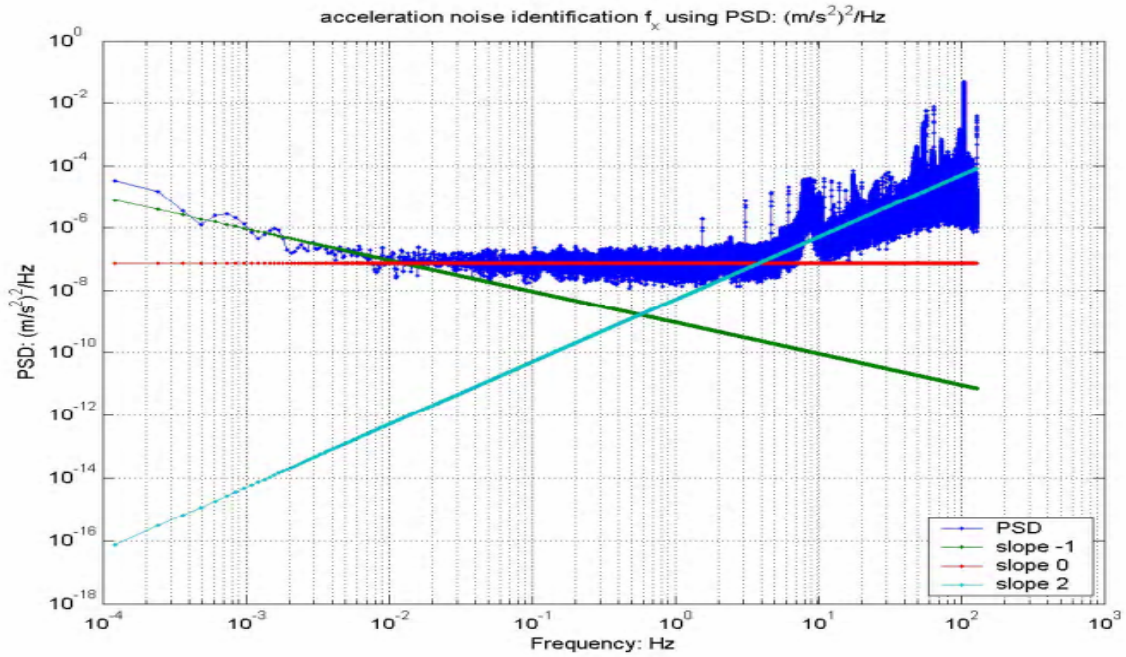


Figure B.35. PSD log-log plot fitting of the x acceleration for H764G using dataset of DOY 178, 2004.

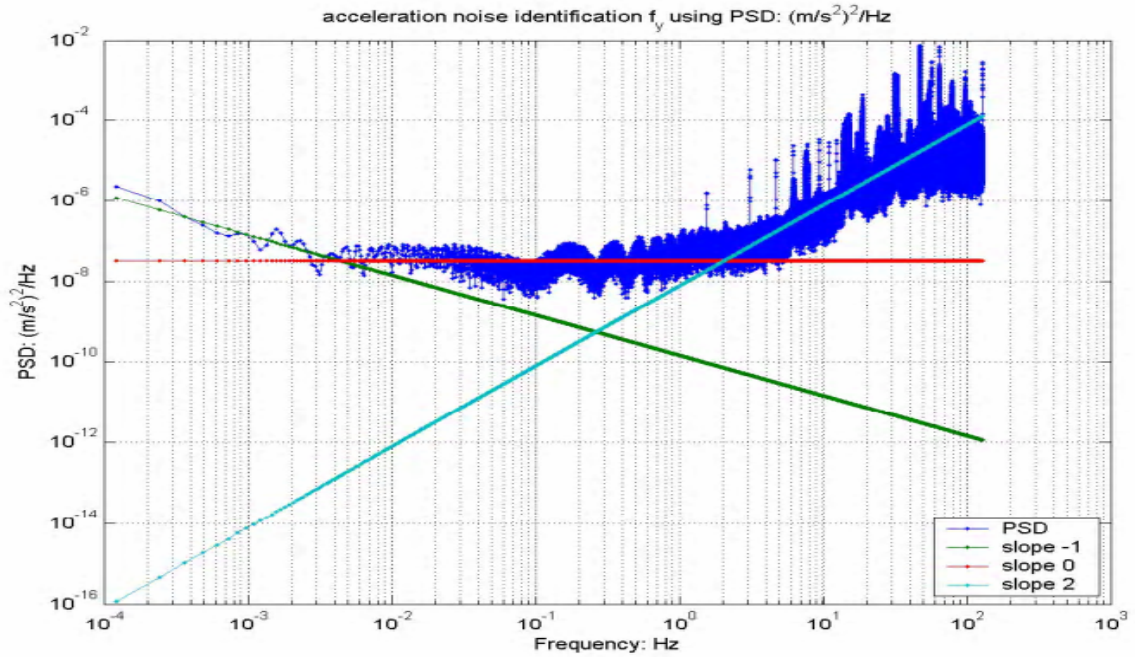


Figure B.36. PSD log-log plot fitting of the y acceleration for H764G using dataset of DOY 178, 2004.

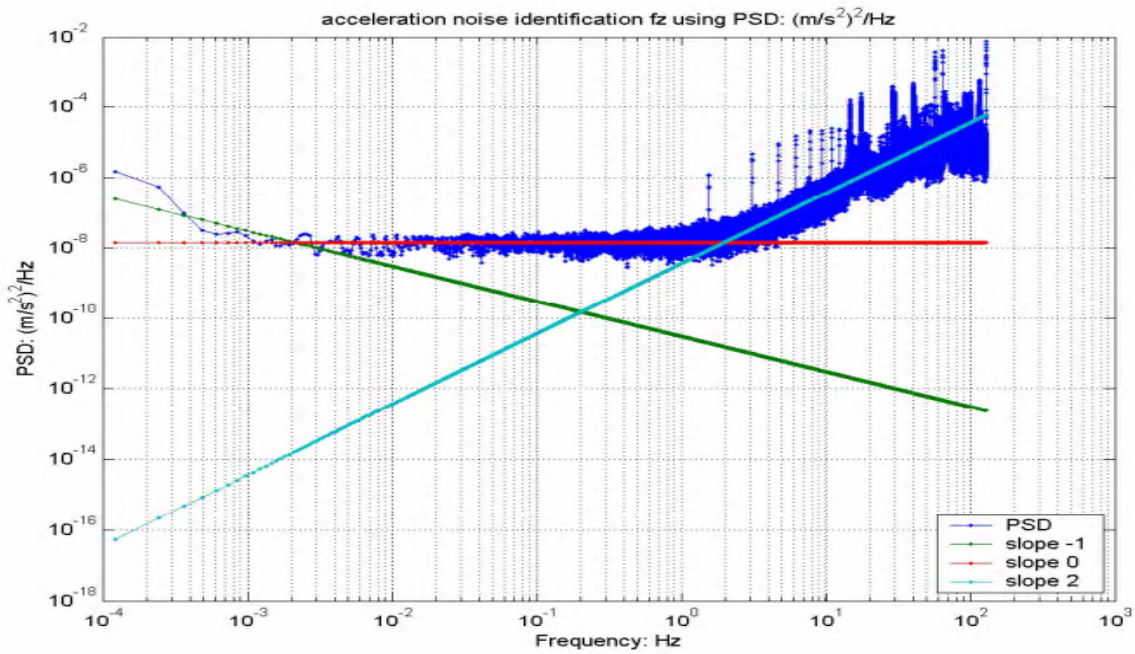


Figure B.37. PSD log-log plot fitting of the z acceleration for H764G using dataset of DOY 178, 2004.

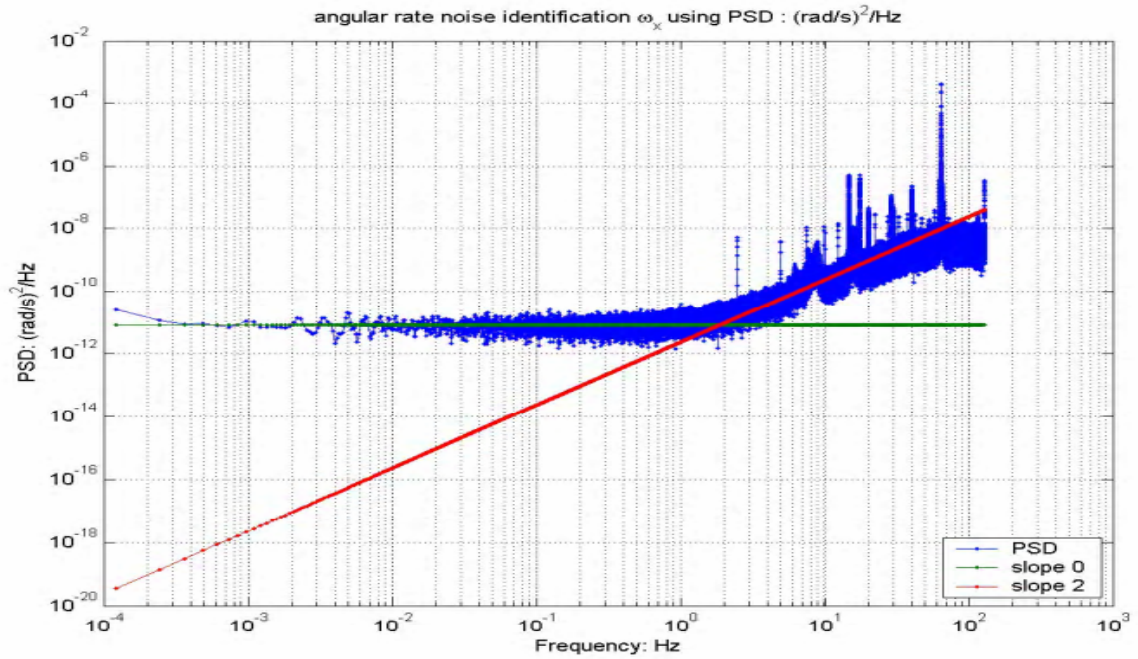


Figure B.38. PSD log-log plot fitting of the x angular rate for H764G using dataset of DOY 178, 2004.

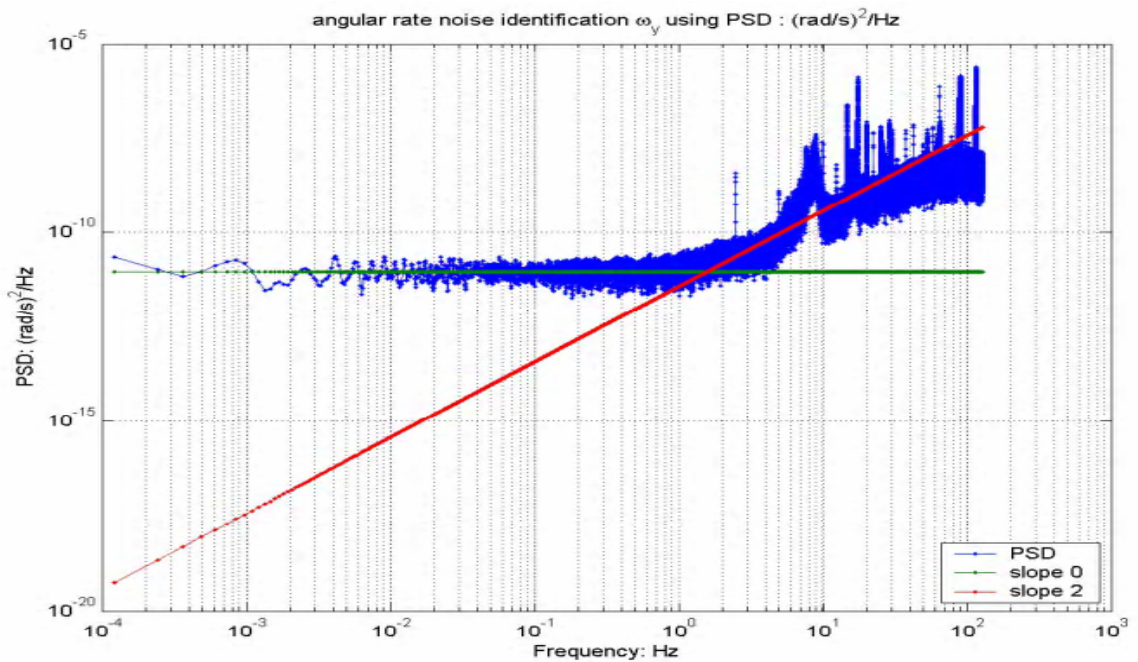


Figure B.39. PSD log-log plot fitting of the y angular rate for H764G using dataset of DOY 178, 2004.

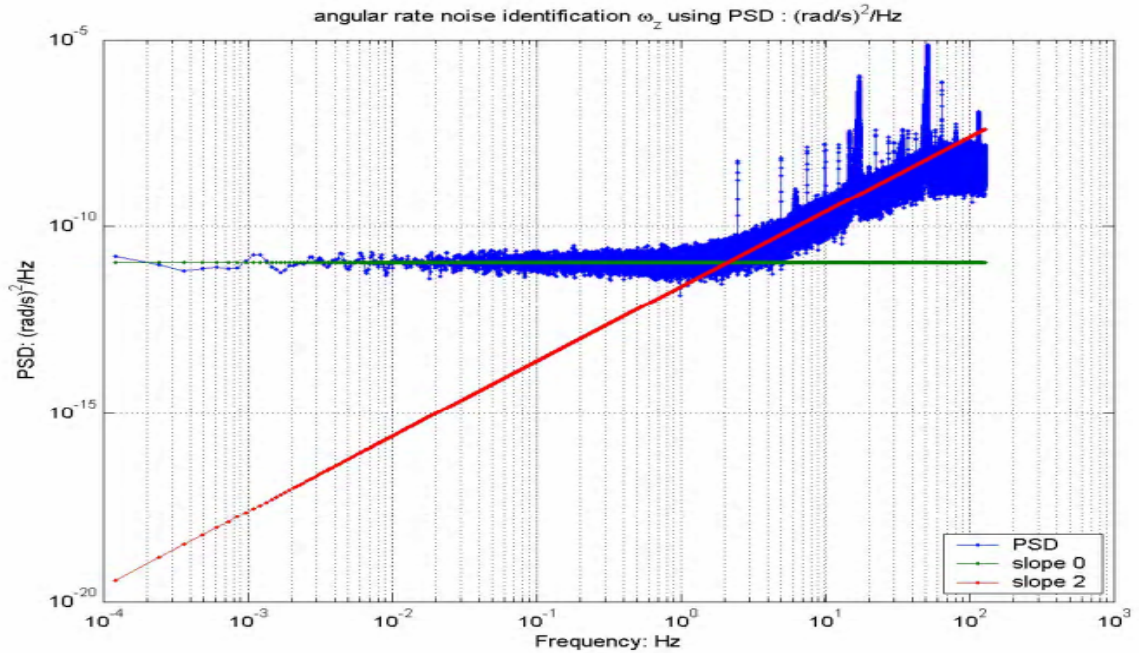


Figure B.40. PSD log-log plot fitting of the z angular rate for H764G using dataset of DOY 178, 2004.

		Q [+2]	N [0]	B [-1]	K [-2]	R [-2]
Error characteristics	f_X	>3 [Hz]	0.003~3 [Hz]	<0.003 [Hz]		
	f_Y	>2 [Hz]	0.003~2 [Hz]	<0.003 [Hz]		
	f_Z	>2 [Hz]	0.003~2 [Hz]	<0.003 [Hz]		
	ω_X	>2 [Hz]	<2 [Hz]			
	ω_Y	>2 [Hz]	<2 [Hz]			
	ω_Z	>2 [Hz]	<2 [Hz]			
		Q [+2] [unit•s]	N [0] [unit•s ^{1/2}]	B [-1] [unit]	K [-2] [unit/s ^{1/2}]	R [-2] [unit/s]
Error coefficients	f_X	0.0000801	0.0001940	0.0000544		
	f_Y	0.0000993	0.0001292	0.0000213		
	f_Z	0.0000676	0.0000843	0.0000097		
	ω_X	0.0000017	0.0000020			
	ω_Y	0.0000022	0.0000021			
	ω_Z	0.0000018	0.0000024			

Table B.10. PSD stochastic error characteristics and coefficients for H764G using dataset of DOY 178, 2004.

B.2.2 PSD analysis of LN100 static data

The data used here is the first static segment of the LN100 dataset of DOY 294, 2004. Figures 2.41-2.46 and Table B.11 present the stochastic error PSD characteristics and their log-log model fitting coefficients. These figures indicate that there exist less spikes in high frequencies (above 1 [Hz]) of the PSD spectrum of this sensor, comparing to that of H764G. However, the overall PSD characteristics are very similar to those of H764G. The quantization noise, rate white noise and flicker noise are all present in the measurements from the three accelerometers, and only the quantization noise and rate white noise are shown in the measurements from the three gyroscopes. The PSD estimation of measurements from the y gyroscope is abnormal, comparing to those from the measurements of x and z gyroscopes, which indicates that it has some problems. Therefore, the PSD-estimated coefficients of the y gyroscope will not contribute to the final coefficient estimation (to be shown in Section B.3).

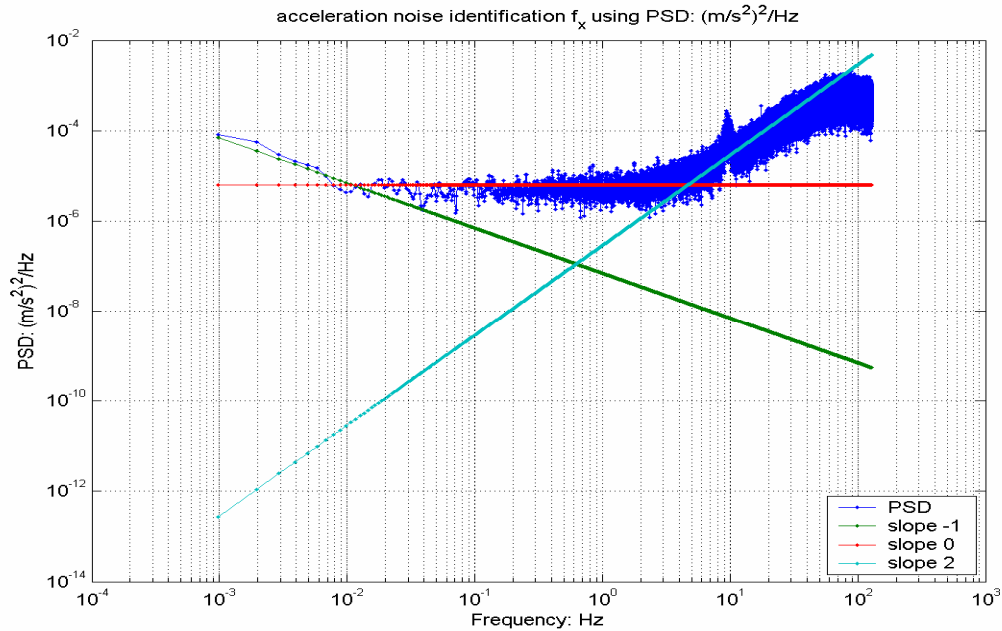


Figure B.41. PSD log-log plot fitting of the x acceleration for LN100 using dataset of DOY 294, 2004.

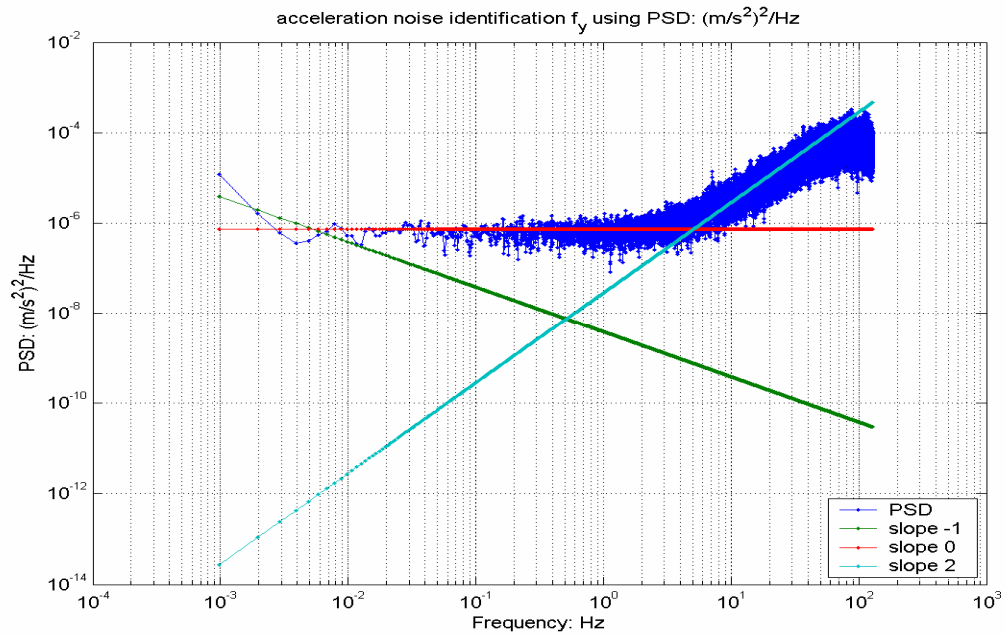


Figure B.42. PSD log-log plot fitting of the y acceleration for LN100 using dataset of DOY 294, 2004.

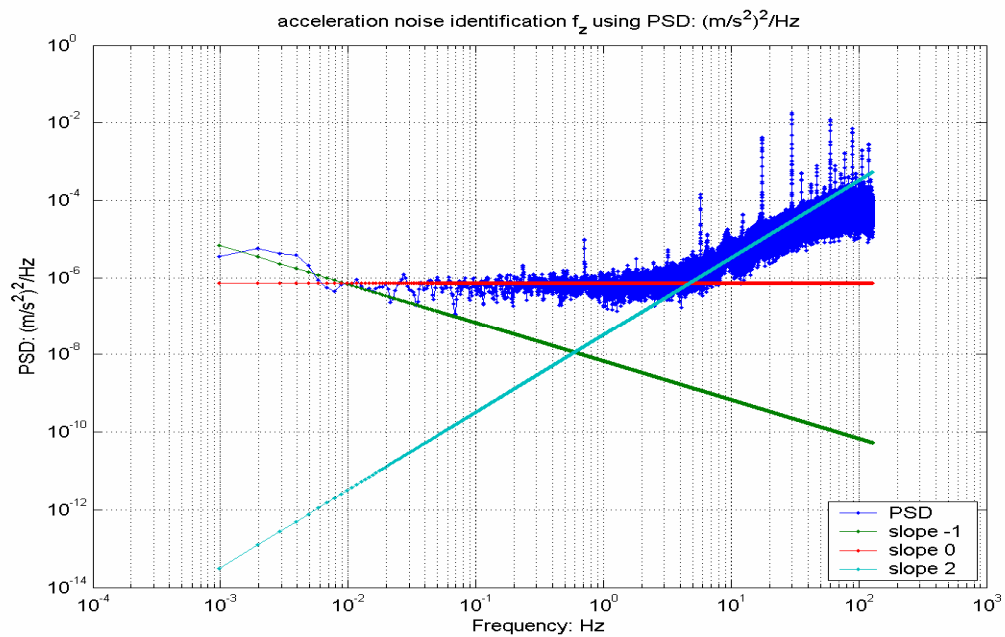


Figure B.43. PSD log-log plot fitting of the z acceleration for LN100 using dataset of DOY 294, 2004.

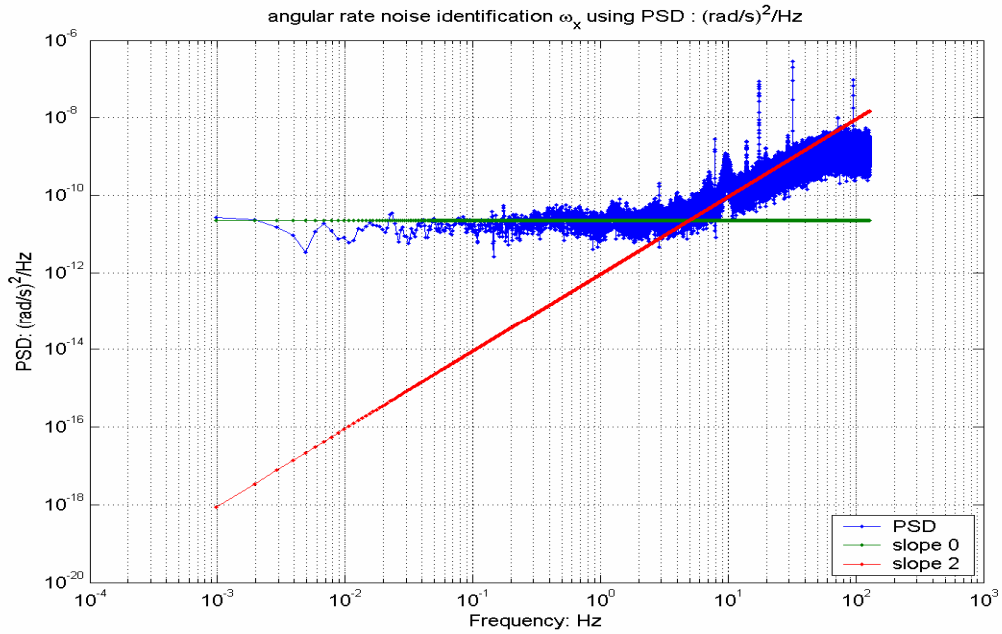


Figure B.44. PSD log-log plot fitting of the x angular rate for LN100 using dataset of DOY 294, 2004.

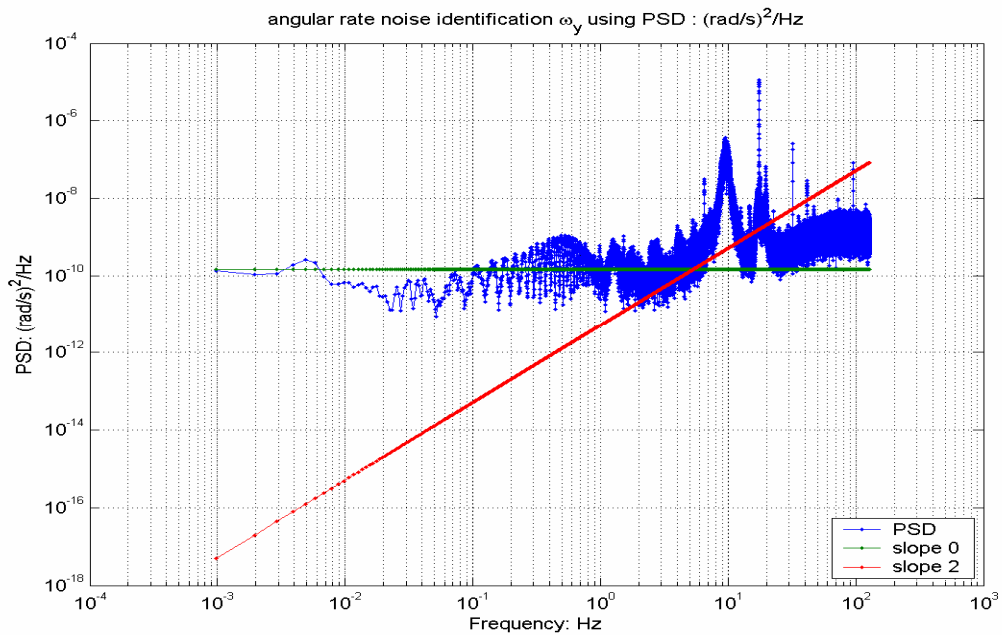


Figure B.45. PSD log-log plot fitting of the y angular rate for LN100 using dataset of DOY 294, 2004.

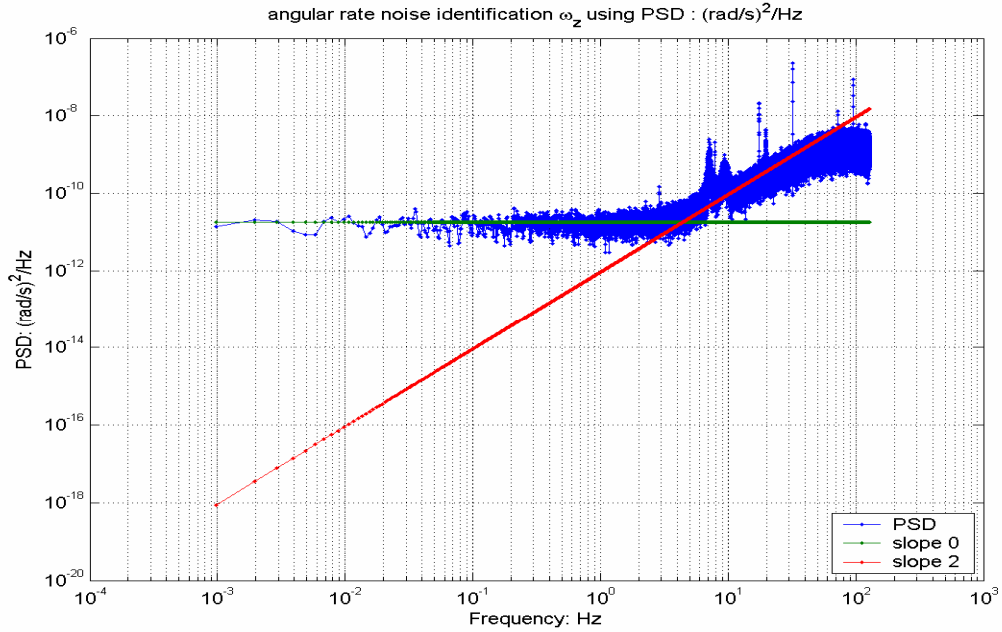


Figure B.46. PSD log-log plot fitting of the z angular rate for LN100 using dataset of DOY 294, 2004.

		Q [+2]	N [0]	B [-1]	K [-2]	R [-2]
Error characteristics	f_X	>4 [Hz]	0.01~4 [Hz]	<0.01 [Hz]		
	f_Y	>4 [Hz]	0.01~4 [Hz]	<0.01 [Hz]		
	f_Z	>4 [Hz]	0.01~4 [Hz]	<0.01 [Hz]		
	ω_X	>4 [Hz]	<4 [Hz]			
	ω_Y	>4 [Hz]	<4 [Hz]			
	ω_Z	>4 [Hz]	<4 [Hz]			
		Q [+2] [unit•s]	N [0] [unit•s ^{1/2}]	B [-1] [unit]	K [-2] [unit/s ^{1/2}]	R [-2] [unit/s]
Error coefficients	f_X	0.0006044	0.0017673	0.0004684		
	f_Y	0.0001894	0.0006072	0.0001095		
	f_Z	0.0002024	0.0006034	0.0001458		
	ω_X	0.0000011	0.0000033			
	ω_Y	0.0000025	0.0000085			
	ω_Z	0.0000011	0.0000030			

Table B.11. PSD stochastic error characteristics and coefficients for LN100 using dataset of DOY 294, 2004.

B.3.2 PSD analysis of HG1700 static data

The data used here is the long dataset of HG1700 collected on DOY 178, 2004. Figures 2.47-2.52 and Table B.12 present the stochastic error PSD characteristics and their log-log model fitted coefficients. There are few spikes in the high frequencies (above 1 [Hz]) of the PSD estimations of this sensor. This indicates that this tactical-grade INS senses well small environmental noise, comparing to the high-end navigation-grade H764G. The PSD characteristics of the three accelerometers are very similar to those of H764G. The quantization noise, rate white noise and flicker noise are all present in the measurements from the three accelerometers (shown in Figures 2.47-2.49). However, the quantization noise is not very obvious in the measurements of the gyroscopes, and the rate white noise almost dominates all the frequency areas of these measurements (shown in Figures 2.50-2.52 and Table B.10).

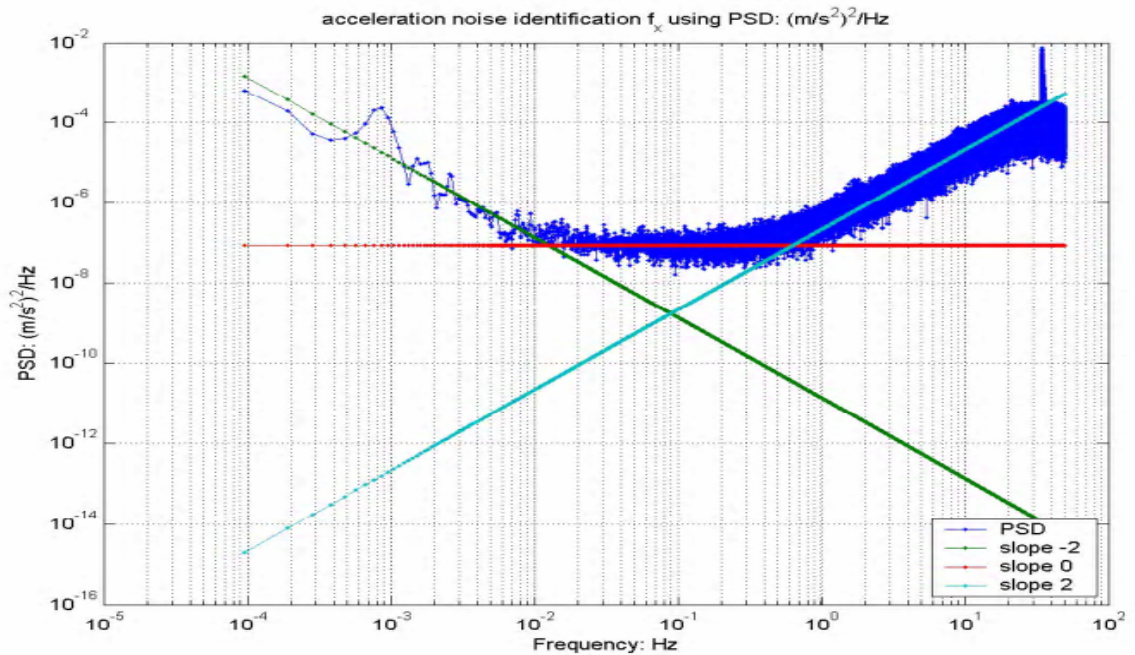


Figure B.47. PSD log-log plot fitting of the x acceleration for HG1700 using dataset of DOY 178, 2004.

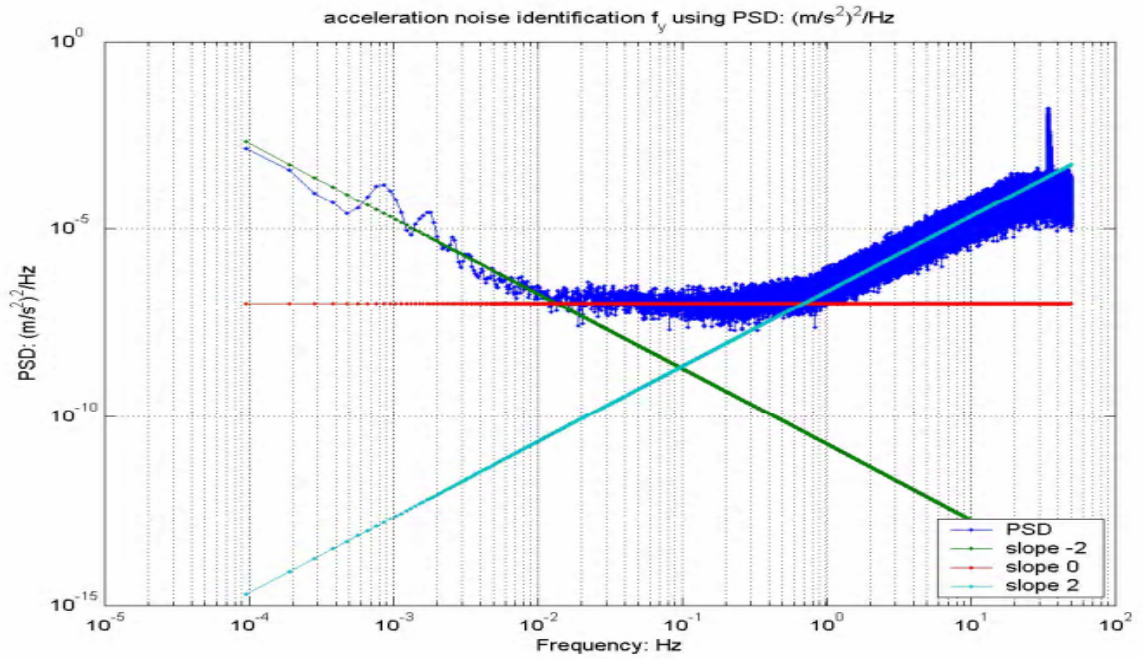


Figure B.48. PSD log-log plot fitting of the y acceleration for HG1700 using dataset of DOY 178, 2004.

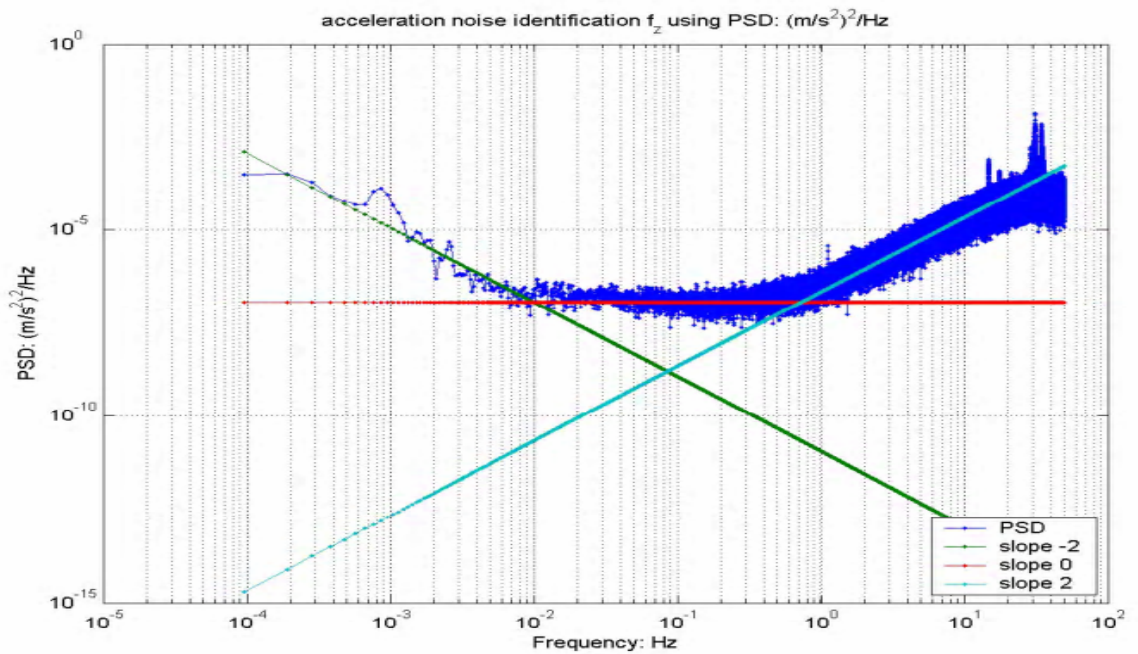


Figure B.49. PSD log-log plot fitting of the z acceleration for HG1700 using dataset of DOY 178, 2004.

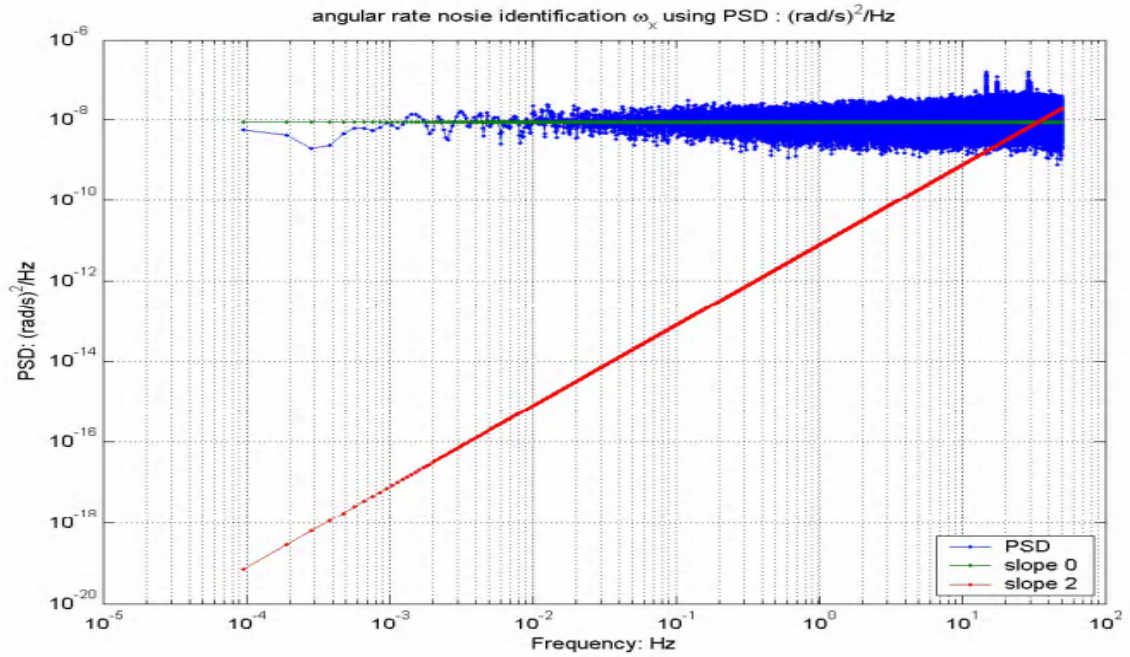


Figure B.50. PSD log-log plot fitting of the x angular rate for HG1700 using dataset of DOY 178, 2004.

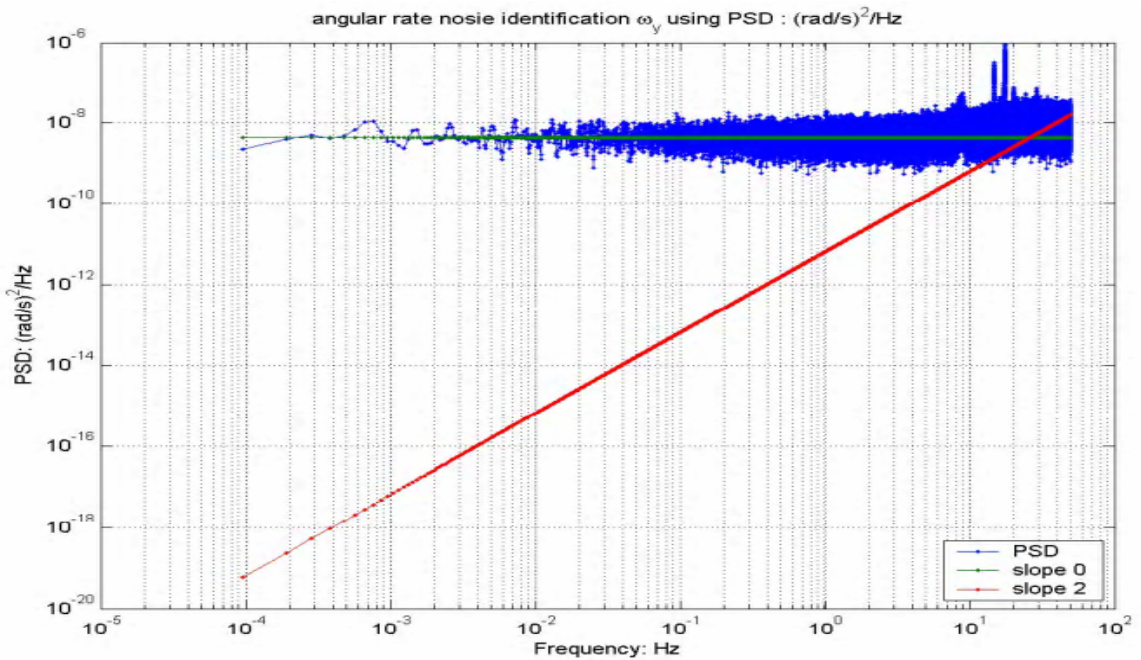


Figure B.51. PSD log-log plot fitting of the y angular rate for HG1700 using dataset of DOY 178, 2004.

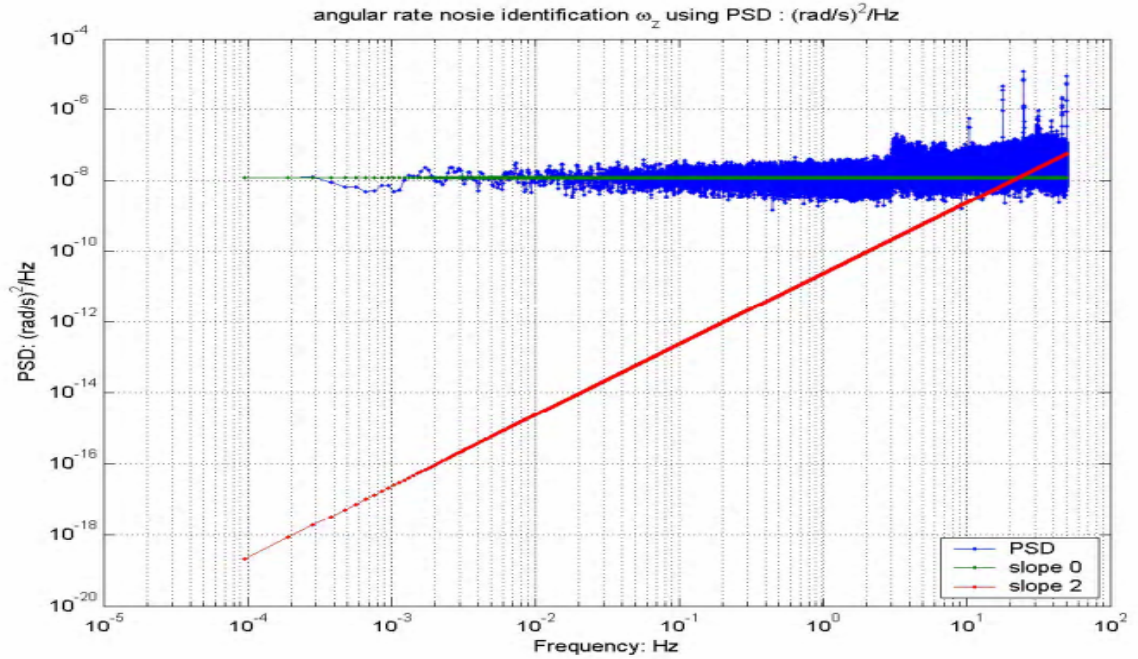


Figure B.52. PSD log-log plot fitting of the z angular rate for HG1700 using dataset of DOY 178, 2004.

		Q [+2]	N [0]	B [-1]	K [-2]	R [-2]
Error characteristics	f_X	>0.6 [Hz]	0.01~0.6 [Hz]	<0.01 [Hz]		
	f_Y	>0.7 [Hz]	0.02~0.7 [Hz]	<0.02 [Hz]		
	f_Z	>0.7 [Hz]	0.01~0.7 [Hz]	<0.01 [Hz]		
	ω_X	>25 [Hz]	<25 [Hz]			
	ω_Y	>25 [Hz]	<25 [Hz]			
	ω_Z	>25 [Hz]	<25 [Hz]			
		Q [+2] [unit*s]	N [0] [unit*s ^{1/2}]	B [-1] [unit]	K [-2] [unit/s ^{1/2}]	R [-2] [unit/s]
Error coefficients	f_X	0.0005210	0.0002096	0.0000165		
	f_Y	0.0005223	0.0002291	0.0000194		
	f_Z	0.0005229	0.0002425	0.0000150		
	ω_X	0.0000031	0.0000665			
	ω_Y	0.0000029	0.0000465			
	ω_Z	0.0000054	0.0000775			

Table B.12. PSD stochastic error characteristics and coefficients for HG1700 using dataset of DOY 178, 2004.

B.4.2 PSD analysis of MEMS IMU400CC static data

The data used here is the long dataset of IMU400CC collected on DOY 178, 2004. Figures 2.53-2.58 and Table B.13 present the stochastic error PSD characteristics and their log-log model fitting coefficients. The inertial measurements of IMU400CC are accelerations and angular rates, different from the accelerometer-integrated velocities and gyroscope-integrated angles of H764G, LN100 and HG1700. Thus, the quantization noise is not shown in these inertial measurements. The rate white noise and flicker noise are all present in the measurements from the three accelerometers and gyroscopes.

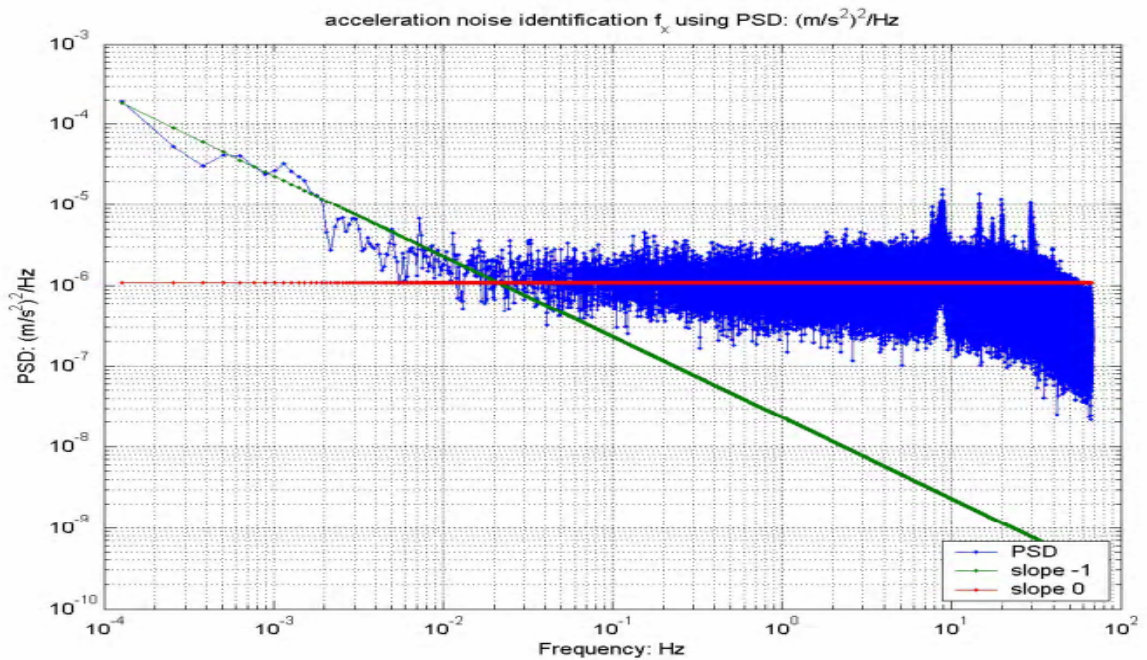


Figure B.53. PSD log-log plot fitting of the x acceleration for IMU400CC using dataset of DOY 178, 2004.

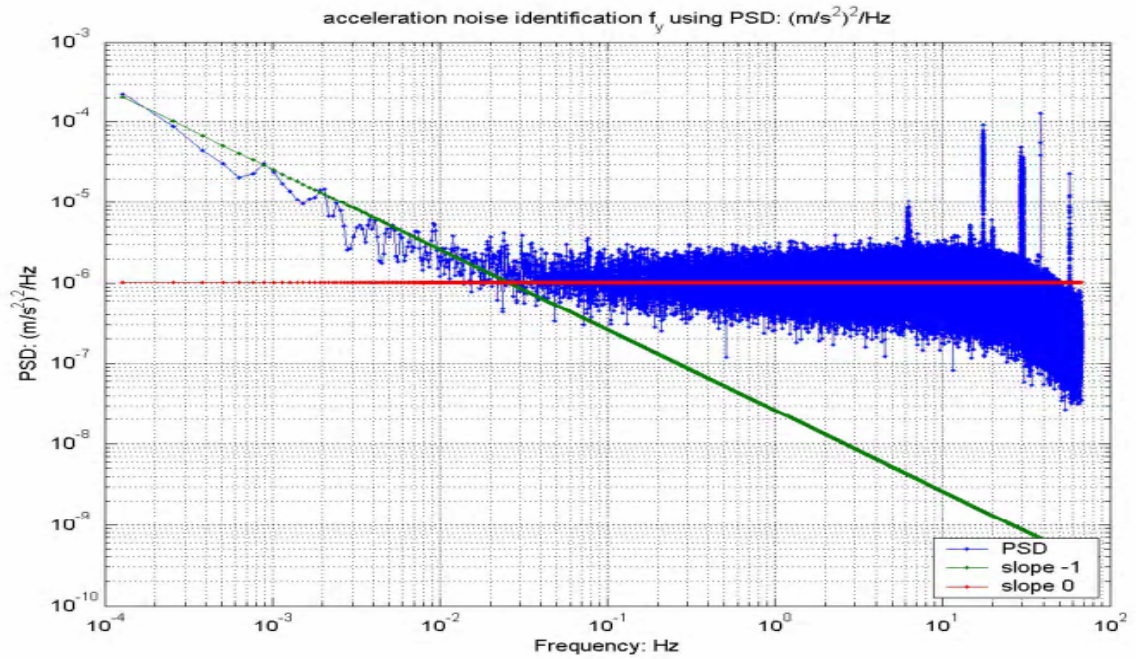


Figure B.54. PSD log-log plot fitting of the y acceleration for IMU400CC using dataset of DOY 178, 2004.

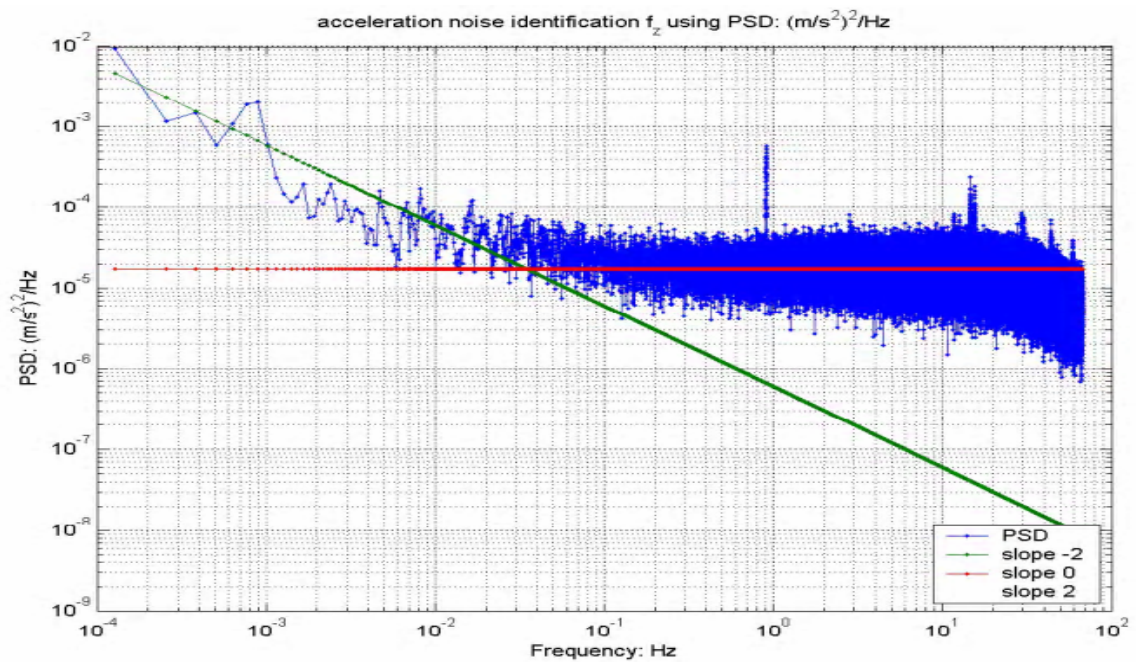


Figure B.55. PSD log-log plot fitting of the z acceleration for IMU400CC using dataset of DOY 178, 2004.

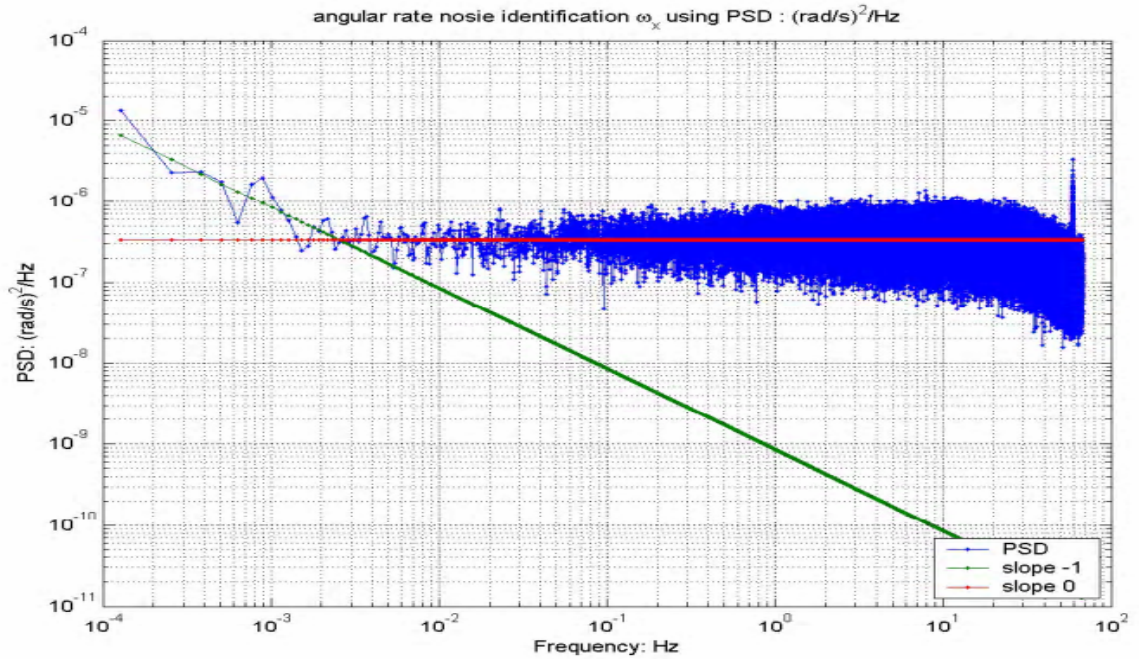


Figure B.56. PSD log-log plot fitting of the x angular rate for IMU400CC using dataset of DOY 178, 2004.

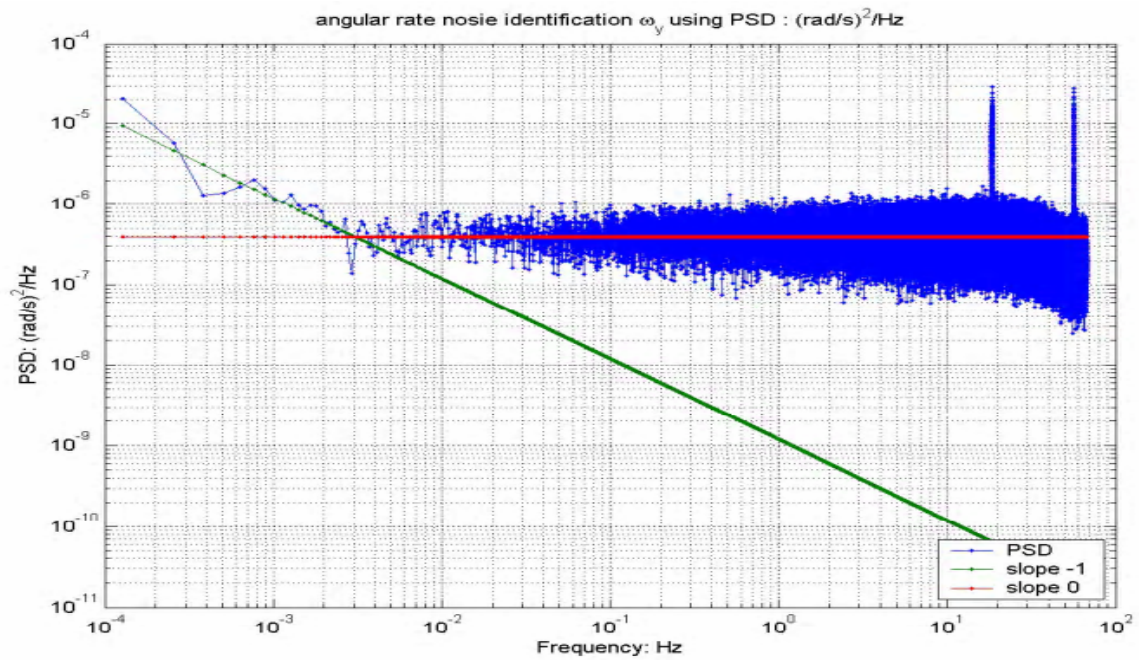


Figure B.57. PSD log-log plot fitting of the y angular rate for IMU400CC using dataset of DOY 178, 2004.

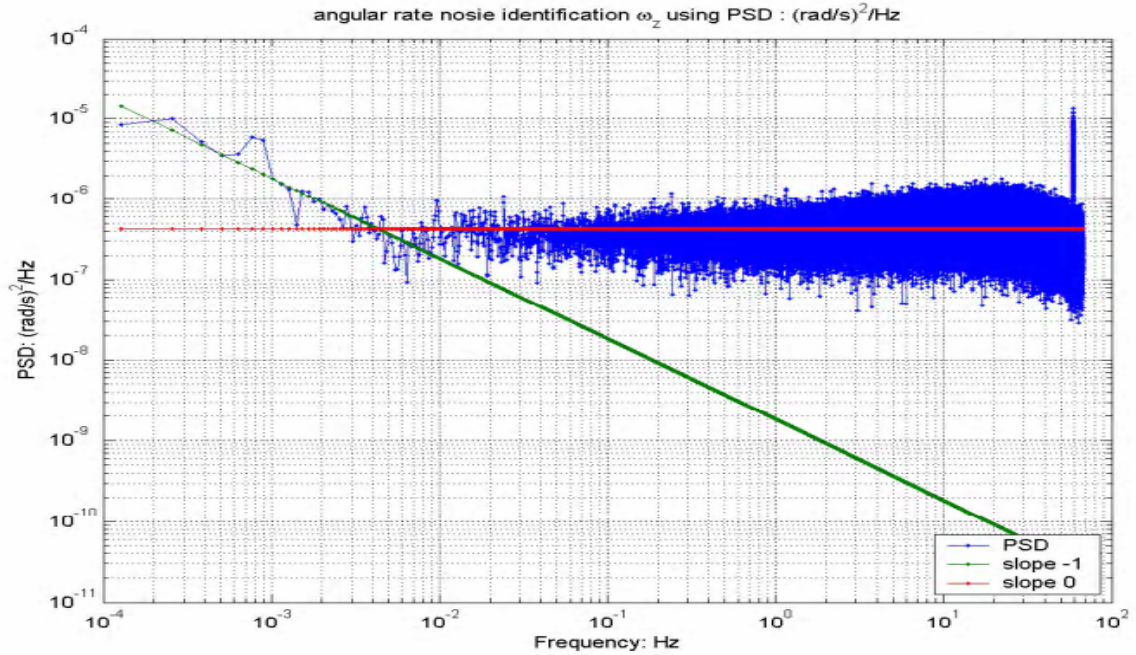


Figure B.58. PSD log-log plot fitting of the z angular rate for IMU400CC using dataset of DOY 178, 2004.

		Q [+2]	N [0]	B [-1]	K [-2]	R [-2]
Error characteristics	f_X		>0.02 [Hz]	<0.02 [Hz]		
	f_Y		>0.02 [Hz]	<0.02 [Hz]		
	f_Z		>0.02 [Hz]	<0.02 [Hz]		
	ω_X		>0.003 [Hz]	<0.003 [Hz]		
	ω_Y		>0.003 [Hz]	<0.003 [Hz]		
	ω_Z		>0.004 [Hz]	<0.004 [Hz]		
		Q [+2] [unit•s]	N [0] [unit•s ^{1/2}]	B [-1] [unit]	K [-2] [unit/s ^{1/2}]	R [-2] [unit/s]
Error coefficients	f_X		0.0007424	0.0002697		
	f_Y		0.0007134	0.0002867		
	f_Z		0.0029605	0.0013737		
	ω_X		0.0004078	0.0000518		
	ω_Y		0.0004424	0.0000613		
	ω_Z		0.0004610	0.0000760		

Table B.13. PSD stochastic error characteristics and coefficients for IMU400CC using dataset of DOY 178, 2004.

B.3 Summary of the INS stochastic error identification using the Allan variance analysis and the PSD method

This section summarizes the stochastic error identification for H764G, LN100, HG1700 and IMU400CC using the Allan variance analysis and the PSD method described in the preceding sections. Table B.14 summarizes the results from Tables 2.4, 2.5, 2.7, 2.9, 2.10, 2.11, 2.12 and 2.13. The estimated coefficients for the three orthogonal accelerometers and the three gyroscopes for the same inertial sensor using the same noise identification technique are averaged and listed in Table B.14, except for the abnormal coefficients marked in red. The cross-comparison of these stochastic error characteristics using the Allan variance analysis and the PSD method indicates that both results match very well except for some coefficients marked in red in Table B.14. The differences between the two methods (marked in red) are found in (1) the quantization noise and the rate random walk of the accelerometers of H764G, and (2) the flicker noise and rate random walk of the accelerometers of HG1700.

Sensor	Data	Method	Q [unit•s]	N [unit•s ^{1/2}]	B [unit]	K [unit/s ^{1/2}]	R [unit/s]
H764G	f _{XYZ}	AVAR	0.0001537	0.0001785	0.0000359	0.0000017	
		PSD	0.0000823	0.0001358	0.0000285		
	ω _{XYZ}	AVAR	0.0000038	0.0000024			
		PSD	0.0000019	0.0000022			
LN100	f _{XYZ}	AVAR	0.0002781	0.0006137	0.0001370		
		PSD	0.0001959	0.0006053	0.0001276		
	ω _{XYZ}	AVAR	0.0000016	0.0000031			
		PSD	0.0000011	0.0000032			
HG1700	f _{XYZ}	AVAR	0.0005020	0.0004426	0.0001360	0.0000252	
		PSD	0.0005221	0.0002271	0.0000170		
	ω _{XYZ}	AVAR		0.0000691			
		PSD	0.0000038	0.0000635			
IMU400 CC	f _{XYZ}	AVAR		0.0007656	0.0002501		
		PSD		0.0007279	0.0002782		
	ω _{XYZ}	AVAR		0.0004388	0.0000707		
		PSD		0.0004371	0.0000630		

Table B.14. INS estimated stochastic error coefficients using the Allan variance (AVAR) analysis and the PSD method.

Based on the common sensor stochastic error characteristics using the Allan variance analysis and the PSD method, the following conclusions are drawn:

- Rate white noise is found in all accelerometers and gyroscopes of H764G, LN100, HG1700 and IMU400CC.
- Quantization noise is found in the accelerometers of H764G, LN100 and HG1700, and in the gyroscopes of H764G and LN100.
- Flicker noise is found in the accelerometers of H764G, LN100, HG1700 and IMU400CC, and in the gyroscopes of IMU400CC.

Sensor	Data	Q [unit•s]	N [unit•s ^{1/2}]	B [unit]
H764G	\mathbf{f}_{XYZ}	0.0001180	0.0001572	0.0000322
	$\boldsymbol{\omega}_{XYZ}$	0.0000028	0.0000023	
LN100	\mathbf{f}_{XYZ}	0.0002370	0.0006095	0.0001323
	$\boldsymbol{\omega}_{XYZ}$	0.0000014	0.0000031	
HG1700	\mathbf{f}_{XYZ}	0.0005121	0.0003349	0.0001360
	$\boldsymbol{\omega}_{XYZ}$		0.0000663	
IMU400CC	\mathbf{f}_{XYZ}		0.0007468	0.0002642
	$\boldsymbol{\omega}_{XYZ}$		0.0004379	0.0000668

Table B.15. The final estimated coefficients of the INS stochastic error models.

The stochastic error coefficients, combining both the Allan variance analysis and the PSD method are listed in Table B.15. The rate random walk shown in the accelerometers of H764G and HG1700 are ignored and the final adopted coefficient B for the accelerometers of HG1700 is from the Allan variance analysis in this table. All other coefficients are averaged to obtain the final coefficients listed in Table B.15. In this table, the quantization noise in the accelerometers of H764G is smaller than that of LN100, while the quantization noise in the gyroscope of H764G is bigger than that of LN100. The quantization noise in the accelerometers of both navigation-grade INS (i.e. H764 and LN100) is smaller than that of the tactical-grade HG1700. The magnitude of the rate white noise in all accelerometers and gyroscopes is increasing from H764G, to LN100, to HG1700 and to IMU400CC, with the exceptions in the accelerometers of LN100, whose accelerometer rate white noise coefficient is bigger than that of HG1700. The flicker noise in the accelerometers of these sensors also follows the order: H764G smallest, LN100, HG1700 and IMU400CC largest.

B.4 INS stochastic error modeling

After the INS stochastic error characteristics have been identified using the aforementioned Allan variance analysis and (or) the PSD method, some random processes are normally used to approximate the noise spectrums of these stochastic errors. Amongst three types of stochastic errors shown in Table B.15, the flicker noise is very complex and currently no sound error models are found to approximate its noise

spectrum. The flicker noise of these inertial sensors shows itself in the lower frequencies (i.e. longer time than hundreds of seconds), thus it may only have some effects on free inertial navigation over a relatively long time. For the GPS/INS integration with relatively frequent GPS measurement update, the flicker noise will be less significant, comparing to other INS stochastic errors. Therefore, the flicker noise coefficients (B) shown in Table B.15 will only serve as the best achievable bias stability for a fully modeled inertial sensor. The other two INS stochastic errors (i.e. quantization noise and rate white noise) can be modeled depending on the different type of inertial measurements. As stated earlier, two different types of inertial measurements are obtained from the four inertial sensors; they are (1) accelerometer-integrated velocities and gyroscope-integrated angles; and (2) direct accelerations from accelerometers and angular rates from gyroscopes. The rate white noise is a white noise sequence in the rate domain corresponding to the second type of the measurements, and it is actually the measurement noise in such a case. In the integrated domain, corresponding to the first type of measurements, the rate white noise is a random walk process, while the quantization noise serves as the measurement noise. Such error models for the quantization noise and rate white noise are used in Chapter 4. The error models for the stochastic errors other than the quantization noise and rate white noise are briefly discussed in Chapter 4.

BIBLIOGRAPHY

1. Allan D. W. (1966). Statistics of Atomic Frequency Standards, *Proc. of the IEEE*, Vol. 54, No. 2, pp. 221-230.
2. Applanix Corp. (2007). <http://www.applanix.com/>, last accessed in Jan. 2007.
3. Arulampalam M. S., S. Maskell, N. Gordon and T. Clapp (2002). A Tutorial on Particle Filters for Online Nonlinear/Non-Gaussian Bayesian Tracking, *IEEE Transactions on Signal Processing*, Vol. 50, No. 2, pp. 174-188.
4. Ash M. E. and M.E. Skeen (1995). Maximum Likelihood Estimation of Fractional Brownian Motion and Markov Noise Parameters, *AIAA Journal of Guidance, Control and Dynamics*, Vol. 18, 1995, pp. 379-382.
5. Azimi-Sadjadi B. and P. S. Krishnaprasad (2000). Approximate Nonlinear Filtering and Its Applications for GPS. *Institute for Systems Research Technical Report*, TR 2000-37.
6. Bar-Itzhak, I.Y. and N. Berman (1988). Control Theoretic Approach to Inertial Navigation Systems, *AIAA Journal of Guidance, Control, and Dynamics*, Vol. 11, No. 3, pp. 237-245
7. Bierman G. J. (1977). *Factorization Methods for Discrete Sequential Estimation*, Dover Publications.
8. Bock Y., R. Nikolaidis, P. J. de Jonge and M. Bevis (2000). Instantaneous Geodetic Positioning at Medium Distances with the Global Positioning System, *Journal of Geophysical Research*, Vol. 105, pp. 28,223-28,254.
9. Bossler J. (1992). GPS Van: Input to GIS, *Proc. of ION GPS-1992*, pp. 427-437.
10. Bossler J., C. C. Goad, P. Johnson and K. Novak, (1991). GPS and GIS Map the Nation's Highways, *Geo Info Systems*, Vol. 1, No. 3, pp. 27-37.
11. Box G. E. P. and G. M. Jenkins (1976). *Time Series Analysis: Forecasting and Control*, San Francisco, Holden-Day.
12. Ching P.C., H. C. So and S. Q. Wu (1999). On Wavelet Denoising and Its Applications to Time Delay Estimation, *IEEE Transactions on Signal Processing*, Vol. 47, Issue 10, pp. 2879-2882.
13. Daubechies I. (1992). *Ten Lectures on Wavelets*, Soc. for Industrial & Applied Math, Philadelphia/PA, May, 1992.
14. de Freitas N., M. Niranjana, A. Gee and A. Doucet (1998). Sequential Monte Carlo Methods for Optimisation of Neural Network Models, *Technical report CUED/F-INFENG/TR 328*, Cambridge University Department of Engineering.

15. Djuric P. M. and Kay S. M. (1998). Spectrum Estimation and Modeling, In: V. K. Madisetti and D. B. Williams, *The digital signal processing handbook (ed)*, CRC Press, New York, *IEEE Press*, 1998.
16. Doucet A., N. de Freitas and N. Gordon (2001). *Sequential Monte-Carlo Methods in Practice*, Springer-Verlag.
17. Edoardo M. (2002). 1/f Noise: a pedagogical review, *eprint arXiv:physics/0204033*.
18. El-Sheimy N. (1996). The Development of VISAT- A Mobile Survey System For GIS Application, Ph.D Dissertation, Department of Geomatics Engineering, The University of Calgary, Calgary, Alberta, Canada.
19. Euler H. J. and B. Schaffrin (1990): On a Measure of the Discernibility between Different Ambiguity Solutions in the Static-Kinematic GPS-Mode, Banff, Canada, In: K.-P. Schwarz and G. Lachapelle (ed.), *Kinematic Systems in Geodesy, Surveying, and Remote Sensing, IAG Symposium*, No. 107, Springer-Verlag, pp. 285-295.
20. Evensen G. (1994). Sequential Data Assimilation with a Nonlinear Quasigeostrophic Model using Monte Carlo Methods to Forecast Error Statistics, *Journal of Geophysical Research*, Vol. 99. No. C5, pp. 10143-10162.
21. Evensen G. (1997). Advanced Data Assimilation for Strongly Nonlinear Dynamics, *Monthly Weather Review*, Vol. 125, Issue 6, pp. 1342-1354.
22. Evensen G. (2007). *Data Assimilation: The Ensemble Kalman Filter*, Springer, Berlin.
23. Farrell J.A. and M. Barth (1999). *The Global Positioning System and Inertial Navigation*, New York, McGraw-Hill.
24. Ford, J. J. and M. E. Evans (2000). Online Estimation of Allan Variance Parameters, *Journal of Guidance, Control, and Dynamics*, Vol. 23, No. 6, pp. 980-987.
25. Fotopoulos G. and M.E. Cannon (2001). An Overview of Multi-reference Station Methods for Cm-level Positioning, *GPS Solution*, Vol. 4, No. 3, pp. 1-10.
26. Gautier, J.D. and B.W. Parkinson (2003): Using the GPS/INS Generalized Evaluation Tool (Comparison of loosely-coupled, tightly-coupled and ultra-tightly coupled integration navigation). *Proc. of ION AM-2003*, Albuquerque, NM, pp. 65-76.
27. Gelb A. (1974). *Applied Optimal Estimation*, MIT Press.
28. Geodetics Inc. (2007), <http://www.geodetics.com/>, last accessed in Jan. 2007.
29. Gordon N. J., D. J. Salmond and A. F. M. Smith (1993). Novel Approach to Nonlinear/non-Gaussian Bayesian State Estimation, *Proc. of IEEE*, Vol. 140, No. 2, pp. 107-113.
30. Grejner-Brzezinska D. A., R. Da and C. K. Toth (1998). GPS Error Modeling and OTF Ambiguity Resolution for High-Accuracy GPS/INS Integrated System, *Journal of Geodesy*, 72(11), pp. 628-638.

31. Grejner-Brzezinska D. A., S. Moafipoor, Y. Jwa, C. K. Toth and J. Kwon (2006): Seamless and Reliable Personal Navigation, *Proc. of ION NTM-2006*, Monterey, CA, CD-ROM, pp. 597-603.
32. Grejner-Brzezinska D. A., Y. Yi and C. K. Toth (2001a). Precision GPS/INS Navigation in Urban Canyons: Dealing with GPS Losses of Lock, *Proc., IAG 2001 Scientific Assembly*, Budapest, Hungary, CD ROM.
33. Grejner-Brzezinska D. A., Y. Yi and C. K. Toth (2001b). Bridging GPS Gaps in Urban Canyons: Benefits of ZUPT, *Navigation*, Vol. 48, No. 4, pp. 217-225.
34. Grejner-Brzezinska D.A. (1999). Direct Exterior Orientation of Airborne Imagery with GPS/INS System: Performance Analysis, *Navigation*, Vol. 46, No. 4, pp. 261-270.
35. Grejner-Brzezinska D.A. and J. Wang (1998). Gravity Modeling for High-Accuracy GPS/INS Integration, *Navigation*, 45(3), pp.209-220
36. Grejner-Brzezinska D.A., (1997). High Accuracy Airborne Integrated Mapping System, *Advances in Positioning and Reference Frames*, F. K. Brunner (Ed.), *IAG Scientific Assembly*, Rio De Janeiro, Brazil, Springer, Berlin/Heidelberg/New York, pp. 337-342.
37. Grejner-Brzezinska, D. A. and Y. Yi (2003). Experimental GPS/INS/Pseudolite System for Kinematic Positioning, *Survey Review*, Vol. 37, No. 288.
38. Grejner-Brzezinska, D. A., C. K. Toth and Y. Yi (2005a): The assessment of the impact of stochastic error modeling, signal denoising and improved gravity compensation on the navigation performance of the multi-GPS/INS sensor assembly, *Proc. of ION AM-2005*, Cambridge, MA, pp. 988-999.
39. Grejner-Brzezinska, D. A., C. K. Toth and Y. Yi (2005b). On Improving Navigation Accuracy of GPS/INS Systems, *Photogrammetric Engineering and Remote Sensing*, Vol. 71, No. 4, April 2005, pp 377-389.
40. Grejner-Brzezinska, D., Y. Yi, R. Salman, D. Kopcha, R. Anderson, J. Davenport and J. Graham (2003): Enhanced Gravity Compensation for Improved Inertial Navigation Accuracy, *Proc. of ION GPS-2003*, Portland, OR, CD-ROM, pp. 2897-2909.
41. Han S. (1997a). An Instantaneous Ambiguity Resolution Technique for Medium Range GPS Kinematic Positioning, *Proc. of ION-1997*, pp. 1489-1800.
42. Han S. (1997b). Carrier-phase-based long-range GPS kinematic positioning, PhD Dissertation, UNISURV S-49, School of Geomatic Engineering, The University of New South Wales, Sydney, Australia.
43. Han S. (1997c). Quality-control Issues Relating to Instantaneous Ambiguity Resolution for Real-time GPS Kinematic Positioning, *Journal of Geodesy*, Vol. 71, Issue: 6, pp. 351-361.

44. Han S., and C., Rizos (1996). Integrated Method for Instantaneous Ambiguity Resolution Using New Generation GPS Receivers, *Proc. of IEEE PLAN-96*, pp. 254-261.
45. Hassan T., C. Ellum, S. Nassar, W. Cheng and N. El-Sheimy (2006). Photogrammetric Bridging of GPS/INS in Urban Centers for Mobile Mapping Applications, *Proc. of ION GPS-2006*, Fort Worth, TX, CD-ROM, pp. 604-610.
46. Hatch R. (1990). Instantaneous Ambiguity Resolution, *Proc. of KIS-90*, Banff, Canada, pp. 299-308.
47. Hatch R. and H. J. Euler (1994). Comparison of Several AROF Kinematic Techniques, *Proc. of ION GPS-1994*, pp. 363-370.
48. Hofmann-Wellenhof B., H. Lichtenegger and J. Collins (1997). *Global Positioning System, Theory and Practice*, Wien, New York: Springer-Verlag.
49. Hopfield H. S. (1969). Two Quadratic Tropospheric Refractivity Profiles for Correction Satellite Data, *Journal of Geophysical Research*, 74(18), 4487-4499.
50. ICD-GPS-200, Interface Control Document of the GPS, <http://www.navcen.uscg.gov/pubs/gps/icd200/default.htm>
51. IEEE Std 1293, (1998). IEEE Standard Specification Format Guide and Test Procedure for Linear, Single-Axis, Nongyroscopic Accelerometers, Sponsored by Gyro and Acceleration Panel of the IEEE Aerospace and Electronic Systems Society, Approved Sept. 25 1998 by IEEE-SA Standards Board, published by The Institute of Electrical and Electronics Engineers, Inc., New York, NY.
52. IEEE Std 528, (2001). IEEE Standard for Inertial Sensor terminology, Sponsored by Gyro and Acceleration Panel of the IEEE Aerospace and Electronic Systems Society, Approved Aug. 7 2001 by IEEE-SA Standards Board, published by The Institute of Electrical and Electronics Engineers, Inc., New York, NY.
53. IEEE Std 647, (1995). IEEE Standard Specification Format Guide and Test Procedure for Single-Axis Laser Gyros, Sponsored by Gyro and Acceleration Panel of the IEEE Aerospace and Electronic Systems Society, Approved Sept. 21 1995 by IEEE Standards Board, published by The Institute of Electrical and Electronics Engineers, Inc., New York, NY.
54. IEEE Std 952, (1997). IEEE Standard Specification Format Guide and Test Procedure for Single-Axis Interferometric Fiber Optic Gyros, Sponsored by Gyro and Acceleration Panel of the IEEE Aerospace and Electronic Systems Society, Approved Sept. 16 1997 by IEEE Standards Board, published by The Institute of Electrical and Electronics Engineers, Inc., New York, NY.
55. Ito K. and K. Xiong (2000). Gaussian Filters for Nonlinear Filtering Problems, *IEEE Transactions on Automatic Control*, 45(5):910-927.
56. Jazwinski A. H. (1970). *Stochastic Process and Filtering Theory*, New York: Academic Press.

57. Jekeli C. (2001). *Inertial Navigation Systems with Geodetic Applications*, deGruyter, Berlin/New York.
58. Julier S. J. and J. K. Uhlmann (1997). A New Extension of the Kalman Filter to Nonlinear Systems, *Proc. of the SPIE AeroSense International Symposium on Aerospace/Defense Sensing, Simulation and Controls*, Orlando, Florida.
59. Julier S. J., J. K. Uhlmann and H. Durrant-Whyte (1995). A New Approach for Filtering Nonlinear Systems, *Proc. of the American Control Conference*, pp. 1628-1632.
60. Kalman R. E. (1960). A New Approach to Linear Filtering and Prediction Problems, *Transactions of the ASME, Series D, Journal of Basic Engineering*, 82, pp.34-45
61. Kashani I., D. A. Grejner-Brzezinska and P. Wielgosz (2005). Towards Instantaneous RTK GPS over 100 km Distances, *Navigation*, Vol. 52, No. 4.
62. Keshner M. (1982). 1/f Noise, *Proc. of the IEEE*, Vol. 70, No. 3, pp. 212-218.
63. Kim D. and R. B. Langley (2000). GPS Ambiguity Resolution and Validation: Methodologies, Trends and Issues, *Proc. of the 7th GNSS Workshop and International Symposium on GPS/GNSS*, Seoul, Korea.
64. King A. D. (1998). Inertial Navigation—Forty Years of Evolution, *GEC Review*, Vol. 13, No. 3, pp. 140-149.
65. Lefebvre T., H. Bruyninckx and J. De Schutter (2002). Comment on “A New Method for the Nonlinear Transformation of Means and Covariances in Filters and Estimators”, *IEEE Transactions on Automatic Control*, 47(8).
66. Leick A. (1995). *GPS Satellite Surveying*, 2nd edition, John Wiley & Sons, New York.
67. Liu J. and R. Chen (1998). Sequential Monte Carlo Methods for Dynamic Systems, *Journal of the American Statistical Association*, 93:1032–1044
68. Ljung L. (1999). System Identification - Theory for the User, *Prentice Hall, Upper Saddle River*, N.J. 2nd edition, 1999.
69. Lu G. (1994). Development of a Multi-Antenna System for Attitude Determination, Ph.D dissertation, Department of Geomatics Engineering, University of Calgary, Alberta, CA, 1994.
70. Matlab (2007). *Online Document of Matlab R13*, last accessed on Jan. 20, 2007.
71. Moafipoor S. (2006). Updating the Navigation Parameters by Direct Feedback from the Image Sensor in a Multi-sensor System, *Proc. of ION GPS-2006*, Fort Worth, TX, CD-ROM, pp. 1085-1092.
72. Mohamed A. H. and K. P. Schwarz (1999). Adaptive Kalman Filtering for GPS/INS, *Journal of Geodesy*, Vol. 73, No. 4, pp. 193-203.
73. Nassar S. (2003). Improving the Inertial Navigation System (INS) Error Model for INS and GPS/INS Applications, Ph.D dissertation, Department of Geomatics Engineering, University of Calgary, Alberta, CA, 2003.

74. Pratt M., B. Burke and P. Misra (1997). Single-Epoch Integer Ambiguity Resolution with GPS L1-L2 Carrier-phase Measurements, *Proc. of ION GPS-1997*, pp. 1737-1746.
75. Press W. H., S. A. Teukolsky, W. T. Vetterling and B. P. Flannery (1992). *Numerical Recipes in C: The Art of Scientific Computing*, Cambridge University Press, 2nd edition.
76. Raquet J. F. (1998). Development of a Method for Kinematic GPS Carrier-Phase Ambiguity Resolution Using Multiple Reference Receivers, Ph.D dissertation, Department of Geomatics Engineering, University of Calgary, Alberta, CA, 1998.
77. Ristic B., S. Arulampalam and N. Gordon (2004). *Beyond the Kalman Filter: Particle Filters for Tracking Applications*, Artech House, Boston, London.
78. Ryan S., G. Lachapelle and M. E. Cannon (1997). DGPS Kinematic Carrier Phase Signal Simulation Analysis in the Velocity Domain, *Proc. of ION GPS-1997*, Kansas City, Missouri, pp. 1035-1046.
79. Salychev O. and B. Schaffrin (1992). New filter approaches for GPS/INS integration, *Proc. of the 6th International Geodetic Symposium on Satellite Positioning*, eds. Kumar M. and Fell P.J., Columbus, OH, pp. 670-680, Vol. II,
80. Salychev O. S. (1995). *Inertial Surveying: ITC Ltd. Experience*, Bauman MSTU Press, Moscow.
81. Salychev O. S. (1998). *Inertial Systems in Navigation and Geophysics*, Bauman MSTU Press, Moscow.
82. Sardy S., P. Tseng and A. Bruce (2001). Robust Wavelet Denoising, *IEEE Transactions on Signal Processing*, Vol. 49, Issue 6, pp. 1146-1152
83. Schaer S. and W. Gurtner (1998). IONEX: The IONosphere Map Exchange Format Version 1, *Proc. of the IGS AC Workshop*, Darmstadt, Germany.
84. Schaffrin B. (2000). Adjustment Computation I, GS 650 Lecture Notes, from Sep. to Dec. 2000, Columbus, OH, USA
85. Schaffrin B. (2001a). Adjustment Computation II, GS 651 Lecture Notes, from Jan. to March. 2001, Columbus, OH, USA
86. Schaffrin B. (2001b). Advanced Adjustment Computation, GS 762 Lecture Notes, from Sep. to Dec. 2001, Columbus, OH, USA
87. Schaffrin B. and Y. Bock (1988). A Unified Scheme for Processing GPS Phase Observations, *Bulletin Geodesique*, 62, pp. 142-160.
88. Schaffrin B. and Y. Pan (1999). Bayesian Wavelet Analysis for Image De-noising, *Photogr./Fernerk./Geoinform.* No. 2, pp. 95-100
89. Schaffrin, B. and E. Grafarend (1986). Generating Classes of Equivalent Linear Models by Nuisance Parameter Elimination, *Manuscripta Geodaetica*, Vol. 11, pp. 262-271.
90. Scherzinger B. (1997). A Position and Orientation Post-Processing Software Package for Inertial/GPS Integration (POSProc), *Proc. of KISS 97*, Banff, Canada.

91. Schwarz K. P., H. Martell, N. El-Sheimy, R. Li, M. Chapman and D. Cosandier (1993). VISAT- A Mobile Highway Survey System of High Accuracy, *Proc. of IEEE-Vehicle Navigation and Information System (VNIS) Conference*, Ottawa, pp. 476-481.
92. Seong S. M., J. G., Lee and C. G. Park (2000). Equivalent ARMA model representation for RLG Random Errors, *IEEE Transactions on Aerospace and Electronic Systems*, Vol. 36, No. 1, pp. 286-290.
93. Serrano L., D. Kim and R. B. Langley (2004). A GPS Velocity Sensor: How Accurate Can It Be? – A First Look, *Proc. of ION 2004 NTM-2004*, San Diego, California, pp. 875-885.
94. Siouris G. (1993). *Aerospace Avionics Systems*, Academic Press, San Diego/New York
95. Skaloud J. (2002). Direct Georeferencing in Aerial Photogrammetric Mapping, *Photogrammetric Engineering and Remote Sensing*, Vol. 68, No. 3, pp. 207-210.
96. Stockwell W. (2005). Bias Stability Measurement: Allan. Variance, http://www.xbow.com/Support/Support_pdf_files/Bias_Stability_Measurement.pdf
97. Teunissen P.J.G (1993). Least-squares Estimation of the Integer GPS Ambiguities, Invited Lecture, Section IV: Theory and Methodology, *IAG General Meeting*, Beijing, China, August 1993.
98. Teunissen P.J.G. (1994). A New Method for Fast Carrier Phase Ambiguity Estimation, *Proc. of IEEE PLANS'94*, pp.562-573.
99. Teunissen, P.J.G. and S. Verhagen (2004). On the Foundation of the Popular Ratio Test for GNSS Ambiguity Resolution, *Proc. of ION GNSS 2004*, September 21-24, Long Beach CA, pp. 2529-2540.
100. Teunissen, P.J.G. and S. Verhagen (2007). GNSS Phase Ambiguity Validation: A Review, *Proceedings, Space, Aeronautical and Navigational Electronics Symposium, SANE2007*, The Institute of Electronics, Information and Communication Engineers (IEICE), Japan, Vol. 107, No. 2, pp. 1-6.
101. Tiberius C and F. Kenselarr (2003). Variance Component Estimation and Precise GPS Positioning: Case Study, *Journal of Surveying Engineering*, Vol. 129, No. 1, pp. 11-18.
102. Tiberius C.C.J.M, P.J.G. Teunissen, and P.J. de Jonge (1997). Kinematic GPS: Performance and Quality Control. *Proc. of KIS'97*, Banff, Canada, pp. 289-299.
103. Titterton D. H. and J. L. Weston (1997). *Strapdown Inertial Navigation Technology*, Peter Peregrinus/IEE, London.
104. van der Merwe R. and E. A. Wan (2003). Sigma-Point Kalman Filters for Probabilistic Inference in Dynamic State-Space Models, *Workshop on Advances in Machine Learning*, Montreal
105. van der Merwe R. and E. A. Wan (2004). Sigma-Point Kalman Filters for Integrated Navigation, *Proc. of ION AM-2004*, Dayton, OH, pp. 641-654.

106. Van der Merwe R., A. Doucet, N. de Freitas and E. Wan (2000). The Unscented Particle Filter. *Technical report CUED/F-INFENG/TR 380*, Cambridge University Department of Engineering.
107. Verhagen S. (2004). Integer Ambiguity Validation: An Open Problem?, *GPS Solutions*, Vol. 8, Issue: 1, April, 2004, pp. 36-43.
108. Verhagen, S. (2005). On Reliability of Integer Ambiguity Resolution. *Navigation*, 52(2), pp. 99–110.
109. Veth M. and J. Raquet (2006). Fusion of Low-Cost Imaging and Inertial Sensors for Navigation, *Proc. of ION GPS 2006*, Fort Worth, TX, CD-ROM, pp. 1093-1103.
110. Vollath U., A. Buecherl, H. Landau, C. Pagels and B. Wagner (2000). Multi-Base RTK Positioning Using Virtual Reference Stations, *Proc. of ION GPS-2000*, Salt Lake City, Utah, CD-ROM, pp. 123-131.
111. Wan E.A. and R. van der Merwe (2001). *Kalman Filtering and Neural Networks, Chapter 7: The Unscented Kalman Filter*, New York: Wiley, Eds. S. Haykin.
112. Wang Z., B. Schaffrin and O.S. Salychev (1995). A Test Strategy for the Wave Algorithm, *Proc. of Mobile Mapping Symposium*, Columbus, OH, pp. 184-192.
113. Wielgosz P., D.A. Grejner-Brzezinska and I. Kashani (2004). Network Approach to Precise GPS Navigation, *Navigation*, Vol. 51, No. 3.
114. Yang M., C. C. Goad and B. Schaffrin (1994). Real-Time On-The-Fly Ambiguity Resolution over Short Baselines in the Presence of Anti-spoofing, *Proc. of GPS-1994*, Salt Lake City, UT, pp. 519-525.
115. Yi Y. and D. A. Grejner-Brzezinska (2004). Kinematic Carrier-phase Positioning Based on Multiple Base and Rover Receivers, *Proc. of the 4th International Symposium of Mobile Mapping Technology (MMT 2004)*, Kunming, China, CD-ROM.
116. Yi Y. and D. A. Grejner-Brzezinska (2005). Nonlinear Bayesian Filters: Alternatives to Extended Kalman Filter in GPS/INS fusion systems, *Proc. of ION GNSS-2005*, Long Beach, CA, CD-ROM, pp. 1391-1400.
117. Yi Y. and D. A. Grejner-Brzezinska (2006a). Performance Comparison of the Nonlinear Bayesian Filters Supporting GPS/INS Integration, *Proc. of ION NTM 2006*, Monterrey, CA, CD-ROM, pp. 977-983.
118. Yi Y. and D. A. Grejner-Brzezinska (2006b). Tightly-coupled GPS/INS Integration Using Unscented Kalman Filter and Particle Filter, *Proc. of ION GPS 2006*, Fort Worth, TX, CD-ROM, pp. 2182-2191.
119. Yi Y. and D.A. Grejner-Brzezinska (2003). Kinematic Carrier-phase GPS Positioning Aided by an Instantaneous Local Ionospheric Model Based on Multiple Base Stations Using Kriging, *Proc. of ION AM-2003*, Albuquerque, NM, CD-ROM, pp. 387-396.

120. Yi Y., D. A. Grejner-Brzezinska and C. K. Toth (2005). Performance Analysis of a Low Cost MEMS IMU and GPS Integration, *Proc. of ION AM-2005*, Cambridge, Massachusetts, CD-ROM, pp. 1026-1036.
121. Yi Y., D. A. Grejner-Brzezinska, C. K. Toth, J. Wang and C. Rizos (2003). GPS + INS + Pseudolites, *Innovation column of GPS World*, July 2003